2019

Deciphering the ovarian proteomic impacts of obesity

Kendra Leah Clark
Iowa State University

Deciphering the ovarian proteomic impacts of obesity

by

Kendra Leah Clark

A dissertation submitted to the graduate faculty

in partial fulfillment of the requirements for the degree of

DOCTOR OF PHILOSOPHY

Major: Genetics and Genomics

Program of Study Committee:
Aileen F. Keating, Major Professor
Jeffrey J. Essner
Donald S. Sakaguchi
Jason W. Ross
Geetu Tuteja

The student author, whose presentation of the scholarship herein was approved by the program of study committee, is solely responsible for the content of this dissertation. The Graduate College will ensure this dissertation is globally accessible and will not permit alterations after a degree is conferred.

Iowa State University

Ames, Iowa

2019

DEDICATION

I dedicate this thesis to my children; whose presence gave me reason. Additionally, I dedicate this work to all the people out there with questionable pasts that everyone gave up on but who never gave up on themselves.

TABLE OF CONTENTS

ABSTRACT

The ovary is the female reproductive organ responsible for the production of both the female gamete, the oocyte, and two major female sex hormones, estradiol and progesterone. During embryonic development, oocytes are formed from primordial germ cells and eventually become surrounded by squamous granulosa cells in a follicular structure, termed primordial. The oocyte numbers encased in primordial follicles are finite at birth and remain arrested in the diplotene stage of meiosis until ovulation or they degenerate through atresia. Once the pool of primordial follicles is depleted, ovarian senescence occurs. We hypothesized that the maternal metabolic changes that occur during lean gestational diabetes mellitus would impact offspring ovarian function both basally and in response to a dietary stressor later in life. We observed impacts on follicle numbers and alterations in the ovarian proteome, suggesting possible impacts on fertility and oocyte quality in relation to *in utero* and metabolic stressors. Additionally, we hypothesized that the ovarian DNA damage response is altered during obesity in adulthood. An elevated response in markers of DNA damage was observed, indicating that the metabolic status of the ovary during obesity initiates a low-level DNA damage response. Intercellular communication is also affected by a metabolic syndrome such as obesity or GDM exposure, with reduction of the gap junction protein Connexin-43 expression in antral follicles from ovaries that experienced obesity. Finally, to elucidate the molecular mechanisms behind the induction of the DNA damage response in the ovary after phosphoramide mustard exposure, we hypothesized that the DNA damage response would be blunted due to reduced abundance of the ATM protein. Using an $Atm^{+/-}$ mouse model to investigate impacts on folliculogenesis and the ovarian proteome, we determined that

Atm haploinsufficiency results in an irregular DNA damage response, alters the ovarian proteome, and impacts the rate of follicle loss after phosphoramide mustard exposure. Taken together, these findings demonstrate that the DNA damage response is initiated in the ovary during times of metabolic stress and in the absence of *Atm*, unhealthy follicles remain in the ovary, potentially contributing to poor oocyte quality or infertility.

CHAPTER 1. GENERAL INTRODUCTION

Dissertation Organization

This dissertation includes four manuscripts relevant to this doctoral work, which have either been published or submitted for publication in peer-reviewed journals. These manuscripts establish the foundation of the dissertation work and are preceded by a general introduction describing the significance of the research topic and review of the literature, and proceeded by a discussion of general findings, conclusions, and future considerations. In addition, portions of the literature review section of the dissertation have been published as an invited review and an additional manuscript published outside of the scope of the dissertation is included in the appendix.

Literature Review

Parts of the literature review are adapted from:

Clark KL, S Ganesan, AF Keating. 2018. Impact of toxicant exposures on ovarian gap junctions. *Reprod. Toxicol*. 81: 140-146.

Ovarian development, structure, and function

Early in mammalian embryonic development, the highly specialized primordial germ cells (PGCs), originate from the post implantation epiblast in response to extra-embryonic signaling from bone morphogenic proteins BMP4, BMP2, and BMP8B [1-3]. The proteins then bind with receptors that phosphorylate mothers against decapentaplegic

homologs SMAD1 and SMAD5, which then dimerize with SMAD4, leading to translocation into the nucleus to initiate the transcriptional regulators of the PCGs – PR domain zinc finger protein 1 (BLIMP1), PR domain zinc finger protein 14 (PRDM14), and transcription factor AP-2 gamma (AP2γ) [4-6]. The PGCs then migrate from the posterior primitive streak into the endoderm, through the hindgut, and into the dorsal mesentery before arriving at the genital ridge [7, 8]. Once at the genital ridge, cell migration is complete and the PGCs associate with the somatic cells of the gonad and eventually acquire their respective sex-specific morphologies and functions. Some of these cells will serve as germline stem cells, which undergo meiosis to produce the female or male gametes. In the female, the PGCs divide synchronously with incomplete cytokinesis to form a cluster of cells connected by intracellular bridges, forming a multi-nucleated germ cell nest [9, 10]. Coordinated somatic cell migration and germ cell apoptosis contribute to the packaging of individual germ cell nuclei, which become surrounded by flattened pre-granulosa cells to form the finite primordial follicle pool [9, 10].

The early mammalian gonad is bipotential, composed of undifferentiated precursor cells that can follow one of two possible fates, male or female. The Wolffian (mesonephric) ducts are the progenitors for the male reproductive tract and the Müllerian (paramesonephric) ducts are the precursors of the female reproductive tract [11]. Sex determination is triggered by the expression and proper function of the testes determining gene sex-determining region Y (*Sry)* in the presence of the Y chromosome, which signals cells to produce testosterone and anti-Müllerian hormone (AMH), resulting in the degeneration of the Müllerian ducts and differentiation of the testes [12, 13]. Conversely, the lack of *Sry* expression results in the regression of the Wolffian ducts and the

differentiation into the female reproductive tract [14]. The exact mechanisms behind early ovarian development are not well understood, though wingless-type MMTV integration site family member 4 (*Wnt4)*, nuclear receptor subfamily 0, group B, member 1 (*Dax1)*, and forkhead box L2 (*FoxL2)* have all been implicated as ovary determining factors [11, 14].

The ovaries are paired, oval-shaped organs, residing on each side of the uterus within the broad ligament below the fallopian tubes (**Figure 1**). The surface of the ovary is formed by a simple squamous-cuboidal epithelium, encasing the ovarian cortex and medulla. The ovarian cortex is home to thousands of follicles and considered the functional zone of the ovary, producing the sex steroids 17β-estradiol (E_2) and progesterone (P_4) within the stromal tissue and in the follicles as they mature. The inner medulla is also composed of supportive stromal tissue, enriched with a neurovascular network which enters at the hilum of the ovary. The structure of the ovary is dynamic, with extensive tissue remodeling occurring during folliculogenesis, ovulation, the formation and regression of the corpus luteum (CL), and follicular atresia.

Folliculogenesis

The follicle is the basic functional unit of the mammalian ovary, with follicle development being crucial for the maturation of oocytes and their subsequent release from the follicle. After the formation of the primordial follicle from the PGC, the oocytes remain in the first meiotic prophase until they receive intraovarian signals to activate growth before eventually becoming gonadotropin dependent. Ovarian folliculogenesis is the progression

of the primordial follicle into a primary, secondary, and antral follicle, in which the oocyte is then maintained prior to ovulation (**Figure 1**).

The initial transition from primordial follicle to primary follicle occurs when the surrounding granulosa cell morphology transitions from a squamous to cuboidal shape, followed by a dramatic increase in cytoplasmic and nuclear volume in the oocyte [15, 16]. Gap junctions begin to form between the granulosa cells and the granulosa cells and oocyte, allowing intercellular communication and the flow of molecules and nutrients [17, 18]. These junctions are described in more detail later. Another structural development as the follicle matures from primordial to primary is the formation of the zona pellucida. The zona pellucida is a glycoprotein polymer capsule that forms around the growing oocyte, providing protection that increases in thickness as oocyte diameter increases and remains with the oocyte even after ovulation, regulating the interaction between the oocyte and sperm during and after fertilization [19].

As the follicle transitions from a primary to secondary stage follicle, the granulosa cells surrounding the oocyte continue to proliferate to form more layers as well as increasing in size [15]. The oocyte in the secondary follicle now has a larger, sphere-shaped nucleus that grows concomitantly with the oocyte. During this time, the oocyte has completed its growth and gains the ability to resume meiosis. Other structural changes begin to occur after the transition to secondary follicle, such as the generation of the theca cell layer [15]. The theca cells proliferate from a population of unspecialized mesenchymal cells in the ovarian stroma to form a layer adjacent to the basal lamina, with the innermost layer known as the theca interna and outer layer called the theca externa [20]. The theca interna are a layer of highly vascularized steroidogenic cells while the theca externa is a

loosely organized layer of non-steroidogenic cells between the theca interna and ovarian stroma [20]. This vascularization enables the follicle to now secrete and respond to steroid hormones.

The first indication of the next stage of follicular development, the antral follicle, is the appearance of an internal cavity in the granulosa cells, characterized by the accumulation of fluid and establishment of polarity in the follicle [15]. At this point in folliculogenesis, there are no more changes in morphologic complexity, just changes in follicle size and cellular positions. The oocyte is surrounded by the granulosa cell layer called the corona radiata, the intermediate granulosa cell layer is termed the cumulus oophorus, followed by the periantral and membrana granulosa, the inner and outermost domains, respectively [15]. Processes that are implicated in the regulation of granulosa cell heterogeneity are cAMP regulatory events in response to follicle stimulating hormone (FSH) stimulation [21] and secretion of growth differentiation factor 9 (GDF-9) from the oocyte [22]. By the end of the antral stage, a dominant follicle, or in the case of multiparous species, follicles, emerge, shunting other recruited follicles towards atresia. The cumulus oophorus layer of the follicle will soon rupture, creating an opening for the oocyte and cumulus cells to be expelled during ovulation into the fallopian tube [23].

After ovulation, the basal lamina that separates the granulosa and theca cell layers degenerates, allowing the capillaries from the theca layer to penetrate into the granulosa layer to form a highly vascularized structure called the corpus luteum (CL), which is critical in providing the endocrine conditions, including the secretion of progesterone, that are necessary for the establishment and maintenance of pregnancy [23]. The luteinization of granulosa cells occurs via the accumulation of cytoplasmic lipid droplets, causing the cells

to enlarge [24]. The vascularization of the CL is driven by vascular endothelial growth factor (VEGF), aiding in the proliferation and support of the CL as it grows and develops connective tissue between the luteinized cells [25]. In the event of no conception, luteolysis occurs and a new cycle can begin.

Unlike male germ cells that are continuously produced throughout the male lifespan, female germ cell numbers are finite at birth, with oocyte numbers reaching their peak even prior to birth. At approximately five months of embryonic age in a human gestation, approximately seven million oocytes are present in the ovary, dropping to around two million at birth and by puberty, this number is estimated to be 250,000 to 400,000 oocytes [15]. When no functional oocytes remain, ovarian senescence (or menopause) occurs. Premature ovarian failure (POF) is defined as ovarian senescence prior to age 40 and affects approximately 1% of women, with often unknown etiology [26]. During a woman's reproductive lifespan, roughly 500 oocytes actually reach ovulation, leaving 99% of all primordial follicles that a woman was initially born with being lost to atresia [15].

Steroidogenesis

The precursor for steroid biosynthesis in the ovary is cholesterol. In the endocrine glands, cholesterol can be synthesized *de novo* from acetate or obtained from circulating cholesterol [27]. The first reaction in steroid hormone biosynthesis is the conversion of cholesterol to pregnenolone via the stimulation of the steroidogenic pathway by luteinizing hormone (LH) in the ovary [28]. This reaction occurs in the mitochondria, after cholesterol is shuttled into the inner mitochondrial matrix by steroid acute regulatory protein (STAR), then further catalyzed by an enzyme encoded by cytochrome P450 family 11, subfamily

A, member1 (CYP11A), C20-22-lyase [28]. The biochemical reactions that lead to the formation of estrogens and androgens in the ovary occur through a series of reactions in the Δ^4 (delta 4) and Δ^5 (delta 5) pathways [29].

The delta 5 pathway utilizes the enzyme 17α-hydroxylase to convert pregnenolone to 17-hydroxypregnenolone, which is then converted to dehydroepiandrosterone (DHEA) via C17-20-lyase [29]. DHEA is then transformed to androstenediol through reduction by 17β-hydroxysteroid oxidoreductase (17β-HSD), though this transformation is reversible via the oxidation of androstenediol [29]. The delta 5 pathway reactions are complete with the generation of androstenediol.

The delta 4 pathway utilizes 3β-hydroxysteroid dehydrogenase (3β-HSD) and Δ^{4-5} isomerase to convert pregnenolone to progesterone via oxidation and unlike the reversible transformation of DHEA/androstenediol in the delta 5 pathway, this reaction is irreversible [29]. After the formation of progesterone, the delta 4 pathway proceeds with the same enzymes in the delta 5 pathway, with 17α-hydroxylase converting progesterone to 17α-hydroxyprogesterone and C17-20-lyase converting 17α-hydroxyprogesterone to androstenedione [29]. The final product of the pathway, testosterone, is converted via 17β-HSD in a reversible reaction.

From these series of biochemical reactions, the androgens androstenedione and testosterone can be further processed via the aromatization reaction encoded by cytochrome P450 family 19, subfamily A, member 1 (CYP19A1) to form the estrogens estrone and estradiol [30]. Additionally, the compounds formed in the delta 5 pathway can be converted to compounds in the delta 4 pathway in an irreversible reaction with 3β-HSD [29]. Deficiencies in the enzymes that catalyze these reactions can result in the

feminization or masculinization of genitalia due to the defects in testosterone biosynthesis [31]. Deficiency in the type 3 isoenzyme of 17β-HSD leads to the formation of both male and female genitalia [31]. Similarly, deficiencies in 17α-hydroxylase and C17-20-lyase results in the lack of testosterone production [32].

Granulosa cells are unable to convert pregnenolone to androstenedione due to lack of 3β-HSD, so estradiol conversion takes place in theca cells from pregnenolone that has been shuttled through the basal lamina from the granulosa cells [33]. Likewise, lack of 17β-HSD in the theca cells leads to the conversion and production of testosterone in the granulosa cells [33]. These mechanisms occur via a series of cooperative interactions of theca and granulosa cells, acting on hormonal signaling from LH and FSH, respectively, and along with the lack of CYP19A1 in theca cells, provides the rationale for the two cell, two-gonadotropin theory [33]. Gene expression that encodes for production of respective enzymes in ovarian cells increase or decreases dependent on hormonal signaling. After ovulation, the synthesis and production of progesterone occurs similar to the production of estradiol, though after cholesterol is converted to pregnenolone, 3β-HSD works to convert pregnenolone to progesterone in the luteinized granulosa and theca cells [23].

Hypothalamic-pituitary-gonadal axis

Endocrine signals regulate the female reproductive cycle mainly via a negative feedback system in the ovary and in the hypothalamus and pituitary glands within the brain, termed the hypothalamic-pituitary-gonadal (HPG) axis. The signal that initiates and drives the reproductive cycle arises from gonadotropin-releasing hormone (GnRH) neurons in the hypothalamus [34, 35]. A pulse of GnRH is released and stimulates the release of LH and

FSH from the pituitary gland, which subsequently travel to the ovary via circulation. These hormones induce morphologic changes that occur during folliculogenesis and formation of the CL, aid in the production of the ovarian steroid hormones estradiol and progesterone, and LH is critical for ovulation to occur.

Once released from the pituitary, FSH acts on FSH receptors in the granulosa cells, marking the beginning of the follicular phase. As the follicles grow, they begin to increase the production and secretion of estradiol with the conversion of androstenedione from the theca cells. Increased amounts of FSH act as a stimulus for inhibin B secretion, which along with estradiol, has a negative feedback effect on FSH release [36, 37]. Luteinizing hormone released from the pituitary binds to receptors in the theca cells and induces the production of androgens that are aromatized in the granulosa cells to produce estradiol [38]. The growing antral follicles compete for FSH, and those who have fewer FSH receptors begin to decline in growth and subsequently become atretic, while a dominant follicle emerges and continues to grow, with the peak of estradiol secretion occurring when this follicle is fully mature and ready for ovulation [37]. At this time, estradiol secretion acts as a positive feedback mechanism and triggers the LH surge required for ovulation [38].

At the end of the follicular phase, the surge of LH initiates ovulation and the beginning of the luteal phase. Prior to the LH surge, a small increase of progesterone occurs and after ovulation and the formation of the CL, progesterone secretion gradually increases and dominates [39]. Maintenance of pregnancy is dependent on progesterone secretion and circulation, utilizing a negative feedback mechanism to decrease the GnRH pulse frequency similar to estradiol during the follicular phase. In humans, if there is an

absence of increased levels of human chorionic gonadotropin (hCG) signaling for successful fertilization and pregnancy [40], estradiol and progesterone levels decline, the CL diminishes, and FSH levels rise to facilitate another menstrual cycle.

Ovarian gap junctions

Gap junction intercellular communication (GJIC) facilitates the exchange of ions, metabolites, Ca^{2+}, inositol phosphates, and/or cyclic nucleotides of up to 1.8 kD in size between cells through contact-dependent mechanisms [17, 18]. Oocyte growth, development, and survival depends upon the supply of nutrients, amino acids, glucose metabolites, and nucleotides transmitted from follicle cells via gap junctions (GJ). Interconnection of ovarian cells via GJ is observed between the innermost layer of cumulus cells and the oocyte, between adjacent cumulus cells, between granulosa cells and also between cumulus and granulosa cells [90]. Gap junctions are made up of six connexin (CX) proteins to form a connexon, a hollow ring in the plasma membrane that enables communication between the cells when coupled with another connexon in an adjacent cell (**Figure 2**), with the capacity to change function based on protein isoform or post translational modification, though this mechanism remains vague [91, 92].

Localization of CX proteins is used for GJ identification in a variety of tissues [93] and the CX family of proteins is very diverse, with 20 proteins in mice and 21 in humans, each the product of a distinct gene [94]. A total of 8 CX proteins are known to be expressed in the ovary, with expression varying in a species-specific manner. Porcine ovaries express *GJB2, GJB4*, *GJB1*, *GJA1,* and *GJA1* [95, 96]. In ovine ovaries, *GJB2, GJB1*, *GJA4*, and *GJA1* have been detected [97-99]. Similar to the sheep, bovine ovaries also express *GJB2,*

GJB1, GJA4, and *GJA1*[100, 101]. In mouse and rat, *GJB1*, *GJA4*, *GJA1*, *GJC1,* and *GJA10* have been detected in the ovary [102]. Pannexin genes have also been implicated in GJ channeling, but less is known about their functions [103]. Pannexin1 (Panx1) has been identified in human ovary and placenta, but no further work has been performed to describe Panx1 function in the female reproductive system [104].

Gap junction proteins are subject to hormonal regulation in various tissue types. Both E_2 and P_4 regulate GJIC in the reproductive system, heart, brain, and liver via complementary or opposing actions dependent on physiological context and tissue phenotype [105]. An increase in *Gja1* mRNA and GJ formation is stimulated by E_2 while, in contrast, an inhibitory effect is mediated by P_4 in the female reproductive system [106, 107]. Follicle stimulating hormone (FSH) and luteinizing hormone (LH) also have similar effects on GJIC in reproductive tissues, where FSH stimulates upregulation of *Gja1* mRNA and protein, and *Gja1* expression is elevated as follicle size increases in response to FSH [108-111]. In contrast, LH stimulates a reduction in *Gja1* mRNA and protein [112-115].

Alterations of CX expression are also detected throughout the stages of the estrous cycle. In sheep, *GJB2* mRNA expression in the corpus luteum (CL) is at its highest at d10 of the estrous cycle and decreases in PGF-induced luteal regression [98]. In bovine, *GJB2* mRNA is highest during the second half of the estrous cycle and after luteal regression [116]. *GJB1* mRNA and protein expression remains relatively stable throughout the estrous cycle [98, 99]. In contrast, *GJA4* mRNA expression is increased after hCG treatment in sheep, and expression of GJA4 protein and mRNA is greatest on d5 of the estrous cycle with a gradual decrease thereafter [97]. *GJA1* mRNA expression in sheep decreases in the granulosa and theca cells after hCG treatment and in the luteal tissue but

is observed to increase in the CL on d5 of the estrous cycle [98, 99]. The expression of bovine *GJA1* mRNA decreases after injection of GnRH and after luteal regression, with higher *GJA1* levels observed in the CL during the early luteal phase [116]. In addition to changes during the estrous cycle, high levels of *GJB2* and *GJA1* mRNA are detected throughout pregnancy in cattle [116].

Ovarian GJ investigations have primarily focused on defining the function and role of ovarian GJA4 and GJA1. The generation of a *Gja4*-null mouse demonstrated arrest of folliculogenesis at the early antral follicular stage and oocytes that do not reach meiotic competence [117, 118]. Interestingly, a genetic variant of *Gja4* is associated with primary ovarian insufficiency in women [119] while another Gja4 gene variant is associated with polycystic ovarian syndrome in women [120]. Deficiency of *Gja1* is postnatally lethal in mice, so *Gja1*$^{-/-}$ prenatal ovaries have been cultured *ex vivo* or via transplant, and these ovaries also have retarded oocyte growth and arrested folliculogenesis [121, 122]. Further supporting the roles of GJA4 and GJA1 in the ovary are chimeric ovary studies which paired wild-type (WT) oocytes with *Gja1*-deficient somatic cells; *Gja1*-deficient oocytes with WT granulosa cells; WT oocyte with *Gja4*-deficient granulosa cells; or *Gja4*-deficient oocytes with WT granulosa cells [123, 124]. In ovaries containing WT granulosa cells with *Gja1*$^{-/-}$ oocytes or WT oocytes and *Gja4*$^{-/-}$ granulosa cells, meiosis occurred, and fertilization could be achieved. In contrast, ovaries with WT granulosa cells and *Gja4*$^{-/-}$ oocytes could not proceed with meiosis and did not achieve fertilization. In ovaries with *Gja1*$^{-/-}$ granulosa cells and WT oocytes, follicles remained in the early preantral stages and contained smaller oocytes [124].

In addition to *Gja4* and *Gja1*, knockout of *Gjc1* and *Gjb2* in mice has been accomplished but leads to embryonic death with cardiovascular defects and insufficient embryonic development, respectively [125-128]. *Gja10* knockout mice have no ovarian defects although they do have deficiencies in the visual system and *Gjb1* null mice remain fertile [129, 130]. Ovarian findings for these genetic mice models lacking *Gja4* and *Gja1* support that ovarian CX proteins have important roles in relation to follicle and oocyte survivability, quality, and growth.

Obesity

Obesity is a preventable metabolic disorder that has become a global health epidemic, with worldwide estimates that roughly 13% of the world's population is considered obese and 39% considered overweight [41] . In the United States these numbers are even more staggering, with nearly 40% of the adult population considered obese [42]. Moreover, the obesity epidemic seems to affect women more than men, with around 42% of adult women experiencing obesity and in some ethnic groups, this number is as high as 50% [42]. Unfortunately, obesity among young girls is also on the rise, with about 18% of girls aged 2-19 considered obese [42]. Obesity is associated with several interrelated disorders including diabetes [43], cardiovascular disease [44], chronic inflammation [45], and cancer [46]. The reproductive phenotypes observed in obese women include early puberty onset [47], poor oocyte quality [48], polycystic ovary syndrome (PCOS) [49], infertility [50], pregnancy complications [51], gestational diabetes [52], congenital abnormalities in offspring [53], and an increased risk of reproductive cancers [54].

The mechanisms in which changes in central metabolism during obesity affect the ovary have previously demonstrated by our group and others. Hyperinsulinemia is common during obesity, impacting the upregulation of the insulin responsive PI3K-PTEN-AKT-FOXO signaling pathway, resulting in increased follicular activation [55, 56]. With increased follicle activation, a reduction of primordial and primary follicle numbers is observed in a model of progressive obesity [56]. Disturbances in the estrous cycle are also observed in the obese rodent model [57]. Changes in cyclicity are attributed to levels of estrogen and progesterone and in premenopausal women, a negative correlation is seen with estrogen levels and body mass index (BMI) and higher levels of progesterone are observed in obese rodent models [58, 59]. Additionally, pathways involved in steroid hormone biosynthesis show disparate expression levels during obesity [60].

Chronic low-grade inflammation is also a systematic response to obesity, having impacts on fertility through inflammatory pathways and constant production of reactive oxygen species (ROS) potentially contributing to accumulation of DNA damage in the ovary [61-63]. Proinflammatory cytokines TNFα, interleukin family members, and NF-κB inflammatory singling members have been implicated in ovarian pathologies such as endometriosis [64], ovarian hyperstimulation [65], and ovarian cancers [66]. Inflammation may contribute to the increased amounts of DNA damage that are present in ovaries during obesity [67-69]. In addition to the elevated levels of basal DNA damage seen in the ovary from obese mice, the ovary is also more susceptible to ovotoxicants, resulting in enhanced damage due to chemical exposures [60, 67-70].

Gestational diabetes mellitus

Gestational diabetes mellitus (GDM), described as glucose intolerance during pregnancy, is a common obstetric disorder that may affect up to 1 in 5 pregnancies dependent on population demographics and diagnostic criteria [71]. With obesity increasing in recent decades, its estimated that GDM prevalence has also increased by ~122% between the late 1980s and mid-2000s [72]. GDM is typically diagnosed between 24 and 28 weeks of gestation and poses immediate health concerns for the mother and her offspring. In the first trimester, offspring may experience restricted intrauterine development, increased congenital anomalies, and spontaneous abortion [73]. In the second and third trimesters, offspring may experience excessive fetal growth, neonatal hypoglycemia, respiratory distress, and polycythemia [73]. While GDM normally resolves upon delivery, both mother and offspring have higher chances of becoming overweight or obese and acquiring type 2 diabetes later in life [74-77].

Normal pregnancy is characterized by changes in insulin sensitivity to regulate glucose control, similar to the non-pregnant state [78]. As pregnancy progresses, insulin sensitivity begins to decline and through changes in maternal estrogen, progesterone, and placental lactogen, insulin sensitivity is around 50% lower towards the end of pregnancy than in the non-pregnant state [79, 80]. Further, pregnant women have a decrease in blood glucose to accommodate the energy requirements for the growing fetus [81]. In contrast, women who have GDM during pregnancy have higher levels of glucose in circulation due to increased insulin resistance, an inadequate insulin response to glucose, and increased hepatic glucose production [82-84].

Pre-existing diabetes and obesity are major risk factors for GDM, with ~50% of all GDM cases occurring in obese women [85] and successful pregnancy outcomes in obese women are more affected by GDM than their lean counterparts [85]. Women who have pre-existing diabetes comprise ~25% of GDM cases, linking back to cases of pre-gestational maternal obesity and possibly attributable to effects on oocyte quality and development [86]. Additionally, women from Hispanic and Asian backgrounds have greater risk of developing GDM than Caucasian and African-American women [87], and prior pregnancies with GDM [72] and history of parental diabetes [88] also contribute to a women's risk of acquiring GDM. Interestingly, around ~30% of GDM cases occur in lean women with no prior history of diabetes [89]. Gestational diabetes is a major health concern due to complications and risks for mother and child during pregnancy, as well as complications that may arise following pregnancy.

Chemical-induced ovotoxicity

Exposure to chemicals during development or in adulthood can have serious implications for female fertility via disruption of normal ovarian function (**Figure 3**). Ovotoxicants can selectively affect a follicle population in the ovary, resulting in either temporary or permanent infertility [131]. Endocrine disrupting chemicals (EDC) are exogenous (natural or synthetic) compounds that disrupt normal actions of endogenous hormones such as their synthesis, secretion, transport, metabolism, binding, and elimination in various organ systems [132]. In the ovary, EDC's have been shown to affect fertility through induction of follicle loss, alteration of ovarian steroidogenesis, mimicry in

receptor signaling, and oocyte competence [133, 134]. The potential sources of exposure to EDC's include plasticizers, pesticides, and solvents [135].

Plasticizers

Di (2-ethylhexyl) phthalate (DEHP) is a commonly used phthalate in the plasticizing process of polyvinyl chloride resin (PVC) products [136]. It is easily released into the environment due to weak bonding capabilities, with exposure occurring via oral ingestion, skin contact and inhalation, subsequently entering the bloodstream [137] DEHP exposure has been associated with testicular, liver, kidney, and ovary tissue disease [137-140]. Detrimental effects of DEHP exposure are observed throughout ovarian development as well as in adult ovaries and include the alteration of germ cell formation and development, meiotic initiation and progression, and primordial follicle development and activation [141-144]. Bisphenol A (BPA) is another common plastic ingredient that is found in polycarbonate food and beverage containers, metal can coatings, pressure printed receipts, and dental sealants [145, 146]. Exposure to BPA occurs when it leaches from its source and into the body. BPA has been shown to affect the female reproductive system via endocrine disruption, reproductive cycle disturbances, miscarriage, altered oocyte maturation, and decreased fertilization [147]. It has also been demonstrated that BPA, via biotransformation, may become a DNA alkylating agent, inducing DNA damage and evoking a protective response in the ovary [148].

Pesticides

Tris(4-chlorophenyl)methanol (TCPM) is a pesticide that has been found in animal tissue globally [149]. TCPM is known byproduct of dichlorodiphenyltrichloroethane (*o, p'* – DDT), which affects the female reproductive system, specifically by altering uterine

contractibility as well as by binding to the estrogen receptor [150, 151]. Glyphosate (N-(phosphonomethyl)glycine) is the main ingredient in one of a commonly used pesticide, and several studies are emerging indicating reproductive effects of glyphosate exposure, including embryonic loss [152], birth defects [153], impaired uterine development [154], placental cell toxicity [155], and premature birth [156]. Impacts of glyphosate exposure on the ovary include impaired folliculogenesis and ovary development, decreased estrogen secretion, increased amounts of oxidative stress, and changes to ovarian morphology [157]. Similar effects were observed in the ovaries of pregnant mice, which resulted in reduced female to male offspring sex ratio [158].

Solvents and industrial chemicals

Perfluorooctane sulfonate (PFOS) is a synthetic surfactant used in a variety of household products and PFOS degradation resistance has led to a bioaccumulation in both humans and animals [159]. PFOS exposure has several negative implications for female reproductive health such as increased incidence of fetal reabsorption [160], pregnancy loss [161]. The industrial chemical, tributyltin (TBT), is an environmental pollutant used frequently as an anti-fouling agent that has shown to bio-accumulate in aquatic species[1 6 2] . TBT exposure occurs in humans through the consumption of contaminated food sources as well as via inhalation or dermal contact [163]. Female reproductive effects of TBT exposure during pregnancy in rats include transplacental transfer of TBT, decreased maternal weight gain, decreased fetal weight, miscarriages, and fetal toxicity [164, 165].

Polycyclic aromatic hydrocarbons

The polycyclic aromatic hydrocarbon (PAH), 7,12-dimethylbenz[a]anthracene (DMBA), is present in smoke or fumes from the burning of organic substances such as coal, car exhaust, and cigarette smoke. DMBA exposure damages ovarian follicles at all stages of development, leading to premature ovarian failure [166-168]. In humans, females who smoke cigarettes (PAH source) experience menopause onset earlier than non-smoking women [169], and offspring of female smokers have fewer oocytes in their ovarian reserve due to *in utero* exposure [170]. Additionally, DMBA exposure induces DNA damage in the ovary and activates the DNA repair response after exposure [171], with the negative effects of DMBA exposure heightened by obesity [68, 70].

Chemotherapeutics

With increasing cancer survival rates, women of all ages are impacted by chemotherapy-induced infertility. Cyclophosphamide (CPA) is an alkylating agent used in the treatment of autoimmune diseases and in anti-cancer chemotherapy in both adults and children. The reproductive effects of CPA exposure include loss of primordial and primary follicles in mice [172], antral follicles in rats [173], and amenorrhea, premature ovarian failure, and infertility in women and young girls [174]. In addition to fertility issues, CPA exposure has been associated with congenital malformations in offspring exposed to CPA *in ute*ro as well as pre-gestational germ cell exposures [175].

Phosphoramide mustard (PM) is an ovotoxic metabolite of CPA [176, 177], which initiates the DNA damage response (DDR) by targeting rapidly dividing cells and inducing

DNA double strand breaks (DSB) [178]. Phosphoramide mustard is also an alkylating agent, creating DNA adducts through the cross-linking of DNA strands, obstructing DNA strand separation during replication [179]. Previous work by our research group and others have demonstrated that PM exposure induces ovarian DNA damage, destroying primordial, primary, and antral follicles, resulting in premature ovarian failure [60, 69, 172, 173, 180, 181]. Phosphoramide mustard can further degrade into another volatile metabolite, chloroethylaziridine (CEZ), an airborne cytotoxic source that is exhaled after CPA administration [182-185]. CEZ potentially contributes to CPA-induced follicle depletion [177] and has been shown to reduce primordial follicle numbers and temporarily reduced secondary follicle numbers in an *ex vivo* model [186].

The exact processes behind chemotherapy-induced follicle loss are unclear, though putative mechanisms have been suggested based on previous animal studies. Direct toxicity to the follicle or oocyte may occur via the toxic reagent crossing through the blood-follicle barrier in the granulosa cells surrounding the oocyte, causing direct damage to the follicular pool [187-190]. Another mechanism suggested to induce follicle loss after chemotherapy is the accelerated activation and maturation of primordial follicles via the phosphoinositide 3-kinase (PI3K) pathway in response to targeted death of larger growing follicles, resulting in follicular "burnout" [191-193]. The methods of follicle depletion may be species-specific and/or drug-specific, but these conclusions have yet to be determined.

DNA damage response

The integrity of the genome is constantly bombarded with insults from endogenous and exogenous sources, with DNA damaging events occurring almost constantly throughout the body. DNA double strand breaks (DSBs) can arise from chromosome breakage, dysfunctional replication fork processing, or telomere deprotection, producing chromosome rearrangements that may result in the disruption of gene structure and/or function [194]. In some instances of tumor progression, this response may hyperactivated, resulting in DNA damage repair in cancer cells, opposing chemotherapy treatment [195]. These perpetual events require an intrinsic response in order to effectively repair the DNA before the cell cycle is allowed to continue. If the damage is too much for repair, the cells are triggered for apoptosis. Mechanisms of DSB repair can vary depending on cellular conditions such as cell cycle phase and chromatin environment.

In mammalian cells, there are two predominate pathways that facilitate the repair of DSBs, homologous recombination (HR) and non-homologous end joining (NHEJ; **Figure 4**) [196-200]. Non-homologous end joining is a rapid mechanism that joins two ends of DNA together with little to no reference to a DNA sequence. The Ku70-Ku80 heterodimer initiates NHEJ via binding to the broken DNA ends and recruiting factors such as DNA-dependent protein kinase catalytic subunit (DNA-PKcs), DNA ligase IV (LIG4), and scaffolding factors x-ray repair cross complementing 4 (XRCC4), XRCC4-like factor (XLF), and paralogue of XRCC4 and XLF (PAXX) [201-205]. To ensure end compatibility, MRE11 homolog, double strand break repair nuclease (MRE11), (RAD50 double strand break repair protein (RAD50), and nibrin (NBS1) come together to form the MRN complex brings the damaged ends together and a synaptic complex is formed, and

DNA end processing is completed by Artemis, DNA polymerases λ and μ, polynucleotide kinase 3'-phosphotase (PNKP), and tyrosyl-DNA phosphodiesterase 1 (TDP1) [206]. The ends are then ligated together, and the repair process is complete.

Conversely, HR requires sequence homology between the broken DNA and DNA donor strand, leading to more direct and precise repair. Homologous recombination mainly occurs during the S or G2 phases of the cell cycle and carries out recombination between sister chromatids [207]. The HR repair mechanism begins with the MRN complex initiating the resection of DNA ends. The endonuclease activity of the MRN complex and exonuclease 1 (EXO1) and DNA2-Bloom syndrome protein (BLM) heterodimer resect the 5' end of the broken strand, creating a 3' single-strand DNA (ssDNA) overhang [208, 209]. The exonuclease activity of the MRN complex then displaces KU70-KU80 from the DNA ends and the RPA complex consisting of replication protein A1 (RPA1), RPA2, and RPA3 coat the ssDNA, but is displaced by recombination mediators breast cancer type 2 susceptibility protein (BRCA2), possibly partnering with partner and localizer of BRCA2 (PALB2), and BRCA-BRCA1-associated RING domain protein (BARD1) heterodimer [198, 210, 211]. Upon displacement of the RPA complex from the ssDNA end, DNA repair protein RAD51 homolog 1 (RAD51) binds to form a nucleoprotein filament. The RAD51 filament then finds the DNA template on the undamaged sister chromatid to begin the RAD51-mediated strand exchange facilitated by the BRCA1-BARD1 heterodimer [212]. A three-stranded DNA helix intermediate supports the formation of heteroduplex DNA that contains the invading and complementary strand. A D-loop is formed on the invading strand is elongated by DNA polymerase using the invaded donor DNA as a template [199]. This process is then terminated by strand ligation and annealing via

synthesis dependent strand annealing, a non-crossover event common to DNA repair and the process of DSB correction is completed [199].

One of the key players in the DNA damage response (DDR) is the ataxia telangiectasia mutated (ATM) protein. ATM is implicated in three critical functions; regulation and simulation of DNA repair, activation of cell cycle checkpoints, and signaling for apoptosis induction [213]. ATM acts a sensor and transducer of DNA damage, phosphorylating several downstream targets after activation including histone 2AX (H2AX) [214], mediator of DNA damage checkpoint protein 1 (MDC1) [215], and BRCA1 [216] for DNA repair; checkpoint kinase 2 (CHK2) for cell cycle arrest [217], p53 [218] for apoptosis; and protein kinase B (AKT) [219] for cell survival (**Figure 5**). DNA DSBs are initially sensed by the MRN complex, a process independent of ATM, and is required for the activation of ATM [220-223]. ATM autophosphorylates at serine 1981 [224, 225], resulting in the production of an active monomer which in turn phosphorylates histone 2AX (H2AX) at serine 139 (γH2AX) [226]. Accumulation of γH2AX at the DSB site recruit's other DNA repair proteins such as BRCA1 and MDC1 to facilitate DNA repair. The phosphorylation of CHK2 at threonine 68 results in activation of P53, which contributes to P21 accumulation, suppressing CDK2 activity and resulting in cell cycle arrest at the G1 phase [227]. In addition to P53 aiding in cell cycle arrest, activation of P53 by ATM results in the accumulation of proapoptotic genes and subsequent cell death when the damage is irreparable [228]. Contrary to P53-mediated cell death, AKT acts as a mediator of cell survival. ATM phosphorylates AKT at serine 473, resulting in the inhibition of apoptotic signals and promotion of cell cycle progression [229].

In the ovary, DNA repair processes are critical for maintaining a robust gamete genome. If damaging alterations in DNA remain in developing follicles, the chances of a healthy oocyte reduce dramatically. Mutations in genes within the DDR pathway such as *Atm* [230] and *Brca1* [231] predispose individuals to increased tumor susceptibility and women carrying these mutations, they may be subject to accelerated ovarian aging or begin with a smaller follicle reserve when compared to unaffected women [232, 233].

Follicular apoptosis and atresia

As previously discussed in this introduction, approximately 99% of all follicles have an atretic fate. Therefore, apoptosis is an essential mechanism involved in ovarian development and folliculogenesis from the early embryonic stage though adult life. Ovarian apoptosis mainly occurs in the granulosa cells or the oocyte, leading to the destruction of the follicle [234]. Presumably, oocyte cell death is the primary form of apoptosis during development and in quiescent follicles, while granulosa cell apoptosis contributes to follicle demise during follicle maturation and growth, though both mechanisms of apoptosis are not limited to these stages [235-237]. While follicles at all stages of development can undergo atresia, the majority of follicles degenerate at the early antral follicle stage [15, 238].

Apoptotic signals can materialize through either cell intrinsic or cell extrinsic pathways. The cell intrinsic pathway is mitochondrial-associated, operated via the B-cell lymphoma 2 (BCL-2) family of cytoplasmic and mitochondrial proteins [239]. The cell extrinsic pathways include “death” ligands FAS ligand (FASL), tumor necrosis factor alpha (TNFα), and TNF-related apoptosis-inducing ligand (TRAIL) [240]. An additional

pathway, the perforin/granzyme pathway, induces apoptosis via the same executioner pathway as the extrinsic and intrinsic pathways, which involves caspase-induced DNA fragmentation [241]. Specific to granulosa cell apoptosis are growth factor-induced elevated levels of cAMP via granzyme B, BCL-2 activation, TNFα, and FASL [242]. These pathways all have the same outcome, a caspase cascade in the final executioner phase of apoptosis, activating the initiators caspase 8 or caspase 9, followed by the activation of executioner caspases 3, 6, and 7 [243]. These caspases cleave various substrates resulting in the fragmentation of DNA and ultimately nuclear collapse. While caspase dependent apoptosis is frequently observed during prenatal and postnatal primordial follicle loss, studies have found the level of caspase-mediated cell death to not be commensurate with the expected loss of primordial follicles, suggesting other apoptotic mechanisms independent of caspase induced cell death in some ovarian follicular populations [244, 245].

Gonadotropins stimulate granzyme B, which in turn activates the intracellular pro-caspases [241]. The protein perforin creates pores within the cell membrane, allowing the release of granzyme B from granules into the cytoplasm of the target cell [246]. While initially found in cytotoxic T lymphocytes and killer cells, granzyme B activity is observed in granulosa cells during early apoptosis, preserving steroidogenic activity in the cell, bypassing mitochondrial-mediated apoptosis [241].

The BCL-2 family of proteins contains both anti-apoptotic and pro-apoptotic proteins and the balance between these factors determines the induction of apoptosis. Anti-apoptotic factors in the BCL-2 family include BCL-2, B-cell lymphoma-extra-large (BCL-X_L), and induced myeloid leukemia cell differentiation protein Mcl-1 (MCL-1), while pro-

apoptotic factors include BH3-interacting domain death agonist (BID), apoptosis regulator BAX (BAX), Bcl-2-related ovarian killer protein (BOK), and BCL2-associated agonist of cell death (BAD) [239, 247]. The mechanism of mitochondrial-initiated apoptosis occurs via the formation of pores in the mitochondrial membrane and altering the membrane potential by pro-apoptotic factors of the BCL-2 family [234]. The openings in the mitochondrial membrane allow the release of cytochrome-c, mitochondria-derived activator of caspases (SMAC), and Interleukin-1beta-converting enzyme (ICE) into the cytoplasm [234]. After cytochrome-c is released into the cytoplasm, it binds with apoptotic protease-activating factor 1 (APAF-1) and pro-caspase 9, forming the apoptosome, ultimately resulting in the caspase 9 activation and subsequent DNA fragmentation [248].

The transmembrane death receptor-mediator interactions that facilitate apoptosis include members of the tumor necrosis factor (TNF) receptor superfamily. Upon binding to the FAS receptor, FAS ligand binds to an adaptor proteins FAS-associated protein with death domain (FADD), whose amino acid tail send the apoptotic signals to the cell [249, 250]. Similarly, the binding of the TNF ligand to the TNF receptor results in the binding of Tumor necrosis factor type 1-asscoiated death domain (TRADD) adapter protein, whose amino acid tail facilitates the transmission of apoptotic signals to the cell [250]. Together, this activity induces DNA fragmentation via action on caspase 8 [249].

The initiation of apoptosis is a preeminent indicator that a follicle is undergoing atresia, but the mechanisms behind the initiation and regulation may vary, with atresia of ovarian follicles being classified in three phenotypes, all involving granulosa cell apoptosis [251]. The majority of follicles undergo “antral atresia”, affecting the middle prolific layers of granulosa cells with apoptosis progressing towards the antrum of the follicle

[251]. This process includes the presence of apoptotic bodies and cytoplasmic blebbing, with the apoptotic cells in this section of the granulosa membrane being engulfed by healthy neighboring granulosa cells and/or infiltrating macrophages [251]. In "basal atresia", the granulosa cells closest to the basal lamina of small antral follicles prematurely luteinize and produce progesterone, but do not complete luteinization, followed by cell death [251]. The third atresia phenotype is "terminal differentiation apoptosis", occurring in the preovulatory follicle, presenting as granulosa cells that form aggregates and float in the antral fluid after sloughing off of the antral surface [252].

Alterations in steroidogenesis have also been suggested in the initiation of follicular atresia. In ovine atretic follicles, the levels of estradiol and the ratio of estradiol to progesterone were considerably lower than their levels in healthy follicles [253]. Additionally, atresia in bovine follicles has been associated with low levels of estrogen and higher levels of progesterone in follicular fluid [254-256]. Treatment with GnRH and androgens and/or withdrawal of estrogen treatment to induce apoptosis in rodents *in vivo* [257, 258]. Growth factors such as insulin-like growth factor (IGF), epidermal growth factor (EGF), and fibroblast growth factor (FGF), gonadotropins LH and FSH, and estrogens are antiapoptotic, while androgens, interleukin-6 (IL-6), and GnRH have atretogenic potential [243], though the precise roles of stage-dependent hormonal regulation on follicular atresia needs to be defined further.

Another mechanism that may influence follicular atresia is autophagy. Autophagy is an intracellular mechanism in which damaged organelles and proteins are degraded, recycled, and reused by the cell. In the prepubertal spiny mouse ovary, during primordial and primary follicle degeneration, autophagy is the dominant form of follicular atresia

[259], while other studies have demonstrated the presence of autophagy marker LC3 in rat granulosa cells [260] or morphological characteristics of autophagy in human granulosa cells after exposure to oxidized low-density lipoprotein [261]. More recently, enhanced granulosa cell autophagy has been determined to be one of the main orchestrators of preantral follicular atresia, while maintaining that granulosa cell apoptosis is responsible for antral follicular degeneration [262].

Summary

The information outlined in this literature review demonstrates that proper ovarian function is integral for normal reproductive capacity. Further, impacts of stressors such as diet, obesity, metabolic status, and ovotoxicants can alter ovarian function maternally, but can also impact offspring through pre-gestational or *in utero* exposures, though the molecular signatures of these events have not been well defined. The work detailed in this dissertation was designed to further elucidate the mechanisms of DNA damage in the ovary due to a metabolic stressor or in the absence of a critical regulator in the DDR. Moreover, we aimed to investigate how a metabolic syndrome potentially affects fertility via impacts of ovarian gap junctions. The impact of these stressors on the ovarian proteome was evaluated, investigating alterations to proteins due to defined environmental and pathological treatment such as GDM, dietary stress, or both, and proteins regulated by ATM and/or altered by PM. Identification of the potential mechanisms governing the DDR, follicular atresia, and the relationship with oocyte quality remain valuable to the field of ovarian biology and are pivotal in discovering methods to potentially mitigate premature ovarian failure.

References

1. Lawson KA, Dunn NR, Roelen BA, Zeinstra LM, Davis AM, Wright CV, Korving JP, Hogan BL. Bmp4 is required for the generation of primordial germ cells in the mouse embryo. Genes Dev 1999; 13:424-436.
2. Ying Y, Liu XM, Marble A, Lawson KA, Zhao GQ. Requirement of Bmp8b for the generation of primordial germ cells in the mouse. Mol Endocrinol 2000; 14:1053-1063.
3. Ying Y, Zhao GQ. Cooperation of endoderm-derived BMP2 and extraembryonic ectoderm-derived BMP4 in primordial germ cell generation in the mouse. Dev Biol 2001; 232:484-492.
4. Hayashi K, Kobayashi T, Umino T, Goitsuka R, Matsui Y, Kitamura D. SMAD1 signaling is critical for initial commitment of germ cell lineage from mouse epiblast. Mech Dev 2002; 118:99-109.
5. Magnusdottir E, Dietmann S, Murakami K, Gunesdogan U, Tang F, Bao S, Diamanti E, Lao K, Gottgens B, Azim Surani M. A tripartite transcription factor network regulates primordial germ cell specification in mice. Nat Cell Biol 2013; 15:905-915.
6. Nakaki F, Hayashi K, Ohta H, Kurimoto K, Yabuta Y, Saitou M. Induction of mouse germ-cell fate by transcription factors in vitro. Nature 2013; 501:222-226.
7. Anderson R, Copeland TK, Scholer H, Heasman J, Wylie C. The onset of germ cell migration in the mouse embryo. Mech Dev 2000; 91:61-68.
8. Molyneaux KA, Stallock J, Schaible K, Wylie C. Time-lapse analysis of living mouse germ cell migration. Dev Biol 2001; 240:488-498.
9. Motta PM, Makabe S, Nottola SA. The ultrastructure of human reproduction. I. The natural history of the female germ cell: origin, migration and differentiation inside the developing ovary. Hum Reprod Update 1997; 3:281-295.
10. Gondos B, Westergaard L, Byskov AG. Initiation of oogenesis in the human fetal ovary: ultrastructural and squash preparation study. Am J Obstet Gynecol 1986; 155:189-195.
11. Wilhelm D, Palmer S, Koopman P. Sex determination and gonadal development in mammals. Physiol Rev 2007; 87:1-28.
12. Sinclair AH, Berta P, Palmer MS, Hawkins JR, Griffiths BL, Smith MJ, Foster JW, Frischauf AM, Lovell-Badge R, Goodfellow PN. A gene from the human sex-determining region encodes a protein with homology to a conserved DNA-binding motif. Nature 1990; 346:240-244.
13. Palmer MS, Sinclair AH, Berta P, Ellis NA, Goodfellow PN, Abbas NE, Fellous M. Genetic evidence that ZFY is not the testis-determining factor. Nature 1989; 342:937-939.
14. Kobayashi A, Behringer RR. Developmental genetics of the female reproductive tract in mammals. Nat Rev Genet 2003; 4:969-980.
15. Hirshfield AN. Development of follicles in the mammalian ovary. Int Rev Cytol 1991; 124:43-101.
16. Gondos B. Granulosa cell-germ cell relationship in the developing rabbit ovary. J Embryol Exp Morphol 1970; 23:419-426.

17. Goldberg GS, Valiunas V, Brink PR. Selective permeability of gap junction channels. Biochim Biophys Acta 2004; 1662:96-101.
18. Neijssen J, Herberts C, Drijfhout JW, Reits E, Janssen L, Neefjes J. Cross-presentation by intercellular peptide transfer through gap junctions. Nature 2005; 434:83-88.
19. Bleil JD, Wassarman PM. Structure and function of the zona pellucida: identification and characterization of the proteins of the mouse oocyte's zona pellucida. Dev Biol 1980; 76:185-202.
20. Magoffin DA. Ovarian theca cell. Int J Biochem Cell Biol 2005; 37:1344-1349.
21. Tsafriri A, Chun SY, Zhang R, Hsueh AJ, Conti M. Oocyte maturation involves compartmentalization and opposing changes of cAMP levels in follicular somatic and germ cells: studies using selective phosphodiesterase inhibitors. Dev Biol 1996; 178:393-402.
22. Vitt UA, Hayashi M, Klein C, Hsueh AJ. Growth differentiation factor-9 stimulates proliferation but suppresses the follicle-stimulating hormone-induced differentiation of cultured granulosa cells from small antral and preovulatory rat follicles. Biol Reprod 2000; 62:370-377.
23. Niswender GD, Menon KM, Jaffe RB. Regulation of the corpus luteum during the menstrual cycle and early pregnancy. Fertil Steril 1972; 23:432-442.
24. Nottola SA, Heyn R, Camboni A, Correr S, Macchiarelli G. Ultrastructural characteristics of human granulosa cells in a coculture system for in vitro fertilization. Microsc Res Tech 2006; 69:508-516.
25. Anasti JN, Kalantaridou SN, Kimzey LM, George M, Nelson LM. Human follicle fluid vascular endothelial growth factor concentrations are correlated with luteinization in spontaneously developing follicles. Hum Reprod 1998; 13:1144-1147.
26. Sullivan SD, Sarrel PM, Nelson LM. Hormone replacement therapy in young women with primary ovarian insufficiency and early menopause. Fertil Steril 2016; 106:1588-1599.
27. Gwynne JT, Strauss JF, 3rd. The role of lipoproteins in steroidogenesis and cholesterol metabolism in steroidogenic glands. Endocr Rev 1982; 3:299-329.
28. Lin D, Sugawara T, Strauss JF, 3rd, Clark BJ, Stocco DM, Saenger P, Rogol A, Miller WL. Role of steroidogenic acute regulatory protein in adrenal and gonadal steroidogenesis. Science 1995; 267:1828-1831.
29. Makris A, Olsen D, Ryan KJ. Significance of the delta 5 and delta 4 steroidogenic pathways in the hamster preovulatory follicle. Steroids 1983; 42:641-651.
30. Simpson ER, Mahendroo MS, Means GD, Kilgore MW, Hinshelwood MM, Graham-Lorence S, Amarneh B, Ito Y, Fisher CR, Michael MD, et al. Aromatase cytochrome P450, the enzyme responsible for estrogen biosynthesis. Endocr Rev 1994; 15:342-355.
31. Geissler WM, Davis DL, Wu L, Bradshaw KD, Patel S, Mendonca BB, Elliston KO, Wilson JD, Russell DW, Andersson S. Male pseudohermaphroditism caused by mutations of testicular 17 beta-hydroxysteroid dehydrogenase 3. Nat Genet 1994; 7:34-39.
32. Auchus RJ. Steroid 17-hydroxylase and 17,20-lyase deficiencies, genetic and pharmacologic. J Steroid Biochem Mol Biol 2017; 165:71-78.

33. Liu YX, Hsueh AJ. Synergism between granulosa and theca-interstitial cells in estrogen biosynthesis by gonadotropin-treated rat ovaries: studies on the two-cell, two-gonadotropin hypothesis using steroid antisera. Biol Reprod 1986; 35:27-36.
34. Schauer C, Tong T, Petitjean H, Blum T, Peron S, Mai O, Schmitz F, Boehm U, Leinders-Zufall T. Hypothalamic gonadotropin-releasing hormone (GnRH) receptor neurons fire in synchrony with the female reproductive cycle. J Neurophysiol 2015; 114:1008-1021.
35. Sisk CL, Richardson HN, Chappell PE, Levine JE. In vivo gonadotropin-releasing hormone secretion in female rats during peripubertal development and on proestrus. Endocrinology 2001; 142:2929-2936.
36. Ying SY. Inhibins, activins, and follistatins: gonadal proteins modulating the secretion of follicle-stimulating hormone. Endocr Rev 1988; 9:267-293.
37. de Ziegler D, Fraisse T, de Candolle G, Vulliemoz N, Bellavia M, Colamaria S. Outlook: Roles of FSH and LH during the follicular phase: insight into natural cycle IVF. Reprod Biomed Online 2007; 15:507-513.
38. Yamaji T, Dierschke DJ, Bhattacharya AN, Knobil E. The negative feedback control by estradiol and progesterone of LH secretion in the ovariectomized rhesus monkey. Endocrinology 1972; 90:771-777.
39. Stocco C, Telleria C, Gibori G. The molecular control of corpus luteum formation, function, and regression. Endocr Rev 2007; 28:117-149.
40. Jarvela IY, Ruokonen A, Tekay A. Effect of rising hCG levels on the human corpus luteum during early pregnancy. Hum Reprod 2008; 23:2775-2781.
41. Organization WH. Obesity and overweight. In. Online; 2016.
42. Hales CMC, M.D; Fryar, C.D.; C.L. Ogden. Prevalence of obesity among adults and youth: United States, 2015-2016. In, 288 ed. Hyattsville, MD: National Center for Health Statistics 2017.
43. Colditz GA, Willett WC, Rotnitzky A, Manson JE. Weight gain as a risk factor for clinical diabetes mellitus in women. Ann Intern Med 1995; 122:481-486.
44. Lavie CJ, Milani RV, Ventura HO. Obesity and cardiovascular disease: risk factor, paradox, and impact of weight loss. J Am Coll Cardiol 2009; 53:1925-1932.
45. Xu H, Barnes GT, Yang Q, Tan G, Yang D, Chou CJ, Sole J, Nichols A, Ross JS, Tartaglia LA, Chen H. Chronic inflammation in fat plays a crucial role in the development of obesity-related insulin resistance. J Clin Invest 2003; 112:1821-1830.
46. Cozzo AJ, Fuller AM, Makowski L. Contribution of Adipose Tissue to Development of Cancer. Compr Physiol 2017; 8:237-282.
47. Burt Solorzano CM, McCartney CR. Obesity and the pubertal transition in girls and boys. Reproduction 2010; 140:399-410.
48. Brewer CJ, Balen AH. The adverse effects of obesity on conception and implantation. Reproduction 2010; 140:347-364.
49. Pasquali R, Casimirri F. The impact of obesity on hyperandrogenism and polycystic ovary syndrome in premenopausal women. Clin Endocrinol (Oxf) 1993; 39:1-16.
50. Gesink Law DC, Maclehose RF, Longnecker MP. Obesity and time to pregnancy. Hum Reprod 2007; 22:414-420.
51. Leddy MA, Power ML, Schulkin J. The impact of maternal obesity on maternal and fetal health. Rev Obstet Gynecol 2008; 1:170-178.

52. Chu SY, Callaghan WM, Kim SY, Schmid CH, Lau J, England LJ, Dietz PM. Maternal obesity and risk of gestational diabetes mellitus. Diabetes Care 2007; 30:2070-2076.
53. Sheffield JS, Butler-Koster EL, Casey BM, McIntire DD, Leveno KJ. Maternal diabetes mellitus and infant malformations. Obstet Gynecol 2002; 100:925-930.
54. Olsen CM, Nagle CM, Whiteman DC, Ness R, Pearce CL, Pike MC, Rossing MA, Terry KL, Wu AH, Risch HA, Yu H, Doherty JA, et al. Obesity and risk of ovarian cancer subtypes: evidence from the Ovarian Cancer Association Consortium. Endocr Relat Cancer 2013; 20:251-262.
55. Nteeba J, Ross JW, Perfield JW, 2nd, Keating AF. High fat diet induced obesity alters ovarian phosphatidylinositol-3 kinase signaling gene expression. Reprod Toxicol 2013; 42:68-77.
56. Nteeba J, Ganesan S, Keating AF. Progressive obesity alters ovarian folliculogenesis with impacts on pro-inflammatory and steroidogenic signaling in female mice. Biol Reprod 2014; 91:86.
57. Akamine EH, Marcal AC, Camporez JP, Hoshida MS, Caperuto LC, Bevilacqua E, Carvalho CR. Obesity induced by high-fat diet promotes insulin resistance in the ovary. J Endocrinol 2010; 206:65-74.
58. Randolph JF, Jr., Sowers M, Gold EB, Mohr BA, Luborsky J, Santoro N, McConnell DS, Finkelstein JS, Korenman SG, Matthews KA, Sternfeld B, Lasley BL. Reproductive hormones in the early menopausal transition: relationship to ethnicity, body size, and menopausal status. J Clin Endocrinol Metab 2003; 88:1516-1522.
59. Freeman EW, Sammel MD, Lin H, Gracia CR. Obesity and reproductive hormone levels in the transition to menopause. Menopause 2010; 17:718-726.
60. Nteeba J, Ganesan S, Madden JA, Dickson MJ, Keating AF. Progressive obesity alters ovarian insulin, phosphatidylinositol-3 kinase, and chemical metabolism signaling pathways and potentiates ovotoxicity induced by phosphoramide mustard in mice. Biol Reprod 2017; 96:478-490.
61. Cerda C, Sanchez C, Climent B, Vazquez A, Iradi A, El Amrani F, Bediaga A, Saez GT. Oxidative stress and DNA damage in obesity-related tumorigenesis. Adv Exp Med Biol 2014; 824:5-17.
62. Wlodarczyk M, Jablonowska-Lietz B, Olejarz W, Nowicka G. Anthropometric and Dietary Factors as Predictors of DNA Damage in Obese Women. Nutrients 2018; 10.
63. Zaki M, Basha W, El-Bassyouni HT, El-Toukhy S, Hussein T. Evaluation of DNA damage profile in obese women and its association to risk of metabolic syndrome, polycystic ovary syndrome and recurrent preeclampsia. Genes Dis 2018; 5:367-373.
64. Carlberg M, Nejaty J, Froysa B, Guan Y, Soder O, Bergqvist A. Elevated expression of tumour necrosis factor alpha in cultured granulosa cells from women with endometriosis. Hum Reprod 2000; 15:1250-1255.
65. Ma CH, Yan LY, Qiao J, Sha W, Li L, Chen Y, Sun QY. Effects of tumor necrosis factor-alpha on porcine oocyte meiosis progression, spindle organization, and chromosome alignment. Fertil Steril 2010; 93:920-926.

66. DiDonato JA, Mercurio F, Karin M. NF-kappaB and the link between inflammation and cancer. Immunol Rev 2012; 246:379-400.
67. Ganesan S, Nteeba J, Keating AF. Impact of obesity on 7,12-dimethylbenz[a]anthracene-induced altered ovarian connexin gap junction proteins in female mice. Toxicol Appl Pharmacol 2015; 282:1-8.
68. Ganesan S, Nteeba J, Keating AF. Enhanced susceptibility of ovaries from obese mice to 7,12-dimethylbenz[a]anthracene-induced DNA damage. Toxicol Appl Pharmacol 2014; 281:203-210.
69. Ganesan S, Nteeba J, Madden JA, Keating AF. Obesity alters phosphoramide mustard-induced ovarian DNA repair in mice. Biol Reprod 2017; 96:491-501.
70. Nteeba J, Ganesan S, Keating AF. Impact of obesity on ovotoxicity induced by 7,12-dimethylbenz[a]anthracene in mice. Biol Reprod 2014; 90:68.
71. Noctor E, Dunne FP. Type 2 diabetes after gestational diabetes: The influence of changing diagnostic criteria. World J Diabetes 2015; 6:234-244.
72. Getahun D, Nath C, Ananth CV, Chavez MR, Smulian JC. Gestational diabetes in the United States: temporal trends 1989 through 2004. Am J Obstet Gynecol 2008; 198:525.e521-525.
73. Buchanan TA, Xiang AH, Page KA. Gestational diabetes mellitus: risks and management during and after pregnancy. Nat Rev Endocrinol 2012; 8:639-649.
74. Kim C. Maternal outcomes and follow-up after gestational diabetes mellitus. Diabet Med 2014; 31:292-301.
75. Bellamy L, Casas JP, Hingorani AD, Williams D. Type 2 diabetes mellitus after gestational diabetes: a systematic review and meta-analysis. Lancet 2009; 373:1773-1779.
76. Vohr BR, Boney CM. Gestational diabetes: the forerunner for the development of maternal and childhood obesity and metabolic syndrome? J Matern Fetal Neonatal Med 2008; 21:149-157.
77. Nehring I, Chmitorz A, Reulen H, von Kries R, Ensenauer R. Gestational diabetes predicts the risk of childhood overweight and abdominal circumference independent of maternal obesity. Diabet Med 2013; 30:1449-1456.
78. Catalano PM, Huston L, Amini SB, Kalhan SC. Longitudinal changes in glucose metabolism during pregnancy in obese women with normal glucose tolerance and gestational diabetes mellitus. Am J Obstet Gynecol 1999; 180:903-916.
79. Catalano PM, Tyzbir ED, Roman NM, Amini SB, Sims EA. Longitudinal changes in insulin release and insulin resistance in nonobese pregnant women. Am J Obstet Gynecol 1991; 165:1667-1672.
80. McLachlan KA, O'Neal D, Jenkins A, Alford FP. Do adiponectin, TNFalpha, leptin and CRP relate to insulin resistance in pregnancy? Studies in women with and without gestational diabetes, during and after pregnancy. Diabetes Metab Res Rev 2006; 22:131-138.
81. Sonagra AD, Biradar SM, K D, Murthy DSJ. Normal pregnancy- a state of insulin resistance. J Clin Diagn Res 2014; 8:Cc01-03.
82. Homko C, Sivan E, Chen X, Reece EA, Boden G. Insulin secretion during and after pregnancy in patients with gestational diabetes mellitus. J Clin Endocrinol Metab 2001; 86:568-573.

83. Kautzky-Willer A, Prager R, Waldhausl W, Pacini G, Thomaseth K, Wagner OF, Ulm M, Streli C, Ludvik B. Pronounced insulin resistance and inadequate beta-cell secretion characterize lean gestational diabetes during and after pregnancy. Diabetes Care 1997; 20:1717-1723.
84. Yen SS, Tsai CC, Vela P. Gestational diabetogenesis: quantitative analyses of glucose-insulin interrelationship between normal pregnancy and pregnancy with gestational diabetes. Am J Obstet Gynecol 1971; 111:792-800.
85. Kim C. Gestational diabetes: risks, management, and treatment options. Int J Womens Health 2010; 2:339-351.
86. Lawrence JM, Contreras R, Chen W, Sacks DA. Trends in the prevalence of preexisting diabetes and gestational diabetes mellitus among a racially/ethnically diverse population of pregnant women, 1999-2005. Diabetes Care 2008; 31:899-904.
87. Hedderson MM, Williams MA, Holt VL, Weiss NS, Ferrara A. Body mass index and weight gain prior to pregnancy and risk of gestational diabetes mellitus. Am J Obstet Gynecol 2008; 198:409.e401-407.
88. Solomon CG, Willett WC, Carey VJ, Rich-Edwards J, Hunter DJ, Colditz GA, Stampfer MJ, Speizer FE, Spiegelman D, Manson JE. A prospective study of pregravid determinants of gestational diabetes mellitus. Jama 1997; 278:1078-1083.
89. Blickstein I, Doyev R, Trojner Bregar A, Brzan Simenc G, Verdenik I, Tul N. The effect of gestational diabetes, pre-gravid maternal obesity, and their combination ('diabesity') on outcomes of singleton gestations. J Matern Fetal Neonatal Med 2018; 31:640-643.
90. N. Dekel A, D.T., Freisen, H. G., Leung, P. C. K., Moger, W., and Ruf, K. B., eds. Endocrinology and Physiology of Reproduction. New York: Plenum Publishing Corporation; 1987: 197-209.
91. Winterhager E, Kidder GM. Gap junction connexins in female reproductive organs: implications for women's reproductive health. Hum Reprod Update 2015; 21:340-352.
92. Clarke H. Control of Mammalian Oocyte Development by Interactions with the Maternal Follicular Environment. Results Probl Cell Differ 2017; 63:17-41.
93. Grazul-Bilska AT, Reynolds LP, Redmer DA. Gap junctions in the ovaries. Biol Reprod 1997; 57:947-957.
94. Sohl G, Willecke K. An update on connexin genes and their nomenclature in mouse and man. Cell Commun Adhes 2003; 10:173-180.
95. Itahana K, Morikazu Y, Takeya T. Differential expression of four connexin genes, Cx-26, Cx-30.3, Cx-32, and Cx-43, in the porcine ovarian follicle. Endocrinology 1996; 137:5036-5044.
96. Itahana K, Tanaka T, Morikazu Y, Komatu S, Ishida N, Takeya T. Isolation and characterization of a novel connexin gene, Cx-60, in porcine ovarian follicles. Endocrinology 1998; 139:320-329.
97. Borowczyk E, Johnson ML, Bilski JJ, Borowicz P, Redmer DA, Reynolds LP, Grazul-Bilska AT. Gap junctional connexin 37 is expressed in sheep ovaries. Endocrine 2006; 30:223-230.

98. Borowczyk E, Johnson ML, Bilski JJ, Borowicz PP, Redmer DA, Reynolds LP, Grazul-Bilska AT. Expression of gap junctional connexins 26, 32, and 43 mRNA in ovarian preovulatory follicles and corpora lutea in sheep. Can J Physiol Pharmacol 2006; 84:1011-1020.
99. Grazul-Bilska AT, Redmer DA, Bilski JJ, Jablonka-Shariff A, Doraiswamy V, Reynolds LP. Gap junctional proteins, connexin 26, 32, and 43 in sheep ovaries throughout the estrous cycle. Endocrine 1998; 8:269-279.
100. Johnson ML, Redmer DA, Reynolds LP, Bilski JJ, Grazul-Bilska AT. Gap junctional intercellular communication of bovine granulosa and thecal cells from antral follicles: effects of luteinizing hormone and follicle-stimulating hormone. Endocrine 2002; 18:261-270.
101. Johnson ML, Redmer DA, Reynolds LP, Grazul-Bilska AT. Expression of gap junctional proteins connexin 43, 32, and 26 throughout follicular development and atresia in cows. Endocrine 1999; 10:43-51.
102. Kidder GM, Mhawi AA. Gap junctions and ovarian folliculogenesis. Reproduction 2002; 123:613-620.
103. Panchin Y, Kelmanson I, Matz M, Lukyanov K, Usman N, Lukyanov S. A ubiquitous family of putative gap junction molecules. Curr Biol 2000; 10:R473-474.
104. Baranova A, Ivanov D, Petrash N, Pestova A, Skoblov M, Kelmanson I, Shagin D, Nazarenko S, Geraymovych E, Litvin O, Tiunova A, Born TL, et al. The mammalian pannexin family is homologous to the invertebrate innexin gap junction proteins. Genomics 2004; 83:706-716.
105. Firestone GL, Kapadia BJ. Minireview: regulation of gap junction dynamics by nuclear hormone receptors and their ligands. Mol Endocrinol 2012; 26:1798-1807.
106. Lye SJ, Nicholson BJ, Mascarenhas M, MacKenzie L, Petrocelli T. Increased expression of connexin-43 in the rat myometrium during labor is associated with an increase in the plasma estrogen:progesterone ratio. Endocrinology 1993; 132:2380-2386.
107. Karasinski J, Galas J, Semik D, Fiertak A, Bilinska B, Kilarski WM. Changes of connexin43 expression in non-pregnant porcine myometrium correlate with progesterone concentration during oestrous cycle. Reprod Domest Anim 2010; 45:959-966.
108. Beyer EC, Kistler J, Paul DL, Goodenough DA. Antisera directed against connexin43 peptides react with a 43-kD protein localized to gap junctions in myocardium and other tissues. J Cell Biol 1989; 108:595-605.
109. Valdimarsson G, De Sousa PA, Kidder GM. Coexpression of gap junction proteins in the cumulus-oocyte complex. Mol Reprod Dev 1993; 36:7-15.
110. Okuma A, Kuraoka A, Iida H, Inai T, Wasano K, Shibata Y. Colocalization of connexin 43 and connexin 45 but absence of connexin 40 in granulosa cell gap junctions of rat ovary. J Reprod Fertil 1996; 107:255-264.
111. Fang WL, Lai SY, Lai WA, Lee MT, Liao CF, Ke FC, Hwang JJ. CRTC2 and Nedd4 ligase involvement in FSH and TGFbeta1 upregulation of connexin43 gap junction. J Mol Endocrinol 2015; 55:263-275.

112. El-Hayek S, Clarke HJ. Follicle-Stimulating Hormone Increases Gap Junctional Communication Between Somatic and Germ-Line Follicular Compartments During Murine Oogenesis. Biol Reprod 2015; 93:47.
113. Granot I, Dekel N. Phosphorylation and expression of connexin-43 ovarian gap junction protein are regulated by luteinizing hormone. J Biol Chem 1994; 269:30502-30509.
114. Granot I, Dekel N. Cell-to-cell communication in the ovarian follicle: developmental and hormonal regulation of the expression of connexin43. Hum Reprod 1998; 13 Suppl 4:85-97.
115. Khan-Dawood FS, Yang J, Dawood MY. Hormonal regulation of connexin-43 in baboon corpora lutea. J Endocrinol 1998; 157:405-414.
116. Berisha B, Bridger P, Toth A, Kliem H, Meyer HH, Schams D, Pfarrer C. Expression and localization of gap junctional connexins 26 and 43 in bovine periovulatory follicles and in corpus luteum during different functional stages of oestrous cycle and pregnancy. Reprod Domest Anim 2009; 44:295-302.
117. Simon AM, Goodenough DA, Li E, Paul DL. Female infertility in mice lacking connexin 37. Nature 1997; 385:525-529.
118. Carabatsos MJ, Sellitto C, Goodenough DA, Albertini DF. Oocyte-granulosa cell heterologous gap junctions are required for the coordination of nuclear and cytoplasmic meiotic competence. Dev Biol 2000; 226:167-179.
119. Bachelot A, Gilleron J, Meduri G, Guberto M, Dulon J, Boucherie S, Touraine P, Misrahi M. A common African variant of human connexin 37 is associated with Caucasian primary ovarian insufficiency and has a deleterious effect in vitro. Int J Mol Med 2018; 41:640-648.
120. Guruvaiah P, Govatati S, Reddy TV, Beeram H, Deenadayal M, Shivaji S, Bhanoori M. Analysis of Connexin37 gene C1019T polymorphism and PCOS susceptibility in South Indian population: case-control study. Eur J Obstet Gynecol Reprod Biol 2016; 196:17-20.
121. Ackert CL, Gittens JE, O'Brien MJ, Eppig JJ, Kidder GM. Intercellular communication via connexin43 gap junctions is required for ovarian folliculogenesis in the mouse. Dev Biol 2001; 233:258-270.
122. Juneja SC, Barr KJ, Enders GC, Kidder GM. Defects in the germ line and gonads of mice lacking connexin43. Biol Reprod 1999; 60:1263-1270.
123. Gittens JE, Barr KJ, Vanderhyden BC, Kidder GM. Interplay between paracrine signaling and gap junctional communication in ovarian follicles. J Cell Sci 2005; 118:113-122.
124. Gittens JE, Kidder GM. Differential contributions of connexin37 and connexin43 to oogenesis revealed in chimeric reaggregated mouse ovaries. J Cell Sci 2005; 118:5071-5078.
125. Gabriel HD, Jung D, Butzler C, Temme A, Traub O, Winterhager E, Willecke K. Transplacental uptake of glucose is decreased in embryonic lethal connexin26-deficient mice. J Cell Biol 1998; 140:1453-1461.
126. Kruger O, Plum A, Kim JS, Winterhager E, Maxeiner S, Hallas G, Kirchhoff S, Traub O, Lamers WH, Willecke K. Defective vascular development in connexin 45-deficient mice. Development 2000; 127:4179-4193.

127. Kumai M, Nishii K, Nakamura K, Takeda N, Suzuki M, Shibata Y. Loss of connexin45 causes a cushion defect in early cardiogenesis. Development 2000; 127:3501-3512.
128. Nishii K, Kumai M, Egashira K, Miwa T, Hashizume K, Miyano Y, Shibata Y. Mice lacking connexin45 conditionally in cardiac myocytes display embryonic lethality similar to that of germline knockout mice without endocardial cushion defect. Cell Commun Adhes 2003; 10:365-369.
129. Hombach S, Janssen-Bienhold U, Sohl G, Schubert T, Bussow H, Ott T, Weiler R, Willecke K. Functional expression of connexin57 in horizontal cells of the mouse retina. Eur J Neurosci 2004; 19:2633-2640.
130. Nelles E, Butzler C, Jung D, Temme A, Gabriel HD, Dahl U, Traub O, Stumpel F, Jungermann K, Zielasek J, Toyka KV, Dermietzel R, et al. Defective propagation of signals generated by sympathetic nerve stimulation in the liver of connexin32-deficient mice. Proc Natl Acad Sci U S A 1996; 93:9565-9570.
131. Hoyer PB, Keating AF. Xenobiotic effects in the ovary: temporary versus permanent infertility. Expert Opin Drug Metab Toxicol 2014; 10:511-523.
132. Craig ZR, Wang W, Flaws JA. Endocrine-disrupting chemicals in ovarian function: effects on steroidogenesis, metabolism and nuclear receptor signaling. Reproduction 2011; 142:633-646.
133. Foster W.F. NMS, YoungLai, E.V. Endocrine disruptors and ovarian function. International Congress Series 2004; 1266:126-132.
134. Patel S, Zhou C, Rattan S, Flaws JA. Effects of Endocrine-Disrupting Chemicals on the Ovary. Biol Reprod 2015; 93:20.
135. Sharara FI, Seifer DB, Flaws JA. Environmental toxicants and female reproduction. Fertil Steril 1998; 70:613-622.
136. Lovekamp-Swan T, Davis BJ. Mechanisms of phthalate ester toxicity in the female reproductive system. Environ Health Perspect 2003; 111:139-145.
137. Engel SM, Wolff MS. Causal inference considerations for endocrine disruptor research in children's health. Annu Rev Public Health 2013; 34:139-158.
138. Lai FN, Liu JC, Li L, Ma JY, Liu XL, Liu YP, Zhang XF, Chen H, De Felici M, Dyce PW, Shen W. Di (2-ethylhexyl) phthalate impairs steroidogenesis in ovarian follicular cells of prepuberal mice. Arch Toxicol 2017; 91:1279-1292.
139. Li L, Liu JC, Zhao Y, Lai FN, Yang F, Ge W, Dou CL, Shen W, Zhang XF, Chen H. Impact of diethylhexyl phthalate on gene expression and development of mammary glands of pregnant mouse. Histochem Cell Biol 2015; 144:389-402.
140. Krotz SP, Carson SA, Tomey C, Buster JE. Phthalates and bisphenol do not accumulate in human follicular fluid. J Assist Reprod Genet 2012; 29:773-777.
141. Rattan S, Brehm E, Gao L, Niermann S, Flaws JA. Prenatal exposure to di(2-ethylhexyl) phthalate disrupts ovarian function in a transgenerational manner in female mice. Biol Reprod 2018; 98:130-145.
142. Kalo D, Hadas R, Furman O, Ben-Ari J, Maor Y, Patterson DG, Tomey C, Roth Z. Carryover Effects of Acute DEHP Exposure on Ovarian Function and Oocyte Developmental Competence in Lactating Cows. PLoS One 2015; 10:e0130896.
143. Liu JC, Lai FN, Li L, Sun XF, Cheng SF, Ge W, Wang YF, Li L, Zhang XF, De Felici M, Dyce PW, Shen W. Di (2-ethylhexyl) phthalate exposure impairs meiotic

progression and DNA damage repair in fetal mouse oocytes in vitro. Cell Death Dis 2017; 8:e2966.
144. Zhang XF, Zhang LJ, Li L, Feng YN, Chen B, Ma JM, Huynh E, Shi QH, De Felici M, Shen W. Diethylhexyl phthalate exposure impairs follicular development and affects oocyte maturation in the mouse. Environ Mol Mutagen 2013; 54:354-361.
145. Fung EY, Ewoldsen NO, St Germain HA, Jr., Marx DB, Miaw CL, Siew C, Chou HN, Gruninger SE, Meyer DM. Pharmacokinetics of bisphenol A released from a dental sealant. J Am Dent Assoc 2000; 131:51-58.
146. Hunt PA, Lawson C, Gieske M, Murdoch B, Smith H, Marre A, Hassold T, VandeVoort CA. Bisphenol A alters early oogenesis and follicle formation in the fetal ovary of the rhesus monkey. Proc Natl Acad Sci U S A 2012; 109:17525-17530.
147. Moore-Ambriz TR, Acuna-Hernandez DG, Ramos-Robles B, Sanchez-Gutierrez M, Santacruz-Marquez R, Sierra-Santoyo A, Pina-Guzman B, Shibayama M, Hernandez-Ochoa I. Exposure to bisphenol A in young adult mice does not alter ovulation but does alter the fertilization ability of oocytes. Toxicol Appl Pharmacol 2015; 289:507-514.
148. Ganesan S, Keating AF. Bisphenol A-Induced Ovotoxicity Involves DNA Damage Induction to Which the Ovary Mounts a Protective Response Indicated by Increased Expression of Proteins Involved in DNA Repair and Xenobiotic Biotransformation. Toxicol Sci 2016; 152:169-180.
149. de Boer J, Wester PG, Evers EH, Brinkman UA. Determination of tris(4-chlorophenyl)methanol and tris(4-chlorophenyl)methane in fish, marine mammals and sediment. Environ Pollut 1996; 93:39-47.
150. Juberg DR, Webb RC, Loch-Caruso R. Characterization of o,p'-DDT-stimulated contraction frequency in rat uterus in vitro. Fundam Appl Toxicol 1991; 17:543-549.
151. Jaga K, Dharmani C. Global surveillance of DDT and DDE levels in human tissues. Int J Occup Med Environ Health 2003; 16:7-20.
152. Ingaramo PI, Varayoud J, Milesi MM, Schimpf MG, Munoz-de-Toro M, Luque EH. Effects of neonatal exposure to a glyphosate-based herbicide on female rat reproduction. Reproduction 2016; 152:403-415.
153. Dallegrave E, Mantese FD, Coelho RS, Pereira JD, Dalsenter PR, Langeloh A. The teratogenic potential of the herbicide glyphosate-Roundup in Wistar rats. Toxicol Lett 2003; 142:45-52.
154. Guerrero Schimpf M, Milesi MM, Ingaramo PI, Luque EH, Varayoud J. Neonatal exposure to a glyphosate based herbicide alters the development of the rat uterus. Toxicology 2017; 376:2-14.
155. Richard S, Moslemi S, Sipahutar H, Benachour N, Seralini GE. Differential effects of glyphosate and roundup on human placental cells and aromatase. Environ Health Perspect 2005; 113:716-720.
156. Parvez S, Gerona RR, Proctor C, Friesen M, Ashby JL, Reiter JL, Lui Z, Winchester PD. Glyphosate exposure in pregnancy and shortened gestational length: a prospective Indiana birth cohort study. Environ Health 2018; 17:23.

157. Hamdaoui L, Naifar M, Rahmouni F, Harrabi B, Ayadi F, Sahnoun Z, Rebai T. Subchronic exposure to kalach 360 SL-induced endocrine disruption and ovary damage in female rats. Arch Physiol Biochem 2018; 124:27-34.
158. Ren X, Li R, Liu J, Huang K, Wu S, Li Y, Li C. Effects of glyphosate on the ovarian function of pregnant mice, the secretion of hormones and the sex ratio of their fetuses. Environ Pollut 2018; 243:833-841.
159. Jensen AA, Leffers H. Emerging endocrine disrupters: perfluoroalkylated substances. Int J Androl 2008; 31:161-169.
160. Case MT, York RG, Christian MS. Rat and rabbit oral developmental toxicology studies with two perfluorinated compounds. Int J Toxicol 2001; 20:101-109.
161. Das KP, Grey BE, Zehr RD, Wood CR, Butenhoff JL, Chang SC, Ehresman DJ, Tan YM, Lau C. Effects of perfluorobutyrate exposure during pregnancy in the mouse. Toxicol Sci 2008; 105:173-181.
162. Fent K. Ecotoxicology of organotin compounds. Crit Rev Toxicol 1996; 26:1-117.
163. Wax PM, Dockstader L. Tributyltin use in interior paints: a continuing health hazard. J Toxicol Clin Toxicol 1995; 33:239-241.
164. Adeeko A, Li D, Forsyth DS, Casey V, Cooke GM, Barthelemy J, Cyr DG, Trasler JM, Robaire B, Hales BF. Effects of in utero tributyltin chloride exposure in the rat on pregnancy outcome. Toxicol Sci 2003; 74:407-415.
165. Harazono A, Ema M, Ogawa Y. Pre-implantation embryonic loss induced by tributyltin chloride in rats. Toxicol Lett 1996; 89:185-190.
166. Igawa Y, Keating AF, Rajapaksa KS, Sipes IG, Hoyer PB. Evaluation of ovotoxicity induced by 7, 12-dimethylbenz[a]anthracene and its 3,4-diol metabolite utilizing a rat in vitro ovarian culture system. Toxicol Appl Pharmacol 2009; 234:361-369.
167. Gelboin HV. Benzo[alpha]pyrene metabolism, activation and carcinogenesis: role and regulation of mixed-function oxidases and related enzymes. Physiol Rev 1980; 60:1107-1166.
168. Mattison D.R. SJD. How xenobiotic chemicals can destroy oocytes. Contemp Obstet. Gynecol. 1980; 15.
169. Harlow BL, Signorello LB. Factors associated with early menopause. Maturitas 2000; 35:3-9.
170. Camlin NJ, Sobinoff AP, Sutherland JM, Beckett EL, Jarnicki AG, Vanders RL, Hansbro PM, McLaughlin EA, Holt JE. Maternal Smoke Exposure Impairs the Long-Term Fertility of Female Offspring in a Murine Model. Biol Reprod 2016; 94:39.
171. Ganesan S, Bhattacharya P, Keating AF. 7,12-Dimethylbenz[a]anthracene exposure induces the DNA repair response in neonatal rat ovaries. Toxicol Appl Pharmacol 2013; 272:690-696.
172. Petrillo SK, Desmeules P, Truong TQ, Devine PJ. Detection of DNA damage in oocytes of small ovarian follicles following phosphoramide mustard exposures of cultured rodent ovaries in vitro. Toxicol Appl Pharmacol 2011; 253:94-102.
173. Ataya KM, Pydyn EF, Ramahi-Ataya AJ. The effect of "activated" cyclophosphamide on human and rat ovarian granulosa cells in vitro. Reprod Toxicol 1990; 4:121-125.

174. Meirow D. Reproduction post-chemotherapy in young cancer patients. Mol Cell Endocrinol 2000; 169:123-131.
175. Rengasamy P. Congenital Malformations Attributed to Prenatal Exposure to Cyclophosphamide. Anticancer Agents Med Chem 2017; 17:1211-1227.
176. Plowchalk DR, Mattison DR. Phosphoramide mustard is responsible for the ovarian toxicity of cyclophosphamide. Toxicol Appl Pharmacol 1991; 107:472-481.
177. Desmeules P, Devine PJ. Characterizing the ovotoxicity of cyclophosphamide metabolites on cultured mouse ovaries. Toxicol Sci 2006; 90:500-509.
178. Surya YA, Rosenfeld JM, Hillcoat BL. Cross-linking of DNA in L1210 cells and nuclei treated with cyclophosphamide and phosphoramide mustard. Cancer Treat Rep 1978; 62:23-29.
179. Phillips DH, Farmer PB, Beland FA, Nath RG, Poirier MC, Reddy MV, Turteltaub KW. Methods of DNA adduct determination and their application to testing compounds for genotoxicity. Environ Mol Mutagen 2000; 35:222-233.
180. Ganesan S, Keating AF. Phosphoramide mustard exposure induces DNA adduct formation and the DNA damage repair response in rat ovarian granulosa cells. Toxicol Appl Pharmacol 2015; 282:252-258.
181. Madden JA, Keating AF. Ovarian xenobiotic biotransformation enzymes are altered during phosphoramide mustard-induced ovotoxicity. Toxicol Sci 2014; 141:441-452.
182. Rauen HM, Norpoth K. [A volatile alkylating agent in the exhaled air following the administration of Endoxan]. Klin Wochenschr 1968; 46:272-275.
183. Lu H, Chan KK. Gas chromatographic-mass spectrometric assay for N-2-chloroethylaziridine, a volatile cytotoxic metabolite of cyclophosphamide, in rat plasma. J Chromatogr B Biomed Appl 1996; 678:219-225.
184. Flowers JL, Ludeman SM, Gamcsik MP, Colvin OM, Shao KL, Boal JH, Springer JB, Adams DJ. Evidence for a role of chloroethylaziridine in the cytotoxicity of cyclophosphamide. Cancer Chemother Pharmacol 2000; 45:335-344.
185. Chan KK ZJ, Wang JJ, Dea P, Muggia FM. . Retention of cytotoxicity of phosphoramide mustard (PM) aqueous solution after its complete degradation. Proc Am Assoc Cancer Res. 1994; 35:300.
186. Madden JA, Hoyer PB, Devine PJ, Keating AF. Involvement of a volatile metabolite during phosphoramide mustard-induced ovotoxicity. Toxicol Appl Pharmacol 2014; 277:1-7.
187. Perez GI, Tao XJ, Tilly JL. Fragmentation and death (a.k.a. apoptosis) of ovulated oocytes. Mol Hum Reprod 1999; 5:414-420.
188. Kerr JB, Hutt KJ, Cook M, Speed TP, Strasser A, Findlay JK, Scott CL. Cisplatin-induced primordial follicle oocyte killing and loss of fertility are not prevented by imatinib. Nat Med 2012; 18:1170-1172; author reply 1172-1174.
189. Kim SY, Nair DM, Romero M, Serna VA, Koleske AJ, Woodruff TK, Kurita T. Transient inhibition of p53 homologs protects ovarian function from two distinct apoptotic pathways triggered by anticancer therapies. Cell Death Differ 2019; 26:502-515.
190. Luan Y, Edmonds ME, Woodruff TK, Kim SY. Inhibitors of apoptosis protect the ovarian reserve from cyclophosphamide. J Endocrinol 2019; 240:243-256.

191. Kalich-Philosoph L, Roness H, Carmely A, Fishel-Bartal M, Ligumsky H, Paglin S, Wolf I, Kanety H, Sredni B, Meirow D. Cyclophosphamide triggers follicle activation and "burnout"; AS101 prevents follicle loss and preserves fertility. Sci Transl Med 2013; 5:185ra162.
192. Chang EM, Lim E, Yoon S, Jeong K, Bae S, Lee DR, Yoon TK, Choi Y, Lee WS. Cisplatin Induces Overactivation of the Dormant Primordial Follicle through PTEN/AKT/FOXO3a Pathway which Leads to Loss of Ovarian Reserve in Mice. PLoS One 2015; 10:e0144245.
193. Morgan S, Lopes F, Gourley C, Anderson RA, Spears N. Cisplatin and doxorubicin induce distinct mechanisms of ovarian follicle loss; imatinib provides selective protection only against cisplatin. PLoS One 2013; 8:e70117.
194. Scully R, Panday A, Elango R, Willis NA. DNA double-strand break repair-pathway choice in somatic mammalian cells. Nat Rev Mol Cell Biol 2019.
195. Abdel-Fatah TM, Arora A, Moseley P, Coveney C, Perry C, Johnson K, Kent C, Ball G, Chan S, Madhusudan S. ATM, ATR and DNA-PKcs expressions correlate to adverse clinical outcomes in epithelial ovarian cancers. BBA Clin 2014; 2:10-17.
196. Paques F, Haber JE. Multiple pathways of recombination induced by double-strand breaks in Saccharomyces cerevisiae. Microbiol Mol Biol Rev 1999; 63:349-404.
197. Sung P, Klein H. Mechanism of homologous recombination: mediators and helicases take on regulatory functions. Nat Rev Mol Cell Biol 2006; 7:739-750.
198. Prakash R, Zhang Y, Feng W, Jasin M. Homologous recombination and human health: the roles of BRCA1, BRCA2, and associated proteins. Cold Spring Harb Perspect Biol 2015; 7:a016600.
199. Hartlerode AJ, Scully R. Mechanisms of double-strand break repair in somatic mammalian cells. Biochem J 2009; 423:157-168.
200. Pannunzio NR, Watanabe G, Lieber MR. Nonhomologous DNA end-joining for repair of DNA double-strand breaks. J Biol Chem 2018; 293:10512-10523.
201. Gottlieb TM, Jackson SP. The DNA-dependent protein kinase: requirement for DNA ends and association with Ku antigen. Cell 1993; 72:131-142.
202. Nick McElhinny SA, Snowden CM, McCarville J, Ramsden DA. Ku recruits the XRCC4-ligase IV complex to DNA ends. Mol Cell Biol 2000; 20:2996-3003.
203. Ahnesorg P, Smith P, Jackson SP. XLF interacts with the XRCC4-DNA ligase IV complex to promote DNA nonhomologous end-joining. Cell 2006; 124:301-313.
204. Buck D, Malivert L, de Chasseval R, Barraud A, Fondaneche MC, Sanal O, Plebani A, Stephan JL, Hufnagel M, le Deist F, Fischer A, Durandy A, et al. Cernunnos, a novel nonhomologous end-joining factor, is mutated in human immunodeficiency with microcephaly. Cell 2006; 124:287-299.
205. Ochi T, Blackford AN, Coates J, Jhujh S, Mehmood S, Tamura N, Travers J, Wu Q, Draviam VM, Robinson CV, Blundell TL, Jackson SP. DNA repair. PAXX, a paralog of XRCC4 and XLF, interacts with Ku to promote DNA double-strand break repair. Science 2015; 347:185-188.
206. Stinson BM MA, Walter JC, Loparo JJ. A mechanism to minimize errors during non-homologous end joining. bioRxiv 2019.
207. Takata M, Sasaki MS, Sonoda E, Morrison C, Hashimoto M, Utsumi H, Yamaguchi-Iwai Y, Shinohara A, Takeda S. Homologous recombination and non-

homologous end-joining pathways of DNA double-strand break repair have overlapping roles in the maintenance of chromosomal integrity in vertebrate cells. Embo j 1998; 17:5497-5508.
208. Mimitou EP, Symington LS. Sae2, Exo1 and Sgs1 collaborate in DNA double-strand break processing. Nature 2008; 455:770-774.
209. Nimonkar AV, Genschel J, Kinoshita E, Polaczek P, Campbell JL, Wyman C, Modrich P, Kowalczykowski SC. BLM-DNA2-RPA-MRN and EXO1-BLM-RPA-MRN constitute two DNA end resection machineries for human DNA break repair. Genes Dev 2011; 25:350-362.
210. San Filippo J, Sung P, Klein H. Mechanism of eukaryotic homologous recombination. Annu Rev Biochem 2008; 77:229-257.
211. Yang H, Li Q, Fan J, Holloman WK, Pavletich NP. The BRCA2 homologue Brh2 nucleates RAD51 filament formation at a dsDNA-ssDNA junction. Nature 2005; 433:653-657.
212. Zhao W, Steinfeld JB, Liang F, Chen X, Maranon DG, Jian Ma C, Kwon Y, Rao T, Wang W, Sheng C, Song X, Deng Y, et al. BRCA1-BARD1 promotes RAD51-mediated homologous DNA pairing. Nature 2017; 550:360-365.
213. Roos WP, Kaina B. DNA damage-induced cell death: from specific DNA lesions to the DNA damage response and apoptosis. Cancer Lett 2013; 332:237-248.
214. Rogakou EP, Boon C, Redon C, Bonner WM. Megabase chromatin domains involved in DNA double-strand breaks in vivo. J Cell Biol 1999; 146:905-916.
215. Lou Z, Minter-Dykhouse K, Franco S, Gostissa M, Rivera MA, Celeste A, Manis JP, van Deursen J, Nussenzweig A, Paull TT, Alt FW, Chen J. MDC1 maintains genomic stability by participating in the amplification of ATM-dependent DNA damage signals. Mol Cell 2006; 21:187-200.
216. Gatei M, Scott SP, Filippovitch I, Soronika N, Lavin MF, Weber B, Khanna KK. Role for ATM in DNA damage-induced phosphorylation of BRCA1. Cancer Res 2000; 60:3299-3304.
217. Falck J, Mailand N, Syljuasen RG, Bartek J, Lukas J. The ATM-Chk2-Cdc25A checkpoint pathway guards against radioresistant DNA synthesis. Nature 2001; 410:842-847.
218. Meulmeester E, Pereg Y, Shiloh Y, Jochemsen AG. ATM-mediated phosphorylations inhibit Mdmx/Mdm2 stabilization by HAUSP in favor of p53 activation. Cell Cycle 2005; 4:1166-1170.
219. Liu Q, Turner KM, Alfred Yung WK, Chen K, Zhang W. Role of AKT signaling in DNA repair and clinical response to cancer therapy. Neuro Oncol 2014; 16:1313-1323.
220. Mirzoeva OK, Petrini JH. DNA damage-dependent nuclear dynamics of the Mre11 complex. Mol Cell Biol 2001; 21:281-288.
221. D'Amours D, Jackson SP. The Mre11 complex: at the crossroads of dna repair and checkpoint signalling. Nat Rev Mol Cell Biol 2002; 3:317-327.
222. Uziel T, Lerenthal Y, Moyal L, Andegeko Y, Mittelman L, Shiloh Y. Requirement of the MRN complex for ATM activation by DNA damage. Embo j 2003; 22:5612-5621.
223. Lee JH, Paull TT. ATM activation by DNA double-strand breaks through the Mre11-Rad50-Nbs1 complex. Science 2005; 308:551-554.

224. Bakkenist CJ, Kastan MB. DNA damage activates ATM through intermolecular autophosphorylation and dimer dissociation. Nature 2003; 421:499-506.
225. Kozlov S, Gueven N, Keating K, Ramsay J, Lavin MF. ATP activates ataxia-telangiectasia mutated (ATM) in vitro. Importance of autophosphorylation. J Biol Chem 2003; 278:9309-9317.
226. Svetlova MP, Solovjeva LV, Tomilin NV. Mechanism of elimination of phosphorylated histone H2AX from chromatin after repair of DNA double-strand breaks. Mutat Res 2010; 685:54-60.
227. Bartek J, Lukas J. Mammalian G1- and S-phase checkpoints in response to DNA damage. Curr Opin Cell Biol 2001; 13:738-747.
228. Lane DP. Cancer. p53, guardian of the genome. Nature 1992; 358:15-16.
229. Viniegra JG, Martinez N, Modirassari P, Hernandez Losa J, Parada Cobo C, Sanchez-Arevalo Lobo VJ, Aceves Luquero CI, Alvarez-Vallina L, Ramon y Cajal S, Rojas JM, Sanchez-Prieto R. Full activation of PKB/Akt in response to insulin or ionizing radiation is mediated through ATM. J Biol Chem 2005; 280:4029-4036.
230. Athma P, Rappaport R, Swift M. Molecular genotyping shows that ataxia-telangiectasia heterozygotes are predisposed to breast cancer. Cancer Genet Cytogenet 1996; 92:130-134.
231. Robson M, Gilewski T, Haas B, Levin D, Borgen P, Rajan P, Hirschaut Y, Pressman P, Rosen PP, Lesser ML, Norton L, Offit K. BRCA-associated breast cancer in young women. J Clin Oncol 1998; 16:1642-1649.
232. Rzepka-Gorska I, Tarnowski B, Chudecka-Glaz A, Gorski B, Zielinska D, Toloczko-Grabarek A. Premature menopause in patients with BRCA1 gene mutation. Breast Cancer Res Treat 2006; 100:59-63.
233. Titus S, Li F, Stobezki R, Akula K, Unsal E, Jeong K, Dickler M, Robson M, Moy F, Goswami S, Oktay K. Impairment of BRCA1-related DNA double-strand break repair leads to ovarian aging in mice and humans. Sci Transl Med 2013; 5:172ra121.
234. Jaaskelainen M, Nieminen A, Pokkyla RM, Kauppinen M, Liakka A, Heikinheimo M, Vaskivuo TE, Klefstrom J, Tapanainen JS. Regulation of cell death in human fetal and adult ovaries--role of Bok and Bcl-X(L). Mol Cell Endocrinol 2010; 330:17-24.
235. Vaskivuo TE, Anttonen M, Herva R, Billig H, Dorland M, te Velde ER, Stenback F, Heikinheimo M, Tapanainen JS. Survival of human ovarian follicles from fetal to adult life: apoptosis, apoptosis-related proteins, and transcription factor GATA-4. J Clin Endocrinol Metab 2001; 86:3421-3429.
236. Hsueh AJ, Billig H, Tsafriri A. Ovarian follicle atresia: a hormonally controlled apoptotic process. Endocr Rev 1994; 15:707-724.
237. Rolaki A, Drakakis P, Millingos S, Loutradis D, Makrigiannakis A. Novel trends in follicular development, atresia and corpus luteum regression: a role for apoptosis. Reprod Biomed Online 2005; 11:93-103.
238. Hirshfield AN, Midgley AR, Jr. Morphometric analysis of follicular development in the rat. Biol Reprod 1978; 19:597-605.
239. Adams JM, Cory S. The Bcl-2 protein family: arbiters of cell survival. Science 1998; 281:1322-1326.

240. Schultz DR, Harrington WJ, Jr. Apoptosis: programmed cell death at a molecular level. Semin Arthritis Rheum 2003; 32:345-369.
241. Amsterdam A, Sasson R, Keren-Tal I, Aharoni D, Dantes A, Rimon E, Land A, Cohen T, Dor Y, Hirsh L. Alternative pathways of ovarian apoptosis: death for life. Biochem Pharmacol 2003; 66:1355-1362.
242. Shen M, Liu Z, Li B, Teng Y, Zhang J, Tang Y, Sun SC, Liu H. Involvement of FoxO1 in the effects of follicle-stimulating hormone on inhibition of apoptosis in mouse granulosa cells. Cell Death Dis 2014; 5:e1475.
243. Regan SLP, Knight PG, Yovich JL, Leung Y, Arfuso F, Dharmarajan A. Granulosa Cell Apoptosis in the Ovarian Follicle-A Changing View. Front Endocrinol (Lausanne) 2018; 9:61.
244. Poljicanin A, Vukusic Pusic T, Vukojevic K, Caric A, Vilovic K, Tomic S, Soljic V, Saraga-Babic M. The expression patterns of pro-apoptotic and anti-apoptotic factors in human fetal and adult ovary. Acta Histochem 2013; 115:533-540.
245. Albamonte MS AM, Vitullo AD. Germ line apoptosis in the mature human ovary. J Med Res Sci 2012:136–145.
246. Trapani JA, Smyth MJ. Functional significance of the perforin/granzyme cell death pathway. Nat Rev Immunol 2002; 2:735-747.
247. Gross A, McDonnell JM, Korsmeyer SJ. BCL-2 family members and the mitochondria in apoptosis. Genes Dev 1999; 13:1899-1911.
248. Hill MM, Adrain C, Duriez PJ, Creagh EM, Martin SJ. Analysis of the composition, assembly kinetics and activity of native Apaf-1 apoptosomes. Embo j 2004; 23:2134-2145.
249. Hsu H, Xiong J, Goeddel DV. The TNF receptor 1-associated protein TRADD signals cell death and NF-kappa B activation. Cell 1995; 81:495-504.
250. Wajant H. The Fas signaling pathway: more than a paradigm. Science 2002; 296:1635-1636.
251. Irving-Rodgers HF, Krupa M, Rodgers RJ. Cholesterol side-chain cleavage cytochrome P450 and 3beta-hydroxysteroid dehydrogenase expression and the concentrations of steroid hormones in the follicular fluids of different phenotypes of healthy and atretic bovine ovarian follicles. Biol Reprod 2003; 69:2022-2028.
252. Van Wezel IL, Dharmarajan AM, Lavranos TC, Rodgers RJ. Evidence for alternative pathways of granulosa cell death in healthy and slightly atretic bovine antral follicles. Endocrinology 1999; 140:2602-2612.
253. Yu YS, Sui HS, Han ZB, Li W, Luo MJ, Tan JH. Apoptosis in granulosa cells during follicular atresia: relationship with steroids and insulin-like growth factors. Cell Res 2004; 14:341-346.
254. Chun SY, Eisenhauer KM, Minami S, Billig H, Perlas E, Hsueh AJ. Hormonal regulation of apoptosis in early antral follicles: follicle-stimulating hormone as a major survival factor. Endocrinology 1996; 137:1447-1456.
255. Chun SY, Billig H, Tilly JL, Furuta I, Tsafriri A, Hsueh AJ. Gonadotropin suppression of apoptosis in cultured preovulatory follicles: mediatory role of endogenous insulin-like growth factor I. Endocrinology 1994; 135:1845-1853.
256. Eisenhauer KM, Chun SY, Billig H, Hsueh AJ. Growth hormone suppression of apoptosis in preovulatory rat follicles and partial neutralization by insulin-like growth factor binding protein. Biol Reprod 1995; 53:13-20.

257. Billig H, Furuta I, Hsueh AJ. Estrogens inhibit and androgens enhance ovarian granulosa cell apoptosis. Endocrinology 1993; 133:2204-2212.
258. Billig H, Furuta I, Hsueh AJ. Gonadotropin-releasing hormone directly induces apoptotic cell death in the rat ovary: biochemical and in situ detection of deoxyribonucleic acid fragmentation in granulosa cells. Endocrinology 1994; 134:245-252.
259. Hulas-Stasiak M, Gawron A. Follicular atresia in the prepubertal spiny mouse (Acomys cahirinus) ovary. Apoptosis 2011; 16:967-975.
260. Choi JY, Jo MW, Lee EY, Yoon BK, Choi DS. The role of autophagy in follicular development and atresia in rat granulosa cells. Fertil Steril 2010; 93:2532-2537.
261. Duerrschmidt N, Zabirnyk O, Nowicki M, Ricken A, Hmeidan FA, Blumenauer V, Borlak J, Spanel-Borowski K. Lectin-like oxidized low-density lipoprotein receptor-1-mediated autophagy in human granulosa cells as an alternative of programmed cell death. Endocrinology 2006; 147:3851-3860.
262. Meng L, Jan SZ, Hamer G, van Pelt AM, van der Stelt I, Keijer J, Teerds KJ. Preantral follicular atresia occurs mainly through autophagy, while antral follicles degenerate mostly through apoptosis. Biol Reprod 2018; 99:853-863.

Figures and Figure Legends

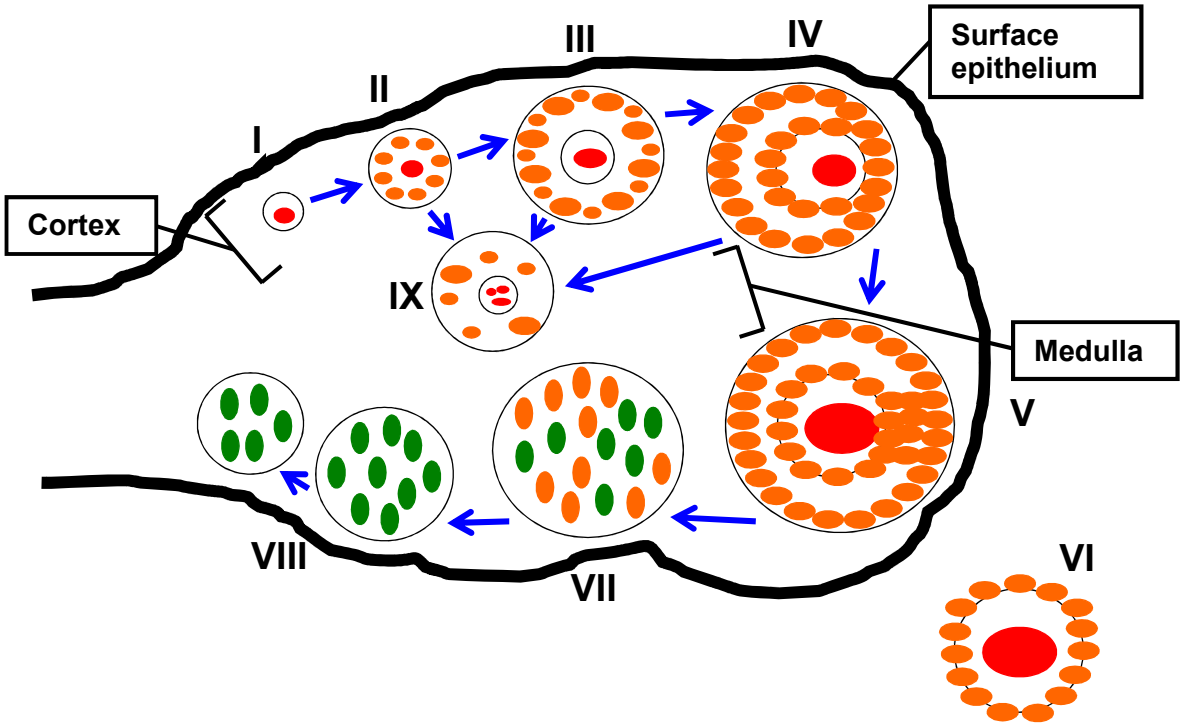

Figure 1. Stages of ovarian follicular development. The stages of folliculogenesis are depicted with red indicating oocyte, orange indicating granulosa cells, and green indicating luteal cells. The stages of follicle maturation are indicated by roman numerals: I – Primordial, II – Primary, III – Secondary, IV – Antral, V – Pre-ovulatory, VI – Ovulated oocyte, VII – Early corpus luteum, VIII – Mature and regressing corpus luteum, IX – Atretic (modified from Clark et al., 2018).

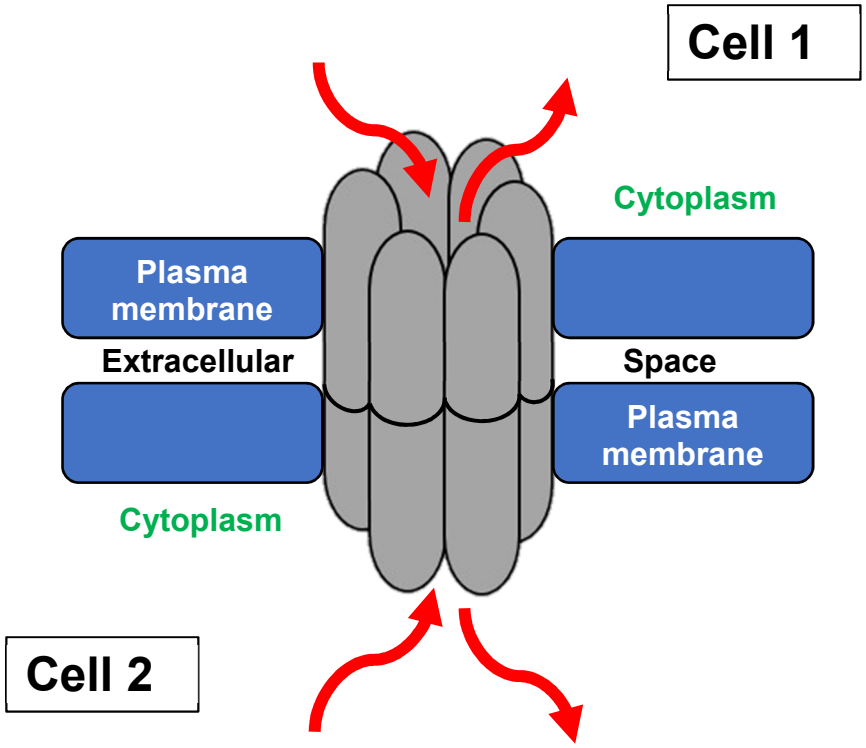

Figure 2. Gap junction organization. Each gap junction is formed of two connexons, one in each respective cell membrane, comprised of six connexin protein subunits in a ring-like structure. Gap junctions facilitate intercellular communication, allowing the flow of various molecules, ions, and electrical impulses between the cytoplasm of adjacent cells.

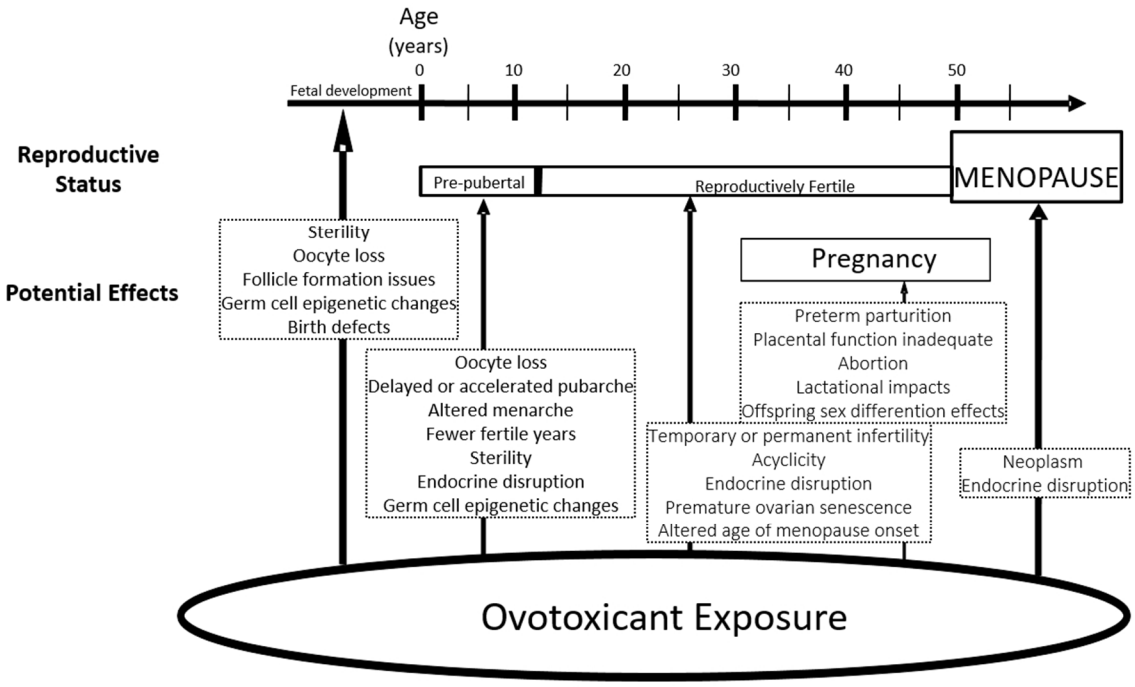

Figure 3. Impacts of ovotoxicant exposure on female fertility across developmental stages. The effects of an ovotoxic exposure on female reproductive function depends primarily on the developmental stage of exposure as well as on the level and duration of chemical exposure. Potential impacts of chemical exposures are summarized at each developmental stage, but these impacts are chemical specific (modified from Clark et al., 2018).

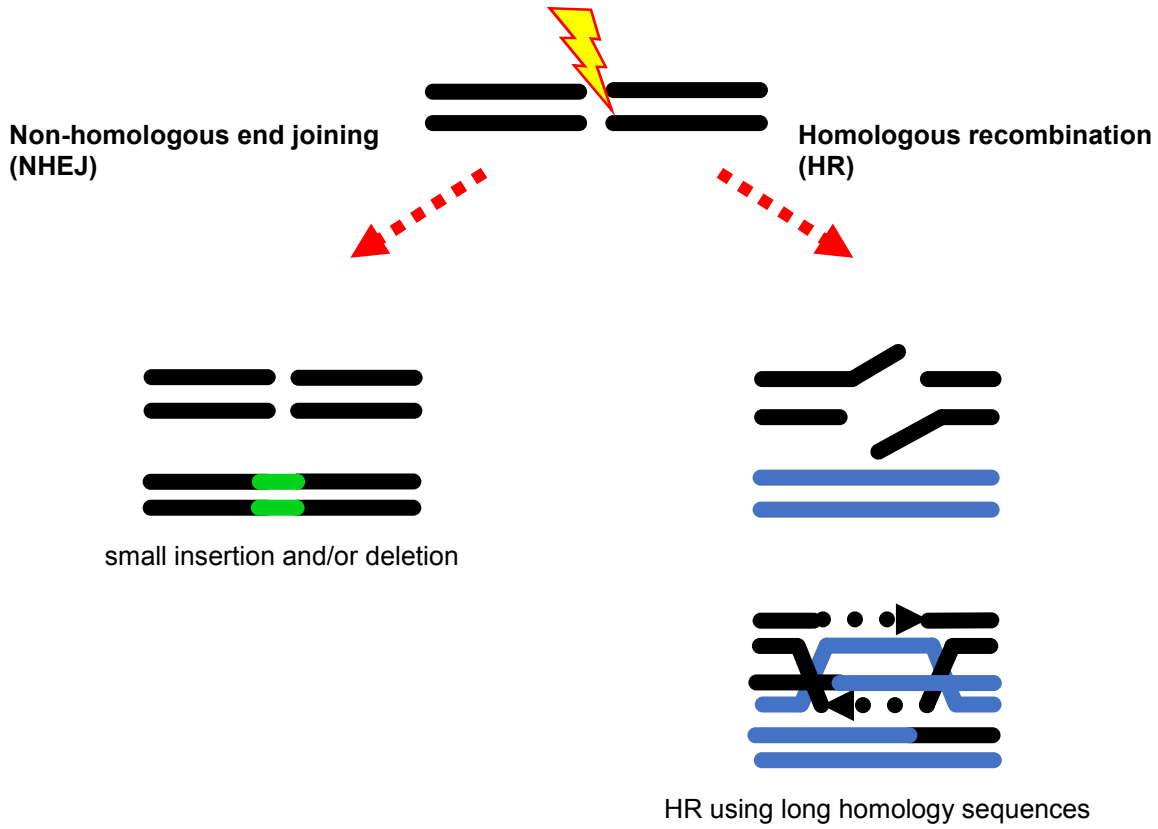

Figure 4. Mechanisms of DNA double strand break repair. Non-homologous end joining (left) and homologous recombination (right).

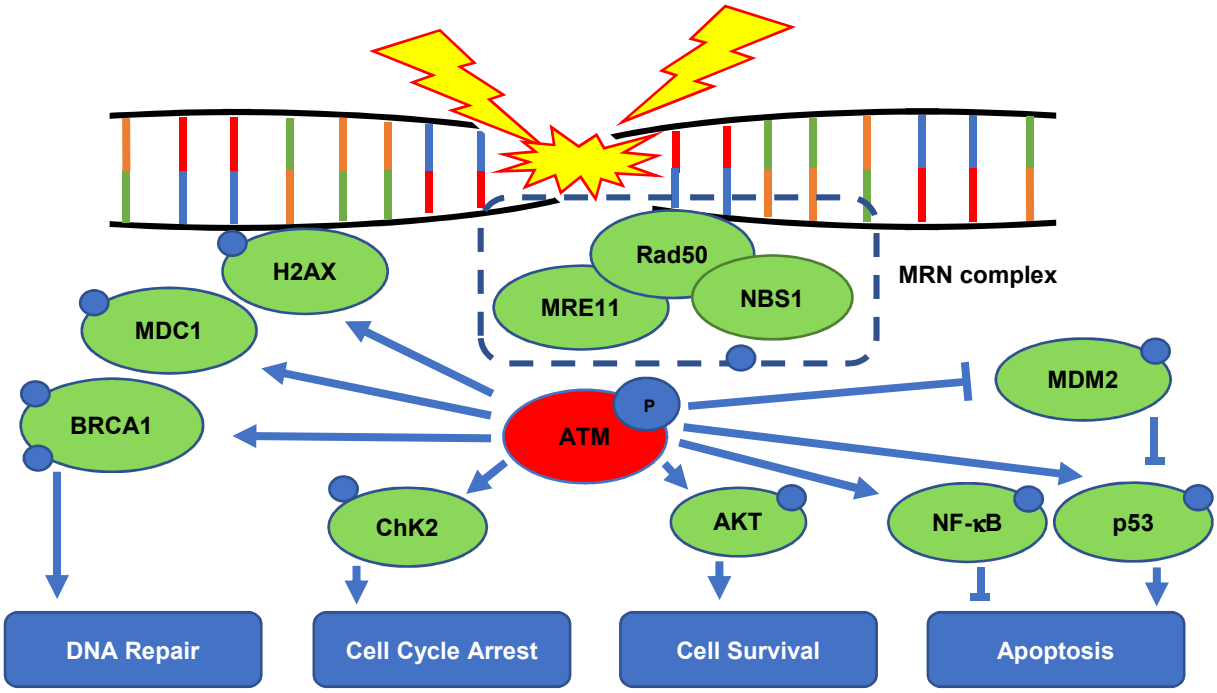

Figure 5. ATM-mediated double strand break repair. Endogenous or exogenous sources of DNA damage can result in DNA double strand breaks. One of the main orchestrators of DNA repair is the ATM protein. The cellular response after a DNA damaging event includes cell cycle arrest, DNA repair, apoptosis, or cell survival.

CHAPTER 2. DEVELOPMENTAL ORIGINS OF OVARIAN DISORDER: IMPACT OF MATERNAL LEAN GESTATIONAL DIABETES ON THE OFFSPRING OVARIAN PROTEOME IN MICE

Kendra L. Clark[1], Omonseigho O. Talton[2], Shanthi Ganesan[1], Laura C. Schulz[2], and Aileen F. Keating[1]

[1]Department of Animal Science - Iowa State University, Ames, Iowa 50011

[2]Department of Obstetrics, Gynecology, and Women's Health - University of Missouri, Columbia, Missouri 65211

A manuscript published in
Biology of Reproduction, 2019

Contribution Statement:

K.L. Clark performed all analyses on ovarian tissue, designed experiments, and interpreted the data and wrote the manuscript. S. Ganesan aided with experimental design. O.O Talton and L.C. Schulz graciously provided the ovarian tissue; LCS edited the manuscript. A.F. Keating designed the experiments, aided in data interpretation and edited the manuscript.

Abstract

Gestational diabetes mellitus (GDM) is an obstetric disorder affecting approximately 10% of pregnancies. The 4HFHS (High Fat High Sucrose) mouse model emulates GDM in lean women. Dams are fed a HFHS diet one week prior to mating and throughout gestation resulting in inadequate insulin response to glucose in mid-late pregnancy. The offspring of HFHS dams have increased adiposity, thus, we hypothesized that maternal metabolic alterations during lean GDM would compromise ovarian function in offspring both basally and in response to a control or HFHS diet in adulthood. Briefly,

D_LP_L were lean dams and control diet pups; D_LP_H were lean dams and HFHS pups; D_HP_L were HFHS dams and control diet pups and D_HP_H were HFHS dams and HFHS pups. A HFHS challenge in the absence of maternal GDM (D_LP_L vs. D_LP_H) increased 3 and decreased 30 ovarian proteins. Maternal GDM in the absence of a dietary stress (D_LP_L vs. D_HP_L) increased abundance of 4 proteins and decreased abundance of 85 proteins in the offspring ovary. Finally, 87 proteins increased, and 4 proteins decreased in offspring ovaries due to dietary challenge and exposure to maternal GDM *in utero* (D_LP_L vs. D_HP_H). Canopy FGF signaling regulator 2 (CNPY2), Deleted in azoospermia-associated protein 1 (DAZAP1), Septin 7 (SEPT7), and Serine/arginine rich splicing factor 2 (SRSF2) were altered across multiple offspring groups. Together, these findings suggest a possible impact on fertility and oocyte quality in relation to GDM exposure in utero as well as in response to a western diet in later life.

***Keywords**:* Gestational diabetes, ovary, proteomics, offspring health

Introduction

The ovary produces the female gamete, the oocyte, and primary sex hormones 17β-estradiol (E_2) and progesterone (P_4). Oocytes arise from primordial germ cells *in utero* and remain encased in primitive follicular structures, arrested at the diplotene stage of meiosis, or they degenerate through programmed cell death termed atresia [1]. Through the natural progression of time or due to factors that may expedite the process, the pool of ovarian oocytes ultimately becomes depleted and ovarian senescence occurs in women [1]. Ovarian failure preceding age 40 is characterized as primary ovarian insufficiency (POI)

[2], which may be attributable to genetics, autoimmune disorders, iatrogenesis, surgical, or unknown etiology, and affects approximately 1% of women [3].

In recent years, globally there has been an expeditious rise in obesity rates in both adults and children, predisposing them for health problems including diabetes [4], cardiovascular disease [5], cancer [6], and reproductive decline [7]. In the overweight or obese female, reproductive complications include POI [8], polycystic ovary syndrome (PCOS) [9], poor oocyte quality [10], decreased fecundity [11], gestational diabetes mellitus (GDM) [12], and offspring congenital abnormalities [13]. Changes in central metabolism negatively affect the ovary, with insulin responsive pathways such as the phosphatidylinositol 3-kinase (PI3K) pathway being upregulated during obesity [14], reduced follicle number [15], altered steroid hormone biosynthesis [16], and inflammation [15]. Additionally, basal ovarian DNA damage and a blunted ovarian response to genotoxicants occurs in obese mice [16-19]. Offspring exposed to maternal obesity have increased risk of neural tube defects [20], glucose intolerance [21], altered neurobehavior [22], intrauterine growth restriction (IUGR) [23], and increased circulating cholesterol and body fat [24]. The reproductive outcomes on female offspring exposed to maternal obesity *in utero* include a decrease in the ovarian follicular reserve [25, 26], decreases in ovarian vascularity [27], and disturbances in the estrous cycle in a rodent model [28].

In association to the rise of obesity in reproductive age women, the prevalence of GDM is also increasing. Defined as glucose intolerance during pregnancy, GDM may affect up to 20% of pregnancies, dependent on population demographics [29], screening and diagnostic criteria [29], and pre-gestational maternal lifestyle factors [30]. Insulin sensitivity naturally decreases during pregnancy for all women [31] but overweight and

obese women have higher risk of developing GDM than their lean counterparts [12, 32] and lean women with GDM have reduced or delayed first-phase insulin response to glucose [31]. Immediate health concerns are posed by GDM, and although GDM normally resolves postpartum, long-term maternal health effects include a 60% higher risk of acquiring Type 2 diabetes [33, 34]. Fetal and neonatal complications include macrosomia [35], hypoglycemia [36], respiratory distress [36], future obesity [37], and predisposition for Type 2 diabetes [38].

When considering our recent findings that progressive obesity alters a variety of ovarian intracellular signaling pathways that could compromise fertility and offspring health [14, 15, 17, 19, 39, 40], we hypothesized that similar alterations would result from exposure of the developing ovary to metabolic alterations *in utero*. A lean GDM model has been developed using acute, high-fat feeding one week prior to conception and throughout gestation, thereby separating effects of pre-conceptional obesity from maternal gestational metabolic alterations on the offspring [41]. We utilized ovaries from offspring who experienced GDM *in utero* and also assessed whether a dietary stress in adulthood would affect the ovarian response to such an insult.

Materials and Methods

Animal procedures and tissue collection

Ovarian tissue utilized in this study was obtained as part of a larger study [42]. Briefly, gestational diabetes was induced in female C57B16/J mice (n = 14) by feeding a high fat, high sucrose (HFHS; 45% kcal/fat (lard and soybean oil) and 17% kcal/sucrose) diet (D12451, Research Diets, Inc) one week prior to mating and for the duration of gestation,

for a total of 4 weeks as described [41, 42]. Control female C57B16/J mice (Jackson Laboratories; n = 20) were fed a chow breeder diet (17% kcal/fat (lard) and 2.4% kcal/sucrose; LabDiet 5008, Purina) throughout the duration of the study. Both groups of females were mated to C57B16/J sires. Female offspring from each litter (control – n = 30; GDM – n = 16) were maintained on the chow breeder diet, until 23 weeks of age, at which point 1-2 females from each litter was fed the HFHS diet until 31 weeks of age, at which time both groups of offspring were humanely sacrificed. Mice were not at the same stage of the estrous cycle at euthanasia. Ovaries were collected from adult females and one ovary was snap-frozen in liquid nitrogen before storage at -80°C. The contralateral ovary was fixed in 4% paraformaldehyde and stored in 70% ethanol prior to histological processing. Ovaries utilized for frozen tissue sections were collected from 10-week-old female C57B16/J mice during the pro-estrus stage of the estrous cycle and fixed in 4% paraformaldehyde overnight at 4°C. For cryoprotection, fixed ovaries were passed in 10% sucrose/PBS solution for 1-3 hours at room temperature followed by 30% sucrose/PBS solution at 4°C overnight prior to embedding in OCT medium (Fisher Healthcare). All animal procedures were approved by the University of Missouri or the Iowa State University Institutional Animal Care and Use Committee and handled according to National Institutes of Health Guide for Care and Use of Laboratory Animals.

Histology and follicle counting

Fixed ovaries were paraffin embedded and serially sectioned (n = 4/treatment) at 5 µm, with every 6th section mounted onto glass slides and stained with hematoxylin and eosin. Healthy follicles containing oocytes with a distinct oocyte nucleus were counted

and classified as previously described [43]. Briefly, primordial follicles were identified by an oocyte surrounded by a single layer of squamous granulosa cells; primary follicles contained the oocyte surrounded by a single layer of cuboidal granulosa cells, and secondary follicles contained an oocyte surrounded by multiple layers of granulosa cells. Slide identify was blinded to prevent counting bias. Follicle counts performed on a Nikon Optiphot using a 5x or 20x objective and bright field images captured on an inverted DMI3000B microscope (Leica) and QICAM MicroPublisher 5.0 (MP5.0-RTV-CLR-10, QIMAGING) camera using QCapture software at a 5x objective. Total follicles counted per ovary were compared between treatments.

Protein isolation, LC-MS/MS, and proteome analysis

Total ovarian protein was isolated (n = 3/treatment) in lysis buffer (50 mM Tris-HCL, 1 mM EDTA, pH 8.5), homogenized, and centrifuged at 10,000 rpm at 4°C for 15 min. Supernatant was collected, and protein content was quantified using bicinchoninic acid assay (BCA; Pierce BCA Protein Assay Kit, Thermofisher). A working protein dilution of 50 μg/μl was prepared with lysis buffer. For LC-MS/MS analysis, total protein (50 μg/μl) was digested with trypsin/Lys-C for 16 hours, dried down and reconstituted in buffer A (47.5μl; 0.1% formic acid/water) and Peptide Retention Time Calibration (PRTC) mixture was utilized as a standard (25 fmol/μl) and was spiked into each sample to serve as an internal control. Protein (10 μg) and PRTC (250 fmol) were injected onto a liquid chromatography column (Agilent Zorbax SB-C18, 0.5mm x 150mm, 5 micron) using an Agilent 1260 Infinity Capillary Pump. Peptides were separated by liquid chromatography and analyzed using a Q Exactive™ Hybrid Quadrupole-Orbitrap Mass Spectrometer with

a higher energy collisional dissociation (HCD) fragmentation cell. The resulting intact and fragmentation pattern was compared to a theoretical fragmentation pattern (from either MASCOT or Sequest HT) to identify peptides. The relative abundance of the identified proteins was based on the areas of the top three unique peptides for each sample. The arithmetic mean of the PRTC was used as normalization factor. For each peptide, the signal intensity was divided by the arithmetic mean of the PRTC before further analysis.

Metaboanalyst 3.0 [44, 45] was used for data analysis. Upon finding data integrity to be satisfactory (no peptide with more than 50% missing replicates, positive values for the area), missing value imputation was performed using a Singular Value Decomposition (SVD) method. Filtering, based on interquartile range, was performed to remove values unlikely to be of use when modeling the data, followed by generalized log transformation (glog 2) before data analysis. The control and treatment samples were compared by the Student's *t*-test. Differences between groups were assessed by the Mann-Whitney rank sum test. All *p*-values were two sided. To adjust for multiple comparisons, Bonferroni correction was applied and only *p*-values less than 0.1 were considered as statistically significant. The principal component analysis (PCA) analysis was performed using the *prcomp* package and pairwise score plots providing an overview of the various separation patterns among the most significant components were accessed. The partial least squares (PLS) regression was then performed using the *plsr* function provided by R *pls* package. The classification and cross-validation were also performed using the *caret* package. The UniProt protein identifiers that were up/down regulated were used to retrieve the corresponding KEGG identifiers using the “Retrieve/ID mapping” tool of UniProt

(accessible at tp://www.uniprot.org/uploadlists/). KEGG identifiers were then used to retrieve biological pathway association of the proteins.

Gene ontology analysis

Gene Ontology (GO) analysis was performed using PANTHER version 14.1 (http://www.pantherdb.org). Proteins identified in the control and experimental samples were compared to the *Mus musculus* reference list for a statistical overrepresentation test to highlight categories in biological process, molecular function, and cellular components with significant fold-enrichment in our samples. The Fisher's Exact test with False Discovery Rate (FDR) correction was used with $P < 0.05$ considered as a statistically significant difference.

Immunofluorescence staining

Slides were deparaffinized in Citrisolv and rehydrated in subsequent washes of ethanol (100%, 95%, 75%), followed by one wash in ddH_2O. Heat mediated antigen retrieval was performed using citrate buffer (10 mM citric acid, 0.5% Tween20, pH 6.0) in a microwave for 22 min. Tissue sections on histology slides were encircled with a histology pap pen to keep liquid concentrated on the tissue during processing, followed by the application of blocking solution (0.1M PBS/0.4% BSA/0.2% Tween20/2.5% goat serum) to the slides for 1 hour at room temperature. In addition, frozen tissue from 10-week-old female C57B16/J mice was utilized to determine localization of canopy FGF signaling regulator 2 (CNPY2), deleted in azoospermia-associated protein 1 (DAZAP1), pre-mRNA serine/arginine rich splicing factor 2 (SRSF2), and septin 7 (SEPT7). Briefly,

frozen slides were thawed on a 37°C slide warmer for 5 minutes, tissue encircled with a histology pap pen, and rehydrated in phosphate buffered saline with 0.1% Tween20 (PBSTw) for 20 minutes at room temperature before addition of blocking solution (described above). Primary antibodies for CNPY2, DAZAP1, SRSF2, SEPT7, phosphorylated histone 2AX (γH2AX), and cleaved caspase-3 (CASP3; dilutions listed in **Supplementary Table 1**) were added into fresh blocking solution, applied to tissue sections and allowed to incubate in a humidified box at 4°C overnight. Slides were washed (3 x 10 min) in PBSTw. Secondary antibodies (**Supplementary Table 1**) were added into fresh blocking solution and incubated at room temperature for 60 min, followed by washes (3 x 10 min) in PBSTw. Slides were allowed to air dry, counterstained and mounted with 4-6-diamidino-2-phenyllindole (DAPI) and stored at 4°C until image capture. Negative technical controls to confirm specificity were performed using secondary antibodies alone (**Supplementary Figure 1**). Images were captured on a Zeiss LSM700 confocal microscope equipped with an AxioCam MRc5 using a 20x objective lens. For γH2AX (n=40 sections; 10 sections per treatment) and cleaved CASP3 (n=40 sections; 10 sections per treatment), immunopositive cells were manually counted in the granulosa cells and/or oocytes of primary, secondary and antral follicles using the cell counter module of ImageJ (https://imagej.nih.gov/ij/plugins/cell-counter.html).

Statistical analysis

Statistical analyses were performed using GraphPad Prism 7.0 One-way ANOVA function with multiple comparisons. Each treatment mean value was compared to the

control (D_LP_L) mean value using Dunnett's correction with significance level set at $P \leq 0.05$.

Results

GDM exposure in utero and subsequent dietary challenge decreased healthy follicle number

The impact of GDM exposure *in utero* and/or dietary stressor later in life on healthy follicle numbers was determined **(Figure 1**). There was no difference in primordial follicle number between treatment groups (D_LP_H; D_HP_L; and D_HP_H) relative to D_LP_L control ($P = 0.1361$; **Figure 1.A**). Dietary stress in adulthood in the D_LP_H mice did not impact primordial, primary, or secondary follicle number (**Figure 1A-D**). GDM exposure *in utero* also did not affect primordial, primary or secondary follicle number (**Figure 1A-D**). The combination of GDM *in utero* with dietary stress in adulthood in the D_HP_H mice numerically reduced primordial follicle number (**Figure 1A**) and decreased ($P < 0.05$) the number of primary and secondary follicles (**Figure 1 B-D**).

Impact of in utero exposure to GDM on DNA damage in the ovary

To determine if offspring from GDM mothers had increased ovarian DNA damage, tissue sections were immunologically stained for γH2AX and positive foci were quantified. The number of ovarian cells (granulosa cells and/or oocytes) that contained positive γH2AX foci in the primary, secondary, or antral follicles were not different between treatment groups (D_LP_L: 30.1 ± 13.5; D_LP_H: 5.5 ± 3.6; D_HP_L: 48.3 ± 20.5; D_HP_H: 9.8 ± 5.7; **Figure 2 A-F**).

Impact of in utero exposure to GDM on apoptosis in the ovary

In order to assess levels of apoptosis in the ovary, immunofluorescence staining was performed to quantify the level of cleaved CASP3. There was no impact of GDM exposure *in utero* or dietary stress on any treatment group in the level of cleaved CASP3 that was detected in the granulosa cells or oocytes of primary, secondary, or antral follicles (D_LP_L: 8.8 ± 2.1; D_LP_H: 12 ± 2.2; D_HP_L: 10.3 ± 3; D_HP_H: 13 ± 7.6; **Figure 3 A-F**).

In utero exposure to lean GDM alters the offspring ovarian proteome

There were 504 ovarian proteins identified in D_HP_L offspring who experienced GDM *in utero* but did not receive the high fat diet in adulthood. Relative to D_LP_L offspring ovaries, 85 proteins were reduced and 4 were increased in abundance in the ovaries of D_HP_L mice (log2foldchange ≥ 1 and *P*-value ≤ 0.1; **Figure 4A; Supplementary Table 2**).

A high fat diet affects the ovarian proteome in adult mice

A total of 470 ovarian proteins were identified in the D_LP_H mice. Relative to the Relative to D_LP_L offspring ovaries, 30 proteins were decreased, and 3 proteins were increased in the ovaries of D_LP_H (log2foldchange ≥ 1 and *P*-value ≤ 0.1; **Figure 4B; Supplementary Table 3**).

Additive effect of dietary stress in later life on the proteome of offspring exposed to lean GDM in utero

In the D_HP_H ovaries, 481 total proteins were identified. When compared to the D_LP_L mice, 4 proteins were increased and 87 proteins were decreased, indicating the

combined effects of GDM exposure *in utero* with an HFD stress in adulthood (log2foldchange ≥ 1 and *P*-value ≤ 0.1; **Figure 4C; Supplementary Table 4**). Furthermore, comparison of the ovarian proteome of the D_HP_H with the D_LP_H mice revealed the additive effects of *in utero* GDM since both of these groups experienced the dietary stressor in adulthood and 5 proteins were increased and 3 proteins were decreased (log2foldchange ≥ 1 and *P*-value ≤ 0.1; **Supplementary Table 5**).

Of these differentially expressed proteins, 8, 49, and 52 proteins were identified that were unique to D_LP_H, D_HP_L, and D_HP_H, respectively. In addition, 20 proteins were shared between the groups exposed to GDM *in utero,* 5 proteins are shared between the groups exposed to the HFD, and 14 proteins were shared between all the treatment groups (**Figure 5**).

Overrepresented gene ontology (GO) analysis of maternal GDM exposure in the absence or presence of dietary stress in adulthood

Proteins identified as being different from the D_LP_L mice (log2foldchange ≥ 1 and *P*-value ≤ 0.1) in each treatment group (D_LP_H – n = 33; D_HP_L – n = 89; and D_HP_H – n = 91) were assigned to biological process, molecular function, and cellular component using PANTHER GO analysis (Fischer's Exact with FDR multiple test correction; $P < 0.05$). For biological process, several of the GO categories that showed substantial enrichment in the D_HP_H ovaries relative to controls were associated with a catabolic or metabolic process (**Supplementary Figure 1A**). There was a 43-fold enrichment of proteins in the D_HP_H ovaries involved in the hydrogen peroxide catabolic process, including the proteins catalase (CAT), apolipoprotein A-IV (APOA4), and peroxiredoxin-5, mitochondrial (PRDX5).

Proteins from D_HP_L were enriched in categories related to protein complex disassembly, depolymerization, and regulation of actin filament activity (**Supplementary Figure 1B**). Actin crosslink formation had the highest fold-enrichment in the GDM only offspring, with proteins such as Filamin-A (FLNA) and myristoylated alanine-rich C-kinase substrate (MARCKS) included in the cluster. There were no significant categories assigned in the HFHS diet alone offspring.

Concerning molecular function, proteins from GDM exposed and HFHS fed offspring ovaries, GO categories that were enriched mainly involved enzymatic activity or binding (**Supplementary Figure 2A**). Transaminase activity included protein-glutamine gamma glutamyltransferase 2 (TGM2) and aspartate aminotransferase, mitochondrial (GOT2). Ovaries from females exposed to GDM *in utero* without a HFHS challenge had more binding categories assigned, with the protein kinase C binding category having a 20-fold enrichment (**Supplementary Figure 2B**). Proteins identified in this category included serine/arginine-rich splicing factor 2 (SRSF2), FLNA, and MARCKS. Similar to the GDM only group, the HFHS only group had all identified GO terms associated with binding (**Supplementary Figure 2C**). Pre-mRNA binding was enriched 61-fold in this group, with SRSF2, polypyrimidine tract-binding protein (PTBP1), and the splicing factor U2AF 65 kda subunit (U2AF2) protein identified in this cluster.

GO terms assigned to cellular component included those involved in cell junctions and various cell complexes. Fascia adherens was enriched 56-fold in the D_HP_H ovaries, with proteins such as vinculin (VCL), alpha-actinin-1 (ACTN1), and spectrin alpha chain, non-erythrocytic 1 (SPTAN1) identified (**Supplementary Figure 3A**). The interchromatin granule cluster was enriched greater than 100-fold, including the proteins SRSF2 and

cleavage and polyadenylation specificity factor subunit 6 (CPSF6) (**Supplementary Figure 3B**). There were substantially less categories identified in the D_LP_H group (**Supplementary Figure 3C**). The cytoplasm cluster had the highest enrichment only being enriched by 1.75-fold, containing proteins such as SRSF2, PTBP1, and tubulin-specific chaperone A (TBCA).

Ovarian localization of CNPY2, DAZAP1, SRSF2 and SEPT7

In order to establish the ovarian localization of selected proteins identified to be of interest from the LC-MS/MS analysis, but for whom the ovarian location is unknown, immunofluorescence staining was performed on ovarian sections from adult C57B16/J mice. From the LC-MS/MS analysis, CNPY2 had a log2fc of -1.65, -1.72, and -2.18 in groups D_LP_H, D_HP_L, and D_HP_H, respectively. Positive immunofluorescence staining for the CNPY2 protein was observed in the theca and granulosa cells, and the pericytoplasmic region of the oocyte in primary, secondary, and antral follicle stages (**Figure 6A**). DAZAP1 had a -2.43 log2fc and -5.13 log2fc in the D_HP_L and D_HP_H groups, respectively, in the LC-MS/MS analysis, but was not altered in the D_LP_H ovaries, suggesting an impact of GDM exposure *in utero*, and further amplification by dietary stress on ovarian DAZAP1 abundance. Immunological staining for DAZAP1 demonstrated positive staining in luteal cells, oocyte nucleus, and granulosa cells (**Figure 6B**). In contrast to the previous proteins selected from our data set, SRSF2 was identified by LC-MS/MS analysis as being increased in groups D_LP_H, D_HP_L, and D_HP_H with log2fc of 1.70, 1.91, and 1.42, respectively, relative to the D_LP_L ovaries. SRSF2 protein was determined by immunofluorescence staining to be localized to the oocyte peri-cytoplasmic region and

nucleus in pre-ovulatory follicles (**Figure 6C**). SEPT7 was noted from the LC-MS/MS analysis to be decreased in the D_LP_H, D_HP_L, and D_HP_H ovaries by -1.04, -1.43, and -1.07 log2fc, respectively. Positive immunofluorescence staining for SEPT7 was observed in the oocyte, granulosa, and theca cells of primary, secondary, and antral follicles (**Figure 6D**).

Discussion

The reproductive phenotypic impacts of obesity and insulin resistance have been well characterized, yet the percentage of the population at risk continues to increase [46]. In parallel with rising obesity rates, the number of women acquiring GDM is also increasing [47]. One of the major risk factors for GDM development is pre-gestational obesity and/or insulin resistance, although interestingly around a third of cases occur in lean women [48].

While the underlying etiology of GDM remains unknown, several experimental animal models have been developed that effectively mimic the most common GDM features. Partial pancreatectomy in post-pubertal rodents results in a mild type 1 diabetes phenotype via the reduction of β-cell numbers, but limitations include the latency for diabetic symptoms to appear [49]. Administration of alloxan and streptozotocin (STZ) impairs and destroys pancreatic β-cells, leading to hyperglycemia and insulin insufficiency [50-52]. Nicotinamide (NA) injection prior to STZ administration protects the pancreas from severe damage and leads to a lower number of fetal malformations [53-55]. Mouse models of GDM are also available via gene knockout or transgenic overexpression but although effective at emulating GDM, many of these genetic models have more severe

phenotypes than typically observed in human cases of GDM and the genetic changes may be passed on to offspring. A commonly used GDM mouse model are females who are heterozygous for a mutation in the leptin receptor (ObR; $Db^{-/+}$), who have reduced glucose homeostasis in the non-pregnant state, but spontaneously develop hyperphagic feeding, increased adiposity, insulin resistance, and glucose intolerance during pregnancy [56], although conflicting results have been noted in other studies [57-59].

Another approach for inducing GDM is via dietary manipulation. Dams consuming a high-fat diet to induce obesity and insulin resistance pre-pregnancy have a GDM phenotype during pregnancy [60-64]. The maternal model utilized in our study is also diet-induced, and includes a high fat and high sugar diet, which is comparable to the diet of the human population, but obesity is absent prior to gestation. With this method, we are able to elucidate the mechanisms behind GDM without the additive effects of obesity. These females exhibit susceptibility to glucose intolerance later in life when challenged with the same diet but in the absence of increased body mass [41]. An obvious drawback with using this model is that there is a confounding effect of differing dietary composition and the HFHS mice in this study received an additional fat source to the controls in the form of sunflower oil. Future studies aimed at assessing any additive impacts of differing fat source on the ovarian endpoints measured are possible in the future, though it is far more plausible that it is the increased adiposity in this model that contributes to the ovarian effects reported herein.

The ramifications of GDM and the health of the offspring also need consideration. In addition to risk of stillbirth, babies born to mothers who experience diabetes during pregnancy have higher rates of macrosomia [35], hypoglycemia [36], respiratory distress

[36], future obesity [37], and like the mother, a predisposition for type 2 diabetes later in life [38]. Offspring that were exposed to our model of GDM *in utero* and later on challenged with the HFHS diet had increased body weight, higher body fat percentage, and increased adipose insulin sensitivity [42]. Reproductive effects on the male offspring from these dams included reduced sperm counts, reduced germ cell apoptosis, and low testosterone [65]. Our results in the female offspring corroborate the reproductive effects noted in the males, with reduced numbers of healthy primary and secondary follicle numbers, as well as a numerical decrease in primordial follicle numbers in the D_HP_H mice illustrating that *in utero* environment coupled with a later stressor in adulthood may have negative impacts on female fertility.

Previous work from our group and others has demonstrated how the metabolic changes that occur during obesity can alter folliculogenesis and the responsive pathways [15, 16, 19, 66-68]. The ovarian PI3K-PTEN-AKT-FOXO3 signaling pathway is involved in follicular activation via an insulin-mediated process [69, 70]. Hyperinsulinemia is common during obesity, and from this we have previously reported changes in the activation of the PI3K pathway, resulting in increased follicular activation [14]. Thus, it is possible that the observed lower number of follicles in the GDM offspring, especially those challenged with the high fat diet later in life, result from the increased body mass and insulin resistance following *in utero* metabolic exposures. In this study, the female mice had increased adiposity as measured by nuclear magnetic resonance imaging as early as 4 weeks of age, despite not being introduced to the HFHS diet until 23 weeks of age [42]. A subject for future analysis would be to define at what rate the introduction of the HFHS diet to GDM offspring diminishes the follicular pool subsequent to GDM exposure alone.

Obesity is also associated with ovarian DNA damage [17, 18, 40] and throughout the body [71]. Interestingly, we did not observe any consequential changes on GDM and/or dietary stress in later life in the abundance of γH2AX, which is considered the gold standard for DNA double strand break localization [72]. As with increased DNA damage detected in obesity, increased granulosa cell apoptosis has also been reported [73]. We did not, however, observe increased granulosa cell apoptosis as detected by cleaved CASP3 protein in our offspring ovaries. The lack of additional DNA damage and cellular apoptosis in our model could be interpreted as that while they have increased body weight and insulin sensitivity, they have not necessarily amassed a metabolic syndrome severe enough to trigger a genotoxic response. This remains to be determined.

Proteomic profiling can be highly informative in investigating alterations to proteins due to a defined environmental and pathological treatment. In an unbiased proteomic approach, we identified several proteins of interest, including DAZAP1, SEPT7, CNPY2, and SRSF2, to be altered by GDM, adult dietary stress, or both. DAZAP1 was substantially decreased in ovaries from female mice exposed to GDM *in utero*, and further impacted by the additional insult of the HFHS diet. The deleted in azoospermia (DAZ) family of proteins are present in male and female germ cells and play a major role in germ cell development and fertility [74]. Mutations in DAZAP1 results in perinatal lethality, with those surviving experiencing reproductive defects such as sterility as well as growth retardation [75]. Fertility defects associated with DAZAP1 have been typically described in males [76, 77], so our finding of alterations to DAZAP1 due to *in utero* GDM and dietary stress and localization in granulosa and luteal cells as well as in the oocyte implies that

DAZAP1 may have important roles in ovarian physiology and female fertility through altering follicle growth and survival, potentially contributing to POI.

The Septin family of proteins have been well characterized as being involved in the spindle positioning and cell division [78-80]. Loss of SEPT7 results in improper spindle organization in the oocyte and disruption of chromosome alignment affecting progression of meiosis [62]. Poor oocyte quality is attributed with increased body mass [10], and the modest decrease in SEPT7 observed in our study suggests that the metabolic stress from a HFHS diet, GDM exposure *in utero*, or both, may affect oocyte quality and/or maturation. SEPT7 was also identified in our enriched cellular component GO analysis in both the GDM exposed groups as septin complex, septin ring, and septin cytoskeleton. In agreement with this possibility, localization of SEPT7 within the follicle and the oocyte, further implicate SEPT7 as an essential player in murine oocyte meiotic maturation, and that SEPT7 is vulnerable to alteration due to metabolic alterations.

CNPY2 is pivotal in the induction of the PERK-CHOP unfolded protein response (UPR) response pathway, which is a highly conserved quality control mechanism for cells that are under endoplasmic reticulum (ER) stress [81]. The luminal chaperone GRP78 dissociates from PERK and CNPY2 during ER stress and unfolded protein accumulation, facilitating the initiation of the UPR response [81]. Furthermore, *Cnpy2* is differentially expressed in human placental tissue from GDM pregnancies, though these results revealed a positive fold change [82] in contrast with our findings of decreased CNPY2 protein abundance. We also determined the localization of CNPY2, with positive immunoreactivity in the theca cells, granulosa cells, and in the peri-cytoplasm of the oocyte.

Also associated with the cellular stress response is SRSF2, which is increased during genotoxic stress [83] and is increased across all treatment groups in our study and was also assigned to several of the GO categories that were highly enriched. SRSF2 is an alternative splicing factor involved in the regulation of apoptotic caspases, with the mechanism for pro-apoptotic or anti-apoptotic caspases determined by the numerous splice variants [84]. Immunohistochemical analysis of SRSF2 revealed expression in the peri-cytoplasm of the oocyte, though analysis of cleaved CASP3 revealed no differences in the levels of apoptotic cells between any of the groups, so increased SRSF2 observed in this study may not be substantial enough to generate a pro-apoptotic response via CASP3. Conversely, SRSF2 may be functioning in an anti-apoptotic response to the metabolic conditions arising from increasing adiposity and/or insulin resistance.

In conclusion, these study findings indicate the impact of GDM and HFHS diets on follicle number and the ovarian proteome and illustrates that GDM sensitizes the offspring ovary to a dietary HFHS stress later in life, consequentially impacting the number of healthy follicles. Further, the altered abundance of ovarian proteins in offspring exposed to maternal GDM emphasizes the potential long-term effects of metabolic alterations *in utero* on ovarian function in the absence of obesity. Many of the proteins identified are those for which we have little understanding of their ovarian function and lay the foundation for future studies to determine their ovarian importance. Taken together, these findings illustrate a possible impact on fertility and oocyte quality provided in a two-hit stress model relative to GDM exposure *in utero* and in response to a western diet later in life and support a developmental origin of ovarian disorder (DOOD).

References

1. Hirshfield AN: Development of follicles in the mammalian ovary. *International review of cytology* 1991, 124:43-101.
2. Coulam CB, Adamson SC, Annegers JF: Incidence of premature ovarian failure. *Obstetrics and gynecology* 1986, 67(4):604-606.
3. Sullivan SD, Sarrel PM, Nelson LM: Hormone replacement therapy in young women with primary ovarian insufficiency and early menopause. *Fertility and sterility* 2016, 106(7):1588-1599.
4. Colditz GA, Willett WC, Rotnitzky A, Manson JE: Weight gain as a risk factor for clinical diabetes mellitus in women. *Annals of internal medicine* 1995, 122(7):481-486.
5. Lavie CJ, Milani RV, Ventura HO: Obesity and cardiovascular disease: risk factor, paradox, and impact of weight loss. *Journal of the American College of Cardiology* 2009, 53(21):1925-1932.
6. Cozzo AJ, Fuller AM, Makowski L: Contribution of Adipose Tissue to Development of Cancer. *Comprehensive Physiology* 2017, 8(1):237-282.
7. Gesink Law DC, Maclehose RF, Longnecker MP: Obesity and time to pregnancy. *Human reproduction (Oxford, England)* 2007, 22(2):414-420.
8. Shrestha A, Olsen J, Ramlau-Hansen CH, Bech BH, Nohr EA: Obesity and age at menarche. *Fertility and sterility* 2011, 95(8):2732-2734.
9. Dravecka I, Lazurova I, Kraus V: Obesity is the major factor determining an insulin sensitivity and androgen production in women with anovulary cycles. *Bratislavske lekarske listy* 2003, 104(12):393-399.
10. Metwally M, Cutting R, Tipton A, Skull J, Ledger WL, Li TC: Effect of increased body mass index on oocyte and embryo quality in IVF patients. *Reproductive biomedicine online* 2007, 15(5):532-538.
11. Brewer CJ, Balen AH: The adverse effects of obesity on conception and implantation. *Reproduction (Cambridge, England)* 2010, 140(3):347-364.
12. Chu SY, Callaghan WM, Kim SY, Schmid CH, Lau J, England LJ, Dietz PM: Maternal obesity and risk of gestational diabetes mellitus. *Diabetes care* 2007, 30(8):2070-2076.
13. Sheffield JS, Butler-Koster EL, Casey BM, McIntire DD, Leveno KJ: Maternal diabetes mellitus and infant malformations. *Obstetrics and gynecology* 2002, 100(5 Pt 1):925-930.
14. Nteeba J, Ross JW, Perfield JW, 2nd, Keating AF: High fat diet induced obesity alters ovarian phosphatidylinositol-3 kinase signaling gene expression. *Reproductive toxicology (Elmsford, NY)* 2013, 42:68-77.
15. Nteeba J, Ganesan S, Keating AF: Progressive obesity alters ovarian folliculogenesis with impacts on pro-inflammatory and steroidogenic signaling in female mice. *Biology of reproduction* 2014, 91(4):86.
16. Nteeba J, Ganesan S, Madden JA, Dickson MJ, Keating AF: Progressive obesity alters ovarian insulin, phosphatidylinositol-3 kinase, and chemical metabolism signaling pathways and potentiates ovotoxicity induced by phosphoramide mustard in mice. *Biology of reproduction* 2017, 96(2):478-490.

17. Ganesan S, Nteeba J, Keating AF: Enhanced susceptibility of ovaries from obese mice to 7,12-dimethylbenz[a]anthracene-induced DNA damage. *Toxicology and applied pharmacology* 2014, 281(2):203-210.
18. Ganesan S, Nteeba J, Madden JA, Keating AF: Obesity alters phosphoramide mustard-induced ovarian DNA repair in mice. *Biology of reproduction* 2017, 96(2):491-501.
19. Nteeba J, Ganesan S, Keating AF: Impact of obesity on ovotoxicity induced by 7,12-dimethylbenz[a]anthracene in mice. *Biology of reproduction* 2014, 90(3):68.
20. Huang HY, Chen HL, Feng LP: Maternal obesity and the risk of neural tube defects in offspring: A meta-analysis. *Obesity research & clinical practice* 2017, 11(2):188-197.
21. Hanafi MY, Saleh MM, Saad MI, Abdelkhalek TM, Kamel MA: Transgenerational effects of obesity and malnourishment on diabetes risk in F2 generation. *Molecular and cellular biochemistry* 2016, 412(1-2):269-280.
22. Grissom NM, Lyde R, Christ L, Sasson IE, Carlin J, Vitins AP, Simmons RA, Reyes TM: Obesity at conception programs the opioid system in the offspring brain. *Neuropsychopharmacology : official publication of the American College of Neuropsychopharmacology* 2014, 39(4):801-810.
23. Radulescu L, Ferechide D, Popa F: The importance of fetal gender in intrauterine growth restriction. *Journal of medicine and life* 2013, 6(1):38-39.
24. Desai M, Jellyman JK, Han G, Beall M, Lane RH, Ross MG: Maternal obesity and high-fat diet program offspring metabolic syndrome. *American journal of obstetrics and gynecology* 2014, 211(3):237.e231-237.e213.
25. Aiken CE, Tarry-Adkins JL, Ozanne SE: Transgenerational effects of maternal diet on metabolic and reproductive ageing. *Mammalian genome : official journal of the International Mammalian Genome Society* 2016, 27(7-8):430-439.
26. Aiken CE, Tarry-Adkins JL, Penfold NC, Dearden L, Ozanne SE: Decreased ovarian reserve, dysregulation of mitochondrial biogenesis, and increased lipid peroxidation in female mouse offspring exposed to an obesogenic maternal diet. *FASEB journal : official publication of the Federation of American Societies for Experimental Biology* 2016, 30(4):1548-1556.
27. Chan KA, Tsoulis MW, Sloboda DM: Early-life nutritional effects on the female reproductive system. *The Journal of endocrinology* 2015, 224(2):R45-62.
28. Connor KL, Vickers MH, Beltrand J, Meaney MJ, Sloboda DM: Nature, nurture or nutrition? Impact of maternal nutrition on maternal care, offspring development and reproductive function. *The Journal of physiology* 2012, 590(9):2167-2180.
29. Noctor E, Dunne FP: Type 2 diabetes after gestational diabetes: The influence of changing diagnostic criteria. *World journal of diabetes* 2015, 6(2):234-244.
30. Reece EA, Leguizamon G, Wiznitzer A: Gestational diabetes: the need for a common ground. *Lancet (London, England)* 2009, 373(9677):1789-1797.
31. Kuhl C: Insulin secretion and insulin resistance in pregnancy and GDM. Implications for diagnosis and management. *Diabetes* 1991, 40 Suppl 2:18-24.
32. Yogev Y, Xenakis EM, Langer O: The association between preeclampsia and the severity of gestational diabetes: the impact of glycemic control. *American journal of obstetrics and gynecology* 2004, 191(5):1655-1660.

33. Bellamy L, Casas JP, Hingorani AD, Williams D: Type 2 diabetes mellitus after gestational diabetes: a systematic review and meta-analysis. *Lancet (London, England)* 2009, 373(9677):1773-1779.
34. Kim C: Maternal outcomes and follow-up after gestational diabetes mellitus. *Diabetic medicine : a journal of the British Diabetic Association* 2014, 31(3):292-301.
35. Wang C, Zhu W, Wei Y, Feng H, Su R, Yang H: Exercise intervention during pregnancy can be used to manage weight gain and improve pregnancy outcomes in women with gestational diabetes mellitus. *BMC pregnancy and childbirth* 2015, 15:255.
36. Gasim T: Gestational diabetes mellitus: maternal and perinatal outcomes in 220 saudi women. *Oman medical journal* 2012, 27(2):140-144.
37. Nehring I, Chmitorz A, Reulen H, von Kries R, Ensenauer R: Gestational diabetes predicts the risk of childhood overweight and abdominal circumference independent of maternal obesity. *Diabetic medicine : a journal of the British Diabetic Association* 2013, 30(12):1449-1456.
38. Vohr BR, Boney CM: Gestational diabetes: the forerunner for the development of maternal and childhood obesity and metabolic syndrome? *The journal of maternal-fetal & neonatal medicine : the official journal of the European Association of Perinatal Medicine, the Federation of Asia and Oceania Perinatal Societies, the International Society of Perinatal Obstet* 2008, 21(3):149-157.
39. Nteeba J, Ortinau LC, Perfield JW, 2nd, Keating AF: Diet-induced obesity alters immune cell infiltration and expression of inflammatory cytokine genes in mouse ovarian and peri-ovarian adipose depot tissues. *Molecular reproduction and development* 2013, 80(11):948-958.
40. Ganesan S, Nteeba J, Keating AF: Impact of obesity on 7,12-dimethylbenz[a]anthracene-induced altered ovarian connexin gap junction proteins in female mice. *Toxicology and applied pharmacology* 2015, 282(1):1-8.
41. Pennington KA, van der Walt N, Pollock KE, Talton OO, Schulz LC: Effects of acute exposure to a high-fat, high-sucrose diet on gestational glucose tolerance and subsequent maternal health in mice. *Biology of reproduction* 2017, 96(2):435-445.
42. Talton OO, Bates K, Salazar SR, Ji T, Schulz LC: Lean maternal hyperglycemia alters offspring lipid metabolism and susceptibility to Diet-Induced obesity in mice. *Biology of reproduction* 2019.
43. Pedersen T, Peters H: Proposal for a classification of oocytes and follicles in the mouse ovary. *Journal of reproduction and fertility* 1968, 17(3):555-557.
44. Xia J, Sinelnikov IV, Han B, Wishart DS: MetaboAnalyst 3.0--making metabolomics more meaningful. *Nucleic acids research* 2015, 43(W1):W251-257.
45. Xia J, Wishart DS: Using MetaboAnalyst 3.0 for Comprehensive Metabolomics Data Analysis. *Current protocols in bioinformatics* 2016, 55:14.10.11-14.10.91.
46. Broughton DE, Moley KH: Obesity and female infertility: potential mediators of obesity's impact. *Fertility and sterility* 2017, 107(4):840-847.
47. Barbour LA: Unresolved controversies in gestational diabetes: implications on maternal and infant health. *Current opinion in endocrinology, diabetes, and obesity* 2014, 21(4):264-270.

48. Blickstein I, Doyev R, Trojner Bregar A, Brzan Simenc G, Verdenik I, Tul N: The effect of gestational diabetes, pre-gravid maternal obesity, and their combination ('diabesity') on outcomes of singleton gestations. *The journal of maternal-fetal & neonatal medicine : the official journal of the European Association of Perinatal Medicine, the Federation of Asia and Oceania Perinatal Societies, the International Society of Perinatal Obstet* 2018, 31(5):640-643.
49. Foglia VG, Cattaneo de Peralta R, Ibarra R, Rivera Cortes L: [Fetal and placental characteristics of pregnancy in pancreatectomized rats]. *Revista de la Sociedad Argentina de Biologia* 1967, 43(5):187-198.
50. Junod A, Lambert AE, Stauffacher W, Renold AE: Diabetogenic action of streptozotocin: relationship of dose to metabolic response. *The Journal of clinical investigation* 1969, 48(11):2129-2139.
51. Tsai MY, Schallinger LE, Josephson MW, Brown DM: Disturbance of pulmonary prostaglandin metabolism in fetuses of alloxan-diabetic rabbits. *Biochimica et biophysica acta* 1982, 712(2):395-399.
52. Kiss AC, Lima PH, Sinzato YK, Takaku M, Takeno MA, Rudge MV, Damasceno DC: Animal models for clinical and gestational diabetes: maternal and fetal outcomes. *Diabetology & metabolic syndrome* 2009, 1(1):21.
53. Masiello P, Broca C, Gross R, Roye M, Manteghetti M, Hillaire-Buys D, Novelli M, Ribes G: Experimental NIDDM: development of a new model in adult rats administered streptozotocin and nicotinamide. *Diabetes* 1998, 47(2):224-229.
54. John CM, Ramasamy R, Al Naqeeb G, Al-Nuaimi AH, Adam A: Nicotinamide supplementation protects gestational diabetic rats by reducing oxidative stress and enhancing immune responses. *Current medicinal chemistry* 2012, 19(30):5181-5186.
55. Abdul Aziz SH, John CM, Mohamed Yusof NI, Nordin M, Ramasamy R, Adam A, Mohd Fauzi F: Animal Model of Gestational Diabetes Mellitus with Pathophysiological Resemblance to the Human Condition Induced by Multiple Factors (Nutritional, Pharmacological, and Stress) in Rats. *BioMed research international* 2016, 2016:9704607.
56. Kaufmann RC, Amankwah KS, Dunaway G, Maroun L, Arbuthnot J, Roddick JW, Jr.: An animal model of gestational diabetes. *American journal of obstetrics and gynecology* 1981, 141(5):479-482.
57. Harrod JS, Rada CC, Pierce SL, England SK, Lamping KG: Altered contribution of RhoA/Rho kinase signaling in contractile activity of myometrium in leptin receptor-deficient mice. *American journal of physiology Endocrinology and metabolism* 2011, 301(2):E362-369.
58. Pollock KE, Stevens D, Pennington KA, Thaisrivongs R, Kaiser J, Ellersieck MR, Miller DK, Schulz LC: Hyperleptinemia During Pregnancy Decreases Adult Weight of Offspring and Is Associated With Increased Offspring Locomotor Activity in Mice. *Endocrinology* 2015, 156(10):3777-3790.
59. Plows JF, Yu X, Broadhurst R, Vickers MH, Tong C, Zhang H, Qi H, Stanley JL, Baker PN: Absence of a gestational diabetes phenotype in the LepRdb/+ mouse is independent of control strain, diet, misty allele, or parity. *Scientific reports* 2017, 7:45130.

60. Holemans K, Caluwaerts S, Poston L, Van Assche FA: Diet-induced obesity in the rat: a model for gestational diabetes mellitus. *American journal of obstetrics and gynecology* 2004, 190(3):858-865.
61. Liang C, DeCourcy K, Prater MR: High-saturated-fat diet induces gestational diabetes and placental vasculopathy in C57BL/6 mice. *Metabolism: clinical and experimental* 2010, 59(7):943-950.
62. Li S, Ou XH, Wei L, Wang ZB, Zhang QH, Ouyang YC, Hou Y, Schatten H, Sun QY: Septin 7 is required for orderly meiosis in mouse oocytes. *Cell cycle (Georgetown, Tex)* 2012, 11(17):3211-3218.
63. Ford SP, Zhang L, Zhu M, Miller MM, Smith DT, Hess BW, Moss GE, Nathanielsz PW, Nijland MJ: Maternal obesity accelerates fetal pancreatic beta-cell but not alpha-cell development in sheep: prenatal consequences. *American journal of physiology Regulatory, integrative and comparative physiology* 2009, 297(3):R835-843.
64. Moore MC, Menon R, Coate KC, Gannon M, Smith MS, Farmer B, Williams PE: Diet-induced impaired glucose tolerance and gestational diabetes in the dog. *Journal of applied physiology (Bethesda, Md : 1985)* 2011, 110(2):458-467.
65. Mao J, Pennington KA, Talton OO, Schulz LC, Sutovsky M, Lin Y, Sutovsky P: In Utero and Postnatal Exposure to High Fat, High Sucrose Diet Suppressed Testis Apoptosis and Reduced Sperm Count. *Scientific reports* 2018, 8(1):7622.
66. Wang N, Luo LL, Xu JJ, Xu MY, Zhang XM, Zhou XL, Liu WJ, Fu YC: Obesity accelerates ovarian follicle development and follicle loss in rats. *Metabolism: clinical and experimental* 2014, 63(1):94-103.
67. Akamine EH, Marcal AC, Camporez JP, Hoshida MS, Caperuto LC, Bevilacqua E, Carvalho CR: Obesity induced by high-fat diet promotes insulin resistance in the ovary. *The Journal of endocrinology* 2010, 206(1):65-74.
68. Wu S, Divall S, Wondisford F, Wolfe A: Reproductive tissues maintain insulin sensitivity in diet-induced obesity. *Diabetes* 2012, 61(1):114-123.
69. John GB, Gallardo TD, Shirley LJ, Castrillon DH: Foxo3 is a PI3K-dependent molecular switch controlling the initiation of oocyte growth. *Developmental biology* 2008, 321(1):197-204.
70. Reddy P, Liu L, Adhikari D, Jagarlamudi K, Rajareddy S, Shen Y, Du C, Tang W, Hamalainen T, Peng SL *et al*: Oocyte-specific deletion of Pten causes premature activation of the primordial follicle pool. *Science (New York, NY)* 2008, 319(5863):611-613.
71. Zaki M, Basha W, El-Bassyouni HT, El-Toukhy S, Hussein T: Evaluation of DNA damage profile in obese women and its association to risk of metabolic syndrome, polycystic ovary syndrome and recurrent preeclampsia. *Genes & diseases* 2018, 5(4):367-373.
72. Fernandez-Capetillo O, Lee A, Nussenzweig M, Nussenzweig A: H2AX: the histone guardian of the genome. *DNA repair* 2004, 3(8-9):959-967.
73. Walzem RL, Chen SE: Obesity-induced dysfunctions in female reproduction: lessons from birds and mammals. *Advances in nutrition (Bethesda, Md)* 2014, 5(2):199-206.

74. Fu XF, Cheng SF, Wang LQ, Yin S, De Felici M, Shen W: DAZ Family Proteins, Key Players for Germ Cell Development. *International journal of biological sciences* 2015, 11(10):1226-1235.
75. Hsu LC, Chen HY, Lin YW, Chu WC, Lin MJ, Yan YT, Yen PH: DAZAP1, an hnRNP protein, is required for normal growth and spermatogenesis in mice. *RNA (New York, NY)* 2008, 14(9):1814-1822.
76. Dai T, Vera Y, Salido EC, Yen PH: Characterization of the mouse Dazap1 gene encoding an RNA-binding protein that interacts with infertility factors DAZ and DAZL. *BMC genomics* 2001, 2:6.
77. Tsui S, Dai T, Roettger S, Schempp W, Salido EC, Yen PH: Identification of two novel proteins that interact with germ-cell-specific RNA-binding proteins DAZ and DAZL1. *Genomics* 2000, 65(3):266-273.
78. Spiliotis ET, Kinoshita M, Nelson WJ: A mitotic septin scaffold required for Mammalian chromosome congression and segregation. *Science (New York, NY)* 2005, 307(5716):1781-1785.
79. Kadota J, Yamamoto T, Yoshiuchi S, Bi E, Tanaka K: Septin ring assembly requires concerted action of polarisome components, a PAK kinase Cla4p, and the actin cytoskeleton in Saccharomyces cerevisiae. *Molecular biology of the cell* 2004, 15(12):5329-5345.
80. Enserink JM, Smolka MB, Zhou H, Kolodner RD: Checkpoint proteins control morphogenetic events during DNA replication stress in Saccharomyces cerevisiae. *The Journal of cell biology* 2006, 175(5):729-741.
81. Hong F, Liu B, Wu BX, Morreall J, Roth B, Davies C, Sun S, Diehl JA, Li Z: CNPY2 is a key initiator of the PERK-CHOP pathway of the unfolded protein response. *Nature structural & molecular biology* 2017, 24(10):834-839.
82. Enquobahrie DA, Williams MA, Qiu C, Meller M, Sorensen TK: Global placental gene expression in gestational diabetes mellitus. *American journal of obstetrics and gynecology* 2009, 200(2):206.e201-213.
83. Merdzhanova G, Edmond V, De Seranno S, Van den Broeck A, Corcos L, Brambilla C, Brambilla E, Gazzeri S, Eymin B: E2F1 controls alternative splicing pattern of genes involved in apoptosis through upregulation of the splicing factor SC35. *Cell death and differentiation* 2008, 15(12):1815-1823.
84. Kedzierska H, Piekielko-Witkowska A: Splicing factors of SR and hnRNP families as regulators of apoptosis in cancer. *Cancer letters* 2017, 396:53-65.

Figure and Figure Legends

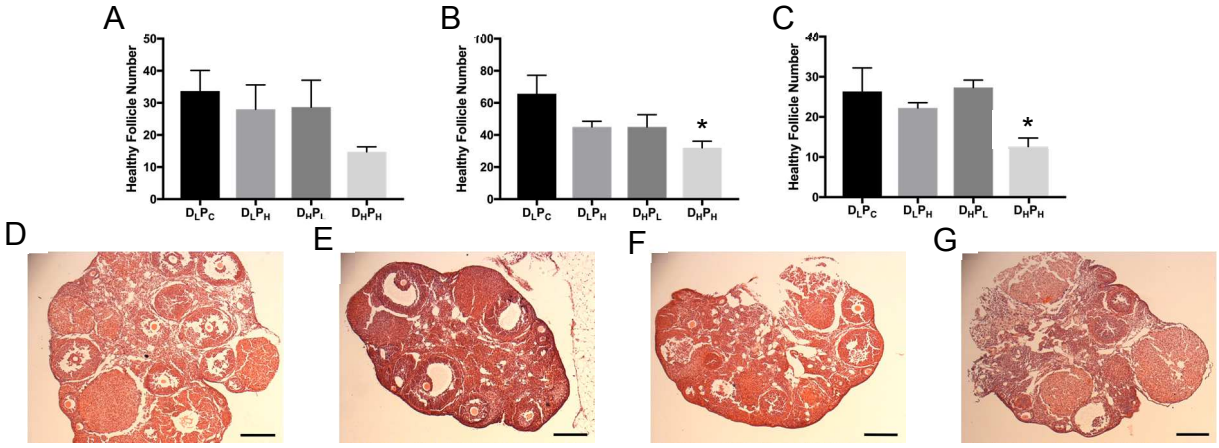

Figure 1: **Effect of GDM and/or HFHS diet on ovarian follicle number**. Follicles were classified as (A) primordial; (B) primary; (C) secondary and counted. Bars represent mean counted follicle number ± SEM. Significant difference from D_LP_L control is indicated by the * symbol at = $P < 0.05$. Representative hematoxylin and eosin stained ovarian sections from (D) D_LP_L; (E) D_LP_H; (F) D_HP_L; and (G) D_HP_H are presented; scale bar = 200 µm.

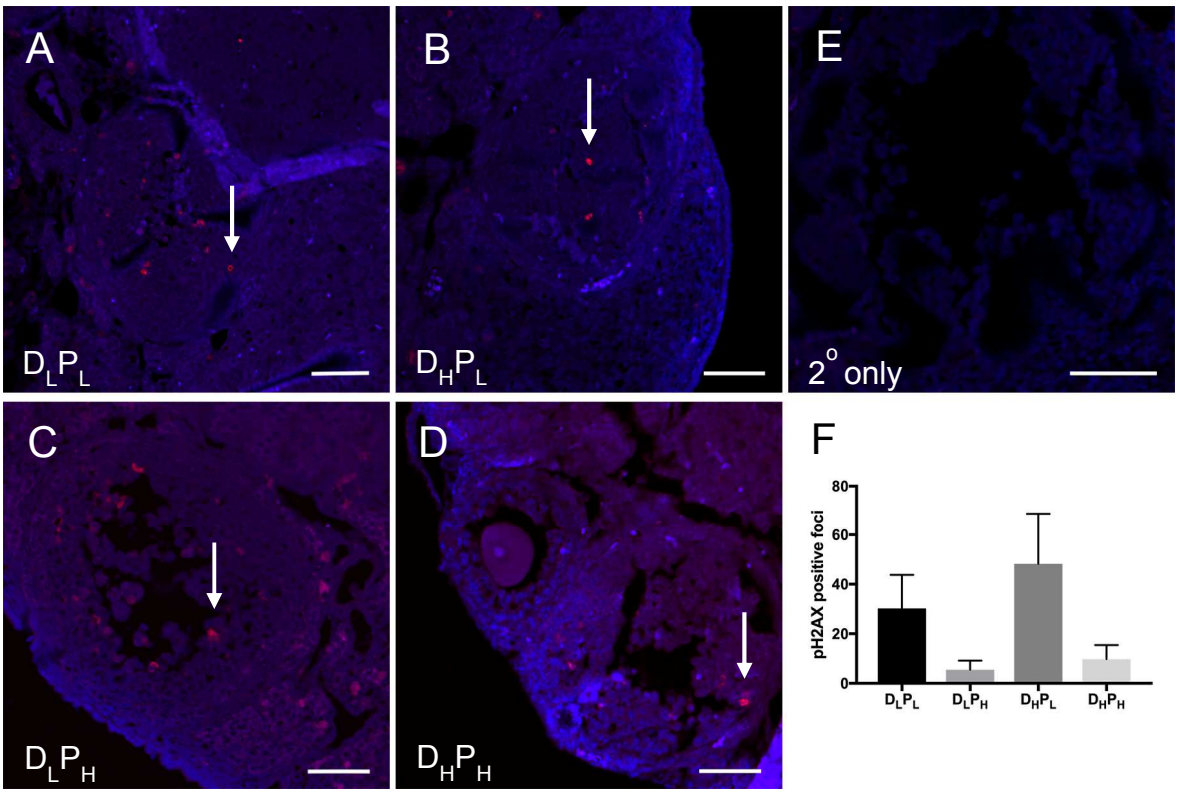

Figure 2: **Effect of GDM and/or dietary stress on ovarian γH2AX.** A primary antibody directed against γH2AX was used to determine ovarian localization in (A) D_LP_L; (B) D_HP_L; (C) D_LP_H; (D) D_HP_H mice. (E) Secondary antibody only control. Red punctate staining indicates γH2AX while cellular DNA is stained in blue; scale bar = 50 μm. Arrows indicate γH2AX positive staining in the granulosa cells of secondary follicles. (F) The bars represent mean number of positive γH2AX foci ± SEM.

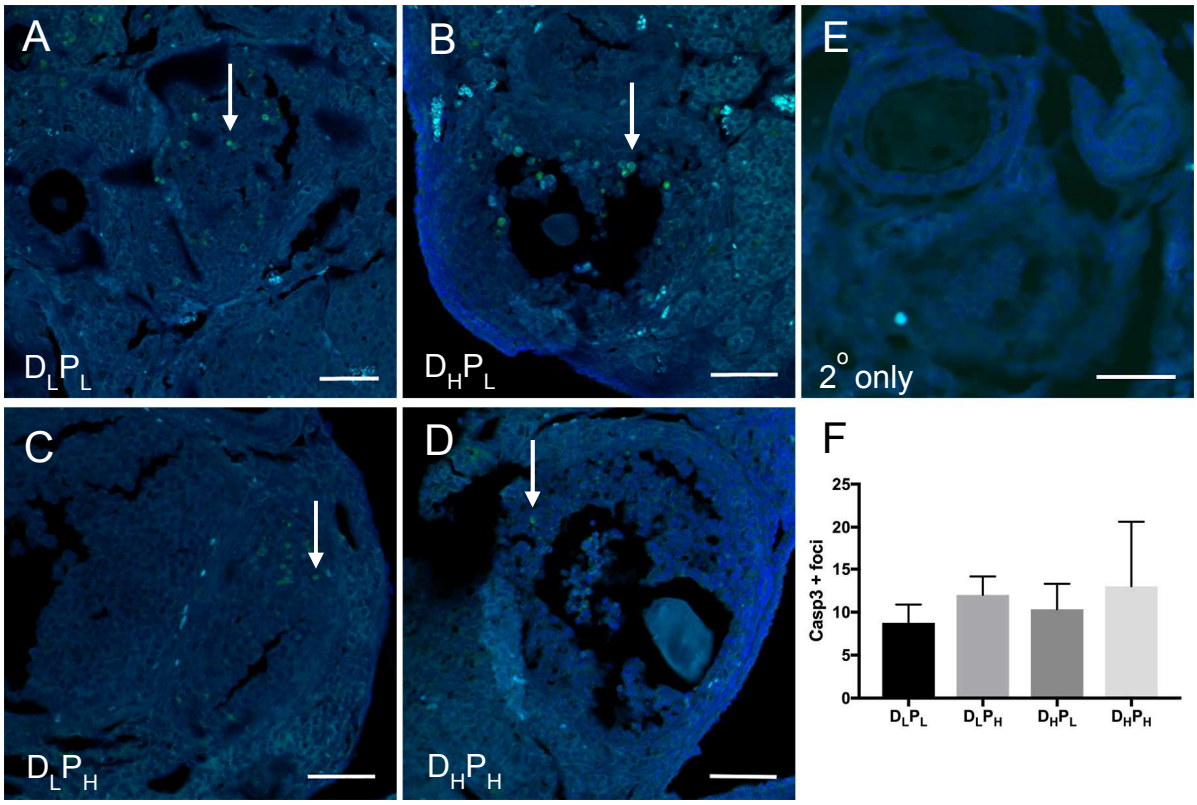

Figure 3: **Effect of GDM and/or dietary stress on ovarian cleaved CASP3.** A primary antibody directed against cleaved CASP3 was used to determine ovarian localization in (A) D_LP_L; (B) D_HP_L; (C) D_LP_H; (D) D_HP_H mice. (E) Secondary antibody only control. Green staining indicates cleaved CASP3 while cellular DNA is stained in blue; scale bar = 50μm. Arrows indicate cleaved CASP3 positive staining in the granulosa cells of secondary follicles. (F) The bars represent mean number of positive CASP3 foci ± SEM.

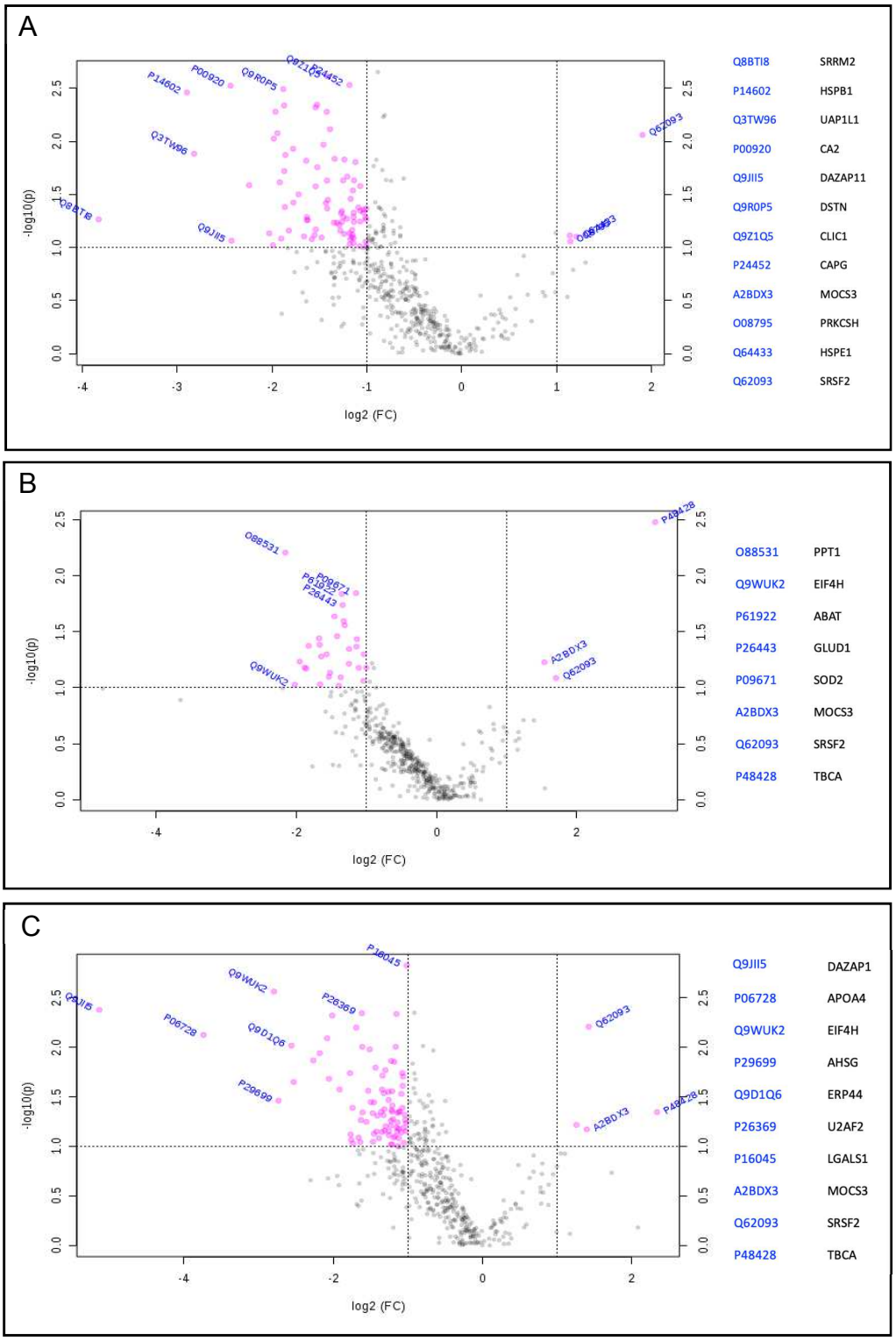

Figure 4: Volcano plots indicating the proteins detected by LC-MS/MS analysis and differing from the D_LP_L group. (A) D_LP_H; (B) D_HP_L; and (C) D_HP_H. The dotted horizontal

line shows where $P = 0.1$, with points above the line having $P < 0.1$ and points below having $P > 0.1$. The dotted vertical lines indicate a log2fold change of $< \pm 1.0$. Pink dots indicate proteins identified that are increased or decreased relative to D_LP_L ovaries, gray dots indicate proteins that did not meet selected thresholds.

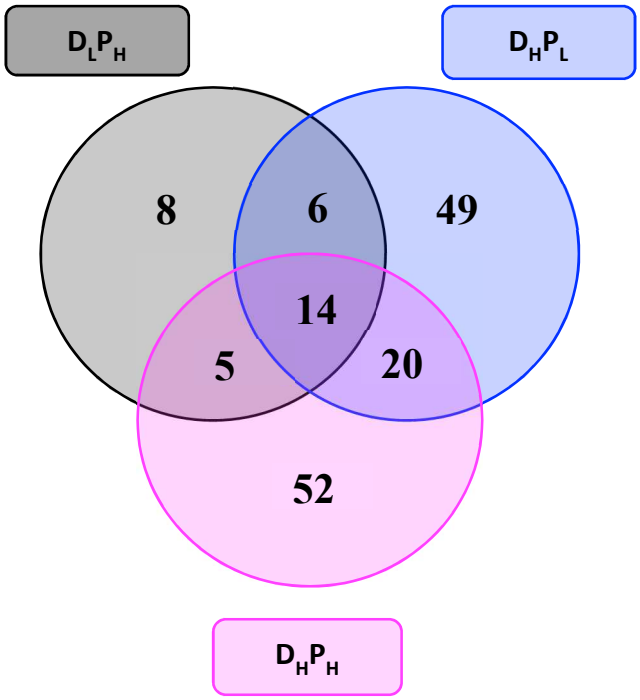

Figure 5: Proteins that are in common or unique between treatments. The Venn diagram presents the number of ovarian proteins identified as being unique to treatment or altered in common by treatment, relative to the D_LP_L group. The number in grey circle indicates the number of proteins identified in the D_LP_H group as being different from the D_LP_L group; the blue circle indicates the number of proteins identified in the D_HP_L group as being different from the D_LP_L group; and the pink circle indicates the number of proteins in the D_HP_H group that differ from the D_LP_L group. Overlapping areas of the circles illustrate the number of proteins that were altered relative to the D_LP_L group by two or more groups.

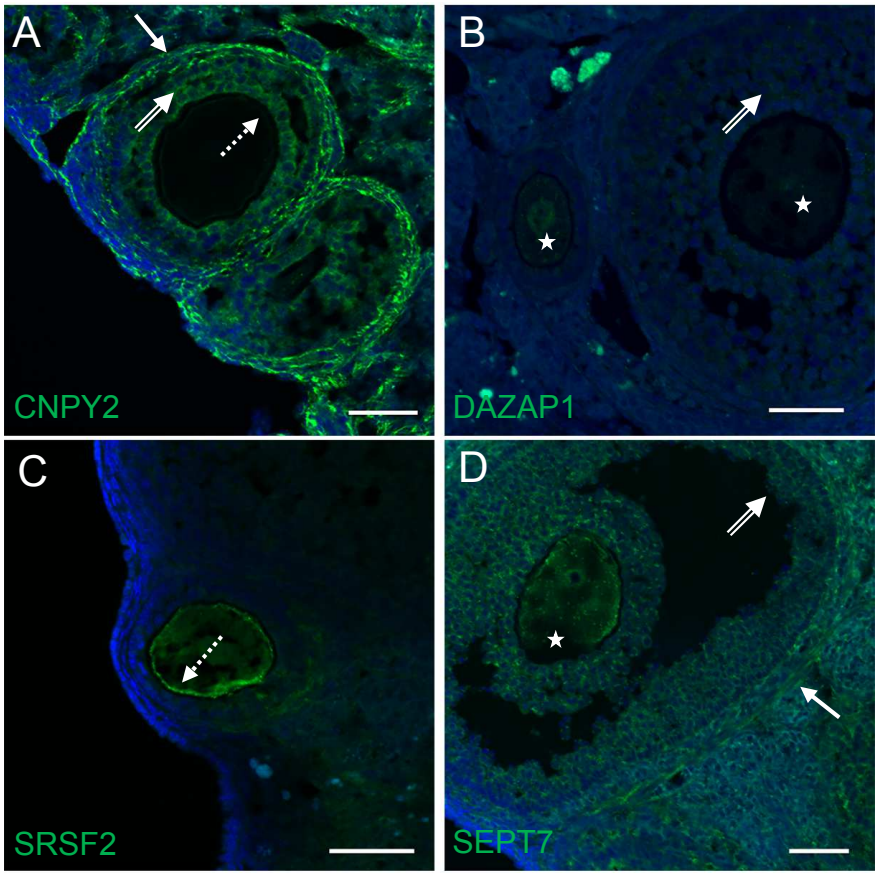

Figure 6: **Localization of ovarian proteins by immunofluorescence staining.** (A) CNPY2 (20x -1x zoom); (B) DAZAP1(20x -1x zoom); (C) SRSF2 (20x -1x zoom); and (D) SEPT7 (20x - 0.5x zoom) protein were localized in the adult mouse ovary. Green staining indicates the protein of interest while cellular DNA is stained in blue. Solid arrow indicates theca cells; double tailed arrow indicates granulosa cells; dotted tail arrow indicates the peri-cytoplasm region of the oocyte; star indicates oocyte; scale bar = 50 µm.

Supplemental Figures and Legends

Supplementary Table 1: Primary and secondary antibodies used.

Primary Antibody	**Host**	**Dilution**	**Supplier**	**Code**
DAZAP1	Rabbit	1:100 (F)	Thermo Fisher	PA5-52083
CNPY2	Rabbit	1:100 (F)	Thermo Fisher	PA5-46131
SEPT7	Rabbit	1:100 (F)	Abcam	Ab211482
SRSF2 (SC35)	Rabbit	1:100 (F)	Thermo Fisher	PA5-78164
γH2AX	Rabbit	1:50 (P)	Cell Signaling	2577
Cleaved caspase 3	Rabbit	1:100 (P)	Cell Signaling	9661
Secondary Antibody	**Host**	**Dilution**	**Supplier**	**Code**
Rabbit IgG 488	Goat	1:500	Thermo Fisher	A11008
Rabbit IgG 568	Goat	1:500	Thermo Fisher	A11011

Supplementary Table 2: Ovarian proteins identified by LC-MS/MS to differ in D_HP_L offspring relative to the D_LP_L mice (log2foldchange ≥ 1 and *P*-value ≤ 0.1).

UniProtID	Protein names	log2(FC)	p value
Q8BTI8	Serine/arginine repetitive matrix protein 2	-3.828	0.054
P14602	Heat shock protein beta-1	-2.897	0.003
Q3TW96	UDP-N-acetylhexosamine pyrophosphorylase-like protein 1	-2.822	0.013
P00920	Carbonic anhydrase 2	-2.437	0.002
Q9JII5	DAZ-associated protein 1	-2.428	0.086
Q9JMG7	Hepatoma-derived growth factor-related protein 3	-2.241	0.025
Q9D1M0	Protein SEC13 homolog	-2.029	0.073
P62889	60S ribosomal protein L30	-1.991	0.095
Q62188	Dihydropyrimidinase-related protein 3	-1.981	0.009
P48758	Carbonyl reductase [NADPH] 1	-1.963	0.005
Q9D0F9	Phosphoglucomutase-1	-1.944	0.008
P60335	Poly(rC)-binding protein 1	-1.918	0.024
P62983	Ubiquitin-40S ribosomal protein S27a	-1.904	0.082
Q9R0P5	Destrin	-1.882	0.003
P26369	Splicing factor U2AF 65 kDa subunit	-1.872	0.004
P16546	Spectrin alpha chain, non-erythrocytic 1	-1.871	0.019
Q64727	Vinculin	-1.865	0.041
Q7TPR4	Alpha-actinin-1	-1.859	0.013
Q8K183	Pyridoxal kinase	-1.823	0.069
Q61598	Rab GDP dissociation inhibitor beta	-1.778	0.011
Q8BTM8	Filamin-A	-1.775	0.037
Q9QXT0	Protein canopy homolog 2	-1.721	0.031
P63254	Cysteine-rich protein 1	-1.663	0.078
P47754	F-actin-capping protein subunit alpha-2	-1.639	0.015
P61922	4-aminobutyrate aminotransferase, mitochondrial	-1.633	0.051
P31230	Aminoacyl tRNA synthase complex-interacting multifunctional protein 1	-1.631	0.055
P21614	Vitamin D-binding protein	-1.625	0.055
Q99L13	3-hydroxyisobutyrate dehydrogenase, mitochondrial	-1.579	0.083
P04104	Keratin, type II cytoskeletal 1	-1.552	0.076
Q99JF8	PC4 and SFRS1-interacting protein	-1.541	0.026
P26443	Glutamate dehydrogenase 1, mitochondrial	-1.541	0.004
Q8BH97	Reticulocalbin-3	-1.539	0.067
Q8C1B7	Septin-11	-1.525	0.004
O35887	Calumenin	-1.522	0.017
Q91V64	Isochorismatase domain-containing protein 1	-1.478	0.080

Supplementary Table 2: (continued)

Q06890	Clusterin	-1.457	0.010
O55131	Septin-7	-1.432	0.038
O08756	3-hydroxyacyl-CoA dehydrogenase type-2	-1.423	0.005
Q9CPY7	Cytosol aminopeptidase	-1.421	0.023
Q9Z2X1	Heterogeneous nuclear ribonucleoprotein F	-1.418	0.042
Q9Z1Q5	Chloride intracellular channel protein 1	-1.417	0.002
Q99MN9	Propionyl-CoA carboxylase beta chain, mitochondrial	-1.410	0.035
O54724	Caveolae-associated protein 1	-1.389	0.007
Q60973	Histone-binding protein RBBP7	-1.348	0.058
P48678	Prelamin-A/C	-1.340	0.014
Q9QZQ8	Core histone macro-H2A.1	-1.315	0.058
P13020	Gelsolin	-1.293	0.061
P99027	60S acidic ribosomal protein P2	-1.281	0.069
P01027	Complement C3	-1.272	0.047
P27659	60S ribosomal protein L3	-1.263	0.057
P01867	Ig gamma-2B chain C region	-1.263	0.0453
Q9D2G2	Dihydrolipoyllysine-residue succinyltransferase component of 2-oxoglutarate dehydrogenase complex, mitochondrial	-1.251	0.023
Q9D0J8	Parathymosin	-1.249	0.051
P99024	Tubulin beta-5 chain	-1.240	0.074
O88531	Palmitoyl-protein thioesterase 1	-1.238	0.014
Q8BG05	Heterogeneous nuclear ribonucleoprotein A3	-1.211	0.053
P70699	Lysosomal alpha-glucosidase	-1.206	0.021
P24452	Macrophage-capping protein	-1.184	0.002
P42208	Septin-2	-1.183	0.073
P40124	Adenylyl cyclase-associated protein 1	-1.180	0.093
Q8BIJ6	Isoleucine--tRNA ligase, mitochondrial	-1.173	0.083
P26350	Prothymosin alpha	-1.170	0.034
Q62261	Spectrin beta chain, non-erythrocytic 1	-1.160	0.080
P63325	40S ribosomal protein S10	-1.155	0.068
Q6IRU2	Tropomyosin alpha-4 chain	-1.153	0.075
P26645	Myristoylated alanine-rich C-kinase substrate	-1.147	0.029
P08207	Protein S100-A10	-1.141	0.051
P83917	Chromobox protein homolog 1	-1.141	0.081
P62960	Nuclease-sensitive element-binding protein 1	-1.139	0.090
Q9WVA3	Mitotic checkpoint protein BUB3	-1.139	0.047
Q03265	ATP synthase subunit alpha, mitochondrial	-1.136	0.057
P55264	Adenosine kinase	-1.136	0.023
Q61545	RNA-binding protein EWS	-1.121	0.015
Q6NVF9	Cleavage and polyadenylation specificity factor subunit 6	-1.090	0.041

Supplementary Table 2: (continued)

P26039	Talin-1	-1.076	0.097
P09813	Apolipoprotein A-II	-1.071	0.056
P63168	Dynein light chain 1, cytoplasmic	-1.070	0.026
Q9WV32	Actin-related protein 2/3 complex subunit 1B	-1.069	0.044
P56399	Ubiquitin carboxyl-terminal hydrolase 5	-1.037	0.046
P24270	Catalase	-1.034	0.043
Q9WVA4	Transgelin-2	-1.015	0.052
Q05920	Pyruvate carboxylase, mitochondrial	-1.013	0.088
Q9QYC0	Alpha-adducin	-1.009	0.054
Q8BFW7	Lipoma-preferred partner homolog	-1.006	0.042
P18760	Cofilin-1	-1.004	0.096
A2BDX3	Adenylyltransferase and sulfurtransferase MOCS3	1.138	0.076
O08795	Glucosidase 2 subunit beta	1.145	0.087
Q64433	10 kDa heat shock protein, mitochondrial	1.209	0.078
Q62093	Serine/arginine-rich splicing factor 2	1.905	0.008

Supplementary Table 3: Ovarian proteins identified by LC-MS/MS to differ in D_LP_H offspring relative to the D_LP_L mice (log2foldchange ≥ 1 and *P*-value ≤ 0.1).

UniProtID	Protein names	log2(FC)	p value
O88531	Palmitoyl-protein thioesterase 1	-2.159	0.006
Q9WUK2	Eukaryotic translation initiation factor 4H	-2.023	0.094
Q9CY58	Plasminogen activator inhibitor 1 RNA-binding protein	-1.954	0.058
P62830	60S ribosomal protein L23	-1.884	0.066
Q9WV54	Acid ceramidase	-1.860	0.067
P01027	Complement C3	-1.826	0.042
P40124	Adenylyl cyclase-associated protein 1	-1.677	0.036
Q99L13	3-hydroxyisobutyrate dehydrogenase, mitochondrial	-1.668	0.041
P17225	Polypyrimidine tract-binding protein 1	-1.664	0.093
Q9QXT0	Protein canopy homolog 2	-1.647	0.053
Q9CPU0	Lactoylglutathione lyase	-1.570	0.050
Q61545	RNA-binding protein EWS	-1.537	0.080
P62889	60S ribosomal protein L30	-1.520	0.073
P21614	Vitamin D-binding protein	-1.457	0.023
P26039	Talin-1	-1.420	0.034
P02088	Hemoglobin subunit beta-1	-1.393	0.096
Q8C1B7	Septin-11	-1.369	0.081
P61922	4-aminobutyrate aminotransferase, mitochondrial	-1.353	0.014
P26443	Glutamate dehydrogenase 1, mitochondrial	-1.340	0.018
O08756	3-hydroxyacyl-CoA dehydrogenase type-2	-1.325	0.025
P0C0S6	Histone H2A.Z	-1.310	0.027
Q9CQ60	6-phosphogluconolactonase	-1.250	0.061
P04104	Keratin, type II cytoskeletal 1	-1.248	0.045
P09671	Superoxide dismutase [Mn], mitochondrial	-1.149	0.014
Q62188	Dihydropyrimidinase-related protein 3	-1.142	0.043
P83917	Chromobox protein homolog 1	-1.137	0.036
P06745	Glucose-6-phosphate isomerase	-1.110	0.066
P26369	Splicing factor U2AF 65 kDa subunit	-1.044	0.086
O55131	Septin-7	-1.037	0.050
Q9CPY7	Cytosol aminopeptidase	-1.003	0.066
A2BDX3	Adenylyltransferase and sulfurtransferase MOCS3	1.539	0.059
Q62093	Serine/arginine-rich splicing factor 2	1.704	0.082
P48428	Tubulin-specific chaperone A	3.120	0.003

Supplementary Table 4: Ovarian proteins identified by LC-MS/MS to differ in D_HP_H offspring relative to the D_LP_L mice (log2foldchange ≥ 1 and *P*-value ≤ 0.1; D_HP_H).

UniProtID	Protein names	log2(FC)	p value
Q9JII5	DAZ-associated protein 1	-5.132	0.004
P06728	Apolipoprotein A-IV	-3.736	0.007
Q9WUK2	Eukaryotic translation initiation factor 4H	-2.794	0.002
P29699	Alpha-2-HS-glycoprotein	-2.734	0.034
Q9D1Q6	Endoplasmic reticulum resident protein 44	-2.558	0.009
Q9CQE8	RNA transcription, translation and transport factor protein	-2.529	0.022
P01027	Complement C3	-2.267	0.013
Q9QXT0	Protein canopy homolog 2	-2.181	0.011
Q62348	Translin	-2.081	0.008
P27659	60S ribosomal protein L3	-2.056	0.020
Q8BMS1	Trifunctional enzyme subunit alpha, mitochondrial	-2.014	0.004
P70670	Nascent polypeptide-associated complex subunit alpha, muscle-specific form	-1.915	0.026
P51859	Hepatoma-derived growth factor	-1.776	0.018
P21981	Protein-glutamine gamma-glutamyltransferase 2	-1.767	0.075
P10126	Elongation factor 1-alpha 1	-1.759	0.085
P17225	Polypyrimidine tract-binding protein 1	-1.742	0.040
Q8CI94	Glycogen phosphorylase, brain form	-1.737	0.093
P40124	Adenylyl cyclase-associated protein 1	-1.691	0.006
O08638	Myosin-11	-1.661	0.081
Q8VDD5	Myosin-9	-1.639	0.090
P61982	14-3-3 protein gamma	-1.628	0.054
P26369	Splicing factor U2AF 65 kDa subunit	-1.616	0.004
Q9D0K2	Succinyl-CoA:3-ketoacid coenzyme A transferase 1, mitochondrial	-1.611	0.009
P01942	Hemoglobin subunit alpha	-1.606	0.045
O35855	Branched-chain-amino-acid aminotransferase, mitochondrial	-1.557	0.056
Q64727	Vinculin	-1.533	0.027
Q8C1B7	Septin-11	-1.512	0.010
P01867	Ig gamma-2B chain C region	-1.497	0.035
P60335	Poly(rC)-binding protein 1	-1.471	0.046
P62301	40S ribosomal protein S13	-1.467	0.089
Q9WUU7	Cathepsin Z	-1.454	0.035
Q9CZ13	Cytochrome b-c1 complex subunit 1, mitochondrial	-1.454	0.074
Q9R1P3	Proteasome subunit beta type-2	-1.434	0.016
Q9D0F9	Phosphoglucomutase-1	-1.421	0.070
Q99PU5	Long-chain-fatty-acid--CoA ligase ACSBG1	-1.408	0.049

Supplementary Table 4: (continued)

Q91V92	ATP-citrate synthase	-1.388	0.082
O35887	Calumenin	-1.358	0.044
P02088	Hemoglobin subunit beta-1	-1.346	0.071
P28474	Alcohol dehydrogenase class-3	-1.346	0.026
P31786	Acyl-CoA-binding protein	-1.340	0.019
Q8K4Z3	NAD(P)H-hydrate epimerase	-1.325	0.048
P62880	Guanine nucleotide-binding protein G(I)/G(S)/G(T) subunit beta-2	-1.321	0.029
P20239	Zona pellucida sperm-binding protein 2	-1.316	0.042
Q9R1T2	SUMO-activating enzyme subunit 1	-1.311	0.069
O08756	3-hydroxyacyl-CoA dehydrogenase type-2	-1.301	0.017
P06801	NADP-dependent malic enzyme	-1.299	0.062
P05202	Aspartate aminotransferase, mitochondrial	-1.261	0.028
O09131	Glutathione S-transferase omega-1	-1.258	0.034
P00920	Carbonic anhydrase 2	-1.255	0.077
Q9CQV8	14-3-3 protein beta/alpha	-1.253	0.070
O08997	Copper transport protein ATOX1	-1.226	0.061
Q9DB15	39S ribosomal protein L12, mitochondrial	-1.225	0.055
Q8BH95	Enoyl-CoA hydratase, mitochondrial	-1.223	0.095
P61922	4-aminobutyrate aminotransferase, mitochondrial	-1.223	0.013
Q9CPU0	Lactoylglutathione lyase	-1.218	0.043
P45591	Cofilin-2	-1.214	0.096
Q9WVA3	Mitotic checkpoint protein BUB3	-1.211	0.027
Q60973	Histone-binding protein RBBP7	-1.210	0.044
P26039	Talin-1	-1.208	0.038
P99027	60S acidic ribosomal protein P2	-1.201	0.053
P62889	60S ribosomal protein L30	-1.189	0.081
P99029	Peroxiredoxin-5, mitochondrial	-1.183	0.014
Q9R1P0	Proteasome subunit alpha type-4	-1.171	0.078
P0DP28	Calmodulin-3	-1.162	0.009
P48678	Prelamin-A/C	-1.154	0.004
Q04447	Creatine kinase B-type	-1.148	0.064
P19157	Glutathione S-transferase P 1	-1.142	0.070
Q9CQF3	Cleavage and polyadenylation specificity factor subunit 5	-1.141	0.057
P26443	Glutamate dehydrogenase 1, mitochondrial	-1.138	0.046
P47754	F-actin-capping protein subunit alpha-2	-1.134	0.099
P50247	Adenosylhomocysteinase	-1.124	0.066
P48758	Carbonyl reductase	-1.121	0.044
P58774	Tropomyosin beta chain	-1.121	0.082
Q8BFW7	Lipoma-preferred partner homolog	-1.109	0.044
Q9D7B6	Isobutyryl-CoA dehydrogenase, mitochondrial	-1.091	0.072

Supplementary Table 4: (continued)

P16546	Spectrin alpha chain, non-erythrocytic 1	-1.087	0.029
Q7TPR4	Alpha-actinin-1	-1.075	0.041
O55131	Septin-7	-1.074	0.018
Q3THE2	Myosin regulatory light chain 12B	-1.069	0.024
Q61545	RNA-binding protein EWS	-1.064	0.019
P57780	Alpha-actinin-4	-1.058	0.064
P35979	60S ribosomal protein L12	-1.053	0.092
Q99MN9	Propionyl-CoA carboxylase beta chain, mitochondrial	-1.043	0.048
P24270	Catalase	-1.035	0.054
P63325	40S ribosomal protein S10	-1.025	0.071
Q9CWJ9	Bifunctional purine biosynthesis protein PURH	-1.023	0.057
P16045	Galectin-1	-1.015	0.001
P97315	Cysteine and glycine-rich protein 1	1.256	0.060
A2BDX3	Adenylyltransferase and sulfurtransferase MOCS3	1.395	0.067
Q62093	Serine/arginine-rich splicing factor 2	1.421	0.006
P48428	Tubulin-specific chaperone A	2.336	0.045

Supplementary Table 5: Ovarian proteins identified by LC-MS/MS to differ between D_LP_H and D_HP_H (log2foldchange ≥ 1 and *P*-value ≤ 0.1).

UniProtID	Protein names	log2(FC)	p value
Q99JI4	26S proteasome non-ATPase regulatory subunit 6	-2.115	0.099
Q8VED5	Keratin, type II cytoskeletal 79	-1.613	0.066
P09671	Superoxide dismutase [Mn], mitochondrial	-1.428	0.009
Q00612	Glucose-6-phosphate 1-dehydrogenase X	1.089	0.015
Q8BH97	Reticulocalbin-3	1.506	0.087
Q9R1P3	Proteasome subunit beta type-2	1.599	0.052
Q8VI64	Protein MGARP	1.852	0.088
Q62348	Translin	1.918	0.019

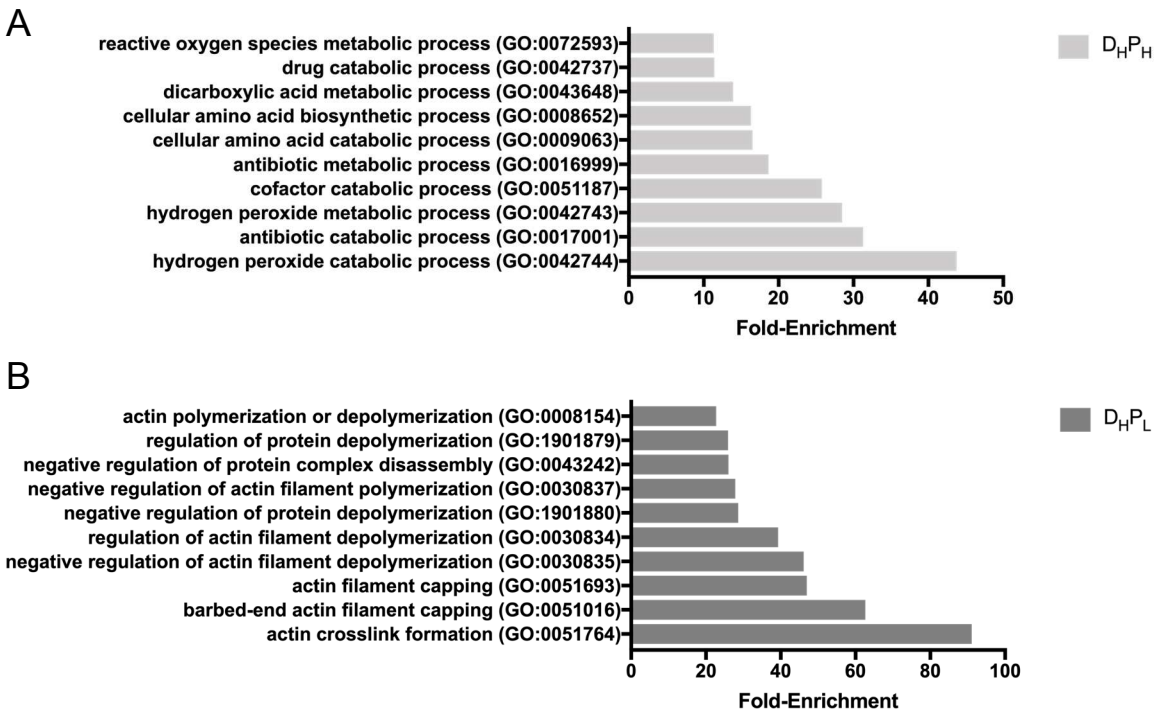

Supplementary Figure 1: Gene Ontology (GO) analysis of proteins identified as over-represented in each treatment group when compared to the D_LP_L group ($P < 0.05$). Functional classification based on Biological Process in (A) D_HP_H and (B) D_HP_L.

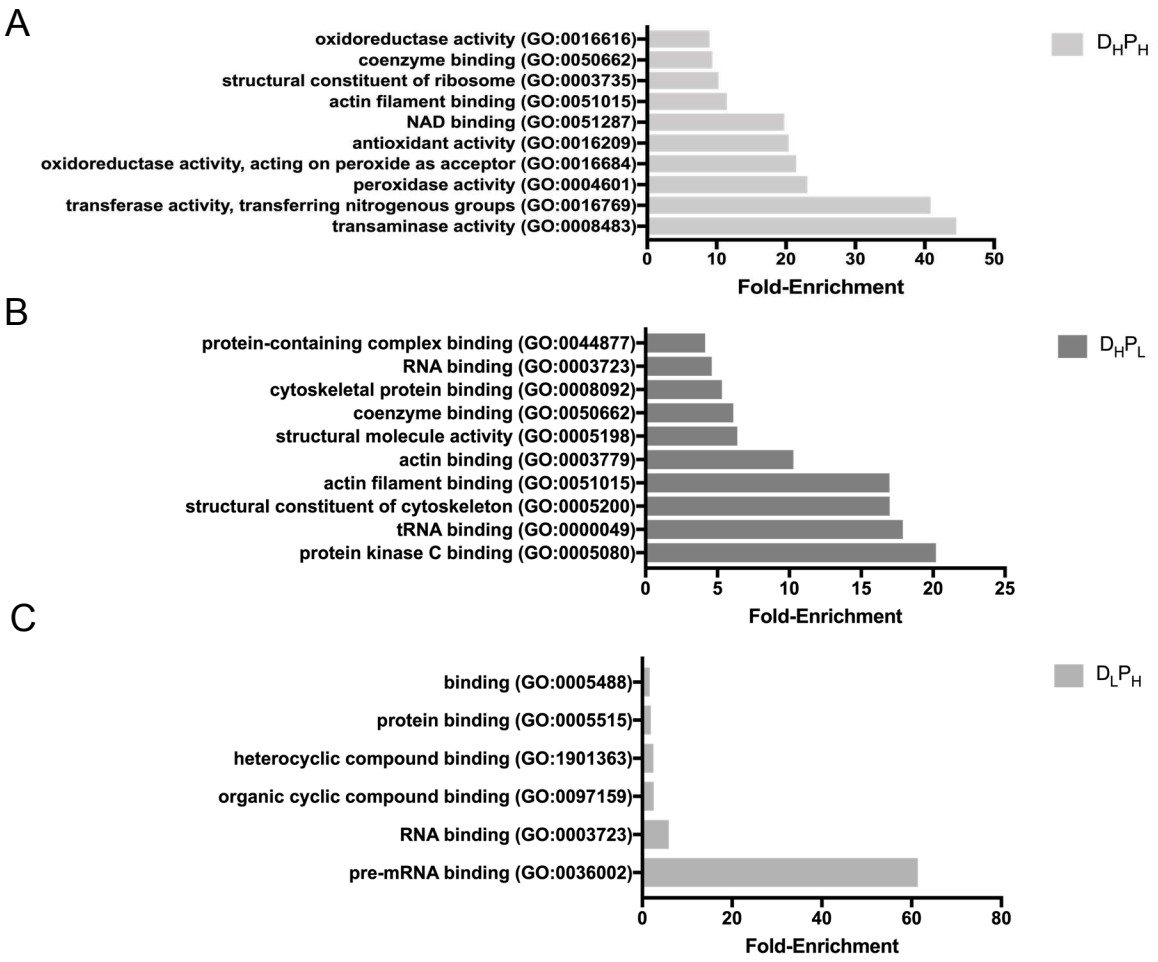

Supplementary Figure 2: Gene Ontology (GO) analysis of proteins identified as over-represented in each treatment group when compared to the D_LP_L group ($P < 0.05$). Functional classification based on Molecular Function in (A) D_HP_H; (B) D_HP_L; and (C) D_LP_H.

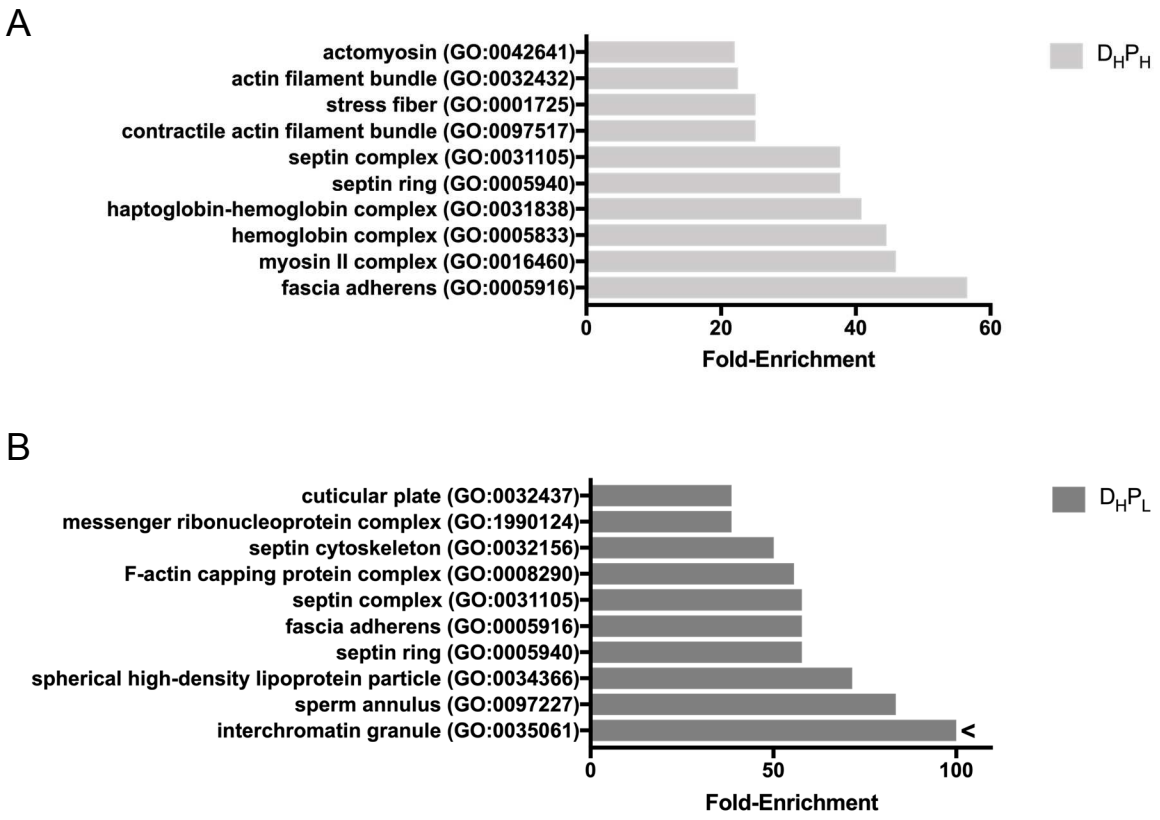

Supplementary Figure 3: Gene Ontology (GO) analysis of proteins identified as over-represented in each treatment group when compared to the D_LP_L group ($P < 0.05$). Functional classification based on Cellular Component in (A) D_HP_H and (B) D_HP_L.

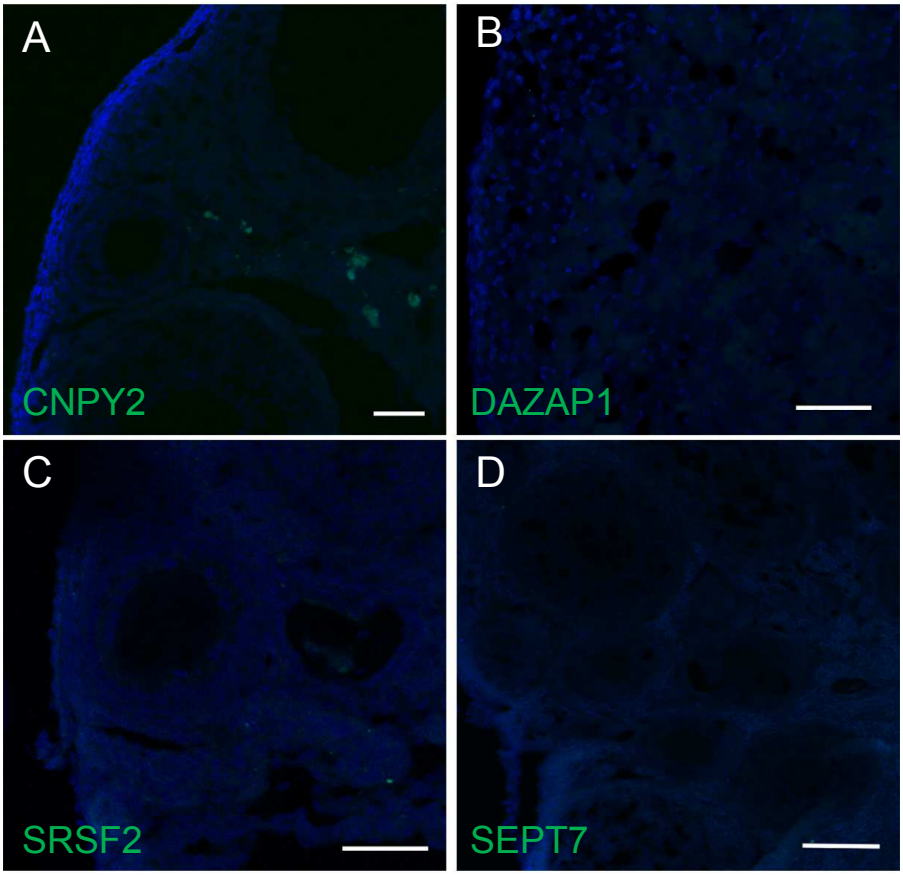

Supplementary Figure 4: Technical control for immunofluorescence staining. Ovaries from an adult mouse were immunologically stained using only the secondary antibody appropriate for (A) CNPY2; (B) DAZAP1; (C) SRSF2; and (D) SEPT7; scale bar = 50 μm.

CHAPTER 3. OBESITY INDUCES BASAL OVARIAN DNA DAMAGE AND REDUCES ATM PHOSPHORYLATION

Kendra L. Clark, Crystal Roach, and Aileen F. Keating*

Department of Animal Science – Iowa State University, Ames, Iowa 50011

A manuscript under consideration at
Biology of Reproduction, 2019

Contribution Statement:
K.L. Clark performed all analyses on ovarian tissue, designed experiments, and interpreted the data and wrote the manuscript. C. Roach aided with performing the experiments. A.F. Keating designed the experiments, aided in data interpretation and edited the manuscript.

Abstract

The prevalence of obesity continues to rise. In the overweight or obese female, reproductive complications include poor oocyte quality, decreased fecundity, gestational diabetes, and higher risk of reproductive cancers. Using lean and hyperphagia-induced obese female mice aged 10 weeks, we determined that the ovary from obese female mice had increased ($P < 0.05$) numbers of γH2AX-positive cells as well as elevated ($P < 0.05$) oocyte levels of ataxia telangiectasia mutated (ATM) protein. Interestingly, total ovarian phosphorylation of ATM at serine 1981 was not altered ($P > 0.05$) by obesity but was increased with follicular maturation. Interestingly, there was greater $ATM^{Ser1981}$ abundance in small relative to large follicles in the obese ovary. Breast cancer type 1 susceptibility protein (BRCA1) was also not altered ($P > 0.05$) in the ovary from the obese female, nor was there any increase ($P > 0.05$) in the phosphorylation of BRCA1 at serine 1423 or serine

1524 during obesity. Apoptosis levels were not elevated ($P > 0.05$) in ovary during obesity as measure by cleaved caspase 3 (CASP3), though some increases were observed dependent of follicle size in both the lean and obese mouse. Deleted in azoospermia-associated protein 1 (DAZAP1) and protein canopy homolog 2 (CNPY2), proteins implicated in ovarian physiology, were unaltered ($P > 0.05$) in the ovary from the obese model relative to the lean. Taken together, these data demonstrate increased markers of DNA damage in the ovary of obese mice, with follicular stage-dependent shifts in both $ATM^{Ser1981}$ and CASP3 protein abundance due to obesity.

Keywords: DNA repair, ovary, obesity

Introduction

Obesity is a preventable metabolic syndrome, associated with several interrelated disorders such as insulin resistance/diabetes [1], cardiovascular disease [2], dyslipidemia [3], chronic inflammation [4], and cancer [5]. The prevalence of obesity in the population continues to rise, with an estimated 40% of adults and 19% of youth being obese/overweight in the United States, though these rates are higher for some ethic groups [6]. A decline in reproductive potential is associated with obesity, and reproductive complications include poor oocyte quality [7], polycystic ovary syndrome (PCOS) [8], decreased fecundity [9], impaired pregnancy success using assisted reproductive technologies [10], gestational diabetes (GDM) [11], and increased risk of offspring health problems [12].

The ovary is the source of the female germ cell, the oocyte, and hormones necessary for female growth and development. Throughout the female lifespan, a finite pool of primordial germ cells will remain in diplotene stage of meiosis until sexual maturity, at which time they are primed for ovulation and subsequent fertilization or they undergo the natural process of degeneration called atresia [13]. Once this pool of primordial follicles is depleted, through the natural progression of time or through factors that expedite the process, ovarian senescence occurs [13]. The depletion of follicles occurring prior to age 40 is considered primary ovarian insufficiency (POI) and often has unknown etiology [14]. Cessation of or dysfunctional ovarian activity predisposes women toward at heightened risk for development of gynecological cancers [15], osteoporosis [16], cardiovascular disease [17], and Alzheimer's disease [18].

The accumulation of DNA damage is considered as a contributing factor to obesity-related disorders due to the chronic low-grade inflammation and constant production of reactive oxygen species (ROS) that may induce endogenous DNA damage throughout the body [19-21]. Obesity is also associated with ovarian DNA damage [22-24] and increased granulosa cell apoptosis [25]. The cellular DNA damage response (DDR) exists to prevent genomic damage by either repairing the damage or triggering the cell towards apoptosis if beyond repair. Central metabolism disturbances during obesity have adverse impacts on the DDR [26, 27]. We have previously demonstrated that progressive obesity alters ovarian folliculogenesis and inflammation [28], the insulin responsive phosphatidylinositol 3-kinase (PI3K) pathway [29], steroid hormone biosynthesis [30], causes basal DNA damage and affects the response to genotoxicant exposures [23, 24, 30, 31].

Ataxia telangiectasia mutated (ATM) protein is a key DDR initiator, sensing DNA damage and transducing downstream targets including breast cancer type 1 susceptibility protein (BRCA1) for DNA repair [32]; serine/threonine-protein kinase Chk2 (CHK2) for cell cycle arrest [33]; p53 for apoptosis [34], and RAC-alpha serine/threonine-protein kinase (AKT) for cell survival [35]. Interestingly, despite hyperphagia-induced obese mice having an increase in ATM protein in response to a genotoxic chemical, there was lack of an appropriate response in the proteins downstream of ATM [23, 24]. This finding provided the rationale for the hypothesis that the ATM-mediated DDR is altered during obesity. Utilizing a model of hyperphagia-induced obesity, this study examined basal obesity-induced impacts on the ovarian DDR.

Materials and Methods

Animal procedure and tissue collection

All experiments were performed according to regulatory guidelines and approved by the Institutional Animal Care and Use Committee (IACUC) at Iowa State University. Female wild-type normal non-agouti (a/a; n = 10; designated lean) and agouti lethal yellow (KK.Cg-Ay/J mice; n = 10; designated obese) were purchased from Jackson Laboratory (Bar Harbor, ME) and maintained in an animal facility at Iowa State University under controlled room temperature (21°C-22°C) and lighting (12hr light:12hr dark) with *ad libitum* access to food and water. At 10 weeks of age, mice were euthanized in the pro-estrus phase of the estrous cycle and ovaries were fixed in 4% paraformaldehyde overnight at 4°C for histological analysis.

Estrous cycle monitoring

The estrous cycle was monitored by performing daily vaginal cytological analysis in the morning. Fresh, wet vaginal smears were collected by pipetting saline into the vagina, smearing onto histology slides and examination with a Nikon OPTIPHOT microscope using a 10X objective. Classification of estrous cycle stages was determined as previously described [36]. Briefly, pro-estrus was characterized by small, round nucleated epithelial cells, some cornified epithelial cells, and little to no leukocytes. Estrus was characterized by several cornified epithelial cells containing pyknotic nuclei. The presence of cornified cells and leukocytes indicated metestrus. In diestrus, nucleated epithelial cells reappeared in the vaginal smears in addition to the presence of polymorphonuclear leukocytes. Obese mice who displayed persistent diestrus (n = 4) were subsequently excluded from further analysis.

Histology

After fixation, ovaries were passed through a 10%, 20%/0.1M PBS gradient for 1-3 h each at room temperature, followed by 30% sucrose/0.1M PBS overnight at 4°C and embedded in optimal cutting temperature (OCT; Fisher Healthcare) compound before being flash frozen on dry ice. Ovaries were serially sectioned at 7 μm with a maximum of 3 sections per slide.

Immunofluorescence staining

Slides were warmed briefly on a 37°C slide warmer and tissue sections were encircled with a histology pap pen (Vector Laboratories) to maintain staining solutions

concentrated on the tissue during processing. Tissue was rehydrated and permeabilized in 0.1M PBS with 0.1% Tween20 (PBSTw) for 20 min, followed by blocking (0.1M PBS/1% BSA/1% DMSO/5% goat serum) for 60 min at room temperature. Primary antibodies (**Supplemental Table 1**) were diluted in fresh blocking solution, applied to the tissue sections and incubated in a humidified box at 4°C overnight. For antigen retrieval, 1% sodium dodecyl sulfate (SDS; Sigma Aldrich) was applied for 5 min after the rehydration step, followed by three washes of PBSTw for 5 min each and addition of blocking solution as described above. After primary antibody incubation, slides were washed 3 times in PBSTw for 10 min per wash. The appropriate secondary antibody (**Supplemental Table 1**) was added to fresh blocking solution, applied to tissue sections and incubated at room temperature for 60 min, followed by 4 washes in PBSTw for 10 min per wash. Slides were air dried, followed by addition of Vectashield with DAPI (H1200, Vector Labs) and stored overnight at 4°C. Negative technical controls to confirm specificity were performed using secondary antibodies alone (**Supplemental Figure 2**). Images were captured on a Zeiss LSM700 confocal microscope equipped with an AxioCam MRc5 using a 5 or 20x objective.

Protein isolation and western blot analysis

Total ovarian protein was isolated by tissue homogenization in lysis buffer (50 mM Tris-HCL, 1 mM EDTA, pH 8.5) followed by centrifugation at 10,000 rpm at 4°C for 15 min. Supernatant was collected and protein content was quantified using a bicinchoninic acid assay (BCA; Pierce BCA Protein Assay Kit, Thermo Fisher). SDS-PAGE was used to separate proteins and then transferred to a nitrocellulose membrane. Membranes were

blocked in 5% milk in 0.2% PBSTw for 60 min at room temperature, followed by incubation with appropriate primary antibodies (**Supplemental Table 1**) in fresh blocking solution at 4°C overnight. Membranes were washed 3 times in PBSTw for 10 min each wash, followed by incubation in secondary antibody (**Supplemental Table 1**) for 60 min at room temperature. Following incubation in secondary antibody, membranes were washed for 3 times in PBSTw, incubated in enhanced chemiluminescence detection substrate (Cell Signaling Technologies) for 7 min and visualized on the Azure c600 (Azure Biosystems). Densitometry of the appropriately-sized bands was measured using ImageJ software [37]. Proteins of interest were normalized to ACTB by dividing protein of interest's densitometric value by the densitometric value obtained from total ACTB.

Quantification of protein abundance

For quantification of ATM (n = 6 ovaries per treatment; 6 sections per ovary), and pATM (n = 6 ovaries per treatment; 6 sections per ovary), the threshold percentage of the total image area was limited to the oocyte using ImageJ software [37]. For γH2AX (6 ovaries per treatment; 6 sections per ovary) and cleaved CASP3 (6 ovaries per treatment; 6 sections per ovary), immunopositive cells were manually counted in primary, secondary and antral follicles using the cell counter module of ImageJ software [37].

Statistical analysis

Statistical analyses were performed using GraphPad Prism 7.0 unpaired t-test function. A P-value ≤ 0.05 was considered statistically significant and a trend for a statistical difference was considered at $P < 0.1$. Values are expressed as mean ± SEM.

Results

Obesity increases basal amounts of DNA damage in the ovary

To determine if obesity increases the amount of basal DNA double strand breaks (DSB) in the ovary, tissue sections were analyzed for localization of γH2AX and positive foci were quantified (**Figure 1**). The number of ovarian cells (granulosa cells and/or oocytes) that contained positive γH2AX foci tended ($P < 0.1$) to be greater in the obese relative to the lean ovary (**Figure 1E**), as well as in both small ($P < 0.05$) and large ($P < 0.1$) follicles (**Figure 1F-G**) in the obese relative to lean ovary. In both the lean and obese ovaries, larger follicles had more ($P < 0.05$) γH2AX positive foci than in smaller follicles (**Figure 1H-I**).

Obesity increases ATM protein level

In order to establish the basal level of ovarian DDR proteins due to progressive obesity, we examined both basal and phosphorylated levels of ATM protein were examined. Basal levels of ATM immunofluorescence were localized in the oocyte of all follicular stages with no difference in localization patterns between lean or obese mice (**Figure 2A-D**). ATM oocyte immunoreactivity was elevated ($P < 0.05$) in the obese ovary (**Figure 2I**) and in the obese ovary relative to the lean in both small and large follicles ($P < 0.05$; **Supplementary Figure 1A-B**). There were no differences in basal ATM abundance between small or large follicles in either the lean or obese ovaries ($P > 0.05$; **Supplementary Figure 1C-D**).

Phosphorylation of ATM at serine 1981 was present in the oocyte and granulosa cells of all follicular stages (**Figure 2E-H**), though no difference ($P > 0.05$) was observed

between the lean or obese ovary (**Figure 2J**). There was an increase in fluorescence intensity in the smaller follicles of the obese ovary relative to the lean ($P < 0.05$), but no changes in larger follicles ($P > 0.05$) (**Supplementary Figure 1E-F**). In the lean ovary, there was greater ($P < 0.05$) $pATM^{Ser1981}$ in larger compared to smaller follicles but no difference ($P > 0.05$) between small and large follicles in the obese ovary (**Supplementary Figure 1G-H**).

Ovarian BRCA1 levels are not impacted by obesity

BRCA1 protein abundance was detected in oocytes of all follicle stages, as well as theca cells, stromal cells, and there was some modest staining in the granulosa cells of larger follicles (**Figure 3A-D)**. Staining intensity visibly increased in the theca cells as follicle size increased. There was no observable effect of obesity on total ovarian BRCA1 protein (**Figure 4A-B**).

Localization of $pBRCA1^{Ser1423}$ in the ovary was observed in the granulosa cells and oocyte nucleus (**Figure 3E-H**). Phosphorylation activity of $BRCA1^{Ser1423}$ was not altered ($P > 0.05$) in the obese relative to the lean ovary (**Figure 4C-D**). Similarly, phosphorylation of $BRCA1^{Ser1524}$ did not differ ($P > 0.05$) between the lean and obese ovary (**Figure 4E-F**), and immunoreactivity was localized to granulosa cells and the cytoplasm of the oocyte (**Figure 3I-L**). Obesity did not ($P > 0.05$) alter the phosphorylation of $pBRCA1^{Ser1423}$ or $BRCA1^{Ser1524}$ relative to total ovarian BRCA1 protein (**Figure 4G-H**).

Apoptosis is not elevated in the obese ovary though a shift between follicle sizes occurs

To assess levels of apoptosis in the obese ovary, tissue sections were analyzed for cleaved CASP3 via immunofluorescence (**Figure 5A-D**) and positive foci were quantified.

The number of total cleaved CASP3 positive granulosa cells were not different ($P > 0.05$) between the lean and obese mice (**Figure 5E**). However, there were more ($P < 0.05$) CASP3 positive foci in smaller follicles of the lean ovary versus the obese ovary (**Figure 5F**) and more ($P < 0.05$) positive foci in the larger follicles relative to the smaller follicles in the obese ovary alone (**Figure 5I**). There were no differences ($P > 0.05$) in numbers of positive CASP3 cells between the large follicles in lean and obese or between the follicle sizes in the lean ovaries alone (**Figure 5G-H**).

Ovarian expression of CNPY2 and DAZAP1 in obesity

We previously identified CNPY2 and DAZAP1 in a proteomic analysis of ovaries exposed to GDM *in utero*, with their abundance being decreased as a result of the metabolic effects of GDM and/or subsequent dietary challenge later in life [38]. CNPY2 was localized mainly to theca cells, with slight staining observed in some of the granulosa cells in larger follicles and the oocyte cytoplasm of some oocytes in all follicle stages except for primordial (**Figure 6A-D**). DAZAP1 had distinct staining throughout the ovary, with localization in the oocyte nucleus, granulosa, and luteal cells (**Figure 6E-H**). Obesity did not impact ($P > 0.05$) on level or localization pattern of CNPY2 or DAZAP1 relative to their lean counterparts (**Figure 6I-L**).

Discussion

The impacts of obesity on health have been well documented, though the percentage of the population, including both adults and children, affected by obesity and obesity-related disorders continues to rise. Reproductive outcomes for obese or overweight

women result in impaired fertility due to poor oocyte quality [10], disturbances in the menstrual cycle [39], PCOS [40], and heightened risk of developing ovarian cancer [41]. The impacts of obesity may also not be limited to the mother, as offspring exposed to maternal obesity *in utero* have increased risk for neural tube defects [42], glucose intolerance [43], intrauterine growth restriction (IUGR) [44], and increased circulating cholesterol and body fat [45]. Female offspring experiencing the metabolic effects of obesity *in utero* also exhibit a diminution of the ovarian follicular reserve [46, 47] and decreases in ovarian vascularity [48].

We have previously demonstrated that hyperphagia-induced obese mice have basal levels of DNA damage in the ovary and a blunted DDR after a genotoxicant exposure [23, 24, 30, 31]. Importantly, those observations were made in mice that were 14 weeks of age and older. This study elected to use mice that were slightly younger, in order to avoid the confounding effect of reduced primordial follicle number which we previously noted from 12 weeks of age onwards [28]. In support of our previous findings, there was increased abundance of γH2AX positive foci in the ovaries from the obese mouse in both small and large follicles. The presence of γH2AX is considered the gold standard for double strand break localization [49], and H2AX is activated upon phosphorylation by ATM at the DNA break site [50, 51]. A higher body mass index (BMI) contributes to the development of DNA lesions [20], but the origins of the elevated amounts of DNA DSBs remains to be elucidated. It is presumable that these lesions are occurring due to the increased inflammation and enhanced ROS production that are present during obesity [52-54]. Thus, our findings recapitulate our previous observations [23, 24] and support that basal DNA damage is present in the ovary of obese females.

ATM is first activated by the MRE11, RAD50, and NBS1 (MRN) complex and is further stabilized at the location of the DNA DSBs by autophosphorylation at serine 1981 [55]. Ablation of this autophosphorylation site results in cessation of ATM's ability to phosphorylate any downstream targets [55]. Further, mutations in the *Atm* gene elicit an inadequate response to DNA damage, increasing both radiosensitivity and cancer predisposition as a result of faulty DNA repair [56]. Other characteristics of *Atm* mutations include neurodegeneration [57], immunodeficiency [58] and infertility [59, 60], though the exact role of the DDR in these etiologies remains to be determined. We determined that there is more basal ATM in the ovary of an obese female, though no measurable differences in the amount of total phosphorylated ATM^{Ser1981} were observed, ATM^{Ser1981} abundance was elevated in smaller compared to larger follicles in the obese mice, , suggesting both dysfunction in ATM phosphorylation and a follicular-stage influence. This is consistent with our previous findings that ATM acts as a sensor for ovarian DNA damage [23, 24, 61, 62], and that there is a disconnect between elevated ATM and the subsequent activation of ATM downstream proteins [23, 24] in the ovary of an obese female.

Another critical protein required for efficient DNA repair is BRCA1. Phosphorylation of BRCA1 at Ser^{1423} and Ser^{1524} is ATM-dependent in the event of DNA damage [63]. Women with a mutated allele of the *Brca1* gene have increased risk of tumor development, specifically breast and ovarian cancers, as a result of defective DNA repair [64]. We have previously demonstrated that progressive obesity reduced ovarian BRCA1 protein in mice aged 18 and 24 weeks [23, 24]. In obese mice aged 10 weeks there were no observable differences in basal BRCA1 abundance or in the amount of phosphorylated BRCA1^{Ser1423} or BRCA1^{Ser1524} relative to lean ovaries. Interestingly, DNA repair gene and

protein activity in the ovary decreases with age [65, 66], emphasizing the importance of the DDR in ovarian aging and fertility. Thus, the obesity-induced decline in BRCA1 that we previously noted may be influenced by either attainment of a certain threshold of obesity or by ovarian age.

If the DNA damage within a cell cannot be repaired, the cell may be shunted towards apoptosis. Apoptosis is coordinated by the activation of caspases, which then proteolytically process various cellular targets through the amplification of apoptotic signals [67]. Caspase 3 (CASP3) is an apoptotic protease involved in ovarian granulosa [68] and luteal [69] cell death, though is not required for oocyte death [68]. Further, increased granulosa cell apoptosis has been reported with obesity [25]. We and others have shown a dramatic increase in ovarian CASP3 positive cells after a genotoxicant exposure [62, 70-72]. There was no increase in total ovarian CASP3 positive foci due to obesity, however, an interesting shift occurred in that the obese ovary had less CASP3 in small compared to large follicles, compared to the lean ovary in which the pattern was switched. Thus, similar to the observations with $ATM^{Ser1981}$, there may be follicle type-specific alterations due to obesity that could alter fertility in females. It is also possible that basal DNA damage isn't being repaired adequately, and that the damaged follicles are not being shunted towards demise, thus contributing to the poor quality of the oocyte frequently seen in obesity, but this remains to be elucidated.

We had previously identified CNPY2 as being altered in the ovary in females who had experienced GDM *in utero*. Specifically, there was a decrease in the abundance of CNPY2 in the ovaries of offspring exposed to GDM *in utero*, adult dietary stress, or both [38]. CNPY2 is implicated in cellular stress response, specifically the induction of the

PERK-CHOP unfolded protein response (UPR), a highly conserved quality control mechanism for cells undergoing endoplasmic reticulum (ER) stress [73]. While we did not observe any changes in the abundance of CNPY2 in the ovaries from the obese mouse in comparison to the lean control, the ovarian localization pattern was confirmed [38], with CNPY2 protein being localized to theca cells, granulosa cells of larger follicles, and the oocyte cytoplasm. The presence of CNPY2 has also been detected in the human placental tissue from GDM pregnancies [74], implicating a role for CNPY2 in the female reproductive system in relation to a metabolic syndrome, necessitating further analysis for the precise role in reproductive health.

Another ovarian protein reduced in female mice exposed to GDM *in utero* and further impacted by a HFHS diet during adulthood is DAZAP1 [38]. DAZAP1 is a member of the deleted in azoospermia (DAZ) family of proteins, which are present in both female and male germ cells [75]. DAZ proteins are critical in germ cell development and fertility, with mutations in DAZAP1 resulting in sterility, growth retardation, and sometimes perinatal death [76]. Another DAZ family protein, deleted in azoospermia-like 1 (DAZL1), results in infertility in both male and female mice when disrupted [77]. Defects associated with DAZAP1 have previously been described in males [78, 79]. Similar to CNPY2, no alterations in ovarian DAZAP1 abundance due to obesity were observed but the ovarian localization pattern recapitulated that previously reported [38]. Localization of DAZAP1 was observed throughout the ovary, with distinct immunostaining in the oocyte nucleus, granulosa cells, and luteal cells.

Taken together, this study confirmed that there is elevated basal DNA damage in the ovaries of obese mice. In addition, the data confirm greater ATM protein abundance in

large compared to small follicles (both lean and obese) and that there is dysfunction in ATM phosphorylation due to obesity. Further, we discovered a shift in CASP3 protein from the small to large follicle types in the obese females. The model used eliminates the confounding effects of different diets since the obese mice overeat the same diet as the lean mice. We did not note any effect on BRCA1 at this stage of obesity, potentially suggesting that there is either a threshold of obesity that must be attained before reduced BRCA1 is noted, or that ovarian aging coupled with obesity has an additive effect on BRCA1 abundance. Estimation of ovarian DNA damage and the resulting alterations in DDR during obesity could potentially aid in diagnosis and prevention of obesity-related reproductive disorders and consideration of DDR-initiating proteins as markers of ovarian health has merit.

References

1. Colditz GA, Willett WC, Rotnitzky A, Manson JE. Weight gain as a risk factor for clinical diabetes mellitus in women. Ann Intern Med 1995; 122:481-486.
2. Lavie CJ, Milani RV, Ventura HO. Obesity and cardiovascular disease: risk factor, paradox, and impact of weight loss. J Am Coll Cardiol 2009; 53:1925-1932.
3. Kang YJ, Wang HW, Cheon SY, Lee HJ, Hwang KM, Yoon HS. Associations of Obesity and Dyslipidemia with Intake of Sodium, Fat, and Sugar among Koreans: a Qualitative Systematic Review. Clin Nutr Res 2016; 5:290-304.
4. Xu H, Barnes GT, Yang Q, Tan G, Yang D, Chou CJ, Sole J, Nichols A, Ross JS, Tartaglia LA, Chen H. Chronic inflammation in fat plays a crucial role in the development of obesity-related insulin resistance. J Clin Invest 2003; 112:1821-1830.
5. Cozzo AJ, Fuller AM, Makowski L. Contribution of Adipose Tissue to Development of Cancer. Compr Physiol 2017; 8:237-282.
6. Hales CMC, M.D; Fryar, C.D.; C.L. Ogden. Prevalence of obesity among adults and youth: United States, 2015-2016. In, 288 ed. Hyattsville, MD: National Center for Health Statistics 2017.
7. Brewer CJ, Balen AH. The adverse effects of obesity on conception and implantation. Reproduction 2010; 140:347-364.
8. Pasquali R, Casimirri F. The impact of obesity on hyperandrogenism and polycystic ovary syndrome in premenopausal women. Clin Endocrinol (Oxf) 1993; 39:1-16.

9. Gesink Law DC, Maclehose RF, Longnecker MP. Obesity and time to pregnancy. Hum Reprod 2007; 22:414-420.
10. Metwally M, Cutting R, Tipton A, Skull J, Ledger WL, Li TC. Effect of increased body mass index on oocyte and embryo quality in IVF patients. Reprod Biomed Online 2007; 15:532-538.
11. Chu SY, Callaghan WM, Kim SY, Schmid CH, Lau J, England LJ, Dietz PM. Maternal obesity and risk of gestational diabetes mellitus. Diabetes Care 2007; 30:2070-2076.
12. Sheffield JS, Butler-Koster EL, Casey BM, McIntire DD, Leveno KJ. Maternal diabetes mellitus and infant malformations. Obstet Gynecol 2002; 100:925-930.
13. Hirshfield AN. Development of follicles in the mammalian ovary. Int Rev Cytol 1991; 124:43-101.
14. Coulam CB, Adamson SC, Annegers JF. Incidence of premature ovarian failure. Obstet Gynecol 1986; 67:604-606.
15. Nagle CM, Dixon SC, Jensen A, Kjaer SK, Modugno F, deFazio A, Fereday S, Hung J, Johnatty SE, Fasching PA, Beckmann MW, Lambrechts D, et al. Obesity and survival among women with ovarian cancer: results from the Ovarian Cancer Association Consortium. Br J Cancer 2015; 113:817-826.
16. Compston JE. Sex steroids and bone. Physiol Rev 2001; 81:419-447.
17. Mosca L, Manson JE, Sutherland SE, Langer RD, Manolio T, Barrett-Connor E. Cardiovascular disease in women: a statement for healthcare professionals from the American Heart Association. Writing Group. Circulation 1997; 96:2468-2482.
18. Scheyer O, Rahman A, Hristov H, Berkowitz C, Isaacson RS, Diaz Brinton R, Mosconi L. Female Sex and Alzheimer's Risk: The Menopause Connection. J Prev Alzheimers Dis 2018; 5:225-230.
19. Cerda C, Sanchez C, Climent B, Vazquez A, Iradi A, El Amrani F, Bediaga A, Saez GT. Oxidative stress and DNA damage in obesity-related tumorigenesis. Adv Exp Med Biol 2014; 824:5-17.
20. Wlodarczyk M, Jablonowska-Lietz B, Olejarz W, Nowicka G. Anthropometric and Dietary Factors as Predictors of DNA Damage in Obese Women. Nutrients 2018; 10.
21. Zaki M, Basha W, El-Bassyouni HT, El-Toukhy S, Hussein T. Evaluation of DNA damage profile in obese women and its association to risk of metabolic syndrome, polycystic ovary syndrome and recurrent preeclampsia. Genes Dis 2018; 5:367-373.
22. Ganesan S, Nteeba J, Keating AF. Impact of obesity on 7,12-dimethylbenz[a]anthracene-induced altered ovarian connexin gap junction proteins in female mice. Toxicol Appl Pharmacol 2015; 282:1-8.
23. Ganesan S, Nteeba J, Keating AF. Enhanced susceptibility of ovaries from obese mice to 7,12-dimethylbenz[a]anthracene-induced DNA damage. Toxicol Appl Pharmacol 2014; 281:203-210.
24. Ganesan S, Nteeba J, Madden JA, Keating AF. Obesity alters phosphoramide mustard-induced ovarian DNA repair in mice. Biol Reprod 2017; 96:491-501.
25. Walzem RL, Chen SE. Obesity-induced dysfunctions in female reproduction: lessons from birds and mammals. Adv Nutr 2014; 5:199-206.

26. Himbert C, Thompson H, Ulrich CM. Effects of Intentional Weight Loss on Markers of Oxidative Stress, DNA Repair and Telomere Length - a Systematic Review. Obes Facts 2017; 10:648-665.
27. Azzara A, Pirillo C, Giovannini C, Federico G, Scarpato R. Different repair kinetic of DSBs induced by mitomycin C in peripheral lymphocytes of obese and normal weight adolescents. Mutat Res 2016; 789:9-14.
28. Nteeba J, Ganesan S, Keating AF. Progressive obesity alters ovarian folliculogenesis with impacts on pro-inflammatory and steroidogenic signaling in female mice. Biol Reprod 2014; 91:86.
29. Nteeba J, Ross JW, Perfield JW, 2nd, Keating AF. High fat diet induced obesity alters ovarian phosphatidylinositol-3 kinase signaling gene expression. Reprod Toxicol 2013; 42:68-77.
30. Nteeba J, Ganesan S, Madden JA, Dickson MJ, Keating AF. Progressive obesity alters ovarian insulin, phosphatidylinositol-3 kinase, and chemical metabolism signaling pathways and potentiates ovotoxicity induced by phosphoramide mustard in mice. Biol Reprod 2017; 96:478-490.
31. Nteeba J, Ganesan S, Keating AF. Impact of obesity on ovotoxicity induced by 7,12-dimethylbenz[a]anthracene in mice. Biol Reprod 2014; 90:68.
32. Gatei M, Scott SP, Filippovitch I, Soronika N, Lavin MF, Weber B, Khanna KK. Role for ATM in DNA damage-induced phosphorylation of BRCA1. Cancer Res 2000; 60:3299-3304.
33. Falck J, Mailand N, Syljuasen RG, Bartek J, Lukas J. The ATM-Chk2-Cdc25A checkpoint pathway guards against radioresistant DNA synthesis. Nature 2001; 410:842-847.
34. Meulmeester E, Pereg Y, Shiloh Y, Jochemsen AG. ATM-mediated phosphorylations inhibit Mdmx/Mdm2 stabilization by HAUSP in favor of p53 activation. Cell Cycle 2005; 4:1166-1170.
35. Liu Q, Turner KM, Alfred Yung WK, Chen K, Zhang W. Role of AKT signaling in DNA repair and clinical response to cancer therapy. Neuro Oncol 2014; 16:1313-1323.
36. Byers SL, Wiles MV, Dunn SL, Taft RA. Mouse estrous cycle identification tool and images. PLoS One 2012; 7:e35538.
37. Schneider CA, Rasband WS, Eliceiri KW. NIH Image to ImageJ: 25 years of image analysis. Nat Methods 2012; 9:671-675.
38. Clark KLT, O.O.; Ganesan, S.; Schulz, L.C.; Keating, A.F. Developmental Origins of Ovarian Disorder: Impact of Maternal Lean Gestational Diabetes on the Offspring Ovarian Proteome in Mice. Biology of Reproduction 2019.
39. Mustaqeem M, Sadullah S, Waqar W, Farooq MZ, Khan A, Fraz TR. Obesity with irregular menstrual cycle in young girls. Mymensingh Med J 2015; 24:161-167.
40. Dravecka I, Lazurova I, Kraus V. Obesity is the major factor determining an insulin sensitivity and androgen production in women with anovulary cycles. Bratisl Lek Listy 2003; 104:393-399.
41. Olsen CM, Nagle CM, Whiteman DC, Ness R, Pearce CL, Pike MC, Rossing MA, Terry KL, Wu AH, Risch HA, Yu H, Doherty JA, et al. Obesity and risk of ovarian cancer subtypes: evidence from the Ovarian Cancer Association Consortium. Endocr Relat Cancer 2013; 20:251-262.

42. Huang HY, Chen HL, Feng LP. Maternal obesity and the risk of neural tube defects in offspring: A meta-analysis. Obes Res Clin Pract 2017; 11:188-197.
43. Hanafi MY, Saleh MM, Saad MI, Abdelkhalek TM, Kamel MA. Transgenerational effects of obesity and malnourishment on diabetes risk in F2 generation. Mol Cell Biochem 2016; 412:269-280.
44. Radulescu L, Ferechide D, Popa F. The importance of fetal gender in intrauterine growth restriction. J Med Life 2013; 6:38-39.
45. Desai M, Jellyman JK, Han G, Beall M, Lane RH, Ross MG. Maternal obesity and high-fat diet program offspring metabolic syndrome. Am J Obstet Gynecol 2014; 211:237.e231-237.e213.
46. Aiken CE, Tarry-Adkins JL, Ozanne SE. Transgenerational effects of maternal diet on metabolic and reproductive ageing. Mamm Genome 2016; 27:430-439.
47. Aiken CE, Tarry-Adkins JL, Penfold NC, Dearden L, Ozanne SE. Decreased ovarian reserve, dysregulation of mitochondrial biogenesis, and increased lipid peroxidation in female mouse offspring exposed to an obesogenic maternal diet. Faseb j 2016; 30:1548-1556.
48. Chan KA, Tsoulis MW, Sloboda DM. Early-life nutritional effects on the female reproductive system. J Endocrinol 2015; 224:R45-62.
49. Fernandez-Capetillo O, Lee A, Nussenzweig M, Nussenzweig A. H2AX: the histone guardian of the genome. DNA Repair (Amst) 2004; 3:959-967.
50. Savic V, Yin B, Maas NL, Bredemeyer AL, Carpenter AC, Helmink BA, Yang-Iott KS, Sleckman BP, Bassing CH. Formation of dynamic gamma-H2AX domains along broken DNA strands is distinctly regulated by ATM and MDC1 and dependent upon H2AX densities in chromatin. Mol Cell 2009; 34:298-310.
51. Meier A, Fiegler H, Munoz P, Ellis P, Rigler D, Langford C, Blasco MA, Carter N, Jackson SP. Spreading of mammalian DNA-damage response factors studied by ChIP-chip at damaged telomeres. Embo j 2007; 26:2707-2718.
52. Setayesh T, Nersesyan A, Misik M, Ferk F, Langie S, Andrade VM, Haslberger A, Knasmuller S. Impact of obesity and overweight on DNA stability: Few facts and many hypotheses. Mutat Res 2018; 777:64-91.
53. Igosheva N, Abramov AY, Poston L, Eckert JJ, Fleming TP, Duchen MR, McConnell J. Maternal diet-induced obesity alters mitochondrial activity and redox status in mouse oocytes and zygotes. PLoS One 2010; 5:e10074.
54. Donmez-Altuntas H, Sahin F, Bayram F, Bitgen N, Mert M, Guclu K, Hamurcu Z, Aribas S, Gundogan K, Diri H. Evaluation of chromosomal damage, cytostasis, cytotoxicity, oxidative DNA damage and their association with body-mass index in obese subjects. Mutat Res Genet Toxicol Environ Mutagen 2014; 771:30-36.
55. So S, Davis AJ, Chen DJ. Autophosphorylation at serine 1981 stabilizes ATM at DNA damage sites. J Cell Biol 2009; 187:977-990.
56. Boder E, Sedgwick RP. Ataxia-telangiectasia; a familial syndrome of progressive cerebellar ataxia, oculocutaneous telangiectasia and frequent pulmonary infection. Pediatrics 1958; 21:526-554.
57. Choy KR, Watters DJ. Neurodegeneration in ataxia-telangiectasia: Multiple roles of ATM kinase in cellular homeostasis. Dev Dyn 2018; 247:33-46.
58. van Os NJH, Jansen AFM, van Deuren M, Haraldsson A, van Driel NTM, Etzioni A, van der Flier M, Haaxma CA, Morio T, Rawat A, Schoenaker MHD, Soresina

A, et al. Ataxia-telangiectasia: Immunodeficiency and survival. Clin Immunol 2017; 178:45-55.
59. Fortuno C, Labarta E. Genetics of primary ovarian insufficiency: a review. J Assist Reprod Genet 2014; 31:1573-1585.
60. Barlow C, Liyanage M, Moens PB, Tarsounas M, Nagashima K, Brown K, Rottinghaus S, Jackson SP, Tagle D, Ried T, Wynshaw-Boris A. Atm deficiency results in severe meiotic disruption as early as leptonema of prophase I. Development 1998; 125:4007-4017.
61. Ganesan S, Keating AF. The ovarian DNA damage repair response is induced prior to phosphoramide mustard-induced follicle depletion, and ataxia telangiectasia mutated inhibition prevents PM-induced follicle depletion. Toxicol Appl Pharmacol 2016; 292:65-74.
62. Ganesan S, Keating AF. Phosphoramide mustard exposure induces DNA adduct formation and the DNA damage repair response in rat ovarian granulosa cells. Toxicol Appl Pharmacol 2015; 282:252-258.
63. Cortez D, Wang Y, Qin J, Elledge SJ. Requirement of ATM-dependent phosphorylation of brca1 in the DNA damage response to double-strand breaks. Science 1999; 286:1162-1166.
64. Robson M, Gilewski T, Haas B, Levin D, Borgen P, Rajan P, Hirschaut Y, Pressman P, Rosen PP, Lesser ML, Norton L, Offit K. BRCA-associated breast cancer in young women. J Clin Oncol 1998; 16:1642-1649.
65. Titus S, Li F, Stobezki R, Akula K, Unsal E, Jeong K, Dickler M, Robson M, Moy F, Goswami S, Oktay K. Impairment of BRCA1-related DNA double-strand break repair leads to ovarian aging in mice and humans. Sci Transl Med 2013; 5:172ra121.
66. Govindaraj V, Keralapura Basavaraju R, Rao AJ. Changes in the expression of DNA double strand break repair genes in primordial follicles from immature and aged rats. Reprod Biomed Online 2015; 30:303-310.
67. Cohen GM. Caspases: the executioners of apoptosis. Biochem J 1997; 326 (Pt 1):1-16.
68. Matikainen T, Perez GI, Zheng TS, Kluzak TR, Rueda BR, Flavell RA, Tilly JL. Caspase-3 gene knockout defines cell lineage specificity for programmed cell death signaling in the ovary. Endocrinology 2001; 142:2468-2480.
69. Carambula SF, Matikainen T, Lynch MP, Flavell RA, Goncalves PB, Tilly JL, Rueda BR. Caspase-3 is a pivotal mediator of apoptosis during regression of the ovarian corpus luteum. Endocrinology 2002; 143:1495-1501.
70. Plowchalk DR, Mattison DR. Phosphoramide mustard is responsible for the ovarian toxicity of cyclophosphamide. Toxicol Appl Pharmacol 1991; 107:472-481.
71. Luan Y, Edmonds ME, Woodruff TK, Kim SY. Inhibitors of apoptosis protect the ovarian reserve from cyclophosphamide. J Endocrinol 2019; 240:243-256.
72. Nguyen QN, Zerafa N, Liew SH, Morgan FH, Strasser A, Scott CL, Findlay JK, Hickey M, Hutt KJ. Loss of PUMA protects the ovarian reserve during DNA-damaging chemotherapy and preserves fertility. Cell Death Dis 2018; 9:618.
73. Hong F, Liu B, Wu BX, Morreall J, Roth B, Davies C, Sun S, Diehl JA, Li Z. CNPY2 is a key initiator of the PERK-CHOP pathway of the unfolded protein response. Nat Struct Mol Biol 2017; 24:834-839.

74. Enquobahrie DA, Williams MA, Qiu C, Meller M, Sorensen TK. Global placental gene expression in gestational diabetes mellitus. Am J Obstet Gynecol 2009; 200:206.e201-213.
75. Fu XF, Cheng SF, Wang LQ, Yin S, De Felici M, Shen W. DAZ Family Proteins, Key Players for Germ Cell Development. Int J Biol Sci 2015; 11:1226-1235.
76. Hsu LC, Chen HY, Lin YW, Chu WC, Lin MJ, Yan YT, Yen PH. DAZAP1, an hnRNP protein, is required for normal growth and spermatogenesis in mice. Rna 2008; 14:1814-1822.
77. Ruggiu M, Speed R, Taggart M, McKay SJ, Kilanowski F, Saunders P, Dorin J, Cooke HJ. The mouse Dazla gene encodes a cytoplasmic protein essential for gametogenesis. Nature 1997; 389:73-77.
78. Dai T, Vera Y, Salido EC, Yen PH. Characterization of the mouse Dazap1 gene encoding an RNA-binding protein that interacts with infertility factors DAZ and DAZL. BMC Genomics 2001; 2:6.
79. Tsui S, Dai T, Roettger S, Schempp W, Salido EC, Yen PH. Identification of two novel proteins that interact with germ-cell-specific RNA-binding proteins DAZ and DAZL1. Genomics 2000; 65:266-273.

Figures and Figure Legends

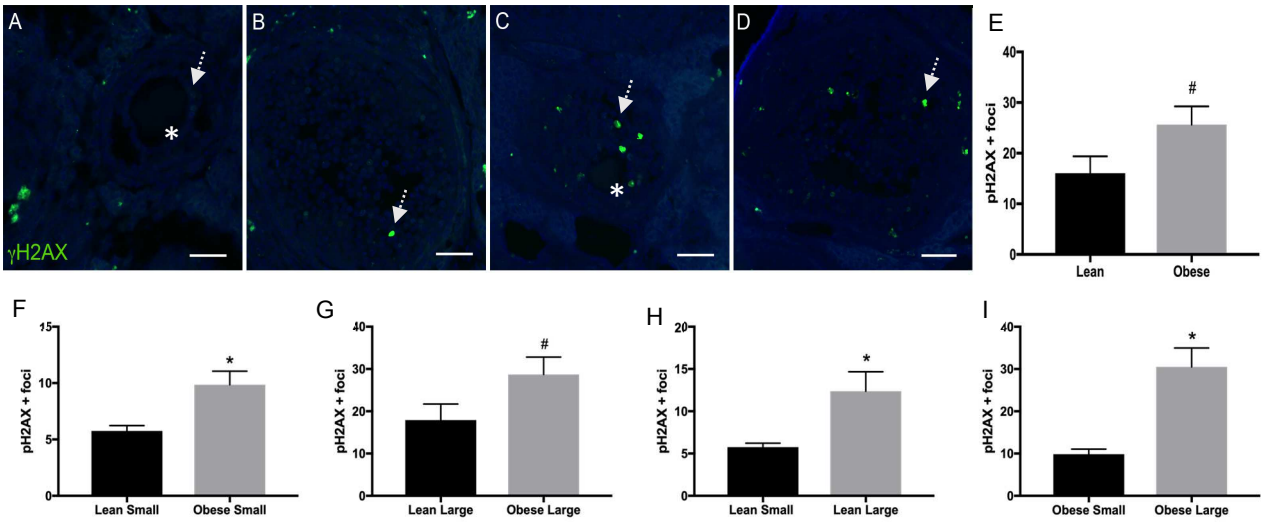

Figure 1. Effect of obesity on ovarian γH2AX abundance. A primary antibody directed against γH2AX was used to determine ovarian localization in (A) small follicles and (B) large follicles of lean mice; in (C) small follicles and (D) large follicles of obese mice. Green punctate staining indicates γH2AX while cellular DNA is stained in blue; scale bar = 50 μm. Dotted tail arrows indicate γH2AX positive staining in the granulosa cells of small or large follicles; asterisk indicates oocyte. The bars represent mean number of positive γH2AX foci ± SEM in (E) all follicles; (F) primordial/primary follicles; (G) secondary/antral follicles; (H) lean small/large follicles; (I) obese small/large follicles; * = $P < 0.05$, # = $P < 0.1$.

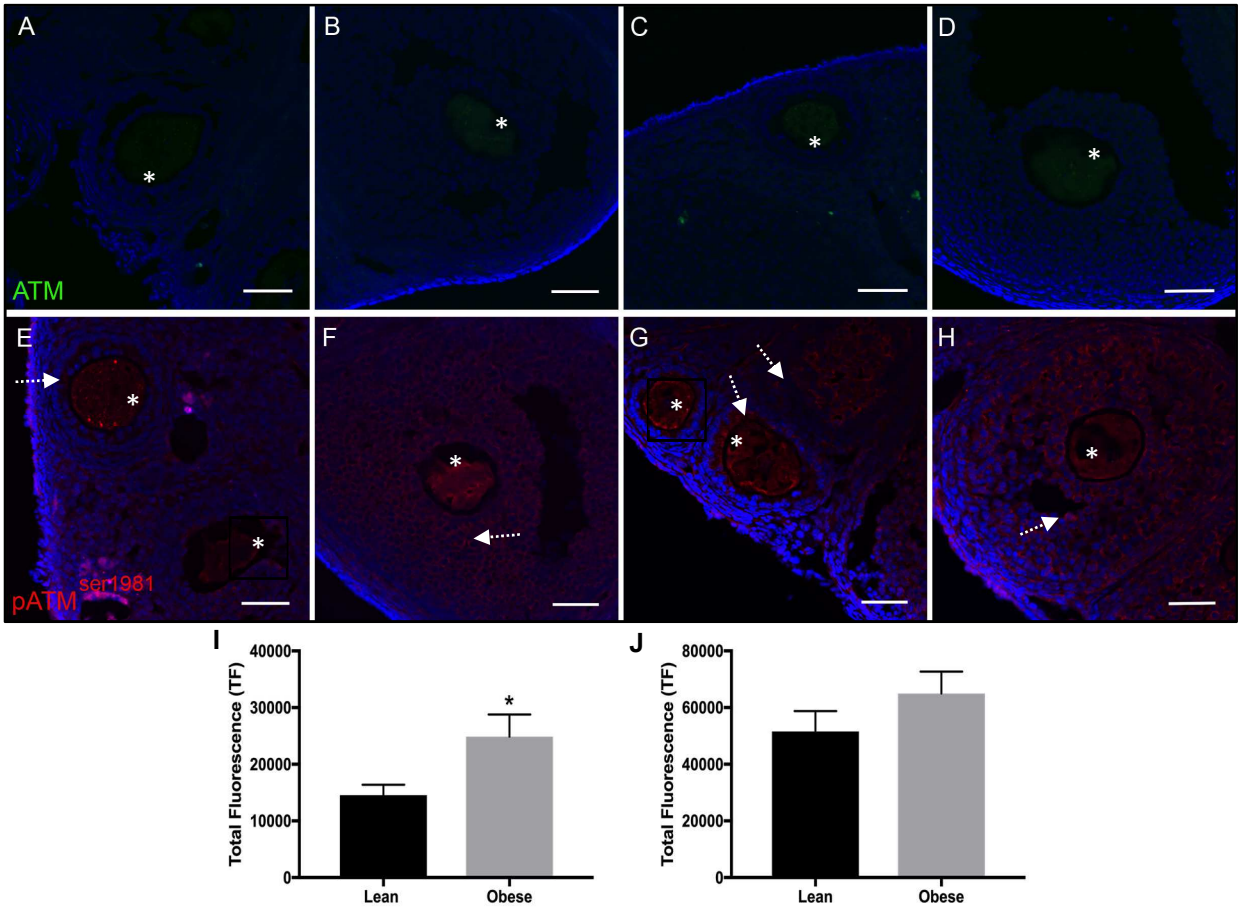

Figure 2. Impact of obesity on the ATM and pATM^{ser1981}. Primary antibody directed against ATM in (A) small follicles of lean mice; (B) large follicles of lean mice; in (C) small follicles of obese mice; (D) large follicles of obese mice, and pATM^{Ser1981} in (E) small follicles of lean mice; (F) large follicles of lean mice; in (G) small follicles of obese mice; (H) large follicles of obese mice. Green staining indicates ATM and red staining indicates pATM^{Ser1981} while cellular DNA is stained in blue; scale bar = 50µm. Dotted tail arrow indicates granulosa cells; asterisk indicates oocyte. The bars represent mean values from the quantification of total fluorescence intensity ± SEM in (I) ATM and (J) pATM^{Ser1981}; * = $P < 0.05$.

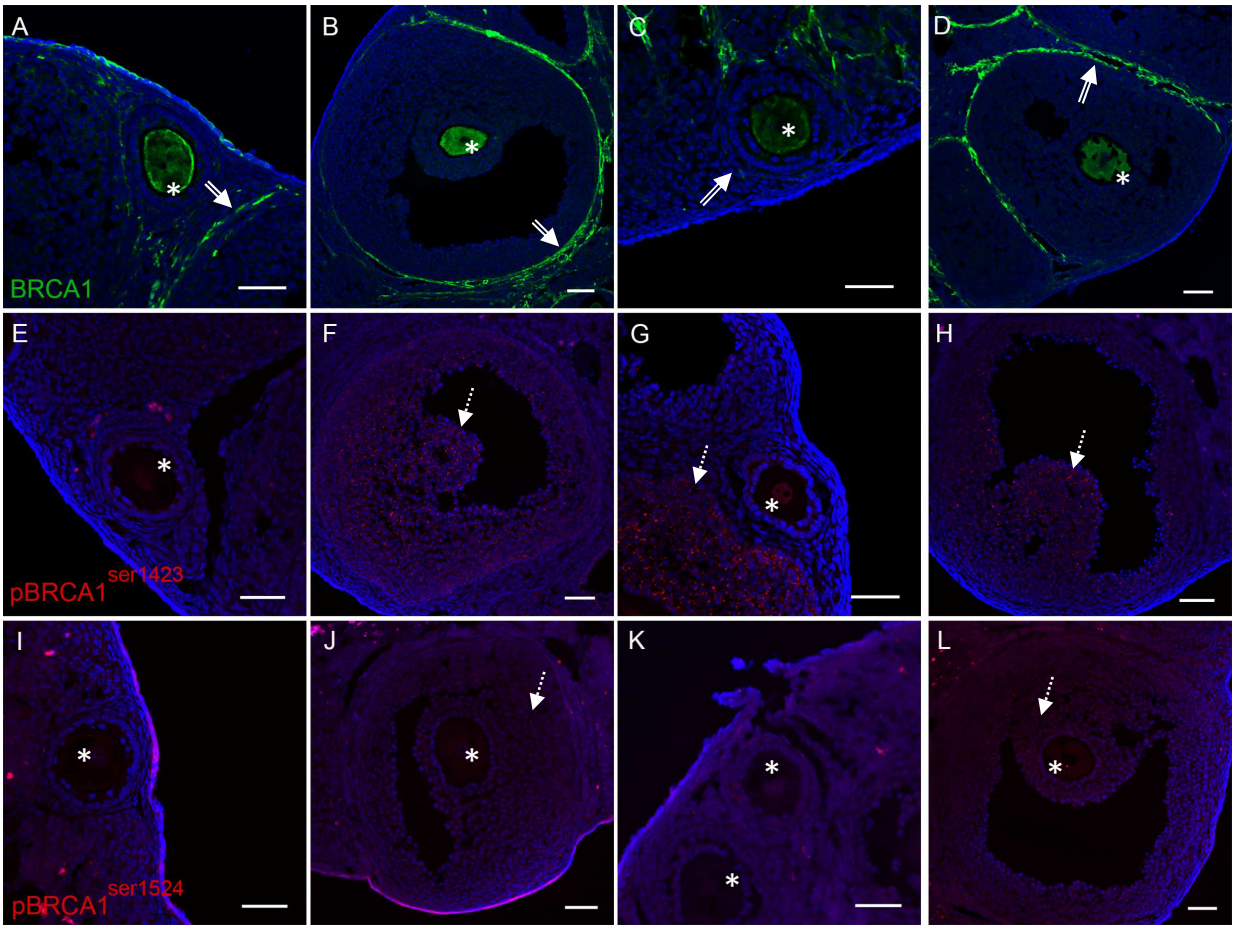

Figure 3. Effect of obesity on BRCA1 localization. Primary antibodies directed against BRCA1 in (A) small follicles of lean mice; (B) large follicles of lean mice; in (C) small follicles of obese mice; (D) large follicles of obese mice; pBRCA1^{Ser1423} in (E) small follicles of lean mice; (F) large follicles of lean mice; in (G) small follicles of obese mice; (H) large follicles of obese mice; pBRCA1^{Ser1524} in (I) small follicles of lean mice; (J) large follicles of lean mice; in (K) small follicles of obese mice; (L) large follicles of obese mice. Green staining indicates BRCA1 and red staining indicates pBRCA^{Ser1423} or pBRCA^{Ser1524} while cellular DNA is stained in blue; scale bar = 50µm. Dotted tail arrow indicates granulosa cells; double tail arrow indicates theca cells; asterisk indicates oocyte.

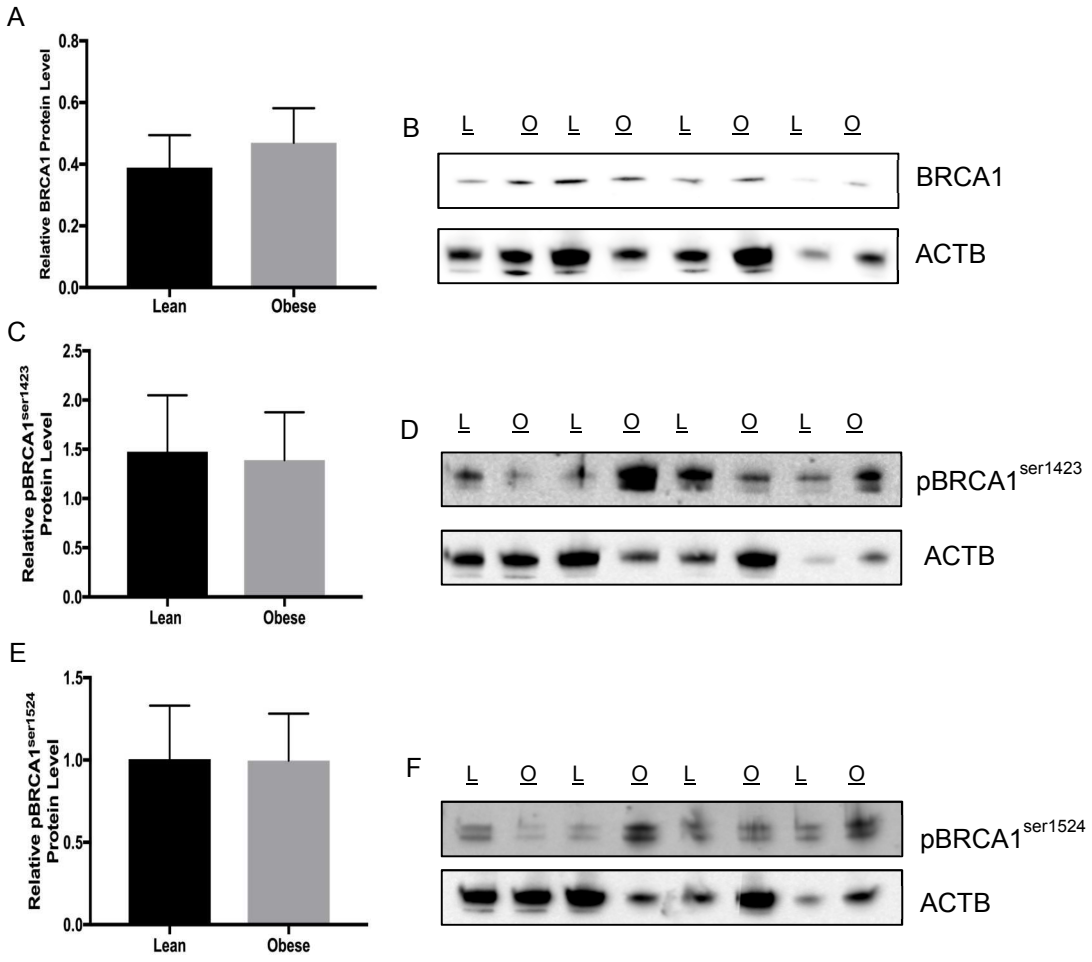

Figure 4. Influence of obesity on total ovarian BRCA1 protein. Abundance of (A, B) BRCA1 protein; (C, D) pBRCA1^{Ser1423} protein; and (E, F) pBRCA1^{Ser1524} in lean and obese ovaries. (A, C, E) bar charts represent mean densitometric values ± SEM. (B, D, F) Western blots for BRCA1, pBRCA1^{Ser1423}, and pBRCA1^{Ser1524}; "L" indicates lean and "O" indicates obese ovary.

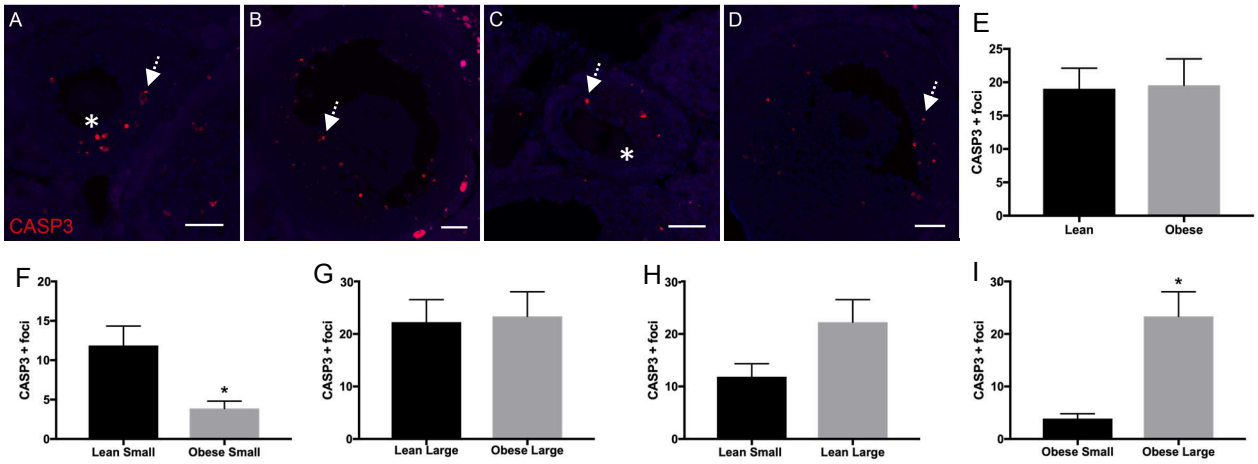

Figure 5. Effect of obesity on ovarian CASP3. A primary antibody directed against cleaved CASP3 was used to determine ovarian localization in (A) small follicles and (B) large follicles of lean mice; in (C) small follicles and (D) large follicles of obese mice. Red punctate staining indicates CASP3 while cellular DNA is stained in blue; scale bar = 50 μm. Arrows indicate CASP3 positive staining in the granulosa cells of small or large follicles; asterisk indicates oocyte. The bars represent mean number of positive CASP3 foci ± SEM in (E) all follicles; (F) primordial/primary follicles; (G) secondary/antral follicles; (H) lean small/large follicles; (I) obese small/large follicles; * = $P < 0.05$.

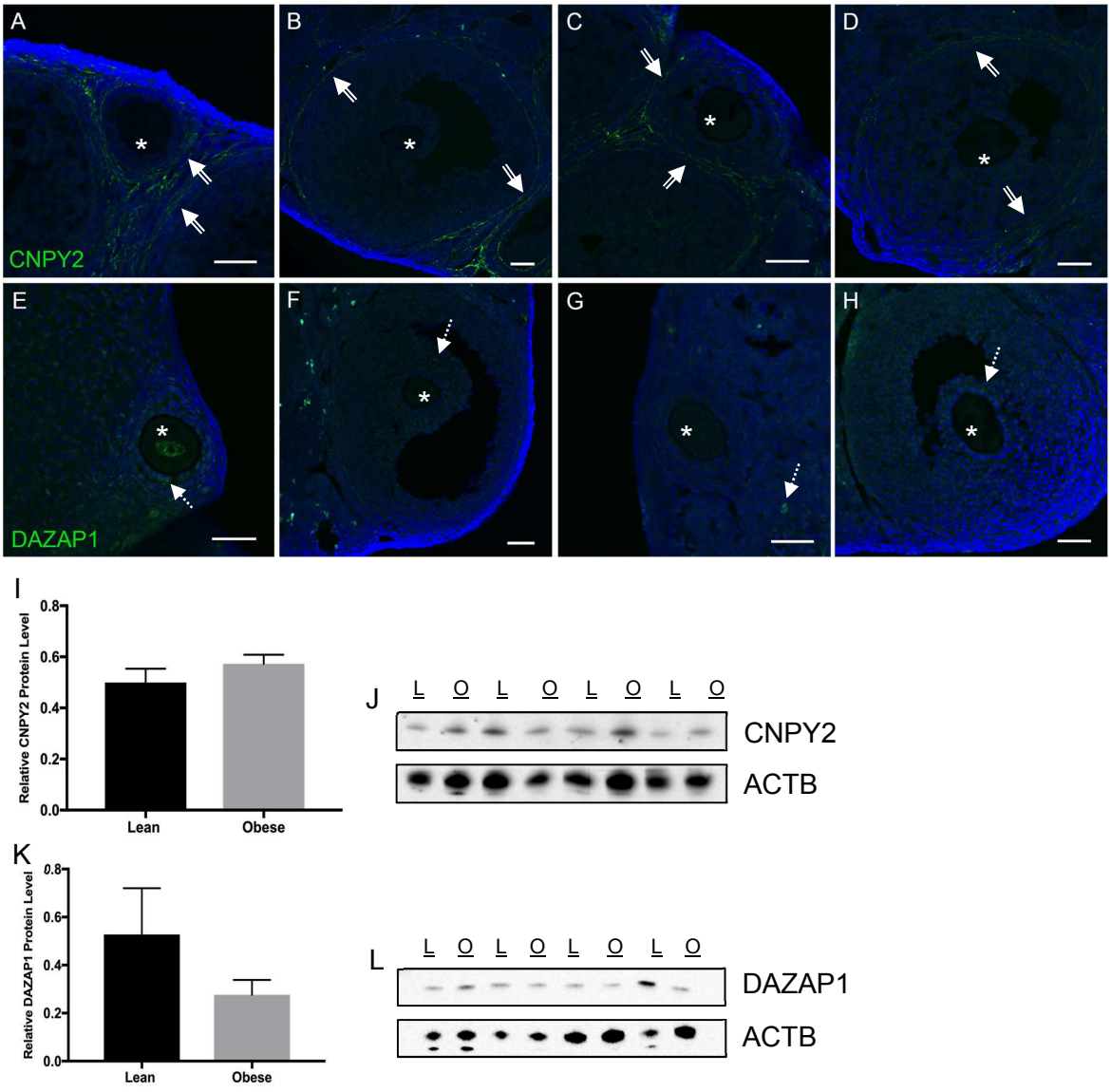

Figure 6. Ovarian abundance of CNPY2 and DAZAP1 and effect of obesity. Primary antibody directed against CNPY2 in (A) small follicles of lean mice; (B) large follicles of lean mice; in (C) small follicles of obese mice; (D) large follicles of obese mice, and DAZAP1 in (E) small follicles of lean mice; (F) large follicles of lean mice; in (G) small follicles of obese mice; (H) large follicles of obese mice. Green staining indicates protein of interest while cellular DNA is stained in blue; scale bar = 50µm. Dotted tail arrow indicates granulosa cells; double tail arrow indicates theca cells; asterisk indicates oocyte.

Abundance and western blot, respectively, of (I, J) CNPY2 protein and (K, L) DAZAP1 protein in lean and obese ovaries. "L" indicates lean ovary and "O" indicates obese ovary.

Supplementary Figures and Legends

Supplementary Table 1. Primary and secondary antibodies used in this study
*designates antigen retrieval method used

Primary Antibody	Host	Dilution (IF/WB)	Supplier	Code
ACTB	Mouse	1:500 (WB)	Santa Cruz	sc-47778
ATM	Rabbit	1:100	abcam	ab32420
pATM$_{ser1981}$	Rabbit	1:100	R & D Systems	AF1655
BRCA1	Rabbit	1:100	Santa Cruz	sc-642
pBRCA1$_{ser1423}$*	Rabbit	1:100/1:350	Thermo Fisher	PA5-36627
pBRCA1$_{ser1524}$*	Rabbit	1:100/1:350	Thermo Fisher	PA5-36829
Cleaved CASP3	Rabbit	1:100	Cell Signaling	9661
CNPY2	Rabbit	1:100/1:500	Thermo Fisher	PA5-46131
DAZAP1	Rabbit	1:100/1:500	Novus Biological	NBP1-82741
γH2AX	Rabbit	1:50	Cell Signaling	2577
Secondary Antibody	Host	Dilution	Supplier	Code
Rabbit IgG 488	Goat	1:500	Thermo Fisher	A11008
Rabbit IgG 568	Goat	1:500	Thermo Fisher	A11011
Rabbit IgG HRP		1:1000 (WB)	Cell Signaling	7074
Mouse IGG HRP		1:500 (WB)	Cell Signaling	7076

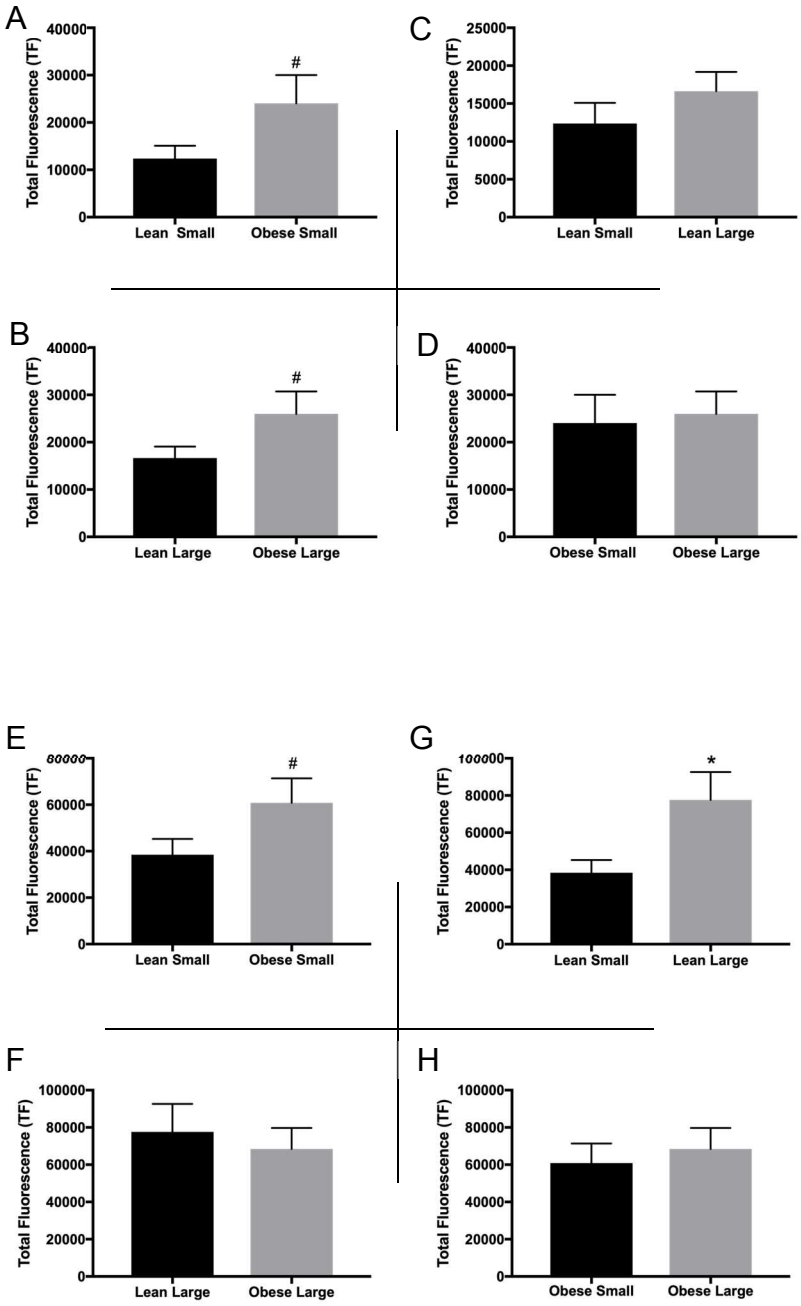

Supplementary Figure 1. Impact of obesity on ATM and pATM^{Ser1981} in different follicle stages. The bars represent mean values from the quantification of fluorescence intensity ± SEM of ATM in (A) primordial/primary follicles; (B) secondary/antral follicles; (C) lean small/large follicles; D) obese small/large follicles and of pATM^{Ser1981}

in (E) primordial/primary follicles; (F) secondary/antral follicles; (G) lean small/large follicles; (H) obese small/large follicles * = $P < 0.05$, # = $P < 0.1$.

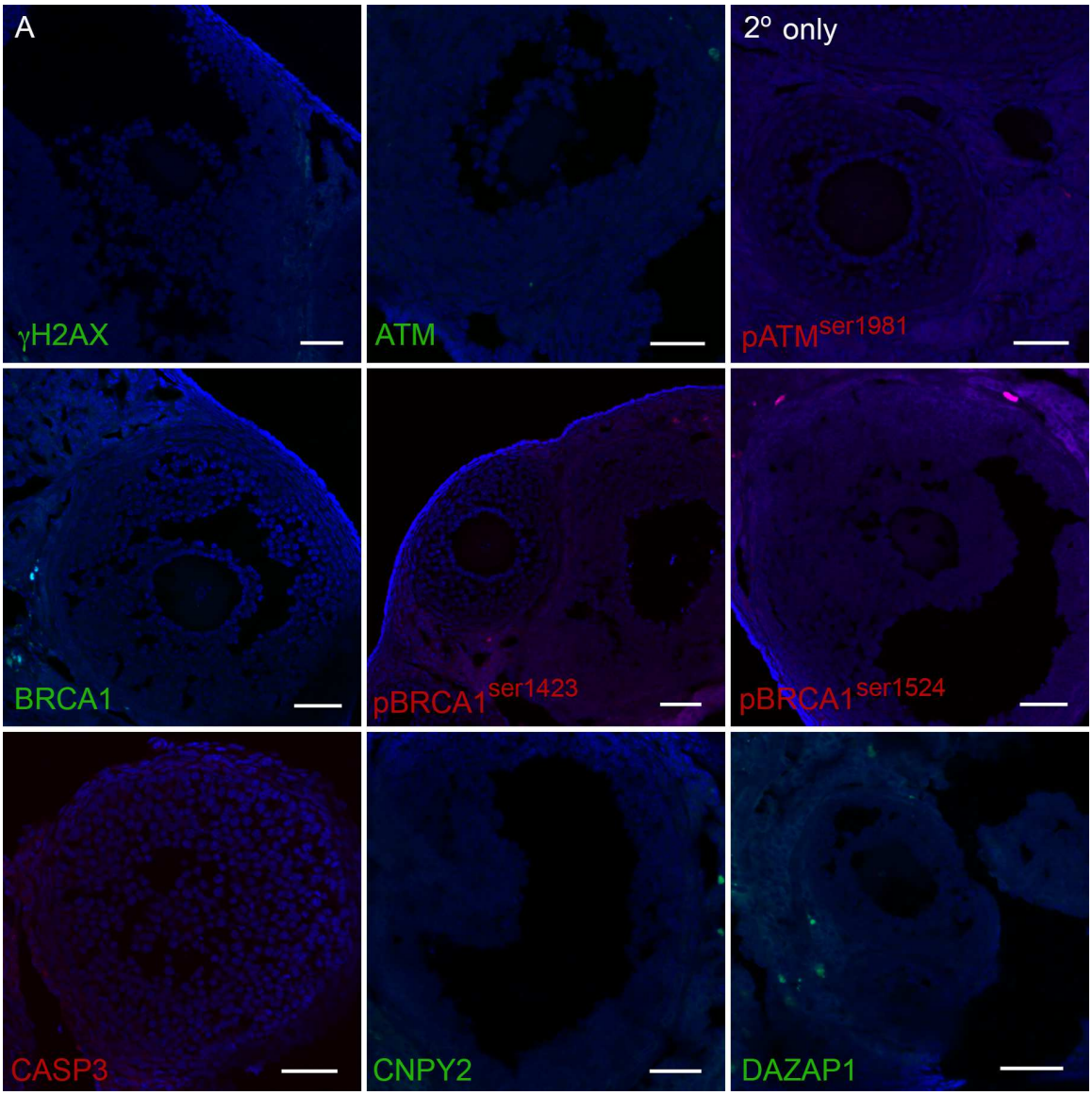

Supplementary Figure 2. Technical controls for immunofluorescence staining. Ovaries from a lean adult mouse were immunologically stained using only the secondary antibody appropriate for (A) γH2AX; (B) ATM; (C) pATM^{Ser1981}; (D) BRCA1; (E) pBRCA1^{Ser1423}; (F) pBRCA^{Ser1524}; (G) CASP3; (H) CNPY2; (I) DAZAP1; cellular DNA is stained in blue; scale bar = 50 μm.

CHAPTER 4: ATAXIA TELANGIECTASIA MUTATED COORDINATES THE OVARIAN DNA REPAIR AND ATRESIA-INITIATING REPSONSE TO PHOSPHORAMIDE MUSTARD

Kendra L. Clark and Aileen F. Keating

Department of Animal Science – Iowa State University, Ames, Iowa 50011

A manuscript published in
Biology of Reproduction, 2019

Contribution Statement:
K.L. Clark performed all analyses on ovarian tissue, designed experiments, and interpreted the data and wrote the manuscript. A.F. Keating designed the experiments, aided in data interpretation, and edited the manuscript.

Abstract

Ataxia telangiectasia mutated (ATM) protein recognizes and repairs DNA double strand breaks (DSB) through activation of cell cycle checkpoints and DNA repair proteins. *Atm* gene mutations increase female reproductive cancer risk. Phosphoramide mustard (PM) induces ovarian DNA damage and destroys primordial follicles, and pharmacological ATM inhibition prevents PM-induced follicular depletion. Wild-type (WT) C57BL/6 or $Atm^{+/-}$ mice were dosed once intraperitoneally with sesame oil (95%) or PM (25 mg/kg) in the proestrus phase of the estrous cycle and ovaries harvested 3 days thereafter. $Atm^{+/-}$ mice spent ~25% more time in diestrus phase than WT. Liquid chromatography with tandem mass spectrometry (LC-MS/MS) on ovarian protein was performed and bioinformatically analyzed. Relative to WT, $Atm^{+/-}$ mice had 64 and 243 proteins increased or decreased in

abundance, respectively. In WT mice, PM increased 162 and decreased 20 proteins. In *Atm*$^{+/-}$ mice, 173 and 37 proteins were increased and decreased, respectively, by PM. Exportin-2 (XPO2) was localized to granulosa cells of all follicle stages and was 7.2-fold greater in *Atm*$^{+/-}$ than WT mice. Cytoplasmic FMR1-interacting protein 1 (CYFIP1) was 6.8-fold lower in *Atm*$^{+/-}$ mice and was located in the surface epithelium with apparent translocation to the ovarian medulla post-PM exposure. PM induced γH2AX, but fewer γH2AX positive foci were identified in *Atm*$^{+/-}$ ovaries. Similarly, cleaved caspase-3 was lower in the *Atm*$^{+/-}$ PM-treated, relative to WT mice. These findings support ATM involvement in ovarian DNA repair and suggest that ATM functions to regulate ovarian atresia.

Keywords: DNA repair, ovary, ovotoxicity, oncofertility

Introduction

The integrity of the genome is constantly insulted by endogenous and exogenous sources and an intrinsic response is needed to effectively repair any damaged DNA. Ataxia telangiectasia mutated (ATM) protein is a major orchestrator of DNA repair and activated ATM precipitates the cellular DNA damage repair response (DDR). The cell cycle is arrested, and the DNA damage is fixed, or the cell is triggered for apoptosis if beyond repair [1]. ATM acts as a sensor and transducer of DNA damage, phosphorylating several downstream targets after activation including histone 2AX (H2AX) [2], mediator of DNA damage checkpoint protein 1 (MDC1) [3], and breast cancer type 1 susceptibility protein (BRCA1) [4] for DNA repair; serine/threonine-protein kinase Chk2 (CHK2) for cell cycle

arrest [5]. After the repair process, ATM influences cellular fate by targeting p53 [6] for apoptosis, and RAC-alpha serine/threonine-protein kinase (AKT) [7] for cell survival. Elevated ATM is associated with a poor tumor response to chemotherapy and platinum resistance [8].

Mutations in *Atm* cause ataxia-telangiectasia (A-T) syndrome, a rare autosomal recessive disease characterized by neurodegeneration, immunodeficiency, increased radiosensitivity, cancer predisposition, and infertility [9]. A-T women have hypoplastic ovaries devoid of primordial follicles [10] and female $Atm^{-/-}$ mice are infertile and lack viable oocytes [11]. Women who are heterozygous carriers of mutated *Atm* have elevated cancer risk, particularly breast and ovarian [12-17], thus, receive anti-cancer therapy; a scenario that further increases their infertility risks.

Cyclophosphamide (CPA) is an alkylating agent used in the treatment of cancers [18] and autoimmune disorders [19, 20] in adults and children. Phosphoramide mustard (PM), an ovotoxic metabolite of CPA [21, 22], destroys rapidly dividing cells by inducing DNA double strand breaks (DSB) [23]. The reproductive effects of PM exposure have been well characterized by our group and others, which include loss of primordial and primary follicles in mice [24-27], antral follicles in rats [28], and amenorrhea, premature ovarian failure, and infertility in women and young girls [29]. In addition to fertility issues, CPA exposure has been associated with congenital malformations in offspring exposed to CPA *in utero* as well as pre-gestational germ cell exposures [30]. Increasing cancer survival rates present the need to identify the mechanisms by which cancer therapies or other chemical exposures cause ovarian damage.

ATM induction is the earliest observed event during PM-induced ovotoxicity and our group made the surprising observation that pharmacological inhibition of ATM prevents PM-induced follicular depletion *ex vivo* [31]. Thus, the hypothesis under investigation in this study was that the DNA damage response would be blunted in $Atm^{+/-}$ deficient mice and unhealthy follicles that normally would be triggered for repair and/or apoptosis would remain in the ovary. Our specific objectives were to determine if lowered ATM abundance affected PM-induced follicle loss and to investigate abundance and localization of ovarian DNA repair and apoptosis proteins after PM exposure in both wild type and ATM-deficient mice.

Materials and Methods

Animal procedure and tissue collection

All experiments were performed according to regulatory guidelines and approved by the Institutional Animal Care and Use Committee (IACUC) and Institutional Biosafety Committee at Iowa State University. Female C57BL/6J (n = 6) and B6.129S6-Atm^{tm1Awb}/J mice (referred to as $Atm^{+/-}$ herein; n = 6) were purchased from Jackson Laboratory (Bar Harbor, ME) and maintained in an animal facility at Iowa State University under controlled room temperature (21°C-22°C) and lighting (12hr light:12hr dark) with *ad libitum* access to food and water. At 10 weeks of age, mice were intraperitoneally (IP) injected once with PM (25 mg/kg) or sesame oil (95%; n = 3 per group) in the pro-estrus phase of the estrous cycle. Mice were euthanized 3 days after dosing at which time body and organ weights were recorded. Organ weights were normalized to body weight. Ovaries were collected and one ovary was fixed in 4% paraformaldehyde overnight at 4°C for histological analysis

while the contralateral ovary was snap frozen in liquid nitrogen and stored at -80°C until processing for protein extraction.

Estrous cycle monitoring

The estrous cycle was monitored by performing vaginal cytology analysis in the morning for 10 days to ensure that mice were at the same stage of the estrous cycle for PM dosing. Briefly, fresh, wet vaginal smears were collected by pipetting saline into the vagina and collecting the samples. Vaginal smears were placed onto histology slides and examined with a Nikon OPTIPHOT microscope using a 10X objective. Classification of estrous cycle stages was determined as previously described [32]. During the follicular phase, pro-estrus was characterized by small, round nucleated epithelial cells, some cornified epithelial cells, and little to no leukocytes. Estrus was characterized by several cornified epithelial cells containing deteriorating nuclei. The presence of cornified cells and leukocytes indicated the metestrus stage. In diestrus, nucleated epithelial cells reappeared in the vaginal smears in addition to the presence of polymorphonuclear leukocytes.

Histology and follicle counting

After fixation, ovaries were passed through a 10%, 20%/0.1M PBS gradient for 1-3 hours each at room temperature, followed by 30% sucrose/0.1M PBS overnight at 4°C and embedded in optimal cutting temperature (OCT) compound before being flash frozen on dry ice. Serial sections were cut at 7 μm on a cryostat (Leica CM1850) and every 6th section was mounted onto glass slides and stained with hematoxylin and eosin for follicle counting, while intermittent sections were retained for immunofluorescence staining.

Healthy follicles containing oocytes with a distinct oocyte nucleus were counted and classified as previously described [33]. Briefly, primordial follicles were identified by an oocyte encircled by a single layer of squamous granulosa cells; primary follicles contained an oocyte surrounded by a single layer of cuboidal granulosa cells; secondary follicles contained an oocyte surrounded by multiple layers of granulosa cells, and antral follicles were identified as those containing an oocyte enclosed by several layers of granulosa cells in conjunction with presence of a fluid filled antral space. Follicle counts and bright field images were captured on an inverted DMI3000B microscope (Leica) and QICAM MicroPublisher 5.0 (MP5.0-RTV-CLR-10, QIMAGING) camera using QCapture software at a 5x objective. Total counted follicle numbers per ovary were compared between treatments.

Protein isolation and proteome analysis

Total ovarian protein was isolated by tissue homogenization in lysis buffer (50 mM Tris-HCL, 1 mM EDTA, pH 8.5) followed by centrifugation at 10,000 rpm at 4°C for 15 min. Supernatant was collected and protein content was quantified using a bicinchoninic acid assay (BCA) and prepared as a working dilution (50 µg/uL) with lysis buffer (Pierce BCA Protein Assay Kit, Thermofisher). Protein (50 µg/µL) was digested with trypsin/Lys-C for 16 hours, dried down and reconstituted in buffer A (47.5µl; 0.1% formic acid/water). Peptide Retention Time Calibration (PRTC) mixture (25 fmol/µl) was spiked into each sample as an internal control. Protein (10 µg) and PRTC (250 fmol) were injected onto a liquid chromatography column (Agilent Zorbax SB-C18, 0.5mm x 150mm, 5 micron) using an Agilent 1260 Infinity Capillary Pump. Peptides were separated by liquid

chromatography and analyzed using a Q Exactive™ Hybrid Quadrupole-Orbitrap Mass Spectrometer with an HCD fragmentation cell. A positive identification was considered only if three positive peptides were identified per protein. The resulting intact and fragmentation pattern was compared to a theoretical fragmentation pattern (from either MASCOT or Sequest HT) to identify peptides. The relative abundance of the identified proteins was based on the areas of the top three unique peptides for each sample.

For each peptide, the signal intensity was divided by the arithmetic mean of the PRTC as the normalization factor before further analysis. MetaboAnalyst 4.0 [34] was used for data analysis. Upon finding data integrity to be satisfactory (no peptide with more than 50% missing replicates, positive values for the area), missing value estimation was imputed using Singular Value Decomposition (SVD) method. Non-informative values that were near-constant throughout the experiment conditions were detected using interquartile range (IQR) estimation method and were deleted. Data transformation was performed based on generalized logarithm transformation (glog) to make individual features more comparable. The control and treatment samples were compared by *t*-test with the adjusted *P*-value (FDR) cutoff of 0.05. Fold change (FC) analysis with threshold of 2 was performed to compare the absolute value of change between control and treatment values. A volcano plot was created to combine the FC and the *t*-test analysis. The PCA analysis was performed using the *prcomp* package and pairwise score plots were created to provide an overview of the various separation patterns among the most significant components. Partial least squared (PLS*)* regression was then performed using the *plsr* function provided by R *pls* package to predict the continuous and discrete variables. A PLS-DA model was built

to classify and cross-validate PLS using the *caret* package. Finally, a dendrogram and a Heatmap were generated to graphically represent the data.

The UniProt protein IDs that were up/down regulated with *P*-values less than 0.05 were used to retrieve the corresponding KEGG IDs using the "Retrieve/ID mapping" tool of UniProt (accessible at http://www.uniprot.org/uploadlists/). KEGG IDs were used to retrieve biological pathway association of the proteins. Enrichment analysis was performed using the Database for Annotation, Visualization and Integrated Discovery (DAVID) 6.8 Tools [35].

Gene Ontology analysis

Gene Ontology (GO) analysis was performed using PANTHER version 14.0 (http://www.pantherdb.org). Proteins identified in the control and experimental samples were compared to the *Mus musculus* reference list and divided into protein class and biological process. The Fisher's Exact test with False Discovery Rate (FDR) correction was used with $P < 0.05$ considered as a significant difference between samples.

Immunofluorescence staining

Slides were warmed briefly on a 37°C slide warmer and tissue sections were encircled with a histology pap pen (Vector Laboratories) to keep staining solutions concentrated on the tissue during processing. Tissue was rehydrated and permeabilized in 0.1M PBS with 0.1% Tween20 (PBSTw) for 20 min, followed by serum blocking (0.1M PBS/1% BSA/1% DMSO/5% goat serum) for 60 min at room temperature. Primary antibodies (**Supplemental Table 1**) were diluted in fresh blocking solution and applied to

the tissue sections and incubated in a humidified box at 4°C overnight. For antigen retrieval, 1% sodium dodecyl sulfate (SDS) was applied for 5 min after rehydration, followed by three washes of PBSTw for 5 min each and addition of blocking solution as described above. After primary antibody incubation, slides were washed 6 times in PBSTw for 5 min per wash. The appropriate secondary antibody (**Supplemental Table 1**) was added to fresh blocking solution, applied to tissue sections and incubated at room temperature for 60 min, followed by 6 washes in PBSTw for 5 min per wash. Slides were air dried, followed by addition of Vectashield with 4,6-diamidino-2-phenylindole (DAPI) (H1200, Vector Labs) and cured overnight at 4°C. Negative technical controls to confirm specificity were performed using secondary antibodies alone (**Supplemental Figure 1**). Images were captured on a Zeiss LSM700 confocal microscope equipped with an AxioCam MRc5 using a 5 or 20x objective.

Quantification of protein abundance

For quantification of BRCA1, H2AX, and cytochrome c (CYCS) immunoreactivity (n = 3 ovaries per treatment; 2 sections per ovary), the threshold percentage of the total ovarian image area was analyzed in whole ovarian sections using ImageJ (https://imagej.nih.gov). When quantifying ATM immunoreactivity, the threshold percentage of the total image area was limited to the oocyte (3 ovaries per treatment; 17-35 oocytes per treatment), while XPO2 immunoreactivity was measured in granulosa cells of antral follicles (3 ovaries per treatment; 18-45 follicles per treatment). For γH2AX (3 ovaries per treatment; 30-39 follicles per treatment) and cleaved CASP3 (3 ovaries per treatment; 33-36 follicles per treatment), immunopositive cells were manually counted in

primary, secondary and antral follicles using the cell counter module of ImageJ (https://imagej.nih.gov/ij/plugins/cell-counter.html).

Statistical analysis

Statistical analyses were performed using GraphPad Prism 7.0 two-way ANOVA function with Tukey multiple comparison tests for follicle numbers, organ weights, and immunofluorescent staining values. The unpaired t-test was used in the evaluation of the estrous cycle and body weights. For the estrous cycle data, the statistical analysis was performed on the raw data and the data is presented as percentage of time spent at that stage of the estrous cycle during the monitoring period. Bars represent mean value ± standard error of the mean (SEM). A P-value ≤ 0.05 was considered statistically significant and a trend for a statistical difference was considered at $P < 0.1$.

Results

Effect of phosphoramide mustard exposure on body and organ weight

Body weight was lower in $Atm^{+/-}$ females relative to WT controls ($P < 0.05$; **Supplemental Figure 2**) at the onset of the experiment. There was no effect of either PM exposure or *Atm* deficiency on weight of the heart, kidney, liver, spleen, uterus or ovary ($P > 0.05$; **Supplemental Figure 2**).

Impact of *Atm* deficiency on estrous cyclicity and follicle number

There was no impact of *Atm* deficiency on the length of time spent in the proestrus, metestrus, or estrus phases of the estrous cycle; however, $Atm^{+/-}$ mice remained in the diestrus phase of the estrous cycle longer than their WT counterparts ($P < 0.05$; **Figure**

1D). There were reduced numbers of primordial ($P < 0.05$), primary ($P < 0.1$), and total ($P < 0.05$) number of follicles in ovaries of *Atm*$^{+/-}$ mice relative to WT controls (**Figure 2E-G**) but no impact of *Atm* deficiency on secondary or antral follicle number (data not shown).

Effect of PM exposure on follicle number

Phosphoramide mustard decreased ($P < 0.05$) the number of healthy primordial follicles in WT ovaries by 77% (**Figure 2E**). However, comparison between the *Atm*$^{+/-}$ mice who received vehicle control and the *Atm*$^{+/-}$ mice who received PM, revealed no effect ($P > 0.05$) of PM exposure on primordial follicle number in *Atm*$^{+/-}$ ovaries, though the number of primordial follicles was reduced by 52% (**Figure 2E**). Phosphoramide mustard decreased the number of healthy primary follicles in the WT ovaries by 37%, but similar to primordial follicle numbers, relative to *Atm*$^{+/-}$ mice who received vehicle control, PM did not reduce primary follicle number in *Atm*$^{+/-}$ mice (**Figure 2F**). PM exposure also did not affect the number of healthy secondary or antral follicles in WT or *Atm*$^{+/-}$ mice (data not shown). Total follicle number was less in both the CT and PM-exposed *Atm*$^{+/-}$ mice and in WT PM-exposed relative to the WT CT mice (**Figure 2G**). There was no PM-induced difference in total follicle number in *Atm*$^{+/-}$ mice (**Figure 2G**). Overall, there was a reduction in 51% of all follicle types in WT ovaries due to PM treatment, with only a 36% decline in all follicles observed in the *Atm*$^{+/-}$ ovaries.

Identification of PM-induced DNA damage and protein markers of ATM-mediated double strand break repair

To determine an altered ovarian DDR and/or atresia in $Atm^{+/-}$ ovaries, protein markers of DNA damage and the DDR were examined. Positive ATM immunofluorescent staining was observed in the oocyte in all follicle stages, with no difference in localization pattern between genotypes or treatment (**Figure 3A**). ATM immunoreactivity decreased in intensity between the PM-treated genotypes ($P < 0.05$), but no other differences were noted (**Figure 3A'**).

To determine if $Atm^{+/-}$ mice have increased amounts of DNA damage basally and to assess the DDR after a genotoxic exposure, the abundance of ovarian γH2AX was investigated and positive γH2AX foci were quantified in all follicular stages (**Figure 3B**). Increased positive γH2AX foci were detected in WT ovaries after PM-treatment ($P < 0.05$; **Figure 3B'**). In the $Atm^{+/-}$ ovaries, PM exposure did not increase γH2AX (**Figure 3B'**). There was no effect of genotype or PM treatment on the abundance of non-phosphorylated H2AX (**Supplemental Figure 3A**).

BRCA1 immunofluorescent staining was observed throughout the ovary in the oocytes of primary, secondary, and antral follicles, theca cells, stromal cells, with moderate staining occurring in the granulosa cells of some antral follicles (**Figure 3C** and **Supplemental Figure 3B**). Whole ovary BRCA1 fluorescence intensity was decreased in PM-treated WT ovaries, relative to the WT controls (**Figure 3C'**). There was lower BRCA1 protein staining in the vehicle control-treated $Atm^{+/-}$ ovaries compared to the corresponding WT controls ($P < 0.05$; **Figure 3C'**). PM exposure in $Atm^{+/-}$ mice did not

impact BRCA1 protein abundance as detected by immunofluorescent staining (**Figure 3C'**).

Granulosa cells that stained positively for cleaved CASP3 were assessed by immunological staining and positive cells quantified in all follicular stages (**Figure 4A**). An increase in CASP3 positive cells in the WT ovaries after PM-treatment ($P < 0.05$) was observed, and this was absent in *Atm*$^{+/-}$ PM-treated ovaries, relative to the corresponding control. Reduced ($P < 0.1$) numbers of cleaved CASP3 cells were observed in *Atm*$^{+/-}$ PM-treated, relative to WT PM exposed ovaries (**Figure 4A'**).

CYCS protein abundance was determined by immunofluorescent staining and was observed throughout the entire ovary. Lack of ATM did not impact basal CYCS, nor was an impact of PM exposure on ovarian CYCS in WT mice observed (**Figure 4B**). There was a trend ($P < 0.1$) for reduced CYCS in *Atm*$^{+/-}$ovaries exposed to PM (**Figure 4B'**).

Proteomic alterations due to *Atm* haploinsufficiency

LC-MS/MS was utilized to determine any proteins of interest that are regulated by ATM. There were 2,123 ovarian proteins identified in vehicle control-treated *Atm*$^{+/-}$ mice and 2,145 ovarian proteins identified in the vehicle control WT mice. Relative to the WT vehicle control-treated ovaries, 64 proteins were increased and 243 were decreased in abundance in the ovaries of *Atm*$^{+/-}$ females ($P \leq 0.05$; **Supplemental Table 2**).

Effect of phosphoramide mustard exposure on the ovarian proteome

In addition to determining proteins regulated by ATM, LC-MS/MS analysis determined those altered by PM treatment. A total of 2,160 proteins were identified in PM-exposed WT ovaries. Relative to the WT controls, 162 proteins were increased, and 20 proteins were reduced in ovaries of WT mice exposed to PM ($P \leq 0.05$; **Supplemental Table 3**). In PM-treated $Atm^{+/-}$ mice, 2,132 proteins were identified, and 173 proteins were increased and 37 decreased compared to $Atm^{+/-}$ mice treated with vehicle control ($P \leq 0.05$; **Supplemental Table 4**). In $Atm^{+/-}$ mice exposed to PM, 116 proteins were decreased and 61 increased ($P \leq 0.05$; **Supplemental Table 5**) compared to WT PM-exposed mice.

Of these differentially expressed proteins that were increased in each PM treated group, 132, 141, and 31 were determined to be unique in WT, $Atm^{+/-}$, and in the PM-treated genotype comparison, respectively (**Figure 5A**). In contrast, 20, 37, and 116 proteins were decreased that were exclusive to the PM-treated WT, $Atm^{+/-}$, and genotype comparisons, accordingly (**Figure 5B**). Within the separate genotypes and in the absence of PM treatment, 39 increased proteins were identified as unique (**Figure 5A**), while 243 proteins were identified as decreased (**Figure 5B**). Additionally, there were 58 shared proteins that were increased between all groups and 49 proteins shared that were decreased between all groups (**Figure 5A-B)**. Forty-nine proteins were shared between the genotypes, with 16 of these proteins being upregulated and 33 downregulated (**Figure 5A-B**).

Gene ontology (GO) and pathway analysis

Differentially abundant proteins between $Atm^{+/-}$ and WT mice were assigned to protein class and biological process using PANTHER GO analysis (Fischer's Exact with FDR multiple test correction; $P < 0.05$). GO analysis distributed 221 hit genes into 21

protein classes for proteins identified as differing in the *Atm*$^{+/-}$ vehicle control relative to the WT vehicle control (**Figure 5C-D**). In the *Atm*$^{+/-}$ PM relative to WT PM, 139 hit genes were distributed into 22 protein classes (**Figure 5C-D**). Most of the proteins identified were classified as nucleic acid binding proteins (28% in vehicle control-treated ovaries, 15% in PM-treated ovaries; **Figure 5C-D**). Protein classes with the greatest assignments were hydrolases, transferases, enzyme modulators, and cytoskeletal proteins. Together, these protein classes comprise of ~65% of proteins identified between the WT and *Atm*$^{+/-}$ vehicle-treated mice and ~58% of those proteins identified in the WT and *Atm*$^{+/-}$ PM-exposed mice.

For biological process, 43 proteins from the control exposure groups and 27 proteins from the PM exposure groups were assigned to the cellular metabolic process cluster, representing around 15% of the proteins over-represented in *Atm*$^{+/-}$ ovaries. Protein-containing complex subunit organization, establishment of cellular localization, and intracellular transport also had several proteins assigned (**Supplemental Figure 4A**).

KEGG ID's were identified via the UniProt ID mapping tool and utilized in a pathway enrichment analysis via DAVID to determine the representation of molecular networks in *Atm*$^{+/-}$ relative to WT ovaries. In PM exposed mice, the metabolic pathways ID was enriched in approximately ~18% of proteins (**Supplemental Figure 4B**). Interestingly, this was not observed in vehicle control-treated mice of either genotype. Other KEGG pathways identified as differing between the genotypes regardless of treatment were spliceosome, ribosome, focal adhesion, and proteoglycans in cancer (**Supplemental Figure 4B**).

Effect of PM exposure on ovarian localization of CYFIP1 and XPO2 in WT and *Atm*$^{+/-}$ mice.

To determine the spatio-temporal distribution of proteins of interest identified in the LC-MS/MS analysis, immunofluorescence staining was performed on whole ovarian sections. In the LC-MS/MS analysis, Cytoplasmic FMR1-interacting protein 1 (CYFIP1) was reduced by 6.83-fold and 5.57-fold in *Atm*$^{+/-}$ vehicle-control and *Atm*$^{+/-}$ PM exposed ovaries, respectively, relative to their wild-type counterparts. CYFIP1 positive cells were uniformly spaced along the ovarian surface epithelium in all ovary samples (**Figure 6A** and **6A'**), however, PM exposure altered this localization and post-PM exposure, CYFIP1 protein was present in the ovarian cortex including granulosa cells and medulla (**Figure 6A** and **6A'**).

Exportin-2 (XPO2) increased in the *Atm*$^{+/-}$ vehicle-control compared to the WT vehicle-control ovaries by 7.20-fold and by 6.40-fold in *Atm*$^{+/-}$ PM-exposed ovaries relative to the WT PM-exposed ovaries as detected by LC-MS/MS analysis. XPO2 immunological staining revealed positive staining in the granulosa cells of all follicular stages and the oocyte, as well as in the corpus luteum (**Figure 6B**).

Discussion

Cells employ a highly conserved pathway to sense, signal, and repair DNA. A key event in DNA repair is activation of ATM, a member of the phosphatidylinositol 3-kinase (PI3K) superfamily, which also includes ataxia telangiectasia and Rad3-related (ATR) and DNA-dependent protein kinase (DNA-PK) [1]. ATM is activated by the MRN complex, which contains MRE11, RAD50, and NBS1 proteins [36], initiating serine 1981

autophosphorylation and homodimer to active monomer dissociation [37, 38]. Over 700 ATM and ATR protein targets have been identified [39], including BRCA1 [4], CHK2 [5], and P53 [6].

The exact mechanisms underlying chemotherapy-induced follicle loss remain unclear. Direct toxicity to the follicle or oocyte may occur [40-43] or accelerated hyperactivation of primordial follicles [44] in response to targeted death of larger growing follicles, resulting in follicular "burnout" [45-47]. PM induces ovarian DNA damage in the oocyte and granulosa cells [22, 24, 25] and our group discovered that ATM inhibition prevents PM-induced follicle depletion [31]. To further explore the events post-genotoxicant induced ovarian damage, both targeted and exploratory approaches were utilized to determine mechanisms involved in the ovarian response to PM exposure and further, $Atm^{+/-}$ mice were employed to interrogate the role of ATM in mediating the PM-induced ovarian response.

In response to PM exposure in WT mice, both primordial and small primary follicle numbers were reduced in WT mice, consistent with our previous findings [26, 27]. Different numbers of growing follicles post-PM treatment were not observed, suggesting lack of hyperactivation of the ovarian reserve. This corresponded with our previous findings in which inhibition of PI3K did not have any effect on the extent of PM-induced follicle loss [48]. The $Atm^{+/-}$ mice had reduced follicle number at all stages of development, highlighting the importance of ATM in basal ovarian physiology and recapitulating phenotypic observations in A-T female patients [9]. $Atm^{-/-}$ female mice [49] and female A-T patients [9] are infertile due to reduced or complete absence of gametes in the ovary. Primordial germ cell migration to the genital ridge is unaffected in $Atm^{-/-}$ mice, but oocytes

undergo apoptotic degeneration prior to birth [11]. Adult *Atm*$^{-/-}$ mouse ovaries are also devoid of oocytes and superovulation is ineffective [49].

Similar to our findings in which ATM was pharmacologically inhibited ATM in *ex vivo* cultured ovaries [31], PM-induced follicle loss was less robust in *Atm*$^{+/-}$ mice, relative to WT mice. The effect was not complete inhibition of PM-induced follicle loss, presumably due to *Atm* haploinsufficiency, rather than complete ATM reduction as observed in the pharmacological approach [31]. The level of basal ATM in *Atm*$^{+/-}$ ovaries did not differ relative to WT, but there was lack of increased ATM after PM exposure, supporting lack of ATM responsiveness to PM exposure in these mice.

Upon DNA damage, ATM phosphorylates H2AX to γH2AX at the DNA DSB site, resulting in a positive feedback loop of DNA repair proteins [50-54] and γH2AX presence is considered the gold standard for DSB localization [55]. The DDR was irregular, as evidenced by fewer γH2AX positive cells, in *Atm*$^{+/-}$ mice post-PM treatment. This was in stark contrast with WT PM mice in which there was accumulation of γH2AX positive cells. This observation was not attributable to reduced total H2AX protein abundance in the *Atm*$^{+/-}$ mice. The numerical lesser abundance of inactive H2AX could be related to reduced ATM, as the two proteins are products of their respective genes, *Atm* and *H2ax*, which are very closely linked in the same cytogenetic region (11q23) in both humans and mice [56].

BRCA1 functions in homologous recombination [57, 58] and nonhomologous end joining DNA repair [59, 60] and is phosphorylated by ATM. Similar to carriers of a mutant *Atm* gene, women with *Brca1* mutations have defective DNA repair and increased risks of breast and ovarian cancers [61]. Relative to ovaries from WT vehicle-control mice, there were lower levels of basal BRCA1 protein in *Atm*$^{+/-}$ vehicle-control ovaries, and in PM-

exposed mice (both WT and *Atm*$^{+/-}$), potentially an indication that BRCA1 is depleted in response to PM exposure as a reflection of BRCA1 function though this remains to be determined. Taken together, these findings suggest that ovarian BRCA1 is a direct ATM target and that PM exposure affects ovarian BRCA1.

When DNA damage exceeds the capacity of the cell for repair, it is shunted towards apoptosis. Pro-apoptotic CASP3 is implicated in granulosa [62] and luteal [63] cell death, though not necessary for oocyte death [62]. Despite a dramatic increase in CASP3 positive cells in the WT mice post-PM exposure, fewer cells positively stained for CASP3 in *Atm*$^{+/-}$ female mice after PM exposure. This finding in the WT mice is consistent with previous studies [21, 25, 43, 64]. DNA damage can also activate the mitochondrial apoptosis pathway and CYCS release [65]. Altered CYCS abundance was not noted in this study, though there was a slight decline in CYCS due to PM exposure in the *Atm*$^{+/-}$ ovaries which was not apparent in the WT ovaries. An association between *Atm* deficiency and mitochondrial dysfunction has been documented [66-68]. Thus, these findings support reduced apoptosis in the *Atm*$^{+/-}$ ovaries in response to PM induction, potentially indicating lack of shunting of damaged follicles towards atresia, as supported by the reduced extent of follicle loss that resulted from PM exposure in the *Atm*$^{+/-}$ mice.

To complement the targeted approach focused on the ovarian DDR and apoptotic proteins, an unbiased proteomic LC-MS/MS approach was employed to determine additional proteins of interest regulated by ATM and altered by PM. The top proteins affected in each comparison are described below, though this does not indicate that proteins that are significantly altered but with a lowered fold-change have lesser importance in the influence of ATM on ovarian function or in the response to PM exposure. KEGG identifiers

from our proteome analysis revealed proteins involved in metabolic pathways including pyridoxine 5'-phosphate oxidase (PNPO) and phosphomannomutase 2 (PMM2), and proteins associated with the spliceosome.

Identification of proteins that are increased when ATM functionality is reduced support that they are proteins regulated by ATM or that experience secondary effects upon ATM loss. RPL29 is associated with ovarian cancer malignancy [69]. ME is involved in the luteal transition [70]. NID1 functions in ovarian steroidogenesis and bisphenol A exposure reduced *Nid1* mRNA in Sertoli cells of mice [71, 72].

Lack of appropriate ATM function resulted in reduced abundance of proteins that have been demonstrated to respond to cellular stress. AHSA1 is regulated by p53 and though roles in the ovary are not understood, AHSA increases PI3K phosphorylation [73] thus suggesting involvement in ovarian processes of importance. PMM2 mutations result in a glycosylation disorder in humans and endoplasmic reticulum stress has been reported in a zebrafish model of PMM2 deficiency [74, 75]. *Nalp14* mRNA transcript is located in the oocytes of follicles up until the preovulatory stage [76] and *Nalp14* mutation is associated with spermatogenic issues in men [77]. Though not well explored, NESP2 was found to be highly expressed in the ovary [78] and NESP1 [79] and NESP3 [80] have roles in the testes supporting a gonadal role for ovarian NESP2.

Identification of proteins increased in response to PM exposure support their involvement in the ovarian protective response (OPR). These findings identify potential targets that could be medicinally induced in the ovary during CPA/PM treatment to minimize ovarian damage that occurs as a treatment side effect. BHMT1 is involved in metabolism of homocysteine which can be regulated in the oocyte via this enzyme [81].

Though the ovarian role is not clear, in the testes, ALD1 is found in the vas deferens and regulated by dihydrotestosterone (DHT) [82]. *Idi1* mRNA is present in reproductive tissue of *Aedes aegypti* mosquito [83], though there is little data on function in mammalian reproductive systems. CP51A is a member of the cytochrome P450 enzyme family of proteins, which are critical in chemical metabolism processes [84]. In the testis, CP51A has an important role in the production of sterols that regulate meiosis [85]. CDN1B or p27kip1 regulates ovarian development in mice through suppression of follicle endowment, activation, and promoting cell death [86].

The proteins that are reduced by PM could represent targets that are used as a mode of action of PM to induce ovotoxicity or could indicate that the abundance of these proteins is reduced due to their being depleted as they are being utilized in the OPR to PM exposure. PDS5B regulates the cohesion of sister chromatids during mitosis and meiosis, a function integral to DNA replication and repair [87]. In males, PDS5B regulates androgen-induced proliferation inactivation [88] and loss of PDS5B has been implicated in prostate cancer [89]. A10A9 has been identified in fluid of ovarian carcinomas and in the serum from ovarian carcinoma patients [90]. DDX18 is a member of the DEAD-box helicase family of proteins [91] and though there is no known specific reproductive tissue roles of DDX18, DDX25 is a gonadotropin-regulated testicular helicase and is essential for spermatogenesis [92]. Increased TPS1 is observed during follicular atresia in primate ovaries [93] and inhibits VEGF, suggesting a role for TSP1 as a mediator for ovarian angiogenesis and follicle development [94]. Little is known about CE162 in reproductive tissues.

In ovaries with reduced basal ATM, ovarian proteins that are responsive to PM exposure were identified, potentially indicating a response that is not solely due to the

genotoxic effects of PM. In addition, considering the importance of maintaining gamete quality, there are likely ATM-independent mechanisms to respond to genotoxicants, and these proteins may be part of that response. KINH maintains chromosomal stability and in mouse oocytes is critical for germinal vesicle breakdown and polar body extrusion [95]. NAL14 is an inflammasome component and *Nlrp14* has been detected in mammalian oocytes [96, 97]. In ovarian cancer stem cells, SYQ/QARS binds to aggregated P53 protein [98]. CNN1 is a tumor suppressor with suppressive effects in ovarian cancer cells [99] and is also observed in Sertoli cells [100], as a marker for peritubular myoid cells which interact with Sertoli cells during seminiferous tubule development [101]. Conversely, ILK has been implicated in pro-metastatic epithelial ovarian cancers [102].

As is the case with the proteins that are increased in response to PM when ATM is deficient, the same is true of those proteins that are reduced in abundance. These reductions could represent utilization of these proteins in the response to PM, and could also indicate that with decreased abundance of ATM, proteins for which no apparent alteration in their overall abundance during PM exposure in the WT ovaries could in fact be functional in that scenario, but then be reduced in ovarian content in ATM deficiency, and that they are depleted at a faster rate or to a greater extent when ATM is insufficient. MGRAP is a mitochondrial transmembrane protein in the ovary (previously named ovary specific acidic protein) [103, 104] and *Mgrap* is regulated by estrogen and suppressed by a GnRH antagonist [105]. MBD2 has been identified in breast cancer cells [106]. AIF1L was identified via microarray as upregulated in ovarian cancer tissue versus normal ovarian tissue [107]. Reduced HMGN5 increases chemosensitivity of human bladder cancer cells through inhibition of PI3K/AKT signaling [108], but it also has an oncogenic role in several

types of cancers including breast [109] and prostate [110]. AFAM has been detected in follicular fluid [111], with serum concentrations remaining stable throughout the menstrual cycle [112] and elevated in polycystic ovary syndrome patients [113].

Two proteins chosen for further characterization to decipher the impact of PM exposure in the ovaries of the WT and $Atm^{+/-}$ mice were CYFIP and XPO2. CYFIP1 was dramatically decreased in ovaries from $Atm^{+/-}$ female mice both basally and in response to PM treatment relative to their wild-type counterparts. *Cyfip1* is frequently deleted or reduced in human epithelial cancers and during invasion of epithelial tumors, with silencing of *Cyfip1* resulting in disorganized epithelial morphogenesis *in vitro* [114]. Our finding of alterations to CYFIP1 in the $Atm^{+/-}$ ovary with localization around the ovarian surface epithelium and the appearance of CYFIP1 positive cells within the ovarian cortex and medulla after PM treatment indicates a possible role of CYFIP1 in ovarian tissue architecture, notable considering the increased rates of ovarian cancers in A-T female patients as well as carriers of a mutated *Atm* allele.

The cellular apoptosis susceptibility protein XPO2 (also known as CSE1L) was greatly increased in the $Atm^{+/-}$ female ovary both due to ATM deficiency and post-PM exposure in contrast to WT ovaries in which this response was not observed. In healthy cells, the function of XPO2 has been proposed as a breakpoint in regulating which cells proliferate and which cells undergo apoptosis [115]. Modifications in abundance of *Xpo2* have been suggested to promote neoplasia in breast cancers [116-119]. Furthermore, increased *Xpo2,* in association with the tumor suppressor gene *Bax* and pro-apoptotic *Casp3*, coincides with reduced anti-apoptotic *Bcl-2* and has been demonstrated in the pathogenesis of endometrial carcinomas [120]. Considering that PM induced ovarian

apoptosis in WT, but not in *Atm*$^{+/-}$ mice, these data suggest that XPO2 may be involved in ATM-mediated apoptosis.

In addition to implications for effective DNA repair, *Atm* haploinsufficiency may impact ovarian aging. BRCA1 mutation carriers undergo earlier menopause, suggestive of decreased ovarian reserve [121-124]. Similarly, DNA repair gene and protein activity in the ovary decreases with age [124, 125] illustrating the relationship between DNA DSB repair and ovarian aging. The *Atm*$^{+/-}$ females spent ~25% more time in the diestrus phase of the estrous cycle. Further, the reduced follicle numbers in the absence of PM exposure supports our observation of altered estrous cycles in the *Atm*$^{+/-}$ females, indicative of POF. When reproductive aging begins, the disorganization of the estrous cycle is characterized by cycles with varying lengths and declining fertility [126]. These results suggest that carriers of the *Atm* mutation may experience earlier menopause onset in addition to subfecundity.

In conclusion, these findings identify proteins involved in the ovarian response to the genotoxicant, PM. This study also underscores the importance of ATM protein to the ability of the ovary to mount the OPR to a genotoxicant. Further, proteins that may be involved in an ATM-independent ovarian response to a DNA damaging insult have been identified, which could lead to therapeutic targets to improve fertility in females who undergo anti-cancer treatments. In addition, the data herein provides strong support for a role of ATM in regulating how follicles that retain DNA damage are shunted towards an atretic demise, further highlighting the importance of ATM in multiple roles in coordination of the OPR. These findings are of importance to women undergoing cancer treatment for whom lessening the ovotoxicity side effects are of paramount importance.

The information reported herein also has value for $Atm^{+/-}$ human carriers and women who experience idiopathic POF. Finally, these data add to the basic understanding of the OPR that is mounted to maintain germline integrity and ovarian function.

References

1. Savitsky K, Bar-Shira A, Gilad S, Rotman G, Ziv Y, Vanagaite L, Tagle DA, Smith S, Uziel T, Sfez S, Ashkenazi M, Pecker I, et al. A single ataxia telangiectasia gene with a product similar to PI-3 kinase. Science 1995; 268:1749-1753.
2. Rogakou EP, Boon C, Redon C, Bonner WM. Megabase chromatin domains involved in DNA double-strand breaks in vivo. J Cell Biol 1999; 146:905-916.
3. Lou Z, Minter-Dykhouse K, Franco S, Gostissa M, Rivera MA, Celeste A, Manis JP, van Deursen J, Nussenzweig A, Paull TT, Alt FW, Chen J. MDC1 maintains genomic stability by participating in the amplification of ATM-dependent DNA damage signals. Mol Cell 2006; 21:187-200.
4. Gatei M, Scott SP, Filippovitch I, Soronika N, Lavin MF, Weber B, Khanna KK. Role for ATM in DNA damage-induced phosphorylation of BRCA1. Cancer Res 2000; 60:3299-3304.
5. Falck J, Mailand N, Syljuasen RG, Bartek J, Lukas J. The ATM-Chk2-Cdc25A checkpoint pathway guards against radioresistant DNA synthesis. Nature 2001; 410:842-847.
6. Meulmeester E, Pereg Y, Shiloh Y, Jochemsen AG. ATM-mediated phosphorylations inhibit Mdmx/Mdm2 stabilization by HAUSP in favor of p53 activation. Cell Cycle 2005; 4:1166-1170.
7. Liu Q, Turner KM, Alfred Yung WK, Chen K, Zhang W. Role of AKT signaling in DNA repair and clinical response to cancer therapy. Neuro Oncol 2014; 16:1313-1323.
8. Abdel-Fatah TM, Arora A, Moseley P, Coveney C, Perry C, Johnson K, Kent C, Ball G, Chan S, Madhusudan S. ATM, ATR and DNA-PKcs expressions correlate to adverse clinical outcomes in epithelial ovarian cancers. BBA Clin 2014; 2:10-17.
9. Boder E, Sedgwick RP. Ataxia-telangiectasia; a familial syndrome of progressive cerebellar ataxia, oculocutaneous telangiectasia and frequent pulmonary infection. Pediatrics 1958; 21:526-554.
10. Fortuno C, Labarta E. Genetics of primary ovarian insufficiency: a review. J Assist Reprod Genet 2014; 31:1573-1585.
11. Barlow C, Liyanage M, Moens PB, Tarsounas M, Nagashima K, Brown K, Rottinghaus S, Jackson SP, Tagle D, Ried T, Wynshaw-Boris A. Atm deficiency results in severe meiotic disruption as early as leptonema of prophase I. Development 1998; 125:4007-4017.

12. Su Y, Swift M. Mortality rates among carriers of ataxia-telangiectasia mutant alleles. Ann Intern Med 2000; 133:770-778.
13. Swift M, Morrell D, Massey RB, Chase CL. Incidence of cancer in 161 families affected by ataxia-telangiectasia. N Engl J Med 1991; 325:1831-1836.
14. Swift M, Reitnauer PJ, Morrell D, Chase CL. Breast and other cancers in families with ataxia-telangiectasia. N Engl J Med 1987; 316:1289-1294.
15. Inskip HM, Kinlen LJ, Taylor AM, Woods CG, Arlett CF. Risk of breast cancer and other cancers in heterozygotes for ataxia-telangiectasia. Br J Cancer 1999; 79:1304-1307.
16. Janin N, Andrieu N, Ossian K, Lauge A, Croquette MF, Griscelli C, Debre M, Bressac-de-Paillerets B, Aurias A, Stoppa-Lyonnet D. Breast cancer risk in ataxia telangiectasia (AT) heterozygotes: haplotype study in French AT families. Br J Cancer 1999; 80:1042-1045.
17. Olsen JH, Hahnemann JM, Borresen-Dale AL, Brondum-Nielsen K, Hammarstrom L, Kleinerman R, Kaariainen H, Lonnqvist T, Sankila R, Seersholm N, Tretli S, Yuen J, et al. Cancer in patients with ataxia-telangiectasia and in their relatives in the nordic countries. J Natl Cancer Inst 2001; 93:121-127.
18. Colvin OM. An overview of cyclophosphamide development and clinical applications. Curr Pharm Des 1999; 5:555-560.
19. Henderson L, Masson P, Craig JC, Flanc RS, Roberts MA, Strippoli GF, Webster AC. Treatment for lupus nephritis. Cochrane Database Syst Rev 2012; 12:Cd002922.
20. Suarez-Almazor ME, Belseck E, Shea B, Wells G, Tugwell P. Cyclophosphamide for rheumatoid arthritis. Cochrane Database Syst Rev 2000:Cd001157.
21. Plowchalk DR, Mattison DR. Phosphoramide mustard is responsible for the ovarian toxicity of cyclophosphamide. Toxicol Appl Pharmacol 1991; 107:472-481.
22. Desmeules P, Devine PJ. Characterizing the ovotoxicity of cyclophosphamide metabolites on cultured mouse ovaries. Toxicol Sci 2006; 90:500-509.
23. Surya YA, Rosenfeld JM, Hillcoat BL. Cross-linking of DNA in L1210 cells and nuclei treated with cyclophosphamide and phosphoramide mustard. Cancer Treat Rep 1978; 62:23-29.
24. Petrillo SK, Desmeules P, Truong TQ, Devine PJ. Detection of DNA damage in oocytes of small ovarian follicles following phosphoramide mustard exposures of cultured rodent ovaries in vitro. Toxicol Appl Pharmacol 2011; 253:94-102.
25. Ganesan S, Keating AF. Phosphoramide mustard exposure induces DNA adduct formation and the DNA damage repair response in rat ovarian granulosa cells. Toxicol Appl Pharmacol 2015; 282:252-258.
26. Ganesan S, Nteeba J, Madden JA, Keating AF. Obesity alters phosphoramide mustard-induced ovarian DNA repair in mice. Biol Reprod 2017; 96:491-501.
27. Madden JA, Keating AF. Ovarian xenobiotic biotransformation enzymes are altered during phosphoramide mustard-induced ovotoxicity. Toxicol Sci 2014; 141:441-452.
28. Ataya KM, Pydyn EF, Ramahi-Ataya AJ. The effect of "activated" cyclophosphamide on human and rat ovarian granulosa cells in vitro. Reprod Toxicol 1990; 4:121-125.

29. Meirow D. Reproduction post-chemotherapy in young cancer patients. Mol Cell Endocrinol 2000; 169:123-131.
30. Rengasamy P. Congenital Malformations Attributed to Prenatal Exposure to Cyclophosphamide. Anticancer Agents Med Chem 2017; 17:1211-1227.
31. Ganesan S, Keating AF. The ovarian DNA damage repair response is induced prior to phosphoramide mustard-induced follicle depletion, and ataxia telangiectasia mutated inhibition prevents PM-induced follicle depletion. Toxicol Appl Pharmacol 2016; 292:65-74.
32. Byers SL, Wiles MV, Dunn SL, Taft RA. Mouse estrous cycle identification tool and images. PLoS One 2012; 7:e35538.
33. Pedersen T, Peters H. Proposal for a classification of oocytes and follicles in the mouse ovary. J Reprod Fertil 1968; 17:555-557.
34. Chong J, Soufan O, Li C, Caraus I, Li S, Bourque G, Wishart DS, Xia J. MetaboAnalyst 4.0: towards more transparent and integrative metabolomics analysis. Nucleic Acids Res 2018; 46:W486-w494.
35. Huang da W, Sherman BT, Lempicki RA. Systematic and integrative analysis of large gene lists using DAVID bioinformatics resources. Nat Protoc 2009; 4:44-57.
36. Uziel T, Lerenthal Y, Moyal L, Andegeko Y, Mittelman L, Shiloh Y. Requirement of the MRN complex for ATM activation by DNA damage. Embo j 2003; 22:5612-5621.
37. Bakkenist CJ, Kastan MB. DNA damage activates ATM through intermolecular autophosphorylation and dimer dissociation. Nature 2003; 421:499-506.
38. Kozlov S, Gueven N, Keating K, Ramsay J, Lavin MF. ATP activates ataxia-telangiectasia mutated (ATM) in vitro. Importance of autophosphorylation. J Biol Chem 2003; 278:9309-9317.
39. Matsuoka S, Ballif BA, Smogorzewska A, McDonald ER, 3rd, Hurov KE, Luo J, Bakalarski CE, Zhao Z, Solimini N, Lerenthal Y, Shiloh Y, Gygi SP, et al. ATM and ATR substrate analysis reveals extensive protein networks responsive to DNA damage. Science 2007; 316:1160-1166.
40. Perez GI, Tao XJ, Tilly JL. Fragmentation and death (a.k.a. apoptosis) of ovulated oocytes. Mol Hum Reprod 1999; 5:414-420.
41. Kerr JB, Hutt KJ, Cook M, Speed TP, Strasser A, Findlay JK, Scott CL. Cisplatin-induced primordial follicle oocyte killing and loss of fertility are not prevented by imatinib. Nat Med 2012; 18:1170-1172; author reply 1172-1174.
42. Kim SY, Nair DM, Romero M, Serna VA, Koleske AJ, Woodruff TK, Kurita T. Transient inhibition of p53 homologs protects ovarian function from two distinct apoptotic pathways triggered by anticancer therapies. Cell Death Differ 2019; 26:502-515.
43. Luan Y, Edmonds ME, Woodruff TK, Kim SY. Inhibitors of apoptosis protect the ovarian reserve from cyclophosphamide. J Endocrinol 2019; 240:243-256.
44. Keating AF, C JM, Sen N, Sipes IG, Hoyer PB. Effect of phosphatidylinositol-3 kinase inhibition on ovotoxicity caused by 4-vinylcyclohexene diepoxide and 7, 12-dimethylbenz[a]anthracene in neonatal rat ovaries. Toxicol Appl Pharmacol 2009; 241:127-134.
45. Kalich-Philosoph L, Roness H, Carmely A, Fishel-Bartal M, Ligumsky H, Paglin S, Wolf I, Kanety H, Sredni B, Meirow D. Cyclophosphamide triggers follicle

activation and "burnout"; AS101 prevents follicle loss and preserves fertility. Sci Transl Med 2013; 5:185ra162.

46. Chang EM, Lim E, Yoon S, Jeong K, Bae S, Lee DR, Yoon TK, Choi Y, Lee WS. Cisplatin Induces Overactivation of the Dormant Primordial Follicle through PTEN/AKT/FOXO3a Pathway which Leads to Loss of Ovarian Reserve in Mice. PLoS One 2015; 10:e0144245.
47. Morgan S, Lopes F, Gourley C, Anderson RA, Spears N. Cisplatin and doxorubicin induce distinct mechanisms of ovarian follicle loss; imatinib provides selective protection only against cisplatin. PLoS One 2013; 8:e70117.
48. Madden JA, Thomas PQ, Keating AF. Phosphoramide mustard induces autophagy markers and mTOR inhibition prevents follicle loss due to phosphoramide mustard exposure. Reprod Toxicol 2017; 67:65-78.
49. Barlow C, Hirotsune S, Paylor R, Liyanage M, Eckhaus M, Collins F, Shiloh Y, Crawley JN, Ried T, Tagle D, Wynshaw-Boris A. Atm-deficient mice: a paradigm of ataxia telangiectasia. Cell 1996; 86:159-171.
50. Paull TT, Rogakou EP, Yamazaki V, Kirchgessner CU, Gellert M, Bonner WM. A critical role for histone H2AX in recruitment of repair factors to nuclear foci after DNA damage. Curr Biol 2000; 10:886-895.
51. Stucki M, Jackson SP. gammaH2AX and MDC1: anchoring the DNA-damage-response machinery to broken chromosomes. DNA Repair (Amst) 2006; 5:534-543.
52. Kobayashi J, Tauchi H, Sakamoto S, Nakamura A, Morishima K, Matsuura S, Kobayashi T, Tamai K, Tanimoto K, Komatsu K. NBS1 localizes to gamma-H2AX foci through interaction with the FHA/BRCT domain. Curr Biol 2002; 12:1846-1851.
53. Ward IM, Minn K, Jorda KG, Chen J. Accumulation of checkpoint protein 53BP1 at DNA breaks involves its binding to phosphorylated histone H2AX. J Biol Chem 2003; 278:19579-19582.
54. Kouzarides T. Chromatin modifications and their function. Cell 2007; 128:693-705.
55. Fernandez-Capetillo O, Lee A, Nussenzweig M, Nussenzweig A. H2AX: the histone guardian of the genome. DNA Repair (Amst) 2004; 3:959-967.
56. Monni O, Knuutila S. 11q deletions in hematological malignancies. Leuk Lymphoma 2001; 40:259-266.
57. Scully R, Chen J, Plug A, Xiao Y, Weaver D, Feunteun J, Ashley T, Livingston DM. Association of BRCA1 with Rad51 in mitotic and meiotic cells. Cell 1997; 88:265-275.
58. Moynahan ME, Chiu JW, Koller BH, Jasin M. Brca1 controls homology-directed DNA repair. Mol Cell 1999; 4:511-518.
59. Wang H, Zeng ZC, Bui TA, DiBiase SJ, Qin W, Xia F, Powell SN, Iliakis G. Nonhomologous end-joining of ionizing radiation-induced DNA double-stranded breaks in human tumor cells deficient in BRCA1 or BRCA2. Cancer Res 2001; 61:270-277.
60. Baldeyron C, Jacquemin E, Smith J, Jacquemont C, De Oliveira I, Gad S, Feunteun J, Stoppa-Lyonnet D, Papadopoulo D. A single mutated BRCA1 allele leads to

impaired fidelity of double strand break end-joining. Oncogene 2002; 21:1401-1410.

61. Robson M, Gilewski T, Haas B, Levin D, Borgen P, Rajan P, Hirschaut Y, Pressman P, Rosen PP, Lesser ML, Norton L, Offit K. BRCA-associated breast cancer in young women. J Clin Oncol 1998; 16:1642-1649.
62. Matikainen T, Perez GI, Zheng TS, Kluzak TR, Rueda BR, Flavell RA, Tilly JL. Caspase-3 gene knockout defines cell lineage specificity for programmed cell death signaling in the ovary. Endocrinology 2001; 142:2468-2480.
63. Carambula SF, Matikainen T, Lynch MP, Flavell RA, Goncalves PB, Tilly JL, Rueda BR. Caspase-3 is a pivotal mediator of apoptosis during regression of the ovarian corpus luteum. Endocrinology 2002; 143:1495-1501.
64. Nguyen QN, Zerafa N, Liew SH, Morgan FH, Strasser A, Scott CL, Findlay JK, Hickey M, Hutt KJ. Loss of PUMA protects the ovarian reserve during DNA-damaging chemotherapy and preserves fertility. Cell Death Dis 2018; 9:618.
65. Igosheva N, Abramov AY, Poston L, Eckert JJ, Fleming TP, Duchen MR, McConnell J. Maternal diet-induced obesity alters mitochondrial activity and redox status in mouse oocytes and zygotes. PLoS One 2010; 5:e10074.
66. Patel AY, McDonald TM, Spears LD, Ching JK, Fisher JS. Ataxia telangiectasia mutated influences cytochrome c oxidase activity. Biochem Biophys Res Commun 2011; 405:599-603.
67. Ambrose M, Goldstine JV, Gatti RA. Intrinsic mitochondrial dysfunction in ATM-deficient lymphoblastoid cells. Hum Mol Genet 2007; 16:2154-2164.
68. Mercer JR, Cheng KK, Figg N, Gorenne I, Mahmoudi M, Griffin J, Vidal-Puig A, Logan A, Murphy MP, Bennett M. DNA damage links mitochondrial dysfunction to atherosclerosis and the metabolic syndrome. Circ Res 2010; 107:1021-1031.
69. Li YL, Ye F, Hu Y, Lu WG, Xie X. Identification of suitable reference genes for gene expression studies of human serous ovarian cancer by real-time polymerase chain reaction. Anal Biochem 2009; 394:110-116.
70. Klinken SP, Stevenson PM. Changes in enzyme activities during the artificially stimulated transition from follicular to luteal cell types in rat ovary. Eur J Biochem 1977; 81:327-332.
71. Tainaka H, Takahashi H, Umezawa M, Tanaka H, Nishimune Y, Oshio S, Takeda K. Evaluation of the testicular toxicity of prenatal exposure to bisphenol A based on microarray analysis combined with MeSH annotation. J Toxicol Sci 2012; 37:539-548.
72. Irving-Rodgers HF, Harland ML, Sullivan TR, Rodgers RJ. Studies of granulosa cell maturation in dominant and subordinate bovine follicles: novel extracellular matrix focimatrix is co-ordinately regulated with cholesterol side-chain cleavage CYP11A1. Reproduction 2009; 137:825-834.
73. Okayama S, Kopelovich L, Balmus G, Weiss RS, Herbert BS, Dannenberg AJ, Subbaramaiah K. p53 protein regulates Hsp90 ATPase activity and thereby Wnt signaling by modulating Aha1 expression. J Biol Chem 2014; 289:6513-6525.
74. Mukaigasa K, Tsujita T, Nguyen VT, Li L, Yagi H, Fuse Y, Nakajima-Takagi Y, Kato K, Yamamoto M, Kobayashi M. Nrf2 activation attenuates genetic endoplasmic reticulum stress induced by a mutation in the phosphomannomutase 2 gene in zebrafish. Proc Natl Acad Sci U S A 2018; 115:2758-2763.

75. Bortot B, Cosentini D, Faletra F, Biffi S, De Martino E, Carrozzi M, Severini GM. PMM2-CDG: phenotype and genotype in four affected family members. Gene 2013; 531:506-509.
76. Horikawa M, Kirkman NJ, Mayo KE, Mulders SM, Zhou J, Bondy CA, Hsu SY, King GJ, Adashi EY. The mouse germ-cell-specific leucine-rich repeat protein NALP14: a member of the NACHT nucleoside triphosphatase family. Biol Reprod 2005; 72:879-889.
77. Westerveld GH, Korver CM, van Pelt AM, Leschot NJ, van der Veen F, Repping S, Lombardi MP. Mutations in the testis-specific NALP14 gene in men suffering from spermatogenic failure. Hum Reprod 2006; 21:3178-3184.
78. Lam le T, Bohm SV, Roberts RG, Morris GE. Nesprin-2 epsilon: a novel nesprin isoform expressed in human ovary and Ntera-2 cells. Biochem Biophys Res Commun 2011; 412:291-295.
79. Gob E, Schmitt J, Benavente R, Alsheimer M. Mammalian sperm head formation involves different polarization of two novel LINC complexes. PLoS One 2010; 5:e12072.
80. Ketema M, Kreft M, Secades P, Janssen H, Sonnenberg A. Nesprin-3 connects plectin and vimentin to the nuclear envelope of Sertoli cells but is not required for Sertoli cell function in spermatogenesis. Mol Biol Cell 2013; 24:2454-2466.
81. Benkhalifa M, Montjean D, Cohen-Bacrie P, Menezo Y. Imprinting: RNA expression for homocysteine recycling in the human oocyte. Fertil Steril 2010; 93:1585-1590.
82. Dassouli A, Darne C, Fabre S, Manin M, Veyssiere G, Jean CI. Vas deferens epithelial cells in subculture: a model to study androgen regulation of gene expression. J Mol Endocrinol 1995; 15:129-141.
83. Diaz ME, Mayoral JG, Priestap H, Nouzova M, Rivera-Perez C, Noriega FG. Characterization of an isopentenyl diphosphate isomerase involved in the juvenile hormone pathway in Aedes aegypti. Insect Biochem Mol Biol 2012; 42:751-757.
84. Foti RS, Dalvie DK. Cytochrome P450 and Non-Cytochrome P450 Oxidative Metabolism: Contributions to the Pharmacokinetics, Safety, and Efficacy of Xenobiotics. Drug Metab Dispos 2016; 44:1229-1245.
85. Debeljak N, Fink M, Rozman D. Many facets of mammalian lanosterol 14alpha-demethylase from the evolutionarily conserved cytochrome P450 family CYP51. Arch Biochem Biophys 2003; 409:159-171.
86. Rajareddy S, Reddy P, Du C, Liu L, Jagarlamudi K, Tang W, Shen Y, Berthet C, Peng SL, Kaldis P, Liu K. p27kip1 (cyclin-dependent kinase inhibitor 1B) controls ovarian development by suppressing follicle endowment and activation and promoting follicle atresia in mice. Mol Endocrinol 2007; 21:2189-2202.
87. Losada A, Yokochi T, Hirano T. Functional contribution of Pds5 to cohesin-mediated cohesion in human cells and Xenopus egg extracts. J Cell Sci 2005; 118:2133-2141.
88. Geck P, Maffini MV, Szelei J, Sonnenschein C, Soto AM. Androgen-induced proliferative quiescence in prostate cancer cells: the role of AS3 as its mediator. Proc Natl Acad Sci U S A 2000; 97:10185-10190.

89. Horoszewicz JS, Leong SS, Kawinski E, Karr JP, Rosenthal H, Chu TM, Mirand EA, Murphy GP. LNCaP model of human prostatic carcinoma. Cancer Res 1983; 43:1809-1818.
90. Ott HW, Lindner H, Sarg B, Mueller-Holzner E, Abendstein B, Bergant A, Fessler S, Schwaerzler P, Zeimet A, Marth C, Illmensee K. Calgranulins in cystic fluid and serum from patients with ovarian carcinomas. Cancer Res 2003; 63:7507-7514.
91. Cordin O, Banroques J, Tanner NK, Linder P. The DEAD-box protein family of RNA helicases. Gene 2006; 367:17-37.
92. Sheng Y, Tsai-Morris CH, Gutti R, Maeda Y, Dufau ML. Gonadotropin-regulated testicular RNA helicase (GRTH/Ddx25) is a transport protein involved in gene-specific mRNA export and protein translation during spermatogenesis. J Biol Chem 2006; 281:35048-35056.
93. Thomas FH, Wilson H, Silvestri A, Fraser HM. Thrombospondin-1 expression is increased during follicular atresia in the primate ovary. Endocrinology 2008; 149:185-192.
94. Greenaway J, Lawler J, Moorehead R, Bornstein P, Lamarre J, Petrik J. Thrombospondin-1 inhibits VEGF levels in the ovary directly by binding and internalization via the low density lipoprotein receptor-related protein-1 (LRP-1). J Cell Physiol 2007; 210:807-818.
95. Kidane D, Sakkas D, Nottoli T, McGrath J, Sweasy JB. Kinesin 5B (KIF5B) is required for progression through female meiosis and proper chromosomal segregation in mitotic cells. PLoS One 2013; 8:e58585.
96. Tian X, Pascal G, Monget P. Evolution and functional divergence of NLRP genes in mammalian reproductive systems. BMC Evol Biol 2009; 9:202.
97. Wang S, Kou Z, Jing Z, Zhang Y, Guo X, Dong M, Wilmut I, Gao S. Proteome of mouse oocytes at different developmental stages. Proc Natl Acad Sci U S A 2010; 107:17639-17644.
98. Yang-Hartwich Y, Soteras MG, Lin ZP, Holmberg J, Sumi N, Craveiro V, Liang M, Romanoff E, Bingham J, Garofalo F, Alvero A, Mor G. p53 protein aggregation promotes platinum resistance in ovarian cancer. Oncogene 2015; 34:3605-3616.
99. Yamane T, Asanoma K, Kobayashi H, Liu G, Yagi H, Ohgami T, Ichinoe A, Sonoda K, Wake N, Kato K. Identification of the Critical Site of Calponin 1 for Suppression of Ovarian Cancer Properties. Anticancer Res 2015; 35:5993-5999.
100. Zhu Q, Emanuele NV, Van Thiel DH. Calponin is expressed by Sertoli cells within rat testes and is associated with actin-enriched cytoskeleton. Cell Tissue Res 2004; 316:243-253.
101. Rebourcet D, O'Shaughnessy PJ, Pitetti JL, Monteiro A, O'Hara L, Milne L, Tsai YT, Cruickshanks L, Riethmacher D, Guillou F, Mitchell RT, van't Hof R, et al. Sertoli cells control peritubular myoid cell fate and support adult Leydig cell development in the prepubertal testis. Development 2014; 141:2139-2149.
102. Bruney L, Liu Y, Grisoli A, Ravosa MJ, Stack MS. Integrin-linked kinase activity modulates the pro-metastatic behavior of ovarian cancer cells. Oncotarget 2016; 7:21968-21981.
103. Hennebold JD, Tanaka M, Saito J, Hanson BR, Adashi EY. Ovary-selective genes I: the generation and characterization of an ovary-selective complementary deoxyribonucleic acid library. Endocrinology 2000; 141:2725-2734.

104. Matsumoto T, Minegishi K, Ishimoto H, Tanaka M, Hennebold JD, Teranishi T, Hattori Y, Furuya M, Higuchi T, Asai S, Kim SH, Miyakoshi K, et al. Expression of ovary-specific acidic protein in steroidogenic tissues: a possible role in steroidogenesis. Endocrinology 2009; 150:3353-3359.
105. Zhou M, Wang Y, Qi S, Wang J, Zhang S. The expression of a mitochondria-localized glutamic acid-rich protein (MGARP/OSAP) is under the regulation of the HPG axis. Endocrinology 2011; 152:2311-2320.
106. Billard LM, Magdinier F, Lenoir GM, Frappart L, Dante R. MeCP2 and MBD2 expression during normal and pathological growth of the human mammary gland. Oncogene 2002; 21:2704-2712.
107. Feng H, Gu ZY, Li Q, Liu QH, Yang XY, Zhang JJ. Identification of significant genes with poor prognosis in ovarian cancer via bioinformatical analysis. J Ovarian Res 2019; 12:35.
108. Gan Y, He L, Yao K, Tan J, Zeng Q, Dai Y, Liu J, Tang Y. Knockdown of HMGN5 increases the chemosensitivity of human urothelial bladder cancer cells to cisplatin by targeting PI3K/Akt signaling. Oncol Lett 2017; 14:6463-6470.
109. Weng M, Song F, Chen J, Wu J, Qin J, Jin T, Xu J. The high-mobility group nucleosome-binding domain 5 is highly expressed in breast cancer and promotes the proliferation and invasion of breast cancer cells. Tumour Biol 2015; 36:959-966.
110. Wang JW ZL, Yang XZ, Ai JK, Xin DQ, Na YQ, Guo YL. . The NSBP1 expression is up-regulated in prostate cancer cell. Basic Med Sci Clin. 2004; 24:393-397.
111. Jerkovic L, Voegele AF, Chwatal S, Kronenberg F, Radcliffe CM, Wormald MR, Lobentanz EM, Ezeh B, Eller P, Dejori N, Dieplinger B, Lottspeich F, et al. Afamin is a novel human vitamin E-binding glycoprotein characterization and in vitro expression. J Proteome Res 2005; 4:889-899.
112. Dieplinger B, Egger M, Gabriel C, Poelz W, Morandell E, Seeber B, Kronenberg F, Haltmayer M, Mueller T, Dieplinger H. Analytical characterization and clinical evaluation of an enzyme-linked immunosorbent assay for measurement of afamin in human plasma. Clin Chim Acta 2013; 425:236-241.
113. Koninger A, Edimiris P, Koch L, Enekwe A, Lamina C, Kasimir-Bauer S, Kimmig R, Dieplinger H. Serum concentrations of afamin are elevated in patients with polycystic ovary syndrome. Endocr Connect 2014; 3:120-126.
114. Silva JM, Ezhkova E, Silva J, Heart S, Castillo M, Campos Y, Castro V, Bonilla F, Cordon-Cardo C, Muthuswamy SK, Powers S, Fuchs E, et al. Cyfip1 is a putative invasion suppressor in epithelial cancers. Cell 2009; 137:1047-1061.
115. Brinkmann U, Brinkmann E, Gallo M, Scherf U, Pastan I. Role of CAS, a human homologue to the yeast chromosome segregation gene CSE1, in toxin and tumor necrosis factor mediated apoptosis. Biochemistry 1996; 35:6891-6899.
116. Tanner MM, Tirkkonen M, Kallioniemi A, Collins C, Stokke T, Karhu R, Kowbel D, Shadravan F, Hintz M, Kuo WL, et al. Increased copy number at 20q13 in breast cancer: defining the critical region and exclusion of candidate genes. Cancer Res 1994; 54:4257-4260.
117. Isola JJ, Kallioniemi OP, Chu LW, Fuqua SA, Hilsenbeck SG, Osborne CK, Waldman FM. Genetic aberrations detected by comparative genomic hybridization predict outcome in node-negative breast cancer. Am J Pathol 1995; 147:905-911.

118. Brinkmann U, Gallo M, Polymeropoulos MH, Pastan I. The human CAS (cellular apoptosis susceptibility) gene mapping on chromosome 20q13 is amplified in BT474 breast cancer cells and part of aberrant chromosomes in breast and colon cancer cell lines. Genome Res 1996; 6:187-194.
119. Tirkkonen M, Johannsson O, Agnarsson BA, Olsson H, Ingvarsson S, Karhu R, Tanner M, Isola J, Barkardottir RB, Borg A, Kallioniemi OP. Distinct somatic genetic changes associated with tumor progression in carriers of BRCA1 and BRCA2 germ-line mutations. Cancer Res 1997; 57:1222-1227.
120. Peiro G, Diebold J, Baretton GB, Kimmig R, Lohrs U. Cellular apoptosis susceptibility gene expression in endometrial carcinoma: correlation with Bcl-2, Bax, and caspase-3 expression and outcome. Int J Gynecol Pathol 2001; 20:359-367.
121. Rzepka-Gorska I, Tarnowski B, Chudecka-Glaz A, Gorski B, Zielinska D, Toloczko-Grabarek A. Premature menopause in patients with BRCA1 gene mutation. Breast Cancer Res Treat 2006; 100:59-63.
122. Finch A, Valentini A, Greenblatt E, Lynch HT, Ghadirian P, Armel S, Neuhausen SL, Kim-Sing C, Tung N, Karlan B, Foulkes WD, Sun P, et al. Frequency of premature menopause in women who carry a BRCA1 or BRCA2 mutation. Fertil Steril 2013; 99:1724-1728.
123. Lin WT, Beattie M, Chen LM, Oktay K, Crawford SL, Gold EB, Cedars M, Rosen M. Comparison of age at natural menopause in BRCA1/2 mutation carriers with a non-clinic-based sample of women in northern California. Cancer 2013; 119:1652-1659.
124. Titus S, Li F, Stobezki R, Akula K, Unsal E, Jeong K, Dickler M, Robson M, Moy F, Goswami S, Oktay K. Impairment of BRCA1-related DNA double-strand break repair leads to ovarian aging in mice and humans. Sci Transl Med 2013; 5:172ra121.
125. Govindaraj V, Keralapura Basavaraju R, Rao AJ. Changes in the expression of DNA double strand break repair genes in primordial follicles from immature and aged rats. Reprod Biomed Online 2015; 30:303-310.
126. Lerner SP, Meredith S, Thayne WV, Butcher RL. Age-related alterations in follicular development and hormonal profiles in rats with 4-day estrous cycles. Biol Reprod 1990; 42:633-638.

Figure and Figure Legends

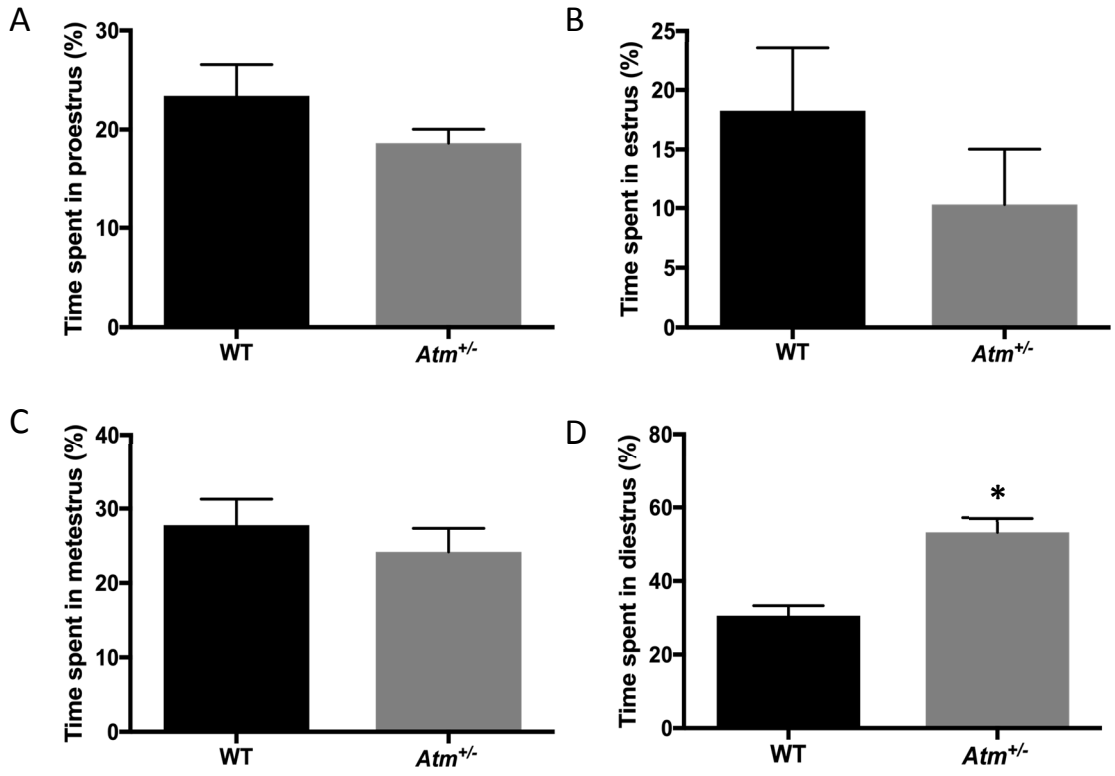

Figure 1. Impact of *Atm* deficiency on estrous cyclicity. The percentage time spent in proestrus (**A**), estrus (**B**), metestrus (**C**), diestrus (**D**) phase of the estrous cycle was calculated based upon vaginal cytological assessments in wildtype (WT) and $Atm^{+/-}$ mice. Difference from WT is indicated by * = $P < 0.05$.

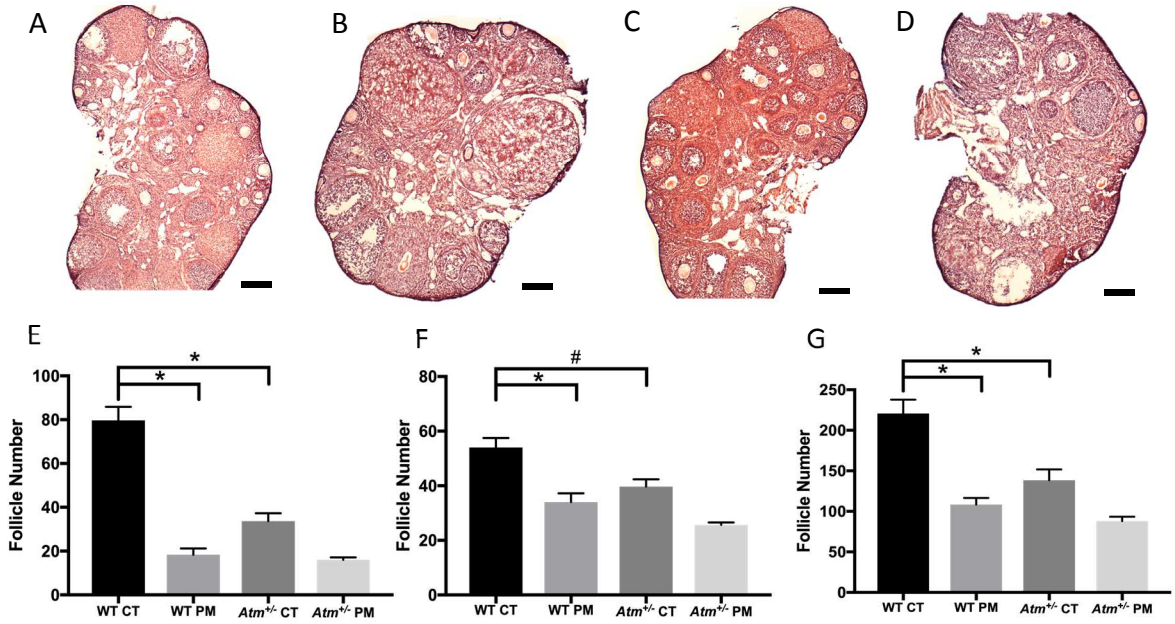

Figure 2. *Atm* deficiency reduces follicle number and alters PM-induced ovotoxicity. Representative hematoxylin and eosin stained ovarian sections from (**A**) WT CT; (**B**) WT PM; (**C**) *Atm*$^{+/-}$ CT; or (**D**) *Atm*$^{+/-}$ PM are presented; scale bar = 200 μm. Follicles were classified as (**E**) primordial; (**F**) primary; (**G**) total and counted. Bars represent mean follicle number ± SEM. Difference between treatments is indicated by the # = $P < 0.1$, * = $P < 0.05$.

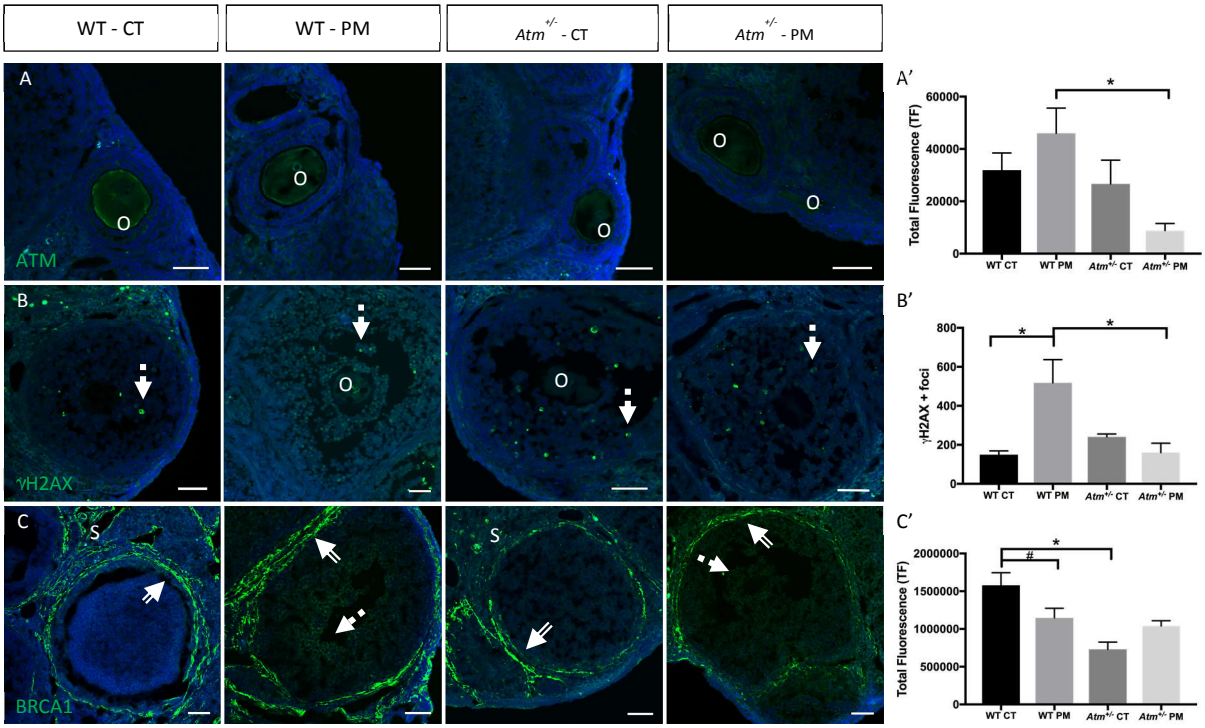

Figure 3. Effect of *Atm* deficiency and PM exposure on DNA damage proteins. Primary antibodies directed against (**A**) ATM, (**B**) γH2AX, and (**C**) BRCA1 were used to determine ovarian localization in WT CT; WT PM; *Atm*$^{+/-}$ CT; and *Atm*$^{+/-}$ PM mice. Green staining indicates the protein of interest while DNA is stained in blue; scale bar = 50 μm (20x magnification (0.5x-1x zoom). Double tailed arrow indicates theca cells; dotted tail arrow indicates granulosa cells; O indicates oocyte. Quantification of mean fluorescence intensity and/or immunopositive foci ± SEM for (**A'**) ATM; (**B'**) γH2AX; (**C'**) BRCA1. Difference between treatments is indicated by * = $P < 0.05$.

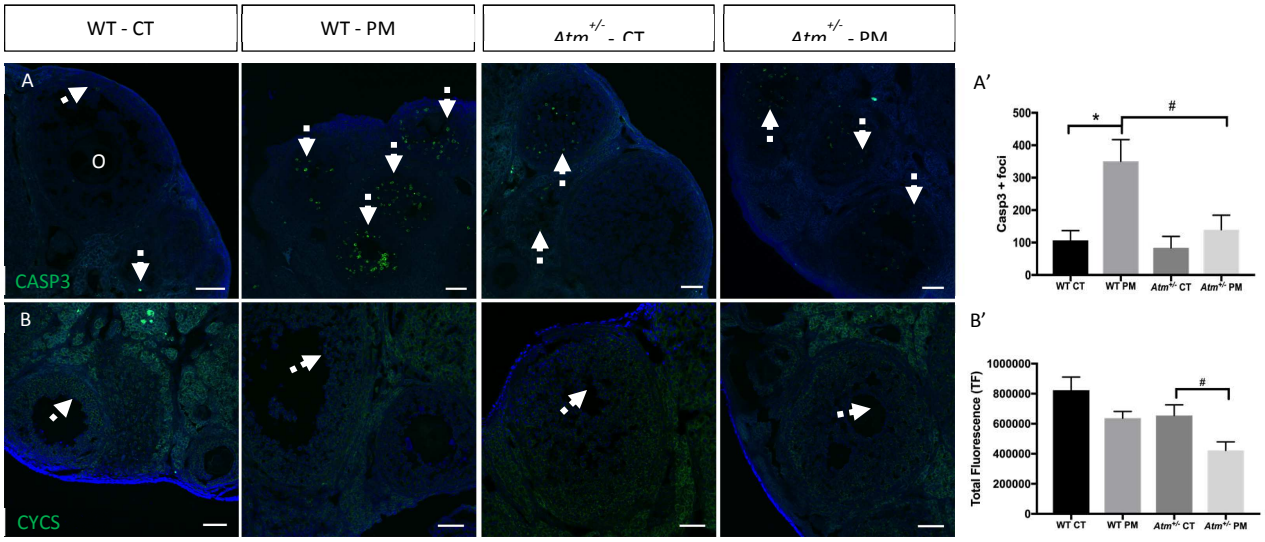

Figure 4. Effect of *Atm* deficiency and PM exposure on cell death proteins. Primary antibodies directed against (**A**) CASP3, and (**B**) CYCS were used to determine ovarian localization in WT CT; WT PM; $Atm^{+/-}$ CT; and $Atm^{+/-}$ PM. Green staining indicates the protein of interest while DNA is stained in blue; scale bar = 50 μm (20x magnification (0.5x-1x zoom). Dotted tail arrow indicates granulosa cells; O indicates oocyte. Quantification of fluorescence intensity and/or immunopositive foci ± SEM for (**A'**) CASP3; and (**B'**) CYCS. Difference between treatments is indicated by # = $P < 0.1$, * = $P < 0.05$.

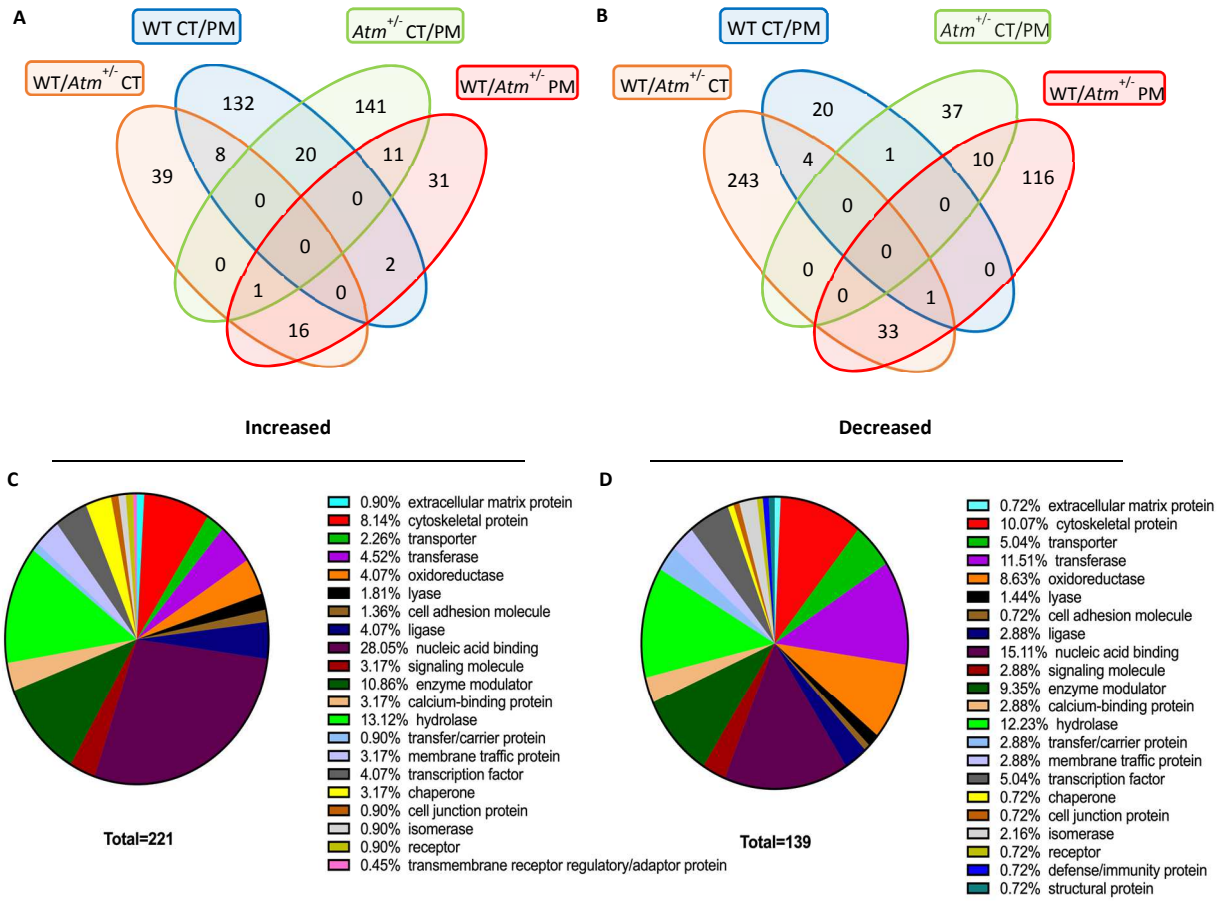

Figure 5. Global proteomic effects of *Atm* deficiency and PM exposure. The Venn diagram presents the number of ovarian proteins identified as being unique to genotype/treatment or altered in common by genotype/treatment. (**A**) Proteins identified as increased; (**B**) Proteins identified as decreased. The number in the orange oval indicates the number of proteins identified in the $Atm^{+/-}$ CT as being different from the WT CT group; the blue oval indicates the number of proteins identified in the WT PM group as being different from the WT CT; the green oval indicates the number of proteins in the $Atm^{+/-}$ PM group that differ from the $Atm^{+/-}$ CT; and the red oval indicates the number of proteins in the $Atm^{+/-}$ PM group that differ from the WT PM. Overlapping areas of the circles illustrate the number of proteins that were altered by two or more groups.

Distribution of the proteins identified in (**C**) *Atm*$^{+/-}$/WT CT and (**D**) *Atm*$^{+/-}$/WT PM according to PANTHER protein class.

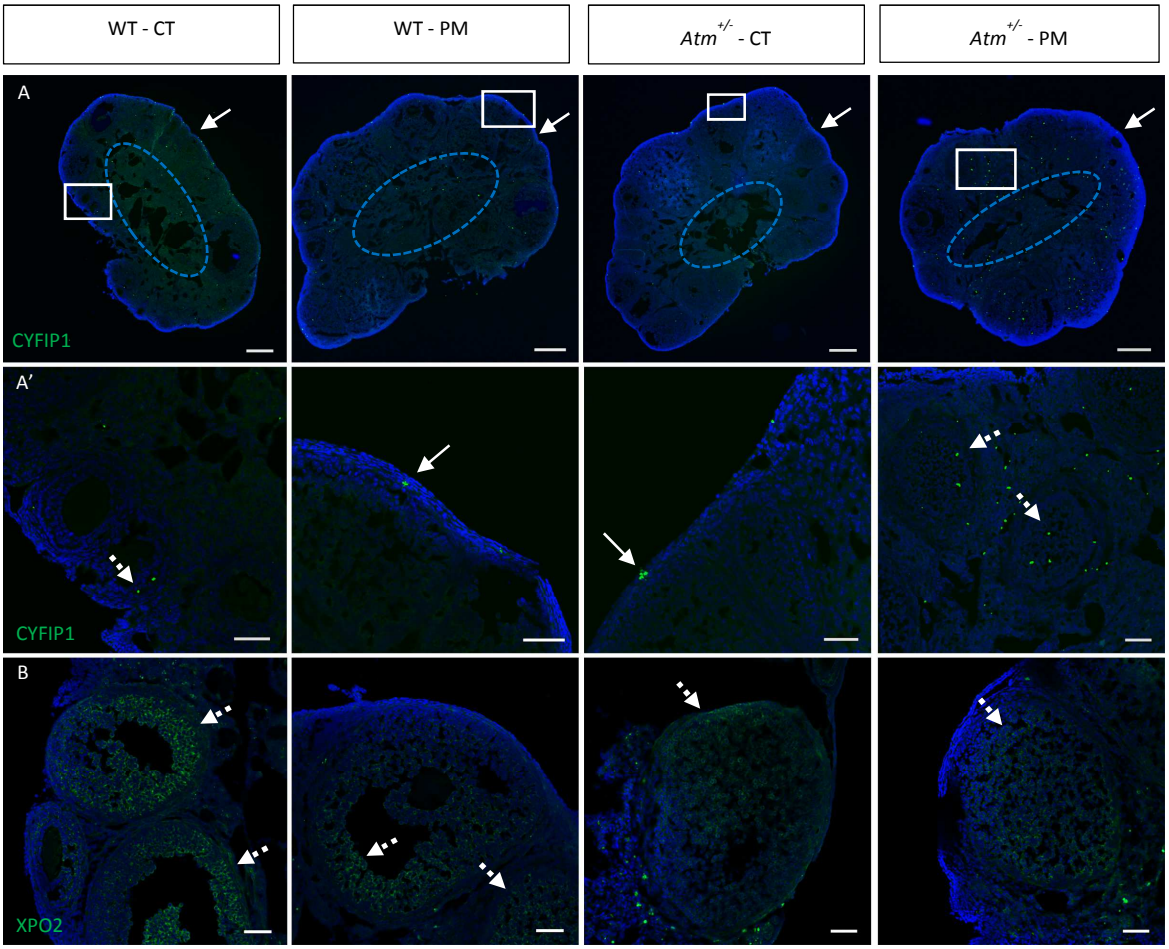

Figure 6. Ovarian localization of CYFIP1 and XPO2. The ovarian location of CYFIP1 and XPO2 proteins were assessed by immunofluorescence staining. (**A**) CYFIP1 (5x magnification); (**A'**) CYFIP1 (20x magnification); (**B**) XPO2 protein were localized in the ovary of WT CT; WT PM; *Atm*$^{+/-}$ CT; and *Atm*$^{+/-}$ PM mice. Green staining indicates the protein of interest while DNA is stained in blue; 5x magnification scale bar = 200 µm, 20x scale bar = 50 µm. Dotted tail arrow indicates granulosa cells; solid arrow indicates ovarian surface epithelium; white box indicates area imaged for 20x magnification; blue dotted circle indicates ovarian medulla.

Supplemental Figures and Legends

Supplemental Table 1: Primary and secondary antibodies used. * denotes antigen retrieval methods utilized for respective antibody.

Primary Antibody	Host	Dilution	Supplier	Code
ATM	Rabbit	1:100	abcam	ab32420
BRCA1	Rabbit	1:100	Santa Cruz	sc-642
Cleaved CASP3	Rabbit	1:100	Cell Signaling	9661
CYFIP1*	Rabbit	1:50	abcam	ab154045
CYTC*	Rabbit	1:100	Cell Signaling	4280
γH2AX	Rabbit	1:50	Cell Signaling	2577
H2AX	Rabbit	1:100	abcam	ab11175
XPO2	Rabbit	1:100	abcam	ab151546
Secondary Antibody	Host	Dilution	Supplier	Code
Rabbit IgG 488	Goat	1:500	Thermo Fisher	A11008

Supplemental Table 2: Ovarian proteins identified by LC-MS/MS to differ in *Atm*$^{+/-}$ mice after vehicle-control relative to WT after vehicle-control (log2foldchange ≥ 0.1 and *P*-value ≤ 0.05).

UniProt ID	Protein names	log2(FC)	p value
Q7TMB8	Cytoplasmic FMR1-interacting protein 1	-6.832	<0.0001
Q8BK64	Activator of 90 kDa heat shock protein ATPase homolog 1	-4.096	<0.0001
Q9Z2M7	Phosphomannomutase 2	-3.617	<0.0001
Q6B966	NACHT, LRR and PYD domains-containing protein 14	-3.508	0.001
Q6ZWQ0	Nesprin-2	-3.484	0.005
Q60715	Prolyl 4-hydroxylase subunit alpha-1	-3.350	<0.0001
Q8BFZ3	Beta-actin-like protein 2	-3.334	0.015
Q9WTI7	Unconventional myosin-Ic	-3.243	0.002
P68372	Tubulin beta-4B chain	-3.122	0.001
Q61205	Platelet-activating factor acetylhydrolase IB subunit gamma	-3.111	<0.0001
Q6A068	Cell division cycle 5-like protein	-3.020	0.010
Q62059	Versican core protein	-3.015	0.004
Q9CWU5	KH domain-containing protein 3	-2.867	0.014
Q9DBR1	5'-3' exoribonuclease 2	-2.825	0.049
P62737	Actin, aortic smooth muscle	-2.773	0.004
Q62005	Zona pellucida sperm-binding protein 1	-2.681	0.001
O08810	116 kDa U5 small nuclear ribonucleoprotein component	-2.660	0.001
O88974	Histone-lysine N-methyltransferase SETDB1	-2.657	0.029
P28654	Decorin	-2.632	<0.0001
Q8BML9	Glutamine--tRNA ligase	-2.607	0.014
Q923D5	WW domain-binding protein 11	-2.513	0.037
Q07076	Annexin A7	-2.505	0.009
P62331	ADP-ribosylation factor 6	-2.494	0.001
Q3THE2	Myosin regulatory light chain 12B	-2.399	0.001
Q9DCH4	Eukaryotic translation initiation factor 3 subunit F	-2.392	0.003
P12815	Programmed cell death protein 6	-2.389	<0.0001
Q8CHT0	Delta-1-pyrroline-5-carboxylate dehydrogenase, mitochondrial	-2.364	0.012

Supplemental Table 2: (continued)

O35643	AP-1 complex subunit beta-1	-2.364	0.016
Q99LJ6	Glutathione peroxidase 7	-2.363	<0.0001
Q9D0I9	Arginine--tRNA ligase, cytoplasmic	-2.284	0.003
Q61768	Kinesin-1 heavy chain	-2.254	0.006
Q9QXS1	Plectin	-2.179	0.002
Q9Z0H3	SWI/SNF-related matrix-associated actin-dependent regulator of chromatin subfamily B member 1	-2.130	0.038
Q8BKC5	Importin-5	-2.128	0.019
D3Z7P3	Glutaminase kidney isoform, mitochondrial	-2.098	0.013
O88492	Perilipin-4	-2.046	0.041
Q9CS42	Ribose-phosphate pyrophosphokinase 2	-2.008	0.006
Q8BGS2	BolA-like protein 2	-1.930	0.012
Q99JX4	Eukaryotic translation initiation factor 3 subunit M	-1.911	<0.0001
Q8CH18	Cell division cycle and apoptosis regulator protein 1	-1.903	0.005
Q9JLM9	Growth factor receptor-bound protein 14	-1.902	0.013
P62245	40S ribosomal protein S15a	-1.885	0.021
P67871	Casein kinase II subunit beta	-1.872	0.021
O08638	Myosin-11	-1.850	0.003
Q8QZY1	Eukaryotic translation initiation factor 3 subunit L	-1.793	0.035
Q9ESZ8	General transcription factor II-I	-1.777	0.028
P82198	Transforming growth factor-beta-induced protein ig-h3	-1.735	0.038
Q9QZE7	Translin-associated protein X	-1.724	0.001
P97310	DNA replication licensing factor MCM2	-1.724	0.001
Q8BIQ5	Cleavage stimulation factor subunit 2	-1.722	0.006
O35841	Apoptosis inhibitor 5	-1.695	0.004
P70372	ELAV-like protein 1	-1.686	<0.0001
Q9WTP7	GTP:AMP phosphotransferase AK3, mitochondrial	-1.658	0.028
D3YXK2	Scaffold attachment factor B1	-1.648	0.001
P35235	Tyrosine-protein phosphatase non-receptor type 11	-1.632	0.014
Q8K297	Procollagen galactosyltransferase 1	-1.630	0.007
Q9JJF0	Nucleosome assembly protein 1-like 5	-1.619	0.020
Q64471	Glutathione S-transferase theta-1	-1.611	0.007
P31324	cAMP-dependent protein kinase type II-beta regulatory subunit	-1.599	0.036

Supplemental Table 2: (continued)

Q9D8T2	Gasdermin-D	-1.579	0.006
P36536	GTP-binding protein SAR1a	-1.570	0.023
P27612	Phospholipase A-2-activating protein	-1.558	0.005
P13439	Uridine 5'-monophosphate synthase	-1.557	0.027
P60229	Eukaryotic translation initiation factor 3 subunit E	-1.546	0.028
Q8VH51	RNA-binding protein 39	-1.497	0.010
Q08091	Calponin-1	-1.492	0.027
P97372	Proteasome activator complex subunit 2	-1.460	<0.0001
P61222	ATP-binding cassette sub-family E member 1	-1.456	0.007
Q91W50	Cold shock domain-containing protein E1	-1.427	0.014
O70194	Eukaryotic translation initiation factor 3 subunit D	-1.423	0.012
Q9CQC6	Basic leucine zipper and W2 domain-containing protein 1	-1.418	0.015
B2RQC6	CAD protein	-1.387	0.023
O70318	Band 4.1-like protein 2	-1.387	0.048
Q80UZ0	FYVE, RhoGEF and PH domain-containing protein 5	-1.382	0.001
Q62193	Replication protein A 32 kDa subunit	-1.356	0.002
Q99JX3	Golgi reassembly-stacking protein 2	-1.345	0.013
P61082	NEDD8-conjugating enzyme Ubc12	-1.337	0.017
Q8K1J6	CCA tRNA nucleotidyltransferase 1, mitochondrial	-1.324	0.021
Q921M7	Protein FAM49B	-1.316	0.048
Q8VDP4	Cell cycle and apoptosis regulator protein 2	-1.314	0.026
Q80VD1	Protein FAM98B	-1.311	0.013
Q01768	Nucleoside diphosphate kinase B	-1.308	0.009
Q8K4Z5	Splicing factor 3A subunit 1	-1.285	0.001
Q8BWY3	Eukaryotic peptide chain release factor subunit 1	-1.270	0.016
Q62523	Zyxin	-1.250	<0.0001
Q9DCL9	Multifunctional protein ADE2R synthetase	-1.243	0.017
Q9D358	Low molecular weight phosphotyrosine protein phosphatase	-1.241	0.033
P63163	Small nuclear ribonucleoprotein-associated protein N	-1.231	0.042
Q6P4T2	U5 small nuclear ribonucleoprotein 200 kDa helicase	-1.229	0.006
Q9CXW4	60S ribosomal protein L11	-1.227	0.003
Q9CQN1	Heat shock protein 75 kDa, mitochondrial	-1.217	0.006

Supplemental Table 2: (continued)

P20918	Plasminogen	-1.209	0.004
Q8K310	Matrin-3	-1.207	0.004
P54071	Isocitrate dehydrogenase	-1.207	0.002
P48962	ADP/ATP translocase 1	-1.196	0.013
P14602	Heat shock protein beta-1	-1.185	0.001
Q3THK7	GMP synthase	-1.182	0.026
Q8BJY1	26S proteasome non-ATPase regulatory subunit 5	-1.182	<0.0001
Q9Z2I9	Succinate--CoA ligase	-1.182	0.049
Q3UPL0	Protein transport protein Sec31A	-1.173	0.041
Q68FD5	Clathrin heavy chain 1	-1.165	0.005
Q9R190	Metastasis-associated protein MTA2	-1.156	0.016
Q5FWK3	Rho GTPase-activating protein 1	-1.151	0.021
P23116	Eukaryotic translation initiation factor 3 subunit A	-1.118	0.008
P63001	Ras-related C3 botulinum toxin substrate 1	-1.116	0.036
P49718	DNA replication licensing factor MCM5	-1.089	0.010
Q8BG32	26S proteasome non-ATPase regulatory subunit 11	-1.084	0.004
Q8BTM8	Filamin-A	-1.084	0.004
P51125	Calpastatin	-1.082	0.023
Q8VCW8	Acyl-CoA synthetase family member 2, mitochondrial	-1.080	0.005
Q6PB66	Leucine-rich PPR motif-containing protein, mitochondrial	-1.078	0.009
P68181	cAMP-dependent protein kinase catalytic subunit beta	-1.075	0.003
Q9EQH2	Endoplasmic reticulum aminopeptidase 1	-1.071	0.019
P47941	Crk-like protein	-1.070	0.013
P97447	Four and a half LIM domains protein 1	-1.055	0.002
P62334	26S proteasome regulatory subunit 10B	-1.053	0.014
Q6PHZ2	Calcium/calmodulin-dependent protein kinase type II subunit delta	-1.048	0.018
P26039	Talin-1	-1.036	0.049
Q921F4	Heterogeneous nuclear ribonucleoprotein L-like	-1.031	0.007
P56546	C-terminal-binding protein 2	-1.027	0.001
P62908	40S ribosomal protein S3	-1.027	0.013
Q80X90	Filamin-B	-1.026	0.050
P70168	Importin subunit beta-1	-1.025	0.010
P35441	Thrombospondin-1	-1.025	0.049
Q8C0C7	Phenylalanine--tRNA ligase alpha subunit	-1.024	0.045

Supplemental Table 2: (continued)

Q9WVJ2	26S proteasome non-ATPase regulatory subunit 13	-1.017	0.007
O35593	26S proteasome non-ATPase regulatory subunit 14	-1.015	0.022
P97855	Ras GTPase-activating protein-binding protein 1	-1.005	0.041
Q99LD8	N(G),N(G)-dimethylarginine dimethylaminohydrolase 2	-0.998	0.020
Q99NB9	Splicing factor 3B subunit 1	-0.995	0.012
Q8BJW6	Eukaryotic translation initiation factor 2A	-0.991	0.026
O88829	Lactosylceramide alpha-2,3-sialyltransferase	-0.983	0.002
O35295	Transcriptional activator protein Pur-beta	-0.980	0.011
Q8R081	Heterogeneous nuclear ribonucleoprotein L	-0.977	0.049
Q9CY64	Biliverdin reductase A	-0.976	0.004
Q9Z1Q9	Valine--tRNA ligase	-0.973	0.013
P57780	Alpha-actinin-4	-0.969	0.001
Q8BGQ7	Alanine--tRNA ligase, cytoplasmic	-0.969	0.039
Q8CIB5	Fermitin family homolog 2	-0.968	0.016
Q9D8W5	26S proteasome non-ATPase regulatory subunit 12	-0.962	0.011
Q6DFW4	Nucleolar protein 58	-0.958	0.002
Q99MR6	Serrate RNA effector molecule homolog	-0.947	<0.0001
Q7TPV4	Myb-binding protein 1A	-0.936	0.006
Q6PE01	U5 small nuclear ribonucleoprotein 40 kDa protein	-0.926	0.004
P62500	TSC22 domain family protein 1	-0.915	0.029
Q9DBG3	AP-2 complex subunit beta	-0.914	0.047
Q9D8N0	Elongation factor 1-gamma	-0.914	0.030
O35286	Pre-mRNA-splicing factor ATP-dependent RNA helicase DHX15	-0.905	0.048
Q9CXY6	Interleukin enhancer-binding factor 2	-0.902	0.001
Q00PI9	Heterogeneous nuclear ribonucleoprotein U-like protein 2	-0.902	0.002
Q8R1B4	Eukaryotic translation initiation factor 3 subunit C	-0.896	0.034
O55023	Inositol monophosphatase 1	-0.894	0.038
P80313	T-complex protein 1 subunit eta	-0.887	0.021
P14869	60S acidic ribosomal protein P0	-0.885	0.007
Q61696	Heat shock 70 kDa protein 1A	-0.885	0.009
Q9CSU0	Regulation of nuclear pre-mRNA domain-containing protein 1B	-0.884	0.037
Q7TPR4	Alpha-actinin-1	-0.882	0.013

Supplemental Table 2: (continued)

Q8K0E8	Fibrinogen beta chain	-0.880	0.006
Q60749	KH domain-containing, RNA-binding, signal transduction-associated protein 1	-0.878	0.004
Q501J6	Probable ATP-dependent RNA helicase DDX17	-0.876	0.003
Q9EQH3	Vacuolar protein sorting-associated protein 35	-0.875	0.001
Q3TXS7	26S proteasome non-ATPase regulatory subunit 1	-0.864	0.029
P62242	40S ribosomal protein S8	-0.862	0.003
P51150	Ras-related protein Rab-7a	-0.860	0.031
Q61656	Probable ATP-dependent RNA helicase DDX5	-0.852	0.002
Q61584	Fragile X mental retardation syndrome-related protein 1	-0.837	0.010
P17225	Polypyrimidine tract-binding protein 1	-0.837	0.008
Q922D8	C-1-tetrahydrofolate synthase, cytoplasmic	-0.835	0.020
Q6PDQ2	Chromodomain-helicase-DNA-binding protein 4	-0.833	0.050
Q9D8S4	Oligoribonuclease, mitochondrial	-0.832	0.049
Q3UEB3	Poly(U)-binding-splicing factor PUF60	-0.832	0.046
Q99PT1	Rho GDP-dissociation inhibitor 1	-0.824	0.012
Q9JK53	Prolargin	-0.823	0.001
P61089	Ubiquitin-conjugating enzyme E2 N	-0.817	0.049
Q9JKF1	Ras GTPase-activating-like protein IQGAP1	-0.809	0.018
P31230	Aminoacyl tRNA synthase complex-interacting multifunctional protein 1	-0.804	0.015
P97311	DNA replication licensing factor MCM6	-0.802	0.040
Q9Z1X4	Interleukin enhancer-binding factor 3	-0.778	0.011
Q6ZWN5	40S ribosomal protein S9	-0.778	0.023
Q91V41	Ras-related protein Rab-14	-0.778	0.036
Q8JZQ9	Eukaryotic translation initiation factor 3 subunit B	-0.761	0.016
P62911	60S ribosomal protein L32	-0.760	0.041
Q99KP6	Pre-mRNA-processing factor 19	-0.751	0.003
P62281	40S ribosomal protein S11	-0.750	0.031
Q9D554	Splicing factor 3A subunit 3	-0.745	0.020
Q9QUI0	Transforming protein RhoA	-0.742	0.021
Q9DBR7	Protein phosphatase 1 regulatory subunit 12A	-0.735	0.014
O89079	Coatomer subunit epsilon	-0.735	0.025
P07901	Heat shock protein HSP 90-alpha	-0.734	0.006
Q6P069	Sorcin	-0.734	0.039

Supplemental Table 2: (continued)

Q8BH04	Phosphoenolpyruvate carboxykinase [GTP], mitochondrial	-0.724	0.012
Q62318	Transcription intermediary factor 1-beta	-0.722	0.015
Q8VIJ6	Splicing factor, proline- and glutamine-rich	-0.721	0.006
Q8BFR5	Elongation factor Tu, mitochondrial	-0.716	0.013
Q91VR5	ATP-dependent RNA helicase DDX1	-0.708	0.005
Q64727	Vinculin	-0.703	0.031
Q61881	DNA replication licensing factor MCM7	-0.695	0.021
Q61233	Plastin-2	-0.685	0.035
Q9WUU7	Cathepsin Z	-0.684	0.039
P46935	E3 ubiquitin-protein ligase NEDD4	-0.674	0.044
A6X935	Inter alpha-trypsin inhibitor, heavy chain 4	-0.673	0.016
P11499	Heat shock protein HSP 90-beta	-0.673	0.014
P14115	60S ribosomal protein L27a	-0.661	0.026
P25206	DNA replication licensing factor MCM3	-0.652	0.020
P51660	Peroxisomal multifunctional enzyme type 2	-0.635	0.004
Q62167	ATP-dependent RNA helicase DDX3X	-0.632	0.025
O88712	C-terminal-binding protein 1	-0.631	0.046
Q8CI94	Glycogen phosphorylase, brain form	-0.629	0.039
P60335	Poly(rC)-binding protein 1	-0.623	0.012
P62311	U6 snRNA-associated Sm-like protein LSm3	-0.623	0.033
Q921F2	TAR DNA-binding protein 43	-0.618	0.007
P80316	T-complex protein 1 subunit epsilon	-0.617	0.017
Q8VEK3	Heterogeneous nuclear ribonucleoprotein U	-0.616	0.001
Q9R0Q7	Prostaglandin E synthase 3	-0.616	0.025
P61079	Ubiquitin-conjugating enzyme E2 D3	-0.615	0.012
P25444	40S ribosomal protein S2	-0.606	0.039
Q923D2	Flavin reductase	-0.603	0.042
Q922R8	Protein disulfide-isomerase A6	-0.602	0.018
P08113	Endoplasmin	-0.599	0.041
Q9JII6	Alcohol dehydrogenase	-0.598	0.036
O35685	Nuclear migration protein nudC	-0.596	0.016
P53994	Ras-related protein Rab-2A	-0.582	0.010
P97461	40S ribosomal protein S5	-0.582	0.009
Q8R326	Paraspeckle component 1	-0.581	0.002
Q91WV0	Protein Dr1	-0.569	0.001
Q9D0E1	Heterogeneous nuclear ribonucleoprotein M	-0.566	0.008
P51410	60S ribosomal protein L9	-0.559	0.005
P62821	Ras-related protein Rab-1A	-0.552	0.009

Supplemental Table 2: (continued)

O08529	Calpain-2 catalytic subunit	-0.530	0.011
Q99JI4	26S proteasome non-ATPase regulatory subunit 6	-0.529	0.045
Q9QZ82	Cholesterol side-chain cleavage enzyme, mitochondrial	-0.514	0.029
Q61990	Poly(rC)-binding protein 2	-0.485	0.011
P35278	Ras-related protein Rab-5C	-0.485	0.030
Q9WUL7	ADP-ribosylation factor-like protein 3	-0.482	0.030
P62830	60S ribosomal protein L23	-0.452	0.039
P42669	Transcriptional activator protein Pur-alpha	-0.439	0.018
P58774	Tropomyosin beta chain	-0.424	0.028
Q99J77	Sialic acid synthase	-0.416	0.045
P62702	40S ribosomal protein S4, X isoform	-0.415	0.003
Q9R0P9	Ubiquitin carboxyl-terminal hydrolase isozyme L1	-0.398	0.023
Q9R0P5	Destrin	-0.355	0.018
P63280	SUMO-conjugating enzyme UBC9	-0.333	0.039
Q62376	U1 small nuclear ribonucleoprotein 70 kDa	-0.266	0.021
P26645	Myristoylated alanine-rich C-kinase substrate	0.380	0.032
Q9JM76	Actin-related protein 2/3 complex subunit 3	0.422	0.048
Q99PL5	Ribosome-binding protein 1	0.444	0.018
Q9JMH6	Thioredoxin reductase 1, cytoplasmic	0.492	0.047
P53996	Cellular nucleic acid-binding protein	0.537	0.024
Q9CQ45	Neudesin	0.570	0.049
Q9CRB2	H/ACA ribonucleoprotein complex subunit 2	0.591	0.002
Q8R050	Eukaryotic peptide chain release factor GTP-binding subunit ERF3A	0.596	0.032
P21619	Lamin-B2	0.680	0.049
P26350	Prothymosin alpha	0.681	0.003
Q62418	Drebrin-like protein	0.711	0.007
P61957	Small ubiquitin-related modifier 2	0.713	0.013
O70310	Glycylpeptide N-tetradecanoyltransferase 1	0.727	0.033
P26041	Moesin	0.773	0.040
Q9CR98	Protein FAM136A	0.779	0.037
Q8VE97	Serine/arginine-rich splicing factor 4	0.798	0.020
Q6P8I4	PEST proteolytic signal-containing nuclear protein	0.845	0.045
P62889	60S ribosomal protein L30	0.864	0.003
Q66JS6	Eukaryotic translation initiation factor 3 subunit J-B	0.886	0.022
P08226	Apolipoprotein E	0.926	0.013

Supplemental Table 2: (continued)

P02104	Hemoglobin subunit epsilon-Y2	0.937	0.030
P55302	Alpha-2-macroglobulin receptor-associated protein	0.945	0.001
Q9R013	Cathepsin F	1.100	0.041
Q9D3D9	ATP synthase subunit delta, mitochondrial	1.179	0.002
Q9CXS4	Centromere protein V	1.185	0.045
P11031	Activated RNA polymerase II transcriptional coactivator p15	1.193	0.015
Q9EQS3	c-Myc-binding protein	1.248	0.036
O55013	Trafficking protein particle complex subunit 3	1.310	0.006
Q920Q6	RNA-binding protein Musashi homolog 2	1.358	0.008
P99024	Tubulin beta-5 chain	1.377	0.004
P83917	Chromobox protein homolog 1	1.440	0.010
Q61009	Scavenger receptor class B member 1	1.448	0.038
Q9JLQ0	CD2-associated protein	1.448	0.007
P56391	Cytochrome c oxidase subunit 6B1	1.449	0.036
Q9D7G0	Ribose-phosphate pyrophosphokinase 1	1.455	0.031
Q9CYA0	Cysteine-rich with EGF-like domain protein 2	1.523	0.030
Q91ZW3	SWI/SNF-related matrix-associated actin-dependent regulator of chromatin subfamily A member 5	1.663	0.008
Q91VD9	NADH-ubiquinone oxidoreductase 75 kDa subunit, mitochondrial	1.712	0.027
P15532	Nucleoside diphosphate kinase A	1.733	0.010
P97927	Laminin subunit alpha-4	1.753	0.033
Q8R2Y2	Cell surface glycoprotein MUC18	1.772	0.008
P99028	Cytochrome b-c1 complex subunit 6, mitochondrial	1.781	0.002
P62880	Guanine nucleotide-binding protein G(I)/G(S)/G(T) subunit beta-2	1.866	0.018
P51881	ADP/ATP translocase 2	1.963	0.003
Q99PV0	Pre-mRNA-processing-splicing factor 8	2.019	0.001
Q9EQX4	Allograft inflammatory factor 1-like	2.034	0.026
P11276	Fibronectin	2.053	0.020
Q9Z0J0	NPC intracellular cholesterol transporter 2	2.066	0.005
Q9DBR0	A-kinase anchor protein 8	2.208	0.008
Q9Z2D6	Methyl-CpG-binding protein 2	2.230	0.041
Q8JZK9	Hydroxymethylglutaryl-CoA synthase, cytoplasmic	2.322	0.018
Q9JHW2	Omega-amidase NIT2	2.414	0.010

Supplemental Table 2: (continued)

Q62219	Transforming growth factor beta-1-induced transcript 1 protein	2.469	0.001
Q9D6J6	NADH dehydrogenase [ubiquinone] flavoprotein 2, mitochondrial	2.480	0.006
P58044	Isopentenyl-diphosphate Delta-isomerase 1	2.675	0.012
P17047	Lysosome-associated membrane glycoprotein 2	2.772	0.001
Q91YT0	NADH dehydrogenase [ubiquinone] flavoprotein 1, mitochondrial	2.933	0.022
P46414	Cyclin-dependent kinase inhibitor 1B	3.050	0.018
Q9CPT4	Myeloid-derived growth factor	3.254	<0.0001
P47915	60S ribosomal protein L29	3.575	<0.0001
Q8BMF3	NADP-dependent malic enzyme, mitochondrial	3.632	0.001
Q8R5J9	PRA1 family protein 3	3.790	0.006
O88322	Nidogen-2	5.652	<0.0001
Q9ERK4	Exportin-2	7.199	<0.0001

Supplemental Table 3: Ovarian proteins identified by LC-MS/MS to differ in WT mice after PM relative to WT after vehicle-control (log2foldchange ≥ 0.1 and *P*-value ≤ 0.05).

UniProtID	Protein names	log2(FC)	p value
Q4VA53	Sister chromatid cohesion protein PDS5 homolog B	-1.447	0.037
P31725	Protein S100-A9	-0.774	0.001
Q8K363	ATP-dependent RNA helicase DDX18	-0.763	<0.0001
P35441	Thrombospondin-1	-0.673	0.017
Q6ZQ06	Centrosomal protein of 162 kDa	-0.654	0.035
P33622	Apolipoprotein C-III	-0.651	0.037
P02088	Hemoglobin subunit beta-1	-0.633	0.010
Q6W8Q3	Purkinje cell protein 4-like protein 1	-0.612	0.024
P01942	Hemoglobin subunit alpha	-0.547	0.012
Q9WTU6	Mitogen-activated protein kinase 9	-0.547	0.001
P02104	Hemoglobin subunit epsilon-Y2	-0.540	0.049
P28654	Decorin	-0.538	0.016
Q9Z2I9	Succinate--CoA ligase [ADP-forming] subunit beta, mitochondrial	-0.508	0.047
Q9JLM9	Growth factor receptor-bound protein 14	-0.466	0.047
Q08879	Fibulin-1	-0.462	0.019
Q01339	Beta-2-glycoprotein 1	-0.440	0.037
P06797	Cathepsin L1	-0.408	0.003
Q62193	Replication protein A 32 kDa subunit	-0.337	0.008
A2BDX3	Adenylyltransferase and sulfurtransferase MOCS3	-0.241	0.033
Q9DCL9	Multifunctional protein ADE2	-0.070	0.022
Q6ZWX6	Eukaryotic translation initiation factor 2 subunit 1	0.175	0.030
P62242	40S ribosomal protein S8	0.195	0.044
P28653	Biglycan	0.207	0.021
Q9Z0N1	Eukaryotic translation initiation factor 2 subunit 3, X-linked	0.220	0.029
Q9EQH3	Vacuolar protein sorting-associated protein 35	0.228	0.031
Q99LF4	tRNA-splicing ligase RtcB homolog	0.228	0.049
P61979	Heterogeneous nuclear ribonucleoprotein K	0.260	0.032
Q61656	Probable ATP-dependent RNA helicase DDX5	0.261	0.022
P62137	Serine/threonine-protein phosphatase PP1-alpha catalytic subunit	0.262	0.014

Supplemental Table 3: (continued)

Q9CQI3	Glia maturation factor beta	0.266	0.004
P14869	60S acidic ribosomal protein P0	0.267	0.044
P25444	40S ribosomal protein S2	0.273	0.020
P83882	60S ribosomal protein L36a	0.275	0.027
P14115	60S ribosomal protein L27a	0.281	0.037
Q9DB29	Isoamyl acetate-hydrolyzing esterase 1 homolog	0.285	0.027
Q8BK64	Activator of 90 kDa heat shock protein ATPase homolog 1	0.300	0.038
P97371	Proteasome activator complex subunit 1	0.300	0.004
Q6PDM2	Serine/arginine-rich splicing factor 1	0.308	0.048
Q9CPR4	60S ribosomal protein L17	0.312	0.027
P47753	F-actin-capping protein subunit alpha-1	0.318	0.007
Q7TMK9	Heterogeneous nuclear ribonucleoprotein Q	0.318	0.016
Q9Z1Q5	Chloride intracellular channel protein 1	0.326	0.013
Q9D8E6	60S ribosomal protein L4	0.335	0.019
P62830	60S ribosomal protein L23	0.337	0.031
P35550	rRNA 2'-O-methyltransferase fibrillarin	0.340	0.021
P47911	60S ribosomal protein L6	0.349	0.011
Q921M3	Splicing factor 3B subunit 3	0.351	0.042
Q9D8B3	Charged multivesicular body protein 4b	0.354	0.046
Q9CX86	Heterogeneous nuclear ribonucleoprotein A0	0.359	0.005
Q9CQV8	14-3-3 protein beta/alpha	0.367	0.010
P54775	26S proteasome regulatory subunit 6B	0.370	0.044
Q61035	Histidine--tRNA ligase, cytoplasmic	0.372	0.011
Q8VI75	Importin-4	0.373	0.013
P14685	26S proteasome non-ATPase regulatory subunit 3	0.377	0.019
Q9EQU5	Protein SET	0.378	0.036
O35326	Serine/arginine-rich splicing factor 5	0.379	0.032
P62196	26S proteasome regulatory subunit 8	0.381	0.014
Q64010	Adapter molecule crk	0.388	0.046
Q99J77	Sialic acid synthase	0.398	0.033
P62996	Transformer-2 protein homolog beta	0.404	0.021
Q61699	Heat shock protein 105 kDa	0.405	0.038
P97461	40S ribosomal protein S5	0.407	0.030
Q91WV0	Protein Dr1	0.423	0.042
Q61171	Peroxiredoxin-2	0.424	0.044
Q9CQ60	6-phosphogluconolactonase	0.427	0.037
Q8VDP4	Cell cycle and apoptosis regulator protein 2	0.429	0.023

Supplemental Table 3: (continued)

Q9CR98	Protein FAM136A	0.435	0.026
Q8CHH9	Septin-8	0.438	0.006
Q6PE01	U5 small nuclear ribonucleoprotein 40 kDa protein	0.441	0.029
P62821	Ras-related protein Rab-1A	0.444	0.014
Q08093	Calponin-2	0.447	0.011
Q62422	Osteoclast-stimulating factor 1	0.449	0.018
P14131	40S ribosomal protein S16	0.456	0.010
Q8VH51	RNA-binding protein 39	0.463	0.048
Q8CCF0	U4/U6 small nuclear ribonucleoprotein Prp31	0.463	0.048
P97822	Acidic leucine-rich nuclear phosphoprotein 32 family member E	0.476	0.014
Q8R5C5	Beta-centractin	0.477	0.006
O88342	WD repeat-containing protein 1	0.488	0.020
O55029	Coatomer subunit beta	0.488	0.019
P16254	Signal recognition particle 14 kDa protein	0.492	0.001
Q64520	Guanylate kinase	0.494	<0.0001
Q9CWM4	Prefoldin subunit 1	0.495	0.042
P51410	60S ribosomal protein L9	0.499	0.001
Q62167	ATP-dependent RNA helicase DDX3X	0.500	0.036
Q9R1P3	Proteasome subunit beta type-2	0.502	0.025
Q62432	Mothers against decapentaplegic homolog 2	0.502	0.009
Q61581	Insulin-like growth factor-binding protein 7	0.505	0.014
Q7TPV4	Myb-binding protein 1A	0.510	0.037
Q64261	Cyclin-dependent kinase 6	0.511	0.023
Q9Z1D1	Eukaryotic translation initiation factor 3 subunit G	0.511	0.005
Q60737	Casein kinase II subunit alpha	0.516	0.020
P61290	Proteasome activator complex subunit 3	0.519	0.025
Q9JIX0	Transcription and mRNA export factor ENY2	0.519	0.027
Q99LP6	GrpE protein homolog 1, mitochondrial	0.527	0.039
Q60972	Histone-binding protein RBBP4	0.531	0.009
P14824	Annexin A6	0.540	0.015
Q9JM14	5'(3')-deoxyribonucleotidase, cytosolic type	0.560	0.032
P07356	Annexin A2	0.562	0.007
P97821	Dipeptidyl peptidase 1	0.562	<0.0001
Q91V76	Ester hydrolase C11orf54 homolog	0.572	0.040
Q9CZ30	Obg-like ATPase 1	0.576	0.050
Q62418	Drebrin-like protein	0.578	0.004
Q6NSR8	Probable aminopeptidase NPEPL1	0.584	0.018

Supplemental Table 3: (continued)

P12815	Programmed cell death protein 6	0.585	0.005
Q9R0P3	S-formylglutathione hydrolase	0.588	0.027
P47811	Mitogen-activated protein kinase 14	0.592	0.047
Q8CFX1	GDH/6PGL endoplasmic bifunctional protein	0.592	0.024
Q9JMH6	Thioredoxin reductase 1, cytoplasmic	0.593	0.017
Q9D0L8	mRNA cap guanine-N7 methyltransferase	0.598	0.030
Q920Q6	RNA-binding protein Musashi homolog 2	0.600	0.015
Q99KQ4	Nicotinamide phosphoribosyltransferase	0.609	0.030
Q64378	Peptidyl-prolyl cis-trans isomerase FKBP5	0.617	0.045
Q8VBV7	COP9 signalosome complex subunit 8	0.619	0.027
Q8K0G8	Epithelial splicing regulatory protein 2	0.624	0.039
Q6IRU2	Tropomyosin alpha-4 chain	0.629	0.013
Q9WVE8	Protein kinase C and casein kinase substrate in neurons protein 2	0.631	0.033
Q3ULJ0	Glycerol-3-phosphate dehydrogenase 1-like protein	0.645	0.014
Q61624	Zinc finger protein 148	0.649	0.040
P61164	Alpha-centractin	0.650	0.032
Q920A5	Retinoid-inducible serine carboxypeptidase	0.656	0.010
Q810B6	Rabankyrin-5	0.659	0.029
Q8VCI0	Phospholipase B-like 1	0.659	0.004
Q9CQC6	Basic leucine zipper and W2 domain-containing protein 1	0.678	0.014
Q91V12	Cytosolic acyl coenzyme A thioester hydrolase	0.679	<0.0001
O08709	Peroxiredoxin-6	0.694	0.026
Q9DAR7	m7GpppX diphosphatase	0.695	0.009
Q9ERR7	Selenoprotein F	0.704	0.035
P06745	Glucose-6-phosphate isomerase	0.720	0.020
Q9CRC9	Glucosamine-6-phosphate isomerase 2	0.725	0.037
O89017	Legumain	0.732	0.024
P48036	Annexin A5	0.745	0.006
P06801	NADP-dependent malic enzyme	0.750	0.029
O09167	60S ribosomal protein L21	0.751	0.048
Q9QUG2	DNA polymerase kappa	0.752	0.025
Q3TYX8	RUN and FYVE domain-containing protein 4	0.781	0.006
P50429	Arylsulfatase B	0.804	0.040
O08738	Caspase-6	0.806	0.003
Q9WVA4	Transgelin-2	0.806	0.001
Q8R0F6	Integrin-linked kinase-associated serine/threonine phosphatase 2C	0.810	0.021

Supplemental Table 3: (continued)

P63280	SUMO-conjugating enzyme UBC9	0.811	0.001
O88448	Kinesin light chain 2	0.826	0.020
Q8BGB7	Enolase-phosphatase E1	0.831	0.032
Q9CXW3	Calcyclin-binding protein	0.833	0.035
Q9D0I9	Arginine--tRNA ligase, cytoplasmic	0.837	0.034
Q60767	Lymphocyte antigen 75	0.839	0.029
Q05793	Basement membrane-specific heparan sulfate proteoglycan core protein	0.840	0.044
Q9CZ04	COP9 signalosome complex subunit 7a	0.858	0.031
P67871	Casein kinase II subunit beta	0.868	0.016
O88447	Kinesin light chain 1	0.871	0.011
Q91V92	ATP-citrate synthase	0.882	0.005
O88844	Isocitrate dehydrogenase [NADP] cytoplasmic	0.939	0.003
P56380	Bis(5'-nucleosyl)-tetraphosphatase [asymmetrical]	0.950	0.042
Q62384	Zinc finger protein ZPR1	0.962	0.028
Q68FL6	Methionine--tRNA ligase, cytoplasmic	0.969	0.009
P42567	Epidermal growth factor receptor substrate 15	1.024	0.021
P35235	Tyrosine-protein phosphatase non-receptor type 11	1.048	0.020
Q920E5	Farnesyl pyrophosphate synthase	1.075	0.007
O35969	Guanidinoacetate N-methyltransferase	1.095	0.048
Q6P6M7	O-phosphoseryl-tRNA(Sec) selenium transferase	1.137	0.042
O88322	Nidogen-2	1.152	0.047
Q9WUA3	ATP-dependent 6-phosphofructokinase, platelet type	1.154	0.002
Q9CPX8	Cytochrome b-c1 complex subunit 10	1.173	0.005
Q8BIW1	Exopolyphosphatase PRUNE1	1.195	0.036
Q7TMR0	Lysosomal Pro-X carboxypeptidase	1.225	0.025
P30412	Peptidyl-prolyl cis-trans isomerase C	1.230	0.010
O54941	SWI/SNF-related matrix-associated actin-dependent regulator of chromatin subfamily E member 1	1.263	0.030
Q80ZJ6	Protein zer-1 homolog	1.265	0.049
Q9Z0S1	3'(2'),5'-bisphosphate nucleotidase 1	1.275	0.020
P22907	Porphobilinogen deaminase	1.364	0.014
Q07797	Galectin-3-binding protein	1.369	0.017
Q8JZK9	Hydroxymethylglutaryl-CoA synthase, cytoplasmic	1.472	0.020
Q60648	Ganglioside GM2 activator	1.476	0.001
Q8C6G8	WD repeat-containing protein 26	1.545	0.001

Supplemental Table 3: (continued)

P70271	PDZ and LIM domain protein 4	1.561	0.024
Q9WUP7	Ubiquitin carboxyl-terminal hydrolase isozyme L5	1.583	0.016
Q8C166	Copine-1	1.825	0.014
Q3UTJ2	Sorbin and SH3 domain-containing protein 2	1.933	0.019
P46414	Cyclin-dependent kinase inhibitor 1B	2.178	0.028
Q8K0C4	Lanosterol 14-alpha demethylase	2.181	0.007
P58044	Isopentenyl-diphosphate Delta-isomerase 1	2.619	0.001
P21300	Aldose reductase-related protein 1	3.167	0.015
O35490	Betaine--homocysteine S-methyltransferase 1	4.134	0.028

Supplemental Table 4: Ovarian proteins identified by LC-MS/MS to differ in *Atm*$^{+/-}$ mice after PM relative *Atm*$^{+/-}$ after vehicle-control (log2foldchange ≥ 0.1 and *P*-value ≤ 0.05).

UniProtID	Protein names	log2(FC)	p value
Q8VI64	Protein MGARP	-1.912	0.010
Q9Z2D6	Methyl-CpG-binding protein 2	-1.814	0.002
Q9EQX4	Allograft inflammatory factor 1-like	-1.672	0.039
Q9JL35	High mobility group nucleosome-binding domain-containing protein 5	-1.487	0.037
O89020	Afamin	-1.483	0.036
Q80SZ7	Guanine nucleotide-binding protein G(I)/G(S)/G(O) subunit gamma-5	-1.446	0.028
Q6ZPZ3	Zinc finger CCCH domain-containing protein 4	-1.425	0.030
Q91VD9	NADH-ubiquinone oxidoreductase 75 kDa subunit, mitochondrial	-1.342	0.014
Q9D0J8	Parathymosin	-1.258	0.017
Q9QZB7	Actin-related protein 10	-1.057	0.016
Q3TCN2	Putative phospholipase B-like 2	-1.049	0.047
P08226	Apolipoprotein E	-1.027	0.035
P10922	Histone H1.0	-0.980	0.036
Q9CZN7	Serine hydroxymethyltransferase, mitochondrial	-0.970	0.034
Q9D3D9	ATP synthase subunit delta, mitochondrial	-0.968	0.009
P70441	Na(+)/H(+) exchange regulatory cofactor NHE-RF1	-0.906	0.036
P26645	Myristoylated alanine-rich C-kinase substrate	-0.895	0.023
P19536	Cytochrome c oxidase subunit 5B, mitochondrial	-0.873	0.039
Q9CQA3	Succinate dehydrogenase [ubiquinone] iron-sulfur subunit, mitochondrial	-0.873	0.020
P61957	Small ubiquitin-related modifier 2	-0.861	0.016
Q8CDB0	MAP kinase-interacting serine/threonine-protein kinase 2	-0.848	0.049
Q9CZ13	Cytochrome b-c1 complex subunit 1, mitochondrial	-0.839	0.015
Q8K2B3	Succinate dehydrogenase [ubiquinone] flavoprotein subunit, mitochondrial	-0.815	0.032
Q62168	Keratin, type I cuticular Ha2	-0.814	0.021
P48428	Tubulin-specific chaperone A	-0.810	0.014
Q5SX40	Myosin-1	-0.797	0.019
Q8C0L6	Peroxisomal N(1)-acetyl-spermine/spermidine oxidase	-0.775	0.045

Supplemental Table 4: (continued)

Q9CT10	Ran-binding protein 3	-0.772	0.039
Q91ZX7	Prolow-density lipoprotein receptor-related protein 1	-0.734	0.041
O35129	Prohibitin-2	-0.701	0.032
P10852	4F2 cell-surface antigen heavy chain	-0.646	0.032
Q9JI75	Ribosyldihydronicotinamide dehydrogenase	-0.551	0.029
Q9CR68	Cytochrome b-c1 complex subunit Rieske, mitochondrial	-0.455	0.022
P45376	Aldose reductase	-0.367	0.037
Q08879	Fibulin-1	-0.355	0.038
Q60931	Voltage-dependent anion-selective channel protein 3	-0.334	0.025
Q8R1I1	Cytochrome b-c1 complex subunit 9	-0.195	0.045
P97447	Four and a half LIM domains protein 1	0.270	0.050
Q8BWM0	Prostaglandin E synthase 2	0.288	0.032
Q9CXZ1	NADH dehydrogenase [ubiquinone] iron-sulfur protein 4, mitochondrial	0.394	0.018
Q8K3C3	Protein LZIC	0.404	0.049
Q99LD8	N(G),N(G)-dimethylarginine dimethylaminohydrolase 2	0.444	0.037
Q9DBG6	Dolichyl-diphosphooligosaccharide--protein glycosyltransferase subunit 2	0.462	0.032
Q8CG70	Prolyl 3-hydroxylase 3	0.466	0.031
O54724	Caveolae-associated protein 1	0.543	0.019
Q923D2	Flavin reductase	0.547	0.034
Q6PE01	U5 small nuclear ribonucleoprotein 40 kDa protein	0.578	0.037
Q9QXE7	F-box-like/WD repeat-containing protein TBL1X	0.606	0.027
Q8BGC4	Prostaglandin reductase-3	0.640	0.023
P51150	Ras-related protein Rab-7a	0.647	0.019
Q9CQ92	Mitochondrial fission 1 protein	0.661	0.009
O88544	COP9 signalosome complex subunit 4	0.664	0.022
Q9Z1X4	Interleukin enhancer-binding factor 3	0.677	0.041
P19096	Fatty acid synthase	0.700	0.043
Q9EQH3	Vacuolar protein sorting-associated protein 35	0.713	0.030
Q91VS7	Microsomal glutathione S-transferase 1	0.722	0.036
Q62261	Spectrin beta chain, non-erythrocytic 1	0.738	0.014
P63085	Mitogen-activated protein kinase 1	0.743	0.041
P05784	Keratin, type I cytoskeletal 18	0.760	0.019
Q9CQ54	NADH dehydrogenase [ubiquinone] 1 subunit C2	0.767	0.013

Supplemental Table 4: (continued)

O55143	Sarcoplasmic/endoplasmic reticulum calcium ATPase 2	0.769	0.005
Q99MR6	Serrate RNA effector molecule homolog	0.792	0.045
Q91YR1	Twinfilin-1	0.794	0.035
P48024	Eukaryotic translation initiation factor 1	0.818	0.034
O70492	Sorting nexin-3	0.824	0.007
P84084	ADP-ribosylation factor 5	0.842	0.042
Q62383	Transcription elongation factor SPT6	0.846	0.033
Q61263	Sterol O-acyltransferase 1	0.847	0.022
Q9JK53	Prolargin	0.850	0.014
P24815	3 beta-hydroxysteroid dehydrogenase/Delta 5-->4-isomerase type 1	0.853	0.007
Q6ZWN5	40S ribosomal protein S9	0.858	0.020
Q64471	Glutathione S-transferase theta-1	0.862	0.045
P62281	40S ribosomal protein S11	0.863	0.007
Q9WVB0	RNA-binding protein with multiple splicing	0.885	0.037
P37804	Transgelin	0.887	0.014
Q3TXS7	26S proteasome non-ATPase regulatory subunit 1	0.889	0.043
Q61074	Protein phosphatase 1G	0.892	0.022
P28654	Decorin	0.892	0.040
P61089	Ubiquitin-conjugating enzyme E2 N	0.902	0.033
Q9CZY3	Ubiquitin-conjugating enzyme E2 variant 1	0.905	0.018
Q9Z1Q9	Valine--tRNA ligase	0.922	0.045
P62242	40S ribosomal protein S8	0.953	0.030
Q9DBC7	cAMP-dependent protein kinase type I-alpha regulatory subunit	0.960	0.012
Q91ZW3	SWI/SNF-related matrix-associated actin-dependent regulator of chromatin subfamily A member 5	0.961	0.041
Q3UYV9	Nuclear cap-binding protein subunit 1	0.965	0.047
P84091	AP-2 complex subunit mu	0.972	0.007
Q9QUI0	Transforming protein RhoA	0.974	0.037
O55023	Inositol monophosphatase 1	0.987	0.022
P35585	AP-1 complex subunit mu-1	0.988	0.030
Q61879	Myosin-10	0.994	0.015
Q9WVQ5	Methylthioribulose-1-phosphate dehydratase	0.994	0.038
P61750	ADP-ribosylation factor 4	1.001	0.016
P62331	ADP-ribosylation factor 6	1.003	0.044
Q9CQN1	Heat shock protein 75 kDa, mitochondrial	1.004	0.021

Supplemental Table 4: (continued)

Q9Z1Z0	General vesicular transport factor p115	1.006	0.045
P52825	Carnitine O-palmitoyltransferase 2, mitochondrial	1.011	0.021
P32020	Non-specific lipid-transfer protein	1.023	0.048
Q8VCW8	Acyl-CoA synthetase family member 2, mitochondrial	1.032	0.005
O35841	Apoptosis inhibitor 5	1.053	0.001
Q8K310	Matrin-3	1.061	0.045
P54071	Isocitrate dehydrogenase [NADP], mitochondrial	1.067	0.015
O70133	ATP-dependent RNA helicase A	1.070	0.036
Q9DBE0	Cysteine sulfinic acid decarboxylase	1.072	0.026
Q7TPV4	Myb-binding protein 1A	1.084	0.017
P70168	Importin subunit beta-1	1.100	0.006
Q921F4	Heterogeneous nuclear ribonucleoprotein L-like	1.104	0.038
Q9DBZ5	Eukaryotic translation initiation factor 3 subunit K	1.108	0.010
P63280	SUMO-conjugating enzyme UBC9	1.113	0.039
Q8BN78	Transcriptional regulator Kaiso	1.116	0.049
Q61656	Probable ATP-dependent RNA helicase DDX5	1.121	0.026
Q8BTM8	Filamin-A	1.133	0.014
Q6A4J8	Ubiquitin carboxyl-terminal hydrolase 7	1.136	0.016
Q61990	Poly(rC)-binding protein 2	1.137	0.019
Q80UZ0	FYVE, RhoGEF and PH domain-containing protein 5	1.143	0.009
Q8BGB7	Enolase-phosphatase E1	1.163	0.031
P14685	26S proteasome non-ATPase regulatory subunit 3	1.174	0.037
Q9WVJ2	26S proteasome non-ATPase regulatory subunit 13	1.176	0.007
Q60749	KH domain-containing, RNA-binding, signal transduction-associated protein 1	1.176	0.045
Q8CGC7	Bifunctional glutamate/proline--tRNA ligase	1.183	0.045
O35114	Lysosome membrane protein 2	1.200	0.041
Q9CZ30	Obg-like ATPase 1	1.212	0.029
P26039	Talin-1	1.220	0.011
Q8VDD5	Myosin-9	1.224	0.027
O89079	Coatomer subunit epsilon	1.233	0.025
Q6PIP5	NudC domain-containing protein 1	1.235	0.024
Q9R0X4	Acyl-coenzyme A thioesterase 9, mitochondrial	1.239	0.025
Q9DBG9	Tax1-binding protein 3	1.243	0.023
P62908	40S ribosomal protein S3	1.265	0.042

Supplemental Table 4: (continued)

Q9CX56	26S proteasome non-ATPase regulatory subunit 8	1.276	<0.0001
Q6NZC7	SEC23-interacting protein	1.283	0.022
O70318	Band 4.1-like protein 2	1.299	0.003
Q8VCR7	Protein ABHD14B	1.299	0.033
Q00PI9	Heterogeneous nuclear ribonucleoprotein U-like protein 2	1.305	0.030
P22682	E3 ubiquitin-protein ligase CBL	1.307	0.032
Q61584	Fragile X mental retardation syndrome-related protein 1	1.310	0.009
P97461	40S ribosomal protein S5	1.310	0.002
Q8BJY1	26S proteasome non-ATPase regulatory subunit 5	1.333	0.013
Q5FWK3	Rho GTPase-activating protein 1	1.336	0.034
O88844	Isocitrate dehydrogenase [NADP] cytoplasmic	1.347	0.041
Q62167	ATP-dependent RNA helicase DDX3X	1.349	0.035
Q9WTP7	GTP:AMP phosphotransferase AK3, mitochondrial	1.355	0.046
Q91W50	Cold shock domain-containing protein E1	1.357	0.013
Q9Z0M5	Lysosomal acid lipase/cholesteryl ester hydrolase	1.367	0.043
Q3UEB3	Poly(U)-binding-splicing factor PUF60	1.384	0.020
Q8CI51	PDZ and LIM domain protein 5	1.393	0.019
Q9JHU4	Cytoplasmic dynein 1 heavy chain 1	1.454	0.050
Q68FD5	Clathrin heavy chain 1	1.458	0.027
Q6P4T2	U5 small nuclear ribonucleoprotein 200 kDa helicase	1.459	0.037
P97823	Acyl-protein thioesterase 1	1.465	0.044
Q8VH51	RNA-binding protein 39	1.482	0.039
Q9ESZ8	General transcription factor II-I	1.504	0.007
P54823	Probable ATP-dependent RNA helicase DDX6	1.538	0.013
Q8CIE6	Coatomer subunit alpha	1.542	0.034
P17427	AP-2 complex subunit alpha-2	1.548	0.046
Q99K48	Non-POU domain-containing octamer-binding protein	1.552	0.029
O35969	Guanidinoacetate N-methyltransferase	1.557	0.008
P10107	Annexin A1	1.562	0.033
P61082	NEDD8-conjugating enzyme Ubc12	1.564	0.046
Q9JKF1	Ras GTPase-activating-like protein IQGAP1	1.567	0.025
O70503	Very-long-chain 3-oxoacyl-CoA reductase	1.569	0.042
Q8BG32	26S proteasome non-ATPase regulatory subunit 11	1.579	0.010

Supplemental Table 4: (continued)

Q91ZJ5	UTP--glucose-1-phosphate uridylyltransferase	1.589	0.020
Q9D0I9	Arginine--tRNA ligase, cytoplasmic	1.601	0.026
Q3UKJ7	WD40 repeat-containing protein SMU1	1.609	0.011
P07214	SPARC	1.613	0.026
O70194	Eukaryotic translation initiation factor 3 subunit D	1.615	0.014
Q921U8	Smoothelin	1.666	0.006
Q64378	Peptidyl-prolyl cis-trans isomerase FKBP5	1.693	0.033
Q9DCG9	Multifunctional methyltransferase subunit TRM112-like protein	1.712	0.012
Q8BK64	Activator of 90 kDa heat shock protein ATPase homolog 1	1.719	0.014
Q07797	Galectin-3-binding protein	1.722	0.049
Q9CZ04	COP9 signalosome complex subunit 7a	1.732	0.011
P0DOV2	Interferon-activable protein 204	1.745	0.011
P62737	Actin, aortic smooth muscle	1.751	0.038
Q8BH64	EH domain-containing protein 2	1.753	0.049
Q3ULJ0	Glycerol-3-phosphate dehydrogenase 1-like protein	1.768	0.041
Q8CHT0	Delta-1-pyrroline-5-carboxylate dehydrogenase, mitochondrial	1.769	0.029
Q9CY64	Biliverdin reductase A	1.779	0.001
Q6P5F9	Exportin-1	1.780	0.021
Q99LD9	Translation initiation factor eIF-2B subunit beta	1.787	0.007
P70372	ELAV-like protein 1	1.796	0.005
Q8R1B4	Eukaryotic translation initiation factor 3 subunit C	1.803	0.034
Q62005	Zona pellucida sperm-binding protein 1	1.844	0.002
Q9EPL8	Importin-7	1.849	0.017
Q60715	Prolyl 4-hydroxylase subunit alpha-1	1.852	0.029
P42567	Epidermal growth factor receptor substrate 15	1.875	0.035
Q99LJ6	Glutathione peroxidase 7	1.887	0.011
Q8BWY3	Eukaryotic peptide chain release factor subunit 1	1.926	0.007
P12815	Programmed cell death protein 6	1.965	0.009
Q9DCH4	Eukaryotic translation initiation factor 3 subunit F	1.983	0.021
Q9WTL7	Acyl-protein thioesterase 2	2.042	0.032
Q99NB9	Splicing factor 3B subunit 1	2.050	0.033
Q9JIF7	Coatomer subunit beta	2.055	0.022
Q07076	Annexin A7	2.074	0.011

Supplemental Table 4: (continued)

Q99JX4	Eukaryotic translation initiation factor 3 subunit M	2.123	0.022
Q01405	Protein transport protein Sec23A	2.165	0.025
D3Z7P3	Glutaminase kidney isoform, mitochondrial	2.167	0.015
B1AZI6	THO complex subunit 2	2.181	0.032
Q9D7I5	Phospholysine phosphohistidine inorganic pyrophosphate phosphatase	2.190	0.007
Q8QZY1	Eukaryotic translation initiation factor 3 subunit L	2.229	0.045
P60229	Eukaryotic translation initiation factor 3 subunit E	2.305	0.011
P31001	Desmin	2.311	0.011
Q8CH18	Cell division cycle and apoptosis regulator protein 1	2.317	0.002
Q80UM3	N-alpha-acetyltransferase 15, NatA auxiliary subunit	2.406	0.002
O08638	Myosin-11	2.450	0.009
Q08091	Calponin-1	2.478	0.015
O55222	Integrin-linked protein kinase	2.522	0.032
Q8BML9	Glutamine--tRNA ligase	2.610	0.015
Q6B966	NACHT, LRR and PYD domains-containing protein 14	2.673	0.039
Q61768	Kinesin-1 heavy chain	3.407	0.009

Supplemental Table 5: Ovarian proteins identified by LC-MS/MS to differ in *Atm*$^{+/-}$ mice after PM relative to WT after PM (log2foldchange ≥ 0.1 and *P*-value ≤ 0.05).

UniProt ID	Protein names	log2(FC)	p value
Q7TMB8	Cytoplasmic FMR1-interacting protein 1	-5.567	<0.0001
Q9WVB3	Transducin-like enhancer protein 6	-3.649	<0.0001
Q91XF0	Pyridoxine-5'-phosphate oxidase	-3.411	0.008
Q9Z2M7	Phosphomannomutase 2	-2.974	<0.0001
Q62059	Versican core protein	-2.912	0.006
Q8BFZ3	Beta-actin-like protein 2	-2.873	0.025
Q6ZPZ3	Zinc finger CCCH domain-containing protein 4	-2.871	0.002
O88974	Histone-lysine N-methyltransferase SETDB1	-2.796	0.003
Q6A068	Cell division cycle 5-like protein	-2.745	0.007
Q8BK64	Activator of 90 kDa heat shock protein ATPase homolog 1	-2.677	<0.0001
O35643	AP-1 complex subunit beta-1	-2.671	0.006
Q9CW03	Structural maintenance of chromosomes protein 3	-2.475	0.004
O08810	116 kDa U5 small nuclear ribonucleoprotein component	-2.456	0.003
O70493	Sorting nexin-12	-2.444	0.004
P68372	Tubulin beta-4B chain	-2.418	0.002
P97496	SWI/SNF complex subunit SMARCC1	-2.316	<0.0001
D3YXK2	Scaffold attachment factor B1	-2.189	0.006
Q9Z0M5	Lysosomal acid lipase/cholesteryl ester hydrolase	-2.054	0.011
Q6PGB6	N-alpha-acetyltransferase 50	-1.987	0.004
Q64520	Guanylate kinase	-1.904	0.001
Q9CX34	Protein SGT1 homolog	-1.881	0.009
Q3THE2	Myosin regulatory light chain 12B	-1.842	0.024
Q8BIG7	Catechol O-methyltransferase domain-containing protein 1	-1.810	0.014
Q8BFY9	Transportin-1	-1.782	0.026
P62331	ADP-ribosylation factor 6	-1.782	0.011
P62317	Small nuclear ribonucleoprotein Sm D2	-1.739	<0.0001
Q9CWL8	Beta-catenin-like protein 1	-1.731	0.014
P13439	Uridine 5'-monophosphate synthase	-1.715	0.021
Q810B6	Rabankyrin-5	-1.707	0.005

Supplemental Table 5: (continued)

P35235	Tyrosine-protein phosphatase non-receptor type 11	-1.682	0.013
Q61205	Platelet-activating factor acetylhydrolase IB subunit gamma	-1.681	0.030
Q8BWF0	Succinate-semialdehyde dehydrogenase, mitochondrial	-1.649	0.001
Q8C166	Copine-1	-1.607	0.045
Q8BHD7	Polypyrimidine tract-binding protein 3	-1.593	0.014
Q06770	Corticosteroid-binding globulin	-1.575	0.038
Q8CCK0	Core histone macro-H2A.2	-1.550	0.011
Q9D0I9	Arginine--tRNA ligase, cytoplasmic	-1.519	0.014
Q80U93	Nuclear pore complex protein Nup214	-1.453	0.010
Q8BGW1	Alpha-ketoglutarate-dependent dioxygenase FTO	-1.447	0.017
Q91VH6	Protein MEMO1	-1.431	0.026
Q61191	Host cell factor 1	-1.426	0.009
P97470	Serine/threonine-protein phosphatase 4 catalytic subunit	-1.425	0.047
Q9QZB7	Actin-related protein 10	-1.381	0.010
Q91WG0	Acylcarnitine hydrolase	-1.371	<0.0001
Q60715	Prolyl 4-hydroxylase subunit alpha-1	-1.329	0.032
Q9Z0H3	SWI/SNF-related matrix-associated actin-dependent regulator of chromatin subfamily B member 1	-1.319	0.042
Q7SIG6	Arf-GAP with SH3 domain, ANK repeat and PH domain-containing protein 2	-1.310	0.031
Q9CZN7	Serine hydroxymethyltransferase, mitochondrial	-1.296	0.017
Q3UL36	Arginine and glutamate-rich protein 1	-1.242	0.014
Q7TSG5	SH3 domain-containing protein 21	-1.240	0.033
P22907	Porphobilinogen deaminase	-1.238	0.041
Q9CZ13	Cytochrome b-c1 complex subunit 1, mitochondrial	-1.231	0.046
Q8CHP5	Partner of Y14 and mago	-1.207	0.009
Q6P8X1	Sorting nexin-6	-1.203	0.047
P28654	Decorin	-1.202	0.015
Q9CS42	Ribose-phosphate pyrophosphokinase 2	-1.187	<0.0001
Q8BP92	Reticulocalbin-2	-1.151	0.029
Q91WV0	Protein Dr1	-1.137	0.005
Q9QYR9	Acyl-coenzyme A thioesterase 2, mitochondrial	-1.129	0.018
P61087	Ubiquitin-conjugating enzyme E2 K	-1.118	0.047
P20918	Plasminogen	-1.117	0.015

Supplemental Table 5: (continued)

P59235	Nucleoporin Nup43	-1.101	0.047
P62737	Actin, aortic smooth muscle	-1.080	0.050
Q8VI75	Importin-4	-1.056	0.009
P21614	Vitamin D-binding protein	-1.052	0.001
Q62426	Cystatin-B	-1.038	0.005
Q9R0Y5	Adenylate kinase isoenzyme 1	-1.012	0.036
P12815	Programmed cell death protein 6	-1.008	0.047
O35841	Apoptosis inhibitor 5	-0.986	0.002
Q9CQA3	Succinate dehydrogenase [ubiquinone] iron-sulfur subunit, mitochondrial	-0.973	0.001
Q99MR8	Methylcrotonoyl-CoA carboxylase subunit alpha, mitochondrial	-0.950	0.002
Q9JJF0	Nucleosome assembly protein 1-like 5	-0.938	0.032
Q64133	Amine oxidase [flavin-containing] A	-0.925	0.019
Q9D8S4	Oligoribonuclease, mitochondrial	-0.905	0.031
Q62523	Zyxin	-0.901	0.013
Q8R1I1	Cytochrome b-c1 complex subunit 9	-0.877	0.023
P01027	Complement C3	-0.872	0.035
Q9D358	Low molecular weight phosphotyrosine protein phosphatase	-0.868	0.034
Q8VE62	Polyadenylate-binding protein-interacting protein 1	-0.862	0.012
Q1HFZ0	tRNA (cytosine(34)-C(5))-methyltransferase	-0.851	0.004
Q64471	Glutathione S-transferase theta-1	-0.844	0.001
Q9JI75	Ribosyldihydronicotinamide dehydrogenase [quinone]	-0.833	0.006
Q91ZX7	Prolow-density lipoprotein receptor-related protein 1	-0.832	0.030
Q9CT10	Ran-binding protein 3	-0.830	0.006
P19001	Keratin, type I cytoskeletal 19	-0.815	0.009
Q64105	Sepiapterin reductase	-0.803	0.041
Q3THS6	S-adenosylmethionine synthase isoform type-2	-0.791	0.046
P97372	Proteasome activator complex subunit 2	-0.790	0.043
Q6PE01	U5 small nuclear ribonucleoprotein 40 kDa protein	-0.789	0.009
Q8VCM7	Fibrinogen gamma chain	-0.779	0.036
P45377	Aldose reductase-related protein 2	-0.778	0.043
Q9JKB3	Y-box-binding protein 3	-0.770	0.010
Q99M74	Keratin, type II cuticular Hb2	-0.753	0.032
Q8CHT0	Delta-1-pyrroline-5-carboxylate dehydrogenase, mitochondrial	-0.749	0.021

Supplemental Table 5: (continued)

P70288	Histone deacetylase 2	-0.748	0.004
O54890	Integrin beta-3	-0.746	0.024
Q99L04	Dehydrogenase/reductase SDR family member 1	-0.739	0.039
Q8CHY7	Tetratricopeptide repeat protein 23	-0.697	0.041
Q6PDG5	SWI/SNF complex subunit SMARCC2	-0.669	0.042
Q9CR00	26S proteasome non-ATPase regulatory subunit 9	-0.669	0.009
Q60598	Src substrate cortactin	-0.654	0.021
P62835	Ras-related protein Rap-1A	-0.618	0.036
P62267	40S ribosomal protein S23	-0.565	0.008
P47753	F-actin-capping protein subunit alpha-1	-0.565	0.022
F6ZDS4	Nucleoprotein TPR	-0.535	0.038
Q9ESZ8	General transcription factor II-I	-0.526	0.048
Q62005	Zona pellucida sperm-binding protein 1	-0.526	0.050
Q9D0J8	Parathymosin	-0.524	0.015
Q8BVY0	Ribosomal L1 domain-containing protein 1	-0.503	0.044
Q9CXT8	Mitochondrial-processing peptidase subunit beta	-0.499	0.048
P62996	Transformer-2 protein homolog beta	-0.421	0.026
Q9DBL1	Short/branched chain specific acyl-CoA dehydrogenase, mitochondrial	-0.413	0.041
P49615	Cyclin-dependent-like kinase 5	-0.396	0.015
Q62432	Mothers against decapentaplegic homolog 2	-0.390	0.043
Q8BHG1	Nardilysin	-0.330	0.006
P14152	Malate dehydrogenase, cytoplasmic	-0.276	0.025
O55135	Eukaryotic translation initiation factor 6	0.490	0.037
P02088	Hemoglobin subunit beta-1	0.545	0.011
Q6ZWY3	40S ribosomal protein S27-like	0.573	0.035
Q80UM3	N-alpha-acetyltransferase 15, NatA auxiliary subunit	0.592	0.035
P10630	Eukaryotic initiation factor 4A-II	0.606	0.034
Q64213	Splicing factor 1	0.617	0.049
Q80W21	Glutathione S-transferase Mu 7	0.695	0.016
Q9CY64	Biliverdin reductase A	0.782	0.010
O55013	Trafficking protein particle complex subunit 3	0.782	0.017
P61750	ADP-ribosylation factor 4	0.797	0.047
P63085	Mitogen-activated protein kinase 1	0.876	0.008
P55096	ATP-binding cassette sub-family D member 3	0.895	0.035
Q8K3C3	Protein LZIC	0.933	0.021

Supplemental Table 5: (continued)

Q3TC72	Fumarylacetoacetate hydrolase domain-containing protein 2A	0.954	0.047
P54775	26S proteasome regulatory subunit 6B	0.969	0.005
Q6NZC7	SEC23-interacting protein	1.059	0.020
Q8BMJ2	Leucine--tRNA ligase, cytoplasmic	1.123	0.022
Q8VCR7	Protein ABHD14B	1.156	0.044
Q9QXT0	Protein canopy homolog 2	1.183	<0.0001
Q9D8Y0	EF-hand domain-containing protein D2	1.188	0.042
Q91W89	Alpha-mannosidase 2C1	1.191	0.008
Q8QZS1	3-hydroxyisobutyryl-CoA hydrolase, mitochondrial	1.198	0.040
Q9EQS3	c-Myc-binding protein	1.200	0.009
Q9EPL8	Importin-7	1.244	0.017
P20060	Beta-hexosaminidase subunit beta	1.274	0.021
Q91YR1	Twinfilin-1	1.283	0.028
Q3UKJ7	WD40 repeat-containing protein SMU1	1.337	0.037
Q99PV0	Pre-mRNA-processing-splicing factor 8	1.351	0.005
P51881	ADP/ATP translocase 2	1.480	0.011
Q4VA53	Sister chromatid cohesion protein PDS5 homolog B	1.483	0.008
Q9D7P6	Iron-sulfur cluster assembly enzyme ISCU, mitochondrial	1.509	0.020
O88447	Kinesin light chain 1	1.552	0.034
P98078	Disabled homolog 2	1.562	0.001
Q99KF1	Transmembrane emp24 domain-containing protein 9	1.604	0.018
O70310	Glycylpeptide N-tetradecanoyltransferase 1	1.608	0.022
P15532	Nucleoside diphosphate kinase A	1.673	0.001
P61759	Prefoldin subunit 3	1.676	0.027
Q91ZJ5	UTP--glucose-1-phosphate uridylyltransferase	1.698	0.044
Q9D287	Pre-mRNA-splicing factor SPF27	1.721	0.014
Q99K51	Plastin-3	1.769	0.025
Q91YE6	Importin-9	1.832	0.038
Q9DAW9	Calponin-3	1.856	0.005
Q9R013	Cathepsin F	1.865	0.001
P54823	Probable ATP-dependent RNA helicase DDX6	1.894	0.007
Q9D6J6	NADH dehydrogenase [ubiquinone] flavoprotein 2, mitochondrial	1.944	0.006
Q8CHP8	Glycerol-3-phosphate phosphatase	2.002	0.017
P83917	Chromobox protein homolog 1	2.006	0.003
P99024	Tubulin beta-5 chain	2.013	0.013

Supplemental Table 5: (continued)

O88587	Catechol O-methyltransferase	2.086	0.049
P17047	Lysosome-associated membrane glycoprotein 2	2.164	0.009
P03953	Complement factor D	2.395	0.015
Q62219	Transforming growth factor beta-1-induced transcript 1 protein	2.404	0.024
Q02248	Catenin beta-1	2.464	0.019
Q91ZW3	SWI/SNF-related matrix-associated actin-dependent regulator of chromatin subfamily A member 5	2.475	0.003
Q9CQ19	Myosin regulatory light polypeptide 9	2.524	0.008
Q8R5J9	PRA1 family protein 3	3.095	0.001
Q3TCH7	Cullin-4A	3.164	0.011
Q8K124	Pleckstrin homology domain-containing family O member 2	3.369	<0.0001
Q8BMF3	NADP-dependent malic enzyme, mitochondrial	3.380	0.003
Q9CPT4	Myeloid-derived growth factor	4.064	<0.0001
Q9ERK4	Exportin-2	6.395	<0.0001

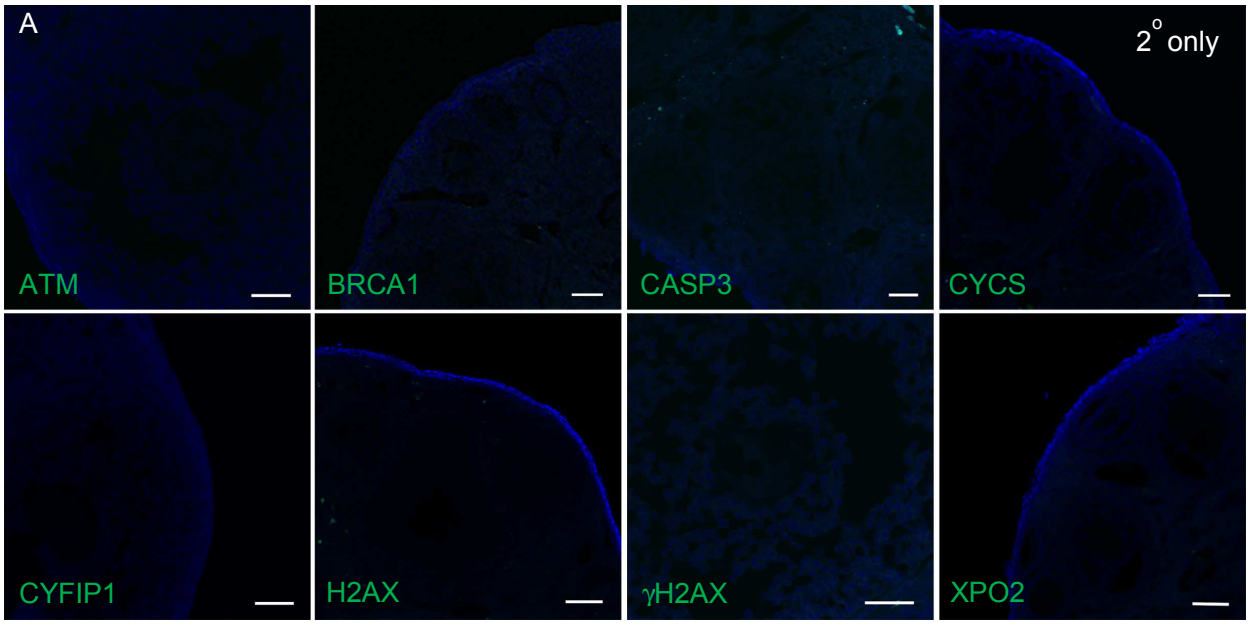

Supplemental Figure 1. Technical control for immunofluorescence staining.

Ovaries from an adult mouse were immunologically stained using only the secondary antibody appropriate for (**A**) ATM; (**B**) BRCA1; (**C**) CASP3; (**D**) CYCS; (**E**) CYFIP1; (**F**) H2AX; (**G**) γH2AX; (**H**) XPO2; scale bar = 50 μm.

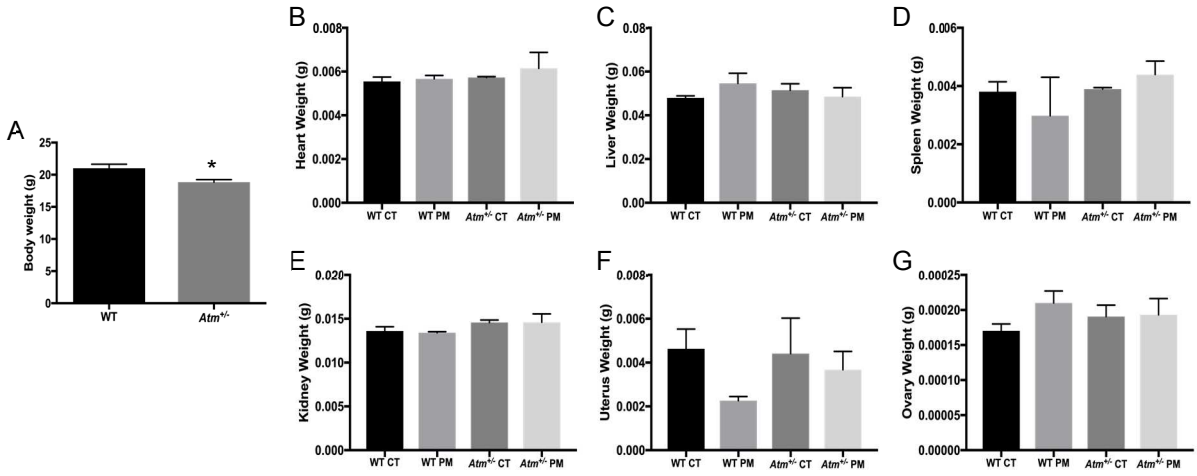

Supplemental Figure 2. Effects of *Atm*$^{+/-}$ deficiency on body weight and subsequent PM exposure on organ weights. (**A**) Body weight measured prior to i.p. dosing with vehicle-control or PM; (**B**) Heart; (**C**) Liver; (**D**) Spleen; (**E**) Kidney; (**F**) Uterus; and (**G**) Ovary weights collected three days post-injection with vehicle-control or PM. Values expressed as mean ± SEM; n = 3 per genotype/treatment. Significant difference indicated by * symbol at = $P < 0.05$

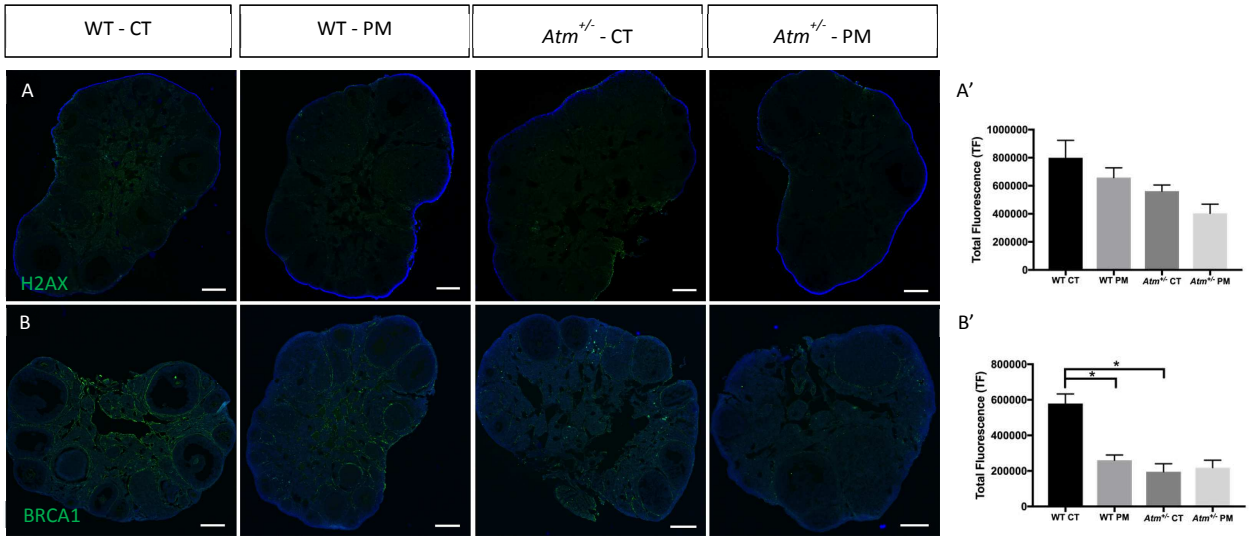

Supplemental Figure 3. Effect of *Atm* deficiency and/or PM exposure on DNA damage markers. Primary antibodies directed against (**A**) H2AX; and (**B**) BRCA1 were used to determine ovarian localization in WT CT; WT PM; *Atm*$^{+/-}$ CT; and *Atm*$^{+/-}$ PM. Green staining indicates the protein of interest while cellular DNA is stained in blue; scale bar = 200µm. Quantification of fluorescence intensity for (**A'**) H2AX; and (**B'**) BRCA1.

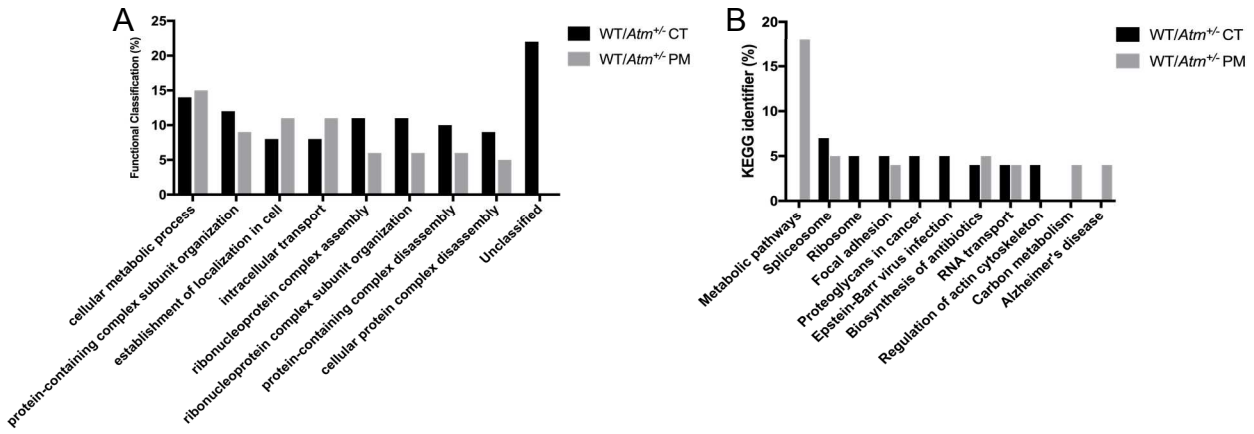

Supplemental Figure 4. **Functional classification and KEGG pathway analysis of proteins identified by LC-MS/MS.** *Atm*$^{+/-}$ mice after PM relative to WT after PM or *Atm*$^{+/-}$ mice after vehicle-control relative to WT after vehicle-control (**A**) Biological Process; and (**B**) KEGG identifier.

CHAPTER 5. LEAN MATERNAL GESTATIONAL DIABETES AND HYPERPHAGIA-INDUCED OBESITY IMPACTS OVARIAN GAP JUNCTION PROTEIN EXPRESSION

Kendra L. Clark and Aileen Keating*

Department of Animal Science – Iowa State University, Ames, Iowa 50011

A manuscript in preparation for submission to *Reproduction*

Contribution Statement:
K.L. Clark performed all analyses on ovarian tissue, designed experiments, and interpreted the data and wrote the manuscript. A.F. Keating designed the experiments, aided in data interpretation, and edited the manuscript.

Abstract

Normal granulosa cell communication and development is critical for cell differentiation and oocyte maturation, and the ovarian gap junction protein connexin 43 (CX43) facilitates cell communication between granulosa cells. We have discovered that gestational diabetes mellitus (GDM) exposure *in utero* and successive dietary challenge decreases healthy follicle populations in the ovary of the female mouse in addition to altering the ovarian proteome. We hypothesized that the abundance of ovarian CX43 would be decreased as a result from *in utero* GDM exposure and the added insult of a HFHS diet later in life. A HFHS challenge in the absence of maternal GDM (D_LP_H) and maternal GDM in the absence of a dietary stress (D_HP_L) did not alter CX43 expression in the offspring ovary. In contrast, a significant ($P < 0.01$) decrease in CX43 expression in

the offspring ovaries due to dietary challenge and exposure to maternal GDM *in utero* (D_HP_H) was observed. Additionally, we hypothesized that hyperphagia-induced obesity would alter ovarian CX43 abundance to contribute to obesity-induced ovarian dysfunction. There was a substantial decrease ($P < 0.01$) in CX43 abundance in the ovary from the obese mouse when compared to lean controls. Taken together, these findings demonstrate that changes in metabolism may impact ovarian CX43 abundance, indicating the importance of CX43 in follicular and oocyte health.

Keywords: gap junction, ovary, gestational diabetes, obesity

Introduction

The female gamete, the oocyte, is surrounded by granulosa cells in a follicular structure. To sustain follicular viability, there must be a source of nutrients and/or communication between granulosa cells and also between granulosa cells and the oocyte. Gap junctions (GJ) facilitate bidirectional communication between follicular cells (Eppig et al., 1996) and are membrane channels that enable the exchange of ions, metabolites, nucleotides, and secondary messengers between cells via a contact dependent mechanism (Goldberg et al., 2004). Ovarian GJ function to transfer amino acids, glucose metabolites and nucleotides to the growing oocyte (Eppig, 1991) and have a role in regulating meiosis in the mature oocyte (Granot and Dekel, 1994, Downs, 1995, Byskov et al., 1997).

Composed of connexons, a ring of six connexin (CX) proteins embedded within the plasma membrane, the GJ docks with another connexon in an adjacent cell, forming an intercellular channel, which is subject to functional regulation dependent on protein isoform or post-translational modifications (Winterhager and Kidder, 2015, Clarke, 2017).

The CX protein family has 20 members in mice and 21 in humans, and localization of specific CX can be used to identify GJ in various tissues (Sohl and Willecke, 2003). There are eight identified CX proteins ovarian and their abundance varies in a species-specific manner. In the rodent model, *Gjb1*/*Cx32*, *Gja4*/*Cx37*, *Gja1*/*Cx43*, *Gjc1*/*Cx45*, and *Gja10*/*Cx62* have been characterized in the ovary (Kidder and Mhawi, 2002).

GJA1/CX43 is an important GJ protein for communication between granulosa cells and is required for proper folliculogenesis (Ackert et al., 2001). Loss of function in the *Gja1* gene is postnatally lethal due to a severe cardiac defect (Juneja et al., 1999), and though the *Gja1*$^{-/-}$ fetus has some germ cells (Juneja et al., 1999), the absence of *Gja1* arrests folliculogenesis prior to the formation of multilaminar follicles, with negative impacts on oocyte growth, resulting in smaller oocyte diameters (Ackert et al., 2001).

Obesity is a metabolic disorder that predisposes individuals for multiple health conditions, and in the overweight or obese female, reproductive complications include poor oocyte quality (Metwally et al., 2007), decreased fertility (Brewer and Balen, 2010), polycystic ovary syndrome (PCOS) (Dravecka et al., 2003), and gestational diabetes mellitus (GDM) (Chu et al., 2007). Metabolic changes that occur during obesity negatively impact ovarian function and increase the insulin-responsive phosphatidylinositol 3-kinase (PI3K) pathway (Nteeba et al., 2013), promote inflammation (Nteeba et al., 2014b), reduce primordial and primary follicle numbers (Nteeba et al., 2014b), increase basal DNA damage and attenuate the DNA damage response (Nteeba et al., 2017, Nteeba et al., 2014a, Ganesan et al., 2017, Ganesan et al., 2015, Ganesan et al., 2014), and alter steroid hormone biosynthesis (Nteeba et al., 2017). We and others have demonstrated that *Cx43* mRNA and/or protein levels decrease during obesity in cardiac tissue in mice (Noyan-Ashraf et

al., 2013), uterine tissue in rats (Elmes et al., 2011), and in the ovary after 7,12-dimethylbenz[a]anthracene (DMBA) exposure (Ganesan and Keating, 2014) as well as during obesity at 18 and 24 weeks of age (Ganesan et al., 2015).

Connexin proteins are also altered in both type 1 and type 2 diabetes. Decreased CX43 abundance is observed in the kidneys (Zhang et al., 2006), retinal pericytes (Li et al., 2003), microvascular endothelial cells (Sato et al., 2002), penile corpora (Pointis, 2006), and epidermis (Wang et al., 2007) of hyperglycemic animal models. In Type 1 diabetic mice, CX43 protein level was decreased in cumulus enclosed oocytes (CEOs) from antral follicles (Chang et al., 2005). While pre-gestational obesity and/or insulin resistance is a major risk factor for a woman developing gestational diabetes mellitus (GDM), interestingly, around a third of GDM cases occur in lean women (Blickstein et al., 2018). Offspring from lean GDM dams (Pennington et al., 2017) were challenged during adulthood with a high-fat high-sucrose diet and had increased body weight, higher body fat percentage and increased adipose insulin sensitivity (Talton et al., 2019). In the female offspring, reduced healthy follicle numbers and an altered ovarian proteome were demonstrated, suggesting long-term effects on oocyte quality and fertility (Clark et al., 2019). Since obesity and Type-1/2 diabetes affects mRNA abundance encoding the *Cx43* gene and CX43 protein abundance in various tissue types, we hypothesized that GDM would impact ovarian CX43 abundance and localization both basally and in response to a high-fat, high-sucrose diet in adulthood. Additionally, we hypothesized that hyperphagia-induced obesity would alter ovarian CX43 abundance to contribute to obesity-induced ovarian dysfunction.

Material and Methods

Animal procedures and tissue collection

In utero GDM model: Ovarian tissue from female mice exposed to GDM *in utero* utilized in this study was obtained as part of a larger study (Clark et al., 2019, Talton et al., 2019). Briefly, GDM was induced in female C57B16/J (Jackson Laboratories; n = 14) mice by feeding a high-fat, high- sucrose (HFHS) diet one week prior to mating and throughout gestation, for a total of 4 weeks (Pennington et al., 2017, Talton et al., 2019). Control female C57B16/J mice (n = 20) were fed a chow breeder diet throughout the duration of the study. Female offspring from each litter (control – n = 30; GDM – n = 16) were maintained on a chow breeder diet, until 23 weeks of age, at which point 1-2 females from each litter were fed a HFHS diet until 31 weeks of age. Briefly, D_LP_L were lean dams and control diet pups; D_LP_H were lean dams and HFHS pups; D_HP_L were HFHS dams and control diet pups and D_HP_H were HFHS dams and HFHS pups. Ovaries were collected and ovaries were fixed in 4% paraformaldehyde and stored in 70% ethanol prior to histological processing.

Adult obese model: Female wild-type normal non-agouti (a/a; n = 6; designated lean) and agouti lethal yellow (KK.Cg-Ay/J mice; n = 6; designated obese) were purchased from Jackson Laboratory (Bar Harbor, ME) and maintained in an animal facility at Iowa State University under controlled room temperature (21°C-22°C) and lighting (12hr light:12hr dark) with *ad libitum* access to food and water. At 10 weeks of age, mice were euthanized in the pro-estrus phase of the estrous cycle. Ovaries were fixed in 4% paraformaldehyde overnight at 4°C for histological analysis.

All animal procedures were approved by the University of Missouri or the Iowa State University Institutional Animal Care and Use Committee and handled according to National Institutes of Health Guide for Care and Use of Laboratory Animals.

Histology

After fixation, ovaries were paraffin embedded or passed through a 10%, 20%/0.1M PBS gradient for 1-3 hours each at room temperature, followed by 30% sucrose/0.1M PBS overnight at 4°C and embedded in optimal cutting temperature (OCT) compound before being flash frozen on dry ice. Ovaries from GDM offspring were sectioned at 5 μm on a rotary microtome (AO Spencer 820) and ovaries from lean and obese mice sectioned at 7 μm on a cryostat (Leica CM1850) and mounted onto glass slides.

Immunofluorescence

Slides were deparaffinized in Citrisolv and rehydrated in washes of ethanol (100%, 95%, 75%), followed by one wash in ddH_2O. Heat-mediated antigen retrieval was performed using citrate buffer (10 mM citric acid, 0.5% Tween20, pH 6.0) by heating in a microwave for 22 min. Tissue sections were encircled with a histology pap pen (Vector Laboratories) to keep liquid concentrated on the tissue during processing, followed by the application of blocking solution (0.1M PBS/0.4% BSA/0.2% Tween20/2.5% goat serum) to the slides for 1 hour at room temperature. For frozen tissue, slides were warmed briefly on a 37°C slide warmer and tissue encircled with a histology pap pen to maintain solutions concentrated on the tissue during processing. Tissue was rehydrated and permeabilized in 0.1M PBS with 0.1% Tween20 (PBSTw) for 20 min, followed by serum blocking (0.1M

PBS/1% BSA/1% DMSO/5% goat serum) for 60 min at room temperature. Primary antibody directed against anti-rabbit CX43 (1:100; ab11370; Abcam) was diluted in fresh blocking solution, applied to the tissue sections, and incubated in a humidified box at 4°C overnight. After primary antibody incubation, slides were washed three times in PBSTw for 10 min per wash. Tissue sections were incubated in goat anti-rabbit Alexa Flour 488 (1:500; A11008; Invitrogen) and incubated at room temperature for 60 min, followed by four washes in PBSTw for 10 min per wash. Slides were air dried, followed by addition of Vectashield with DAPI (H1200, Vector Labs) and cured overnight at 4°C. Negative technical controls to confirm specificity were performed using secondary antibodies alone. Images were captured on a Zeiss LSM700 confocal microscope equipped with an AxioCam MRc5 using a 20x objective.

Quantification of protein abundance

For quantification of CX43 immunoreactivity, the total image area threshold measures in granulosa cells of antral follicles from the GDM study (n = 4 ovaries per treatment; 3 follicles per ovary) and hyperphagia-induced obesity study (n = 6 ovaries per treatment; 3 follicles per ovary) were analyzed using ImageJ (Schneider et al., 2012).

Statistical analysis

Statistical analyses were performed using GraphPad Prism 7.0 two-way ANOVA function for comparison of more than two treatments, comparing treatment with control or unpaired t-tests when two treatments were compared. Values are expressed as mean ± SEM, $P < 0.05$.

Results

Effects of *in utero* GDM exposure on ovarian localization of CX43

CX43 immunoreactivity was observed in the granulosa cells of primary, secondary, and antral follicles (**Figure 1A-C**) from ovaries of female mice that were fed a HFHS for 8 weeks (D_LP_H), in the ovaries of female mice that were subjected to GDM during fetal development (D_HP_L), in offspring ovaries that experienced GDM exposure during development and received a HFHS in adulthood (D_HP_H), and the control offspring who were not exposed to either treatment (D_LP_L). Positive CX43 immunostaining was also present in the granulosa lutein cells of the corpus luteum (**Figure 1D**), though was not present in squamous cells surrounding the primordial follicles.

Impact of hyperphagia-induced obesity on ovarian CX43 localization

Positive CX43 immunofluorescence staining was observed in granulosa cells in primary follicles, secondary follicles, antral follicles, and the granulosa lutein cells of the corpus luteum in the lean and the obese ovaries (**Figure 2B-E**). There was no CX43 immunostaining detected in the squamous follicular cells of primordial follicles (**Figure 2A**).

Impact of *in utero* GDM exposure on ovarian CX43 protein abundance

To determine if *in utero* exposure to GDM and/or dietary stressor later in life had an impact on CX43 abundance, fluorescence intensity was measured in the granulosa cells of the antral follicles. In the ovaries of mice exposed to only a HFHS diet in adulthood (D_LP_H) or only GDM *in utero* (D_HP_L), there were no differences in CX43 abundance in the

granulosa cells of antral follicles relative to controls not exposed to GDM or a dietary stressor (**Figure 3A-C, 3F**). An additive effect of dietary stress in later life (D_HP_H) reduced ($P = 0.002$) CX43 intensity in the granulosa cells of the antral follicles from ovaries of the offspring exposed to GDM *in utero* (**Figure 3D,F**).

Effects of hyperphagia-induced obesity on ovarian CX43 protein abundance

To determine if hyperphagia-induced obesity affected CX43 abundance, fluorescence intensity was measured in the granulosa cells of the antral follicles. Hyperphagia-induced obesity resulted in a decrease ($P = 0.006$) in CX43 immunoreactivity in the granulosa cells of the antral follicles with respect to the lean control mice (**Figure 4A-B,D**).

Discussion

Diet-induced obesity (DIO) models effectively mimic the gradual weight gain of humans, with the subtle accumulation of fat over a period of time. Metabolic consequences of a high-fat diet (HFD) become apparent after only a few days (Williams et al., 2014). CX43 protein is documented to vary in response to DIO: a HFD reduced CX43 abundance in atrial myocytes (Meng et al., 2017). In addition, uterine CX43 was reduced in HFD-fed relative to control diet-fed rats, and differences are apparent depending on whether the animal is experiencing parturition or not (Muir et al., 2016). In a model of adipocyte-specific *Gja1* knockdown, mice fed a HFD gained weight similarly as the wild-type (WT) fed the HFD over an 8 week time period, but demonstrated insulin resistance unlike their WT counterparts (Kim et al., 2017), implying some involvement of CX43 in metabolic

regulation. Conversely, CX43 protein is increased in the kidney glomerulus during DIO in rats (Zhao et al., 2018). Thus, there are tissue-specific differences in the response and evidence for an effect of DIO on abundance of the CX43 protein.

Changes in CX43 that are associated with diabetes include increased protein in vascular endothelial cells (VECs) (Dlugosova et al., 2009), smooth muscle cells (SMCs) (Alonso et al., 2010), myocytes (Howarth et al., 2008), sinoatrial node (Howarth et al., 2007), bladder detrusor muscle (Suadicani et al., 2009), and in the dermis after injury (Qiu et al., 2003, Wang et al., 2007). Conversely, CX43 levels are decreased in the SMCs of post-glomerular arterioles and mesangial cells in the diabetic kidney (Takenaka et al., 2011, Dronavalli, 2008), retinal pericytes and microvascular endothelial cells of the retina (Li et al., 2003, Fernandes et al., 2004), penile corpora (Pointis, 2006), and epidermis during wound healing (Kamibayashi et al., 1993).

The continuous rise of obesity in the global population has detrimental effects on the reproductive health of women and young girls including primary ovarian insufficiency (Shrestha et al., 2011), polycystic ovary syndrome (PCOS) (Dravecka et al., 2003), poor oocyte quality (Metwally et al., 2007), and decreased fecundity (Brewer and Balen, 2010). Ovarian folliculogenesis is regulated by a series of extrinsic and intrinsic signaling pathways, with definite roles for intraovarian gap junctions in oocyte development and maturation (Kidder and Mhawi, 2002). CX43 is one of the major ovarian gap junction proteins, and is essential for folliculogenesis, with *Cx43*-null ovaries having arrested follicle maturation and reduced oocyte growth (Ackert et al., 2001, Gittens et al., 2005). Additionally, in chimeric ovary studies that paired wild-type (WT) oocytes with *Cx43* deficient somatic cells and *Cx43* deficient oocytes with WT granulosa cells, fertilization

could be achieved in *Cx43* null oocytes supported by WT granulosa cells. In ovaries containing the *Cx43*$^{-/-}$ granulosa cells and WT oocytes, however, follicles halted at preantral stages and had smaller oocytes (Gittens et al., 2005, Gittens and Kidder, 2005). These functional studies provide strong support for the importance of CX43-mediated GJIC between granulosa cells in promoting follicular maturation. In the ovary of a Type 1 diabetic mouse model, CX43 protein level is decreased in cumulus enclosed oocytes (CEOs) derived from antral follicles (Chang et al., 2005). In this study, increased CX43 abundance was observed in granulosa cells of follicles as they mature, consistent with the requirements of intercellular communication for follicle growth and development as it prepares for ovulation (Eppig, 1991, Eppig et al., 1996).

Gap junction proteins are subject to hormonal regulation in the ovary and their abundance is dynamic throughout the estrous cycle. Estradiol (E_2) increases *Gja1* mRNA and stimulates GJ formation, while an inhibitory effect occurs with progesterone (P_4) (Lye et al., 1993, Karasinski et al., 2010). Follicle stimulating hormone (FSH) and luteinizing hormone (LH) also impact GJs, with FSH increasing *Gja1* mRNA and protein expression as follicle size enlarges (Valdimarsson et al., 1993, Beyer et al., 1989, Okuma et al., 1996, Fang et al., 2015) and LH suppressing *Gja1* mRNA and protein abundance (El-Hayek and Clarke, 2015, Granot and Dekel, 1994, Granot and Dekel, 1998, Khan-Dawood et al., 1998).

Considering impacts of obesity and/or diabetes on CX43 protein abundance, we sought to define whether this was also the case in the ovary. To investigate this posit, two different models of obesity were employed. The first is the ovaries from offspring who experienced GDM *in utero* in the absence of maternal obesity (Talton et al., 2019) and who

also were challenged with a high fat high sugar (HFHS) diet in adulthood. The second model used ovaries from adult mice who experienced hyperphagia-induced obesity.

Our group has recently described the impacts of lean *in utero* GDM on the offspring ovary as well as a dietary stressor later in life, which include reduced numbers of pre-antral follicles and an altered ovarian proteome (Clark et al., 2019). This model allowed us to investigate the underlying effects of maternal GDM without additive effects of maternal obesity on oocyte quality or development. Exposure to metabolic events such as diabetes during pregnancy predispose both the mother (Bellamy et al., 2009, Kim, 2014) and offspring (Vohr and Boney, 2008) to type 2 diabetes later in life, furthered by obesity (Nehring et al., 2013) and hypoglycemia (Gasim, 2012) in the offspring. Offspring that were exposed to our model of GDM *in utero* and later on challenged with the HFHS diet had increased body weight, higher body fat percentage, and increased adipose insulin sensitivity (Talton et al., 2019). We discovered that neither a HFHS diet nor GDM exposure alone affected CX43 protein abundance in antral follicles relative to the WT control. Interestingly, however, the two-hit stress of *in utero* GDM coupled with HFHS diet consumption in adulthood considerably reduced antral follicle CX43 protein abundance. The mice were aged 31 weeks and we have previously determined that aging contributes to a decline in CX43 protein abundance (Ganesan et al., 2015), however, these were compared to age-matched control females. Additionally, we had previously determined that GDM exposure and/or dietary stress does not result in increased apoptosis within the follicle (Clark et al., 2019), so the reduced levels of CX43 in the antral follicles are not attributable to a reduction in antral follicle number or viability. Additional experiments utilizing this same model at earlier timepoints would be beneficial in further

deciphering effects of GDM in sensitizing the offspring ovary to metabolic stressors later in life, resulting in potential negative impacts on fertility through a breakdown on GJ proteins and GJIC in the absence of advanced age.

The GDM model was designed to elucidate the effects of diabetes in the absence of obesity, and we also utilized a model in which the confounding effects of differing diets was absent. The lethal yellow mouse has a mutation which results in hypothalamic agouti overexpression, leading to hyperphagia due to altered alpha-melanocyte stimulating hormone and cocaine- and amphetamine regulated (Lu et al., 1994). We have previously determined that progressive obesity using this model as well as aging in lean and obese mice reduces both *Cx43* mRNA and protein levels (Ganesan et al., 2015) but have not examined the effects of obesity on CX43 at a time point of prime reproductive status. We have determined that, as early as 10 weeks, CX43 protein levels are markedly decreased due to obesity without any additive effects from dietary content. Similar to ovaries subject to GDM *in utero*, we observed no difference in numbers of cells marked for apoptosis (Clark *et al*, under review), indicating that reduced CX43 expression in the hyperphagia-induced obese model is not simply due to increased amounts of granulosa cell death.

Conclusions

These findings demonstrate the impact of obesity and altered metabolic programming on ovarian CX43 abundance. While it remains to be determined how this observation may impact fertility, decreased levels of CX43 protein in ovaries exposed to the metabolic changes that occur during obesity or GDM exposure *in utero* may indicate

an early target for improving ovarian function and underscore the importance of CX43 for follicular and oocyte health.

Declaration of Interest

The authors declare that there is no conflict of interest that could be perceived as prejudicing the impartiality of this research.

Funding

This work was funded by the Bailey Career Development Award from Iowa State University (AFK).

Author Contribution Statement

KLC and AFK contributed to experimental conception and design. KLC performed the experiments and analyzed the data. KLC wrote the first draft of the paper. All authors reviewed and approved the final manuscript.

References

ACKERT, C. L., GITTENS, J. E., O'BRIEN, M. J., EPPIG, J. J. & KIDDER, G. M. 2001. Intercellular communication via connexin43 gap junctions is required for ovarian folliculogenesis in the mouse. *Dev Biol,* 233**,** 258-70.

ALONSO, F., KRATTINGER, N., MAZZOLAI, L., SIMON, A., WAEBER, G., MEDA, P. & HAEFLIGER, J. A. 2010. An angiotensin II- and NF-kappaB-dependent mechanism increases connexin 43 in murine arteries targeted by renin-dependent hypertension. *Cardiovasc Res,* 87**,** 166-76.

BELLAMY, L., CASAS, J. P., HINGORANI, A. D. & WILLIAMS, D. 2009. Type 2 diabetes mellitus after gestational diabetes: a systematic review and meta-analysis. *Lancet,* 373**,** 1773-9.

BEYER, E. C., KISTLER, J., PAUL, D. L. & GOODENOUGH, D. A. 1989. Antisera directed against connexin43 peptides react with a 43-kD protein localized to gap junctions in myocardium and other tissues. *J Cell Biol,* 108**,** 595-605.

BLICKSTEIN, I., DOYEV, R., TROJNER BREGAR, A., BRZAN SIMENC, G., VERDENIK, I. & TUL, N. 2018. The effect of gestational diabetes, pre-gravid maternal obesity, and their combination ('diabesity') on outcomes of singleton gestations. *J Matern Fetal Neonatal Med,* 31**,** 640-643.

BREWER, C. J. & BALEN, A. H. 2010. The adverse effects of obesity on conception and implantation. *Reproduction,* 140**,** 347-64.

BYSKOV, A. G., YDING ANDERSEN, C., HOSSAINI, A. & GUOLIANG, X. 1997. Cumulus cells of oocyte-cumulus complexes secrete a meiosis-activating substance when stimulated with FSH. *Mol Reprod Dev,* 46**,** 296-305.

CHANG, A. S., DALE, A. N. & MOLEY, K. H. 2005. Maternal diabetes adversely affects preovulatory oocyte maturation, development, and granulosa cell apoptosis. *Endocrinology,* 146**,** 2445-53.

CHU, S. Y., CALLAGHAN, W. M., KIM, S. Y., SCHMID, C. H., LAU, J., ENGLAND, L. J. & DIETZ, P. M. 2007. Maternal obesity and risk of gestational diabetes mellitus. *Diabetes Care,* 30**,** 2070-6.

CLARK, K. L., TALTON, O. O., GANESAN, S., SCHULZ, L. C. & KEATING, A. F. 2019. Developmental Origins of Ovarian Disorder: Impact of Maternal Lean Gestational Diabetes on the Offspring Ovarian Proteome in Mice. *Biol Reprod*.

CLARKE, H. 2017. Control of Mammalian Oocyte Development by Interactions with the Maternal Follicular Environment. *Results Probl Cell Differ,* 63**,** 17-41.

DLUGOSOVA, K., WEISMANN, P., BERNATOVA, I., SOTNIKOVA, R., SLEZAK, J. & OKRUHLICOVA, L. 2009. Omega-3 fatty acids and atorvastatin affect connexin 43 expression in the aorta of hereditary hypertriglyceridemic rats. *Can J Physiol Pharmacol,* 87**,** 1074-82.

DOWNS, S. M. 1995. The influence of glucose, cumulus cells, and metabolic coupling on ATP levels and meiotic control in the isolated mouse oocyte. *Dev Biol,* 167**,** 502-12.

DRAVECKA, I., LAZUROVA, I. & KRAUS, V. 2003. Obesity is the major factor determining an insulin sensitivity and androgen production in women with anovulary cycles. *Bratisl Lek Listy,* 104**,** 393-9.

DRONAVALLI, S. D., I.; BAKRIS, G.L. 2008. The pathogenesis of diabetic nephropathy. *Nature Clinical Practice Endocrinology and Metabolism* 4**,** 444-452.

EL-HAYEK, S. & CLARKE, H. J. 2015. Follicle-Stimulating Hormone Increases Gap Junctional Communication Between Somatic and Germ-Line Follicular Compartments During Murine Oogenesis. *Biol Reprod,* 93**,** 47.

ELMES, M. J., TAN, D. S., CHENG, Z., WATHES, D. C. & MCMULLEN, S. 2011. The effects of a high-fat, high-cholesterol diet on markers of uterine contractility during parturition in the rat. *Reproduction,* 141**,** 283-90.

EPPIG, J. J. 1991. Intercommunication between mammalian oocytes and companion somatic cells. *Bioessays,* 13**,** 569-74.

EPPIG, J. J., O'BRIEN, M. & WIGGLESWORTH, K. 1996. Mammalian oocyte growth and development in vitro. *Mol Reprod Dev,* 44**,** 260-73.

FANG, W. L., LAI, S. Y., LAI, W. A., LEE, M. T., LIAO, C. F., KE, F. C. & HWANG, J. J. 2015. CRTC2 and Nedd4 ligase involvement in FSH and TGFbeta1 upregulation of connexin43 gap junction. *J Mol Endocrinol,* 55**,** 263-75.

FERNANDES, R., GIRAO, H. & PEREIRA, P. 2004. High glucose down-regulates intercellular communication in retinal endothelial cells by enhancing degradation of connexin 43 by a proteasome-dependent mechanism. *J Biol Chem,* 279**,** 27219-24.

GANESAN, S. & KEATING, A. F. 2014. Impact of 7,12-dimethylbenz[a]anthracene exposure on connexin gap junction proteins in cultured rat ovaries. *Toxicol Appl Pharmacol,* 274**,** 209-14.

GANESAN, S., NTEEBA, J. & KEATING, A. F. 2014. Enhanced susceptibility of ovaries from obese mice to 7,12-dimethylbenz[a]anthracene-induced DNA damage. *Toxicol Appl Pharmacol,* 281**,** 203-10.

GANESAN, S., NTEEBA, J. & KEATING, A. F. 2015. Impact of obesity on 7,12-dimethylbenz[a]anthracene-induced altered ovarian connexin gap junction proteins in female mice. *Toxicol Appl Pharmacol,* 282**,** 1-8.

GANESAN, S., NTEEBA, J., MADDEN, J. A. & KEATING, A. F. 2017. Obesity alters phosphoramide mustard-induced ovarian DNA repair in mice. *Biol Reprod,* 96**,** 491-501.

GASIM, T. 2012. Gestational diabetes mellitus: maternal and perinatal outcomes in 220 saudi women. *Oman Med J,* 27**,** 140-4.

GITTENS, J. E., BARR, K. J., VANDERHYDEN, B. C. & KIDDER, G. M. 2005. Interplay between paracrine signaling and gap junctional communication in ovarian follicles. *J Cell Sci,* 118**,** 113-22.

GITTENS, J. E. & KIDDER, G. M. 2005. Differential contributions of connexin37 and connexin43 to oogenesis revealed in chimeric reaggregated mouse ovaries. *J Cell Sci,* 118**,** 5071-8.

GOLDBERG, G. S., VALIUNAS, V. & BRINK, P. R. 2004. Selective permeability of gap junction channels. *Biochim Biophys Acta,* 1662**,** 96-101.

GRANOT, I. & DEKEL, N. 1994. Phosphorylation and expression of connexin-43 ovarian gap junction protein are regulated by luteinizing hormone. *J Biol Chem,* 269**,** 30502-9.

GRANOT, I. & DEKEL, N. 1998. Cell-to-cell communication in the ovarian follicle: developmental and hormonal regulation of the expression of connexin43. *Hum Reprod,* 13 Suppl 4**,** 85-97.

HOWARTH, F. C., CHANDLER, N. J., KHARCHE, S., TELLEZ, J. O., GREENER, I. D., YAMANUSHI, T. T., BILLETER, R., BOYETT, M. R., ZHANG, H. & DOBRZYNSKI, H. 2008. Effects of streptozotocin-induced diabetes on connexin43 mRNA and protein expression in ventricular muscle. *Mol Cell Biochem,* 319**,** 105-14.

HOWARTH, F. C., NOWOTNY, N., ZILAHI, E., EL HAJ, M. A. & LEI, M. 2007. Altered expression of gap junction connexin proteins may partly underlie heart rhythm disturbances in the streptozotocin-induced diabetic rat heart. *Mol Cell Biochem,* 305**,** 145-51.

JUNEJA, S. C., BARR, K. J., ENDERS, G. C. & KIDDER, G. M. 1999. Defects in the germ line and gonads of mice lacking connexin43. *Biol Reprod,* 60**,** 1263-70.

KAMIBAYASHI, Y., OYAMADA, M., OYAMADA, Y. & MORI, M. 1993. Expression of gap junction proteins connexin 26 and 43 is modulated during differentiation of keratinocytes in newborn mouse epidermis. *J Invest Dermatol,* 101**,** 773-8.

KARASINSKI, J., GALAS, J., SEMIK, D., FIERTAK, A., BILINSKA, B. & KILARSKI, W. M. 2010. Changes of connexin43 expression in non-pregnant porcine myometrium correlate with progesterone concentration during oestrous cycle. *Reprod Domest Anim,* 45**,** 959-66.

KHAN-DAWOOD, F. S., YANG, J. & DAWOOD, M. Y. 1998. Hormonal regulation of connexin-43 in baboon corpora lutea. *J Endocrinol,* 157**,** 405-14.

KIDDER, G. M. & MHAWI, A. A. 2002. Gap junctions and ovarian folliculogenesis. *Reproduction,* 123**,** 613-20.

KIM, C. 2014. Maternal outcomes and follow-up after gestational diabetes mellitus. *Diabet Med,* 31**,** 292-301.

KIM, S. N., KWON, H. J., IM, S. W., SON, Y. H., AKINDEHIN, S., JUNG, Y. S., LEE, S. J., RHYU, I. J., KIM, I. Y., SEONG, J. K., LEE, J., YOO, H. C., GRANNEMAN, J. G. & LEE, Y. H. 2017. Connexin 43 is required for the maintenance of mitochondrial integrity in brown adipose tissue. *Sci Rep,* 7**,** 7159.

LI, A. F., SATO, T., HAIMOVICI, R., OKAMOTO, T. & ROY, S. 2003. High glucose alters connexin 43 expression and gap junction intercellular communication activity in retinal pericytes. *Invest Ophthalmol Vis Sci,* 44**,** 5376-82.

LU, D., WILLARD, D., PATEL, I. R., KADWELL, S., OVERTON, L., KOST, T., LUTHER, M., CHEN, W., WOYCHIK, R. P., WILKISON, W. O. & ET AL. 1994. Agouti protein is an antagonist of the melanocyte-stimulating-hormone receptor. *Nature,* 371**,** 799-802.

LYE, S. J., NICHOLSON, B. J., MASCARENHAS, M., MACKENZIE, L. & PETROCELLI, T. 1993. Increased expression of connexin-43 in the rat myometrium during labor is associated with an increase in the plasma estrogen:progesterone ratio. *Endocrinology,* 132**,** 2380-6.

MENG, T., CHENG, G., WEI, Y., MA, S., JIANG, Y., WU, J., ZHOU, X. & SUN, C. 2017. Exposure to a chronic high-fat diet promotes atrial structure and gap junction remodeling in rats. *Int J Mol Med,* 40**,** 217-225.

METWALLY, M., CUTTING, R., TIPTON, A., SKULL, J., LEDGER, W. L. & LI, T. C. 2007. Effect of increased body mass index on oocyte and embryo quality in IVF patients. *Reprod Biomed Online,* 15**,** 532-8.

MUIR, R., BALLAN, J., CLIFFORD, B., MCMULLEN, S., KHAN, R., SHMYGOL, A., QUENBY, S. & ELMES, M. 2016. Modelling maternal obesity: the effects of a chronic high-fat, high-cholesterol diet on uterine expression of contractile-associated proteins and ex vivo contractile activity during labour in the rat. *Clin Sci (Lond),* 130**,** 183-92.

NEHRING, I., CHMITORZ, A., REULEN, H., VON KRIES, R. & ENSENAUER, R. 2013. Gestational diabetes predicts the risk of childhood overweight and abdominal circumference independent of maternal obesity. *Diabet Med,* 30**,** 1449-56.

NOYAN-ASHRAF, M. H., SHIKATANI, E. A., SCHUIKI, I., MUKOVOZOV, I., WU, J., LI, R. K., VOLCHUK, A., ROBINSON, L. A., BILLIA, F., DRUCKER, D. J. & HUSAIN, M. 2013. A glucagon-like peptide-1 analog reverses the molecular

pathology and cardiac dysfunction of a mouse model of obesity. *Circulation,* 127**,** 74-85.

NTEEBA, J., GANESAN, S. & KEATING, A. F. 2014a. Impact of obesity on ovotoxicity induced by 7,12-dimethylbenz[a]anthracene in mice. *Biol Reprod,* 90**,** 68.

NTEEBA, J., GANESAN, S. & KEATING, A. F. 2014b. Progressive obesity alters ovarian folliculogenesis with impacts on pro-inflammatory and steroidogenic signaling in female mice. *Biol Reprod,* 91**,** 86.

NTEEBA, J., GANESAN, S., MADDEN, J. A., DICKSON, M. J. & KEATING, A. F. 2017. Progressive obesity alters ovarian insulin, phosphatidylinositol-3 kinase, and chemical metabolism signaling pathways and potentiates ovotoxicity induced by phosphoramide mustard in mice. *Biol Reprod,* 96**,** 478-490.

NTEEBA, J., ROSS, J. W., PERFIELD, J. W., 2ND & KEATING, A. F. 2013. High fat diet induced obesity alters ovarian phosphatidylinositol-3 kinase signaling gene expression. *Reprod Toxicol,* 42**,** 68-77.

OKUMA, A., KURAOKA, A., IIDA, H., INAI, T., WASANO, K. & SHIBATA, Y. 1996. Colocalization of connexin 43 and connexin 45 but absence of connexin 40 in granulosa cell gap junctions of rat ovary. *J Reprod Fertil,* 107**,** 255-64.

PENNINGTON, K. A., VAN DER WALT, N., POLLOCK, K. E., TALTON, O. O. & SCHULZ, L. C. 2017. Effects of acute exposure to a high-fat, high-sucrose diet on gestational glucose tolerance and subsequent maternal health in mice. *Biol Reprod,* 96**,** 435-445.

POINTIS, G. 2006. Connexin43: emerging role in erectile function. *Int J Biochem Cell Biol,* 38**,** 1642-6.

QIU, C., COUTINHO, P., FRANK, S., FRANKE, S., LAW, L. Y., MARTIN, P., GREEN, C. R. & BECKER, D. L. 2003. Targeting connexin43 expression accelerates the rate of wound repair. *Curr Biol,* 13**,** 1697-703.

SATO, T., HAIMOVICI, R., KAO, R., LI, A. F. & ROY, S. 2002. Downregulation of connexin 43 expression by high glucose reduces gap junction activity in microvascular endothelial cells. *Diabetes,* 51**,** 1565-71.

SCHNEIDER, C.A., RASBAND, W.S. & ELICEIRI, K.W. 2012. NIH Image to ImageJ: 25 years of image analysis. *Nat Methods,* 9, 671-675.

SHRESTHA, A., OLSEN, J., RAMLAU-HANSEN, C. H., BECH, B. H. & NOHR, E. A. 2011. Obesity and age at menarche. *Fertil Steril,* 95**,** 2732-4.

SOHL, G. & WILLECKE, K. 2003. An update on connexin genes and their nomenclature in mouse and man. *Cell Commun Adhes,* 10**,** 173-80.

SUADICANI, S. O., URBAN-MALDONADO, M., TAR, M. T., MELMAN, A. & SPRAY, D. C. 2009. Effects of ageing and streptozotocin-induced diabetes on connexin43 and P2 purinoceptor expression in the rat corpora cavernosa and urinary bladder. *BJU Int,* 103**,** 1686-93.

TAKENAKA, T., INOUE, T., OKADA, H., OHNO, Y., MIYAZAKI, T., CHASTON, D. J., HILL, C. E. & SUZUKI, H. 2011. Altered gap junctional communication and renal haemodynamics in Zucker fatty rat model of type 2 diabetes. *Diabetologia,* 54**,** 2192-201.

TALTON, O. O., BATES, K., SALAZAR, S. R., JI, T. & SCHULZ, L. C. 2019. Lean maternal hyperglycemia alters offspring lipid metabolism and susceptibility to Diet-Induced obesity in mice. *Biol Reprod*.

VALDIMARSSON, G., DE SOUSA, P. A. & KIDDER, G. M. 1993. Coexpression of gap junction proteins in the cumulus-oocyte complex. *Mol Reprod Dev,* 36**,** 7-15.

VOHR, B. R. & BONEY, C. M. 2008. Gestational diabetes: the forerunner for the development of maternal and childhood obesity and metabolic syndrome? *J Matern Fetal Neonatal Med,* 21**,** 149-57.

WANG, C. M., LINCOLN, J., COOK, J. E. & BECKER, D. L. 2007. Abnormal connexin expression underlies delayed wound healing in diabetic skin. *Diabetes,* 56**,** 2809-17.

WILLIAMS, L. M., CAMPBELL, F. M., DREW, J. E., KOCH, C., HOGGARD, N., REES, W. D., KAMOLRAT, T., THI NGO, H., STEFFENSEN, I. L., GRAY, S. R. & TUPS, A. 2014. The development of diet-induced obesity and glucose intolerance in C57BL/6 mice on a high-fat diet consists of distinct phases. *PLoS One,* 9**,** e106159.

WINTERHAGER, E. & KIDDER, G. M. 2015. Gap junction connexins in female reproductive organs: implications for women's reproductive health. *Hum Reprod Update,* 21**,** 340-52.

ZHANG, X., CHEN, X., WU, D., LIU, W., WANG, J., FENG, Z., CAI, G., FU, B., HONG, Q. & DU, J. 2006. Downregulation of connexin 43 expression by high glucose induces senescence in glomerular mesangial cells. *J Am Soc Nephrol,* 17**,** 1532-42.

ZHAO, Y., LI, G., WANG, Y. & LIU, Z. 2018. Alteration of Connexin43 expression in a rat model of obesity-related glomerulopathy. *Exp Mol Pathol,* 104**,** 12-18.

Figures and Figure Legends

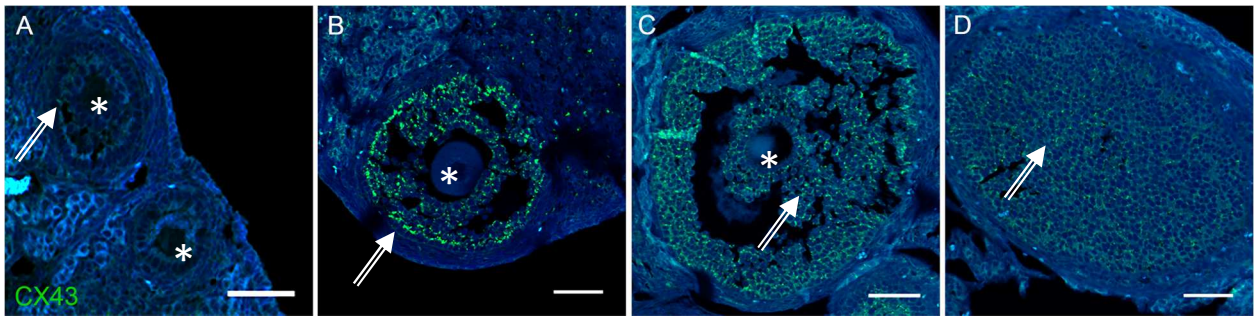

Figure 1: Localization of CX43 in the 31-week-old ovary. Immunofluorescence staining to detect CX43 location and abundance was performed. Positive staining in (A) primary; (B) secondary; (C) antral follicles; and (D) corpus luteum are presented. Green staining indicates CX43 while cellular DNA is stained in blue. Arrows indicate CX43 positive staining in granulosa cells. Asterix indicates oocyte. Scale bar = 50 μm.

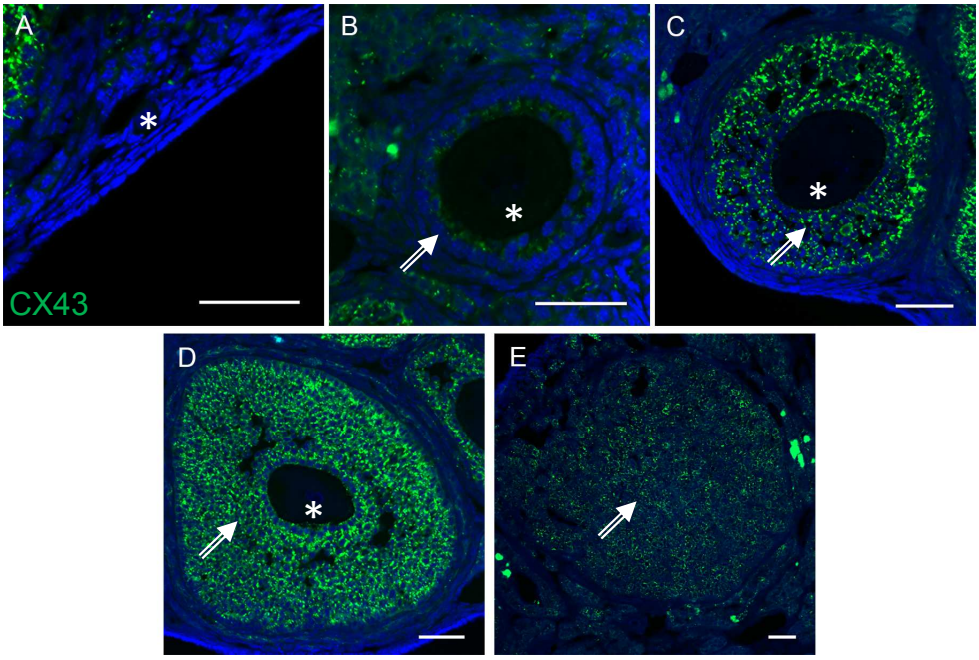

Figure 2: Localization of CX43 in the 10-week-old ovary. The localization and abundance of CX43 in (A) primordial; (B) primary; (C) secondary; (D) antral follicles; and (E) corpus luteum was determined using immunofluorescence staining. Green staining indicates CX43 while cellular DNA is stained in blue. Arrows indicate CX43 positive staining in granulosa cells. Asterix indicates oocyte. Scale bar = 50 μm.

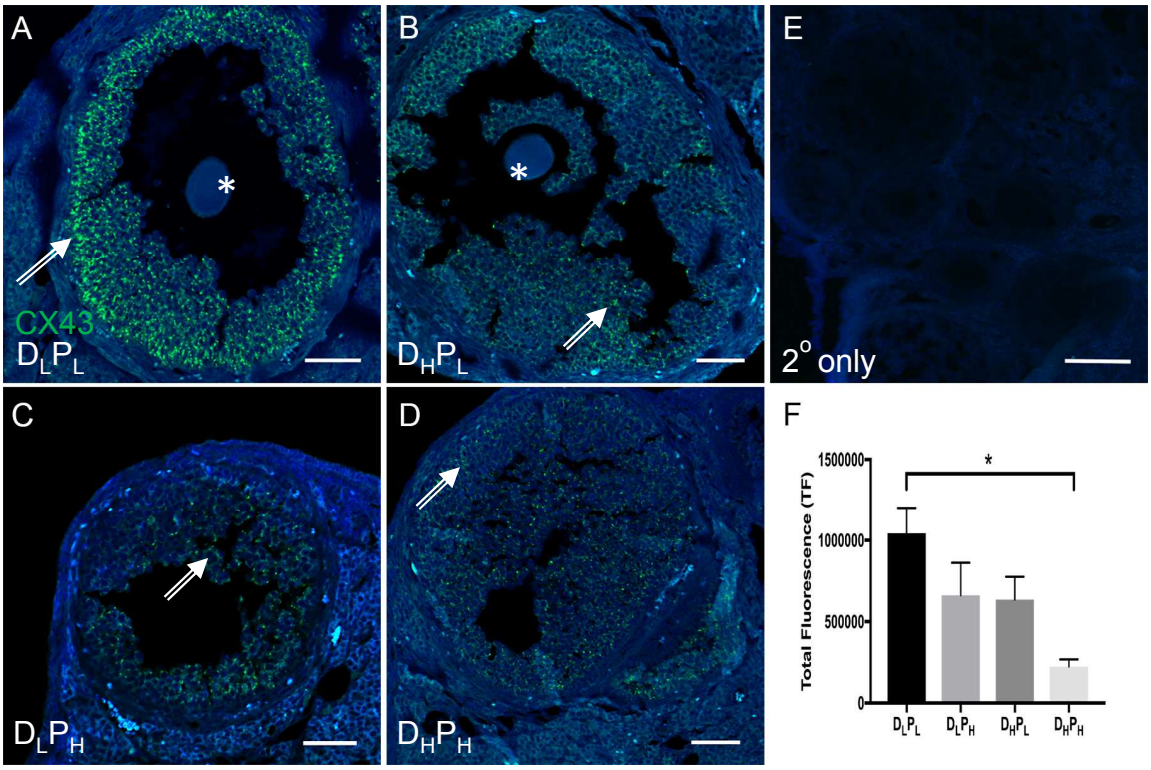

Figure 3: Effect of GDM and/or dietary stress on ovarian CX43. The abundance and location of CX43 protein in (A) D_LP_L; (B) D_HP_L; (C) D_LP_H; (D) D_HP_H mice was investigated using immunofluorescence staining. (E) Secondary antibody only control panel. Green staining indicates CX43 while cellular DNA is stained in blue. Arrows indicate CX43 positive staining. Asterix indicates oocyte. (F) The bars represent relative total fluorescence intensity ± SEM, * = $P < 0.05$. Scale bar = 50 μm.

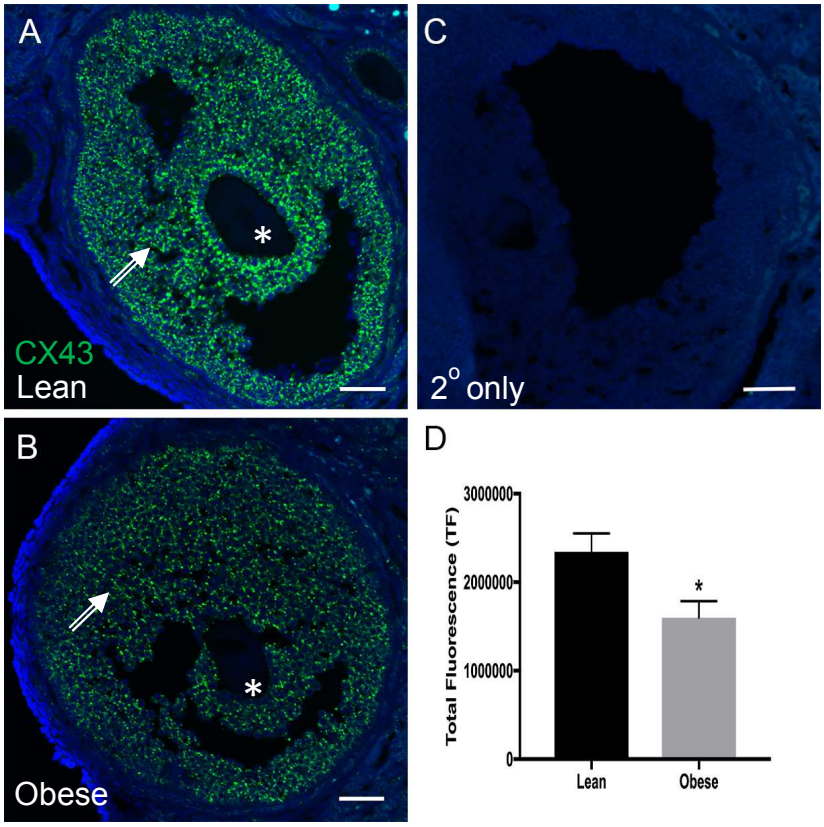

Figure 4: Effect of hyperphagia-induced obesity on ovarian CX43. Using ovaries from (A) Lean or (B) Obese mice, immunofluorescence staining was utilized to determine CX43 protein localization and abundance. Panel C illustrates the ovary in which only the secondary antibody was used in the staining procedure. Green staining indicates CX43 while cellular DNA is stained in blue. Arrows indicate CX43 positive staining. Asterix indicates oocyte. (D) The bars represent relative total fluorescence intensity ± SEM, * = $P < 0.05$. Scale bar = 50 μm.

CHAPTER 6. GENERAL CONCLUSIONS

Dissertation Summary

The studies conducted in this dissertation demonstrate the impacts of stressors such as obesity, *in utero* exposure to gestational diabetes, and chemotherapeutic drug administration on the ovarian proteome as well as on the ovarian DNA damage response. This work is relevant to the field of women's reproductive health and medicine, lending more insight into the dynamics of the molecular mechanisms that govern ovarian physiology and providing potentially novel targets to aid in planning or procedures that can help lessen the effects of harmful events to the germline and/or maternal health.

In chapter 2, we investigated the impacts of *in utero* gestational diabetes exposure on the ovaries from the adult offspring, some of which were subsequently challenged with a high-fat, high-sucrose diet later in life. Previous work by our group has determined that the metabolic alterations that occur during obesity such as hyperinsulinemia and hyperleptinemia have negative impacts on ovarian function [1-7], therefore, we hypothesized that the metabolic changes that occur during GDM in the absence of obesity would compromise ovarian function in the offspring both basally and in response to an environmental stressor later in life. The goal of this project was to determine what, if any, alterations occurred in the ovary, such as impacts on folliculogenesis, DNA damage, apoptosis, and changes in the ovarian proteome. Our results demonstrated that the two-hit stress model of GDM exposure *in utero* and later exposure to a HFHS diet in adulthood reduced follicle numbers relative to the age-matched control mice. The ovarian proteome was altered in all of the treatment groups from this study, though most significantly in the ovaries from offspring exposed to GDM *in utero* regardless of dietary challenge.

Interestingly, these metabolic alterations did not evoke a substantial DNA damage or apoptotic response in the ovary. The findings from this study illustrate that *in utero* exposure to GDM sensitizes the offspring ovary to an environmental stressor later in life, highlighting potential long-term effects to the health of the offspring in the presence of a metabolic event during development, potentially contributing to fertility issues and oocyte quality and laying the foundation for the developmental origin of ovarian disorder.

In chapter 3, we furthered our investigation of the impacts of a metabolic state on the ovary, focusing more on the DNA damage response during obesity. Utilizing a model of hyperphagia-induced obesity, we hypothesized that the DNA damage response would be altered during obesity. Our results discovered elevated levels of ATM in the oocytes from the obese mouse and increased amounts of γH2AX-positive cells in the ovary, indicating a low-level DNA response. Though other markers of the DNA damage response such as cleaved-caspase 3, BRCA1, and phospho-specific markers of BRCA1 and ATM were not increased globally, there were responses observed that were specific to follicle size. Additionally, the proteins CNPY2 and DAZAP1 that were identified in the proteomic study from offspring exposed to GDM *in utero* and a HFHS diet were not altered in our 10-week-old obese model. The data from this study illustrates that obesity elicits a universal DNA damage response from the ovary as well as a follicle stage-specific response. This provides rationale for the consideration of utilizing markers of the DNA damage response in diagnosis of ovarian health as well as the diagnosis and prevention of obesity-related reproductive disorders.

Based upon the findings described in chapter 4, we sought to further elucidate the molecular aspects of ATM-mediated DNA damage repair initiation. Previous work by our

group had determined that after chemical exposure, the DNA damage response was active within 24 hours of exposure [8-11], and that inhibition of the key transducer ATM resulted in the retention of follicles after chemical exposure, potentially contributing to germline DNA damage [11]. From this, we hypothesized that the DNA damage response is blunted in *Atm*-deficient mice, and that unhealthy follicles that would normally be triggered for repair and/or apoptosis remain, resulting in impaired fertility and increased amounts of retained DNA damage. The results determined that *Atm* deficiency results in fewer follicles basally, but no substantial follicle loss is observed between PM-exposed $Atm^{+/-}$ mice and $Atm^{+/-}$ controls, indicative of irregular activity in the DNA repair pathway. Moreover, the altered abundance of ovarian proteins during *Atm* deficiency highlights the critical interactions relative to DNA damage repair and the maintenance of genomic stability. These findings demonstrate the role of ATM in ovarian DNA repair and perhaps follicular atresia, indicating the importance of the pathway in response to a genotoxic stress.

Finally, in chapter 5, we examined the impacts of metabolic disorder on abundance of a gap junction protein, connexin-43 (CX43) in the ovary. Our previous finding that *in utero* GDM exposure and subsequent dietary challenge reduces healthy follicle numbers in the ovary [12] led to the hypothesis that abundance of CX43 would be decreased in this two-hit stress model. Additionally, using our model of hyperphagia-induced obesity, we hypothesized that CX43 abundance would decrease thus contributing to obesity-induced ovarian dysfunction. In both models, a decrease in CX43 abundance was observed in the antral follicles of the treatment ovaries relative to their respective controls. Together, these

findings demonstrate that changes in central metabolism impact CX43 abundance in the ovary with implications in follicular and oocyte health.

Albeit this work provides novel and interesting information on female reproductive function and health, it does meet with some limitations, most importantly that this research was performed in a rodent model and translation to other species, including humans, may not be coextensive. In the second chapter, we observed a decline in follicle numbers in our two-hit stress model, but age of the animals is a possible confounding factor to the study. Additionally, mice were not euthanized at the same stage of the estrous cycle as the ovaries were collected as a secondary and not the primary endpoint of interest. For this reason, we omitted antral follicle counts as we acknowledge that variation in the estrous cycle could have impacted this data. In chapter 3, four of the ten mice in the obese group were removed from the study since they were experiencing persistent diestrus, thus, reducing our overall number of observations in these experiments. Tandem mass spectroscopy liquid chromatography was utilized in this dissertation to establish novel proteomic impacts of the various exposures on the ovary. While a valuable tool in gleaning greater amounts of information from limited tissue source, there are considerations to be made including the fact that the protein was isolated from the entire ovary and post-translational protein modifications are not identified. For future proteomic studies it would be beneficial to isolate particular structures such as granulosa cell or theca cell layers, oocytes, whole follicles, and corpus lutea to determine protein dynamics localized to these tissue/cell types which may not be detectable when performing proteomics from whole ovarian tissue.

Future Outlooks

With the continuous rise in obesity, strategies to preserve and improve ovarian function during altered metabolic states are urgent. Continued investigation into established mechanisms, the identification and pursuit of novel targets in less characterized pathways and bridging the gap between the two will be the key to diminishing adverse reproductive outcomes. The work done by our group and others has established that obesity has several negative impacts on fertility including alterations in folliculogenesis [1, 13], the phosphatidylinositol 3-kinase (PI3K) pathway [2, 4], steroid hormone biosynthesis [1], increases amounts of inflammation [1, 3], DNA damage [5-7], and enhances susceptibility to genotoxic exposures [7, 14]. One of the studies included in this dissertation investigated the effects of an *in utero* metabolic exposure [12], but as more and more women become obese or overweight at younger ages, more pre-gestational exposures to obesity are occurring. An area for further consideration is investigating offspring reproductive effects throughout the lifespan, from development *in utero*, prepubertal stages, adolescence, adulthood, and advanced years. Of other interest would be investigating the transformation from obesity to weight loss and the plasticity of these effects that are observed during obesity.

Mutations in genes within the DDR pathway such as *Atm* [15] and *Brca1* [16] cause individual to have increased tumor susceptibility, therefore increasing their chances of being exposed to some form of anti-neoplastic therapy. While there have been great advances in cancer treatments, improving cancer survival rates, women who undergo various forms of cancer treatments have irreversible consequences on fertility from off-target effects from the harsh, yet life-saving drugs. The group especially impacted are pre-

menopausal women and girls and those who are heterozygous carriers of the *Atm* mutation. As a further insult to the reproductive health of women carrying these mutations, they may be subject to accelerated ovarian aging or begin with a smaller follicle reserve when compared to unaffected women [17]. Additionally, pregnancy outcomes are not well documented after pre-gestational chemotherapy treatment, with insight arising mostly from clinical data which presents several limitations such retrospective questionnaires, data pulled from various clinics, and varying chemotherapeutic agents [18]. Further investigations into fertility outcomes post-chemotherapy and the role of the DNA damage response could lead to planning or procedures that can help to lessen the effects of DNA damage on the germline.

Conclusion

Collectively, the research in this dissertation illustrates the importance of ovarian health and physiology, and the dynamic processes behind it in order to maintain a healthy reproductive status. Metabolic events, direct or indirect chemical exposures, and chemotherapy are sources of negative or ovotoxic effects on the ovary, thus identifying the mechanisms which cause follicle loss can lead to the development of preventative therapies which are less invasive than the current standards of gamete preservation. In addition to positive fertility outcomes, the perpetuation of female health also relies on proper ovarian signaling and function, preventing the onset of other disorders related to the cessation or dysfunction of ovarian activity. Identification of the potential mechanisms behind follicular atresia and the relationship with oocyte quality remain valuable to the field of ovarian biology and are pivotal in discovering methods to potentially mitigate premature ovarian failure.

References

1. Nteeba J, Ganesan S, Keating AF. Progressive obesity alters ovarian folliculogenesis with impacts on pro-inflammatory and steroidogenic signaling in female mice. Biol Reprod 2014; 91:86.
2. Nteeba J, Ganesan S, Madden JA, Dickson MJ, Keating AF. Progressive obesity alters ovarian insulin, phosphatidylinositol-3 kinase, and chemical metabolism signaling pathways and potentiates ovotoxicity induced by phosphoramide mustard in mice. Biol Reprod 2017; 96:478-490.
3. Nteeba J, Ortinau LC, Perfield JW, 2nd, Keating AF. Diet-induced obesity alters immune cell infiltration and expression of inflammatory cytokine genes in mouse ovarian and peri-ovarian adipose depot tissues. Mol Reprod Dev 2013; 80:948-958.
4. Nteeba J, Ross JW, Perfield JW, 2nd, Keating AF. High fat diet induced obesity alters ovarian phosphatidylinositol-3 kinase signaling gene expression. Reprod Toxicol 2013; 42:68-77.
5. Ganesan S, Nteeba J, Keating AF. Impact of obesity on 7,12-dimethylbenz[a]anthracene-induced altered ovarian connexin gap junction proteins in female mice. Toxicol Appl Pharmacol 2015; 282:1-8.
6. Ganesan S, Nteeba J, Madden JA, Keating AF. Obesity alters phosphoramide mustard-induced ovarian DNA repair in mice. Biol Reprod 2017; 96:491-501.
7. Ganesan S, Nteeba J, Keating AF. Enhanced susceptibility of ovaries from obese mice to 7,12-dimethylbenz[a]anthracene-induced DNA damage. Toxicol Appl Pharmacol 2014; 281:203-210.
8. Ganesan S, Bhattacharya P, Keating AF. 7,12-Dimethylbenz[a]anthracene exposure induces the DNA repair response in neonatal rat ovaries. Toxicol Appl Pharmacol 2013; 272:690-696.
9. Ganesan S, Keating AF. Phosphoramide mustard exposure induces DNA adduct formation and the DNA damage repair response in rat ovarian granulosa cells. Toxicol Appl Pharmacol 2015; 282:252-258.
10. Ganesan S, Keating AF. Bisphenol A-Induced Ovotoxicity Involves DNA Damage Induction to Which the Ovary Mounts a Protective Response Indicated by Increased Expression of Proteins Involved in DNA Repair and Xenobiotic Biotransformation. Toxicol Sci 2016; 152:169-180.
11. Ganesan S, Keating AF. The ovarian DNA damage repair response is induced prior to phosphoramide mustard-induced follicle depletion, and ataxia telangiectasia mutated inhibition prevents PM-induced follicle depletion. Toxicol Appl Pharmacol 2016; 292:65-74.
12. Clark KL, Talton OO, Ganesan S, Schulz LC, Keating AF. Developmental Origins of Ovarian Disorder: Impact of Maternal Lean Gestational Diabetes on the Offspring Ovarian Proteome in Mice. Biol Reprod 2019.
13. Thornton K, Asemota OA, Jindal SK, Charron M, Buyuk E. Obesity and high fat diet impair response to superovulation by suppressing genes involved in ovarian folliculogenesis. Fertility and Sterility 2015; 104:e121.
14. Nteeba J, Ganesan S, Keating AF. Impact of obesity on ovotoxicity induced by 7,12-dimethylbenz[a]anthracene in mice. Biol Reprod 2014; 90:68.

15. Athma P, Rappaport R, Swift M. Molecular genotyping shows that ataxia-telangiectasia heterozygotes are predisposed to breast cancer. Cancer Genet Cytogenet 1996; 92:130-134.
16. Robson M, Gilewski T, Haas B, Levin D, Borgen P, Rajan P, Hirschaut Y, Pressman P, Rosen PP, Lesser ML, Norton L, Offit K. BRCA-associated breast cancer in young women. J Clin Oncol 1998; 16:1642-1649.
17. Rzepka-Gorska I, Tarnowski B, Chudecka-Glaz A, Gorski B, Zielinska D, Toloczko-Grabarek A. Premature menopause in patients with BRCA1 gene mutation. Breast Cancer Res Treat 2006; 100:59-63.
18. Valentini A, Finch A, Lubinski J, Byrski T, Ghadirian P, Kim-Sing C, Lynch HT, Ainsworth PJ, Neuhausen SL, Greenblatt E, Singer C, Sun P, et al. Chemotherapy-induced amenorrhea in patients with breast cancer with a BRCA1 or BRCA2 mutation. J Clin Oncol 2013; 31:3914-3919.

APPENDIX. ISOLATION AND CULTURE OF PRIMARY EMBRYONIC ZEBRAFISH NEURAL TISSUE

Bhavika B. Patel*[1,2], Kendra L. Clark*[3,4], Emily M. Kozik[1], Linkan Dash[1,4], Julie A. Kuhlman[1], and Donald S. Sakaguchi[1,2#]

[1]Department of Genetics, Development, and Cell Biology, Iowa State University, Ames, Iowa 50011

[2]Neuroscience Program

[3]Department of Animal Science, Iowa State University, Ames, Iowa 50011

[4] Genetic and Genomics Program

**These two authors contributed equally*

A manuscript published in
Journal of Neuroscience Methods, 2019: p.108419
(Article in press)

Contribution Statement:

B.B Patel and K.L. Clark designed experiments, interpreted the data, and wrote the manuscript. E.M. Kozik aided with designing and performing the experiments. L. Dash aided in interpreting the data. J.A. Kuhlman and D.S. Sakaguchi designed the experiments, aided in data interpretation, and edited the manuscript.

Abstract

Background

Primary cell culture is a valuable tool to utilize in parallel with *in vivo* studies in order to maximize our understanding of the mechanisms surrounding neurogenesis and central nervous system (CNS) regeneration and plasticity. The zebrafish is an important model for biomedical research and primary neural cells are readily obtainable from their

embryonic stages via tissue dissociation. Further, transgenic reporter lines with cell type-specific expression allows for observation of distinct cell populations within the dissociated tissue.

New Method

Here, we define an efficient method for *ex vivo* quantification and characterization of neuronal and glial tissue dissociated from embryonic zebrafish.

Results

Zebrafish brain dissociated cells have been documented to survive in culture for at least 9 days *in vitro* (div). Anti-HuC/D and anti-Acetylated Tubulin antibodies were used to identify neurons in culture; at 3 div approximately 48% of cells were HuC/D positive and 85% expressed serotonin, suggesting our protocol can efficiently isolate neurons from whole embryonic zebrafish brains. Live time-lapse imaging was also carried out to analyze cell migration *in vitro.*

Comparison with Existing Methods

Primary cultures of zebrafish neural cells typically have low rates of survivability *in vitro.* We have developed a culture system that has long term cell viability, enabling direct analysis of cell-cell and cell-extracellular matrix interactions.

Conclusions

These results demonstrate a practical method for isolating, dissociating and culturing of embryonic zebrafish neural tissue. This approach could further be utilized to better understand zebrafish regeneration *in vitro.*

Keywords: Primary neuron culture; zebrafish; time-lapse microscopy; cell migration

Introduction

The use of zebrafish, *Danio rerio,* has emerged as a powerful tool in several aspects of developmental biology and biomedical research, frequently utilized as an *in vivo* model for several etiologies due to their optical clarity and external embryonic development [1]. The zebrafish boasts a fully sequenced genome, which makes it favorable to use for gene editing technologies such as TALEN or CRIPSR/Cas9 [2]. Likewise, the availability of cell and tissue specific fluorescent reporter lines allows for direct observations in the developing organism [3].

During embryonic development, neurogenesis begins in the zebrafish soon after gastrulation, defined by rapid proliferation and differentiation of neural progenitor cells, driving the formation of distinct brain and retinal structures as early as 2 days post fertilization (dpf) [4, 5]. Complementary to the dynamic shaping of the early nervous system, regeneration of mature neural tissue has been observed in the adult zebrafish. Functional and anatomical recovery of the CNS after brain or spinal cord injury occurs after initiation of axon regeneration and neurogenesis from putative stem cells [6], existing mature neurons [7], and radial glial cells [8]. These investigations have been crucial to our understanding of the cellular and molecular processes of neurogenesis and may potentially lead to the application of these findings in treating CNS disease or injury.

In addition to *in vivo* models, *in vitro* models have also been productive in gaining insights on the mechanisms of neuron specification and the active analysis of neural migration, though these studies have been primarily conducted in cells isolated from mammalian models [9-11]. *In vitro* methods utilizing neural tissue from both larval and adult zebrafish have been previously described and are becoming more prevalent, though

methods commonly result in a heterogeneous population of cells isolated from whole zebrafish embryos, known as primary cells [12-15]. Some methods have successfully isolated more specific groups of cells such as the spinal cord [16-18], brainstem [19], adult zebrafish brain [20, 21], and embryonic zebrafish brain [17]. Additionally, primary neuron cultures from specific cell types have been generated by fluorescence-activated cell sorting (FACS) and magnetic-activated cell sorting (MACS) [22-25]. The benefit of a primary culture system is that it allows direct observation of cell-type specific processes, which can easily be subject to molecular manipulation [21, 26, 27], chemical toxicity screening [28, 29], and/or live imaging [24, 30]. Further, zebrafish brain-derived cells can provide insight into mechanisms specific to lower vertebrates and help provide a better understanding of regeneration and plasticity that may be applicable to human medicine.

Here, we report an efficient method to isolate and dissociate zebrafish neural tissue adapted from a previous method of neural progenitor isolation from fetal mouse intestine [31]. Current protocols have demonstrated little quantitative assessment of zebrafish neural tissue derived cells. We sought to characterize the various cell types in culture using immunocytochemistry experiments. Zebrafish brain-derived cells were cultured for up to 9 days *in vitro* (div) with characterization of cells at 3 and 6 div. Our results produced a clean and efficient method for utilizing zebrafish as a source for primary neural culture. Further, we performed time-lapse imaging to better understand the dynamic nature of the dissociated cells and analyzed migration rates for different cell morphologies.

Methods

Fish stocks and husbandry

Embryos were obtained from the wild-type zebrafish line NHGRI (Zebrafish International Resource Center - ZIRC) and from zebrafish lines *Tg(elavl3:GFP)* [32] (provided by Dr. Robert Cornell, University of Iowa) and *Tg(gfap:GFP)*^{mi2001} [33]. Adult fish used for the generation of embryos were raised at 28.5°C in a light/dark cycle according to standard zebrafish husbandry protocols [34]. All experiments were performed within U.S. laws, guidelines, and policies for laboratory animals and were approved by the Institutional Animal Care and Use Committee (IACUC) and Institutional Biosafety Committee at Iowa State University.

Embryo collection and gnotobiotic techniques

Fertilized embryos were collected after natural spawning. At 24 hours post fertilization (hpf), developing embryos were incubated in 100 units/mL penicillin, 100 µg/mL streptomycin, and 0.25 µg/mL Amphotericin B Anti-biotic/Anti-mycotic solution (Sigma Aldrich, St. Louis, MO) in sterile embryo media (0.63g marine salt/liter) for 2-6 hours at 29.6°C. Embryos were rinsed in fresh sterile embryo media, washed in 0.005% sodium hypochlorite for 2 minutes, a subsequent rinse of sterile embryo media, then washed in 0.01% polyvinylpyrrolidone-iodine for 2 minutes. After disinfection, the embryos were rinsed two times in sterile embryo media and raised in an incubator at 29.6°C until 48-hpf (modified from [35]). At 48-hpf, surviving embryos were selected, rinsed in 0.005% sodium hypochlorite and placed in fresh sterile embryo media before being processed for cell culture.

Embryo extract preparation

Embryo extract was prepared as detailed in Kinikoglu et al., 2013. Briefly, 200 3-dpf wild-type embryos were rinsed with 0.5% sodium hypochlorite in sterile embryo medium followed by three subsequent washes in calcium-magnesium-free PBS. Embryos were transferred to a 1.5 mL microcentrifuge tube and excess PBS was removed, leaving only enough PBS to cover the embryos in the tube. Embryos were then homogenized on ice using a pestle, followed by addition of 1 mL L-15 basal media, and centrifugation at 900 rpm at 4°C for 6 minutes. The supernatant was removed and filtered through a 0.22 μm sterile filter and stored at -20°C. Prepared embryo extract can be utilized for several rounds of culture.

Dissection and dissociation

Embryos were staged to long pec stage (48-hpf) and where required, selected for GFP expression [34]. Embryos still in the chorion at the time of processing were manually removed from the chorions using fine forceps. For dissection, embryos were anesthetized in 0.01% MS222 (tricaine methanesulfonate, Sigma Aldrich) in Hank's Balanced Salt Solution (HBSS; Sigma Aldrich). Removal of the whole brain was done by first separating the head from the remaining embryo at the anterior portion of the spinal cord and then applying gentle pressure immediately anterior of the optic tectum. The whole brain was released from the cut posterior portion of the head. Tissue was collected in HBSS on ice with a maximum of 20 brains per tube, then spun down at 1500 rpm for 5 minutes at 4°C and remaining HBSS removed. For dissociation, Accumax™ (Innovative Cell Technologies, Inc, San Diego, CA) was added at a volume of 200 μL, followed by a 7-

minute incubation in a 37°C water bath. To stop the dissociation reaction, 700 µL of zebrafish culture media was added to the tube and mixed by gentle pipetting. The sample was then spun again at 1500 rpm for 5 minutes at 4°C and the cell-free supernatant discarded. The remaining pellet was resuspended in 100 µL of fresh culture media and placed on ice until plating.

Substrate preparation and cell culture

Entactin-Collagen IV-Laminin (ECL; Millipore, Burlington, MA) was diluted in L-15 basal media to a final concentration of 10 µg/mL and vortexed. Using a 12-channel micropipette, 100 µL of ECL solution was added into each well of a 96-well plate (Greiner Bio-One, Kremsmünster, Austria). The plate was sealed using Parafilm and stored overnight at 4°C.

For propidium iodide experiments, 12 mm glass coverslips were cleaned with RBS-35 detergent (1:50 in deionized (DI) water; Thermo Fisher Scientific, Waltham, MA) and boiled for 15 minutes. Coverslips were rinsed in DI water and sterilized under ultraviolet light for 1 hour. Coverslips were coated with ECL diluted in L-15 basal media (10 µg/mL) overnight at 4°C.

After dissociation, a Trypan blue (Sigma Aldrich) viable cell count was performed using a hemocytometer. The zebrafish brain-derived neural cells were plated at 6,000 cells/well in 96 well plates. Zebrafish complete media was composed of L-15 (Sigma Aldrich), supplemented with 2.5 mM L-alanyl-L-glutamine (GlutaMAX; Thermo Fisher Scientific), 15 ng/mL epidermal growth factor (human recombinant EGF; Thermo Fisher

Scientific), 10% fetal bovine serum (FBS; Atlanta Biologicals, Flowery Branch, GA) and 5% zebrafish embryo extract.

Cells were maintained in ambient temperature in a sterile environment. For time-lapse studies, media from wells was removed, the wells rinsed with sterile HBSS and fresh media was added prior to placing the 96 well plate into the ImageXpress Micro XLS. For immunocytochemistry experiments to characterize cells, media was changed every other day and cells were cultured for 3, 6 or 9 div.

Immunocytochemistry

After 3 or 6 days, the cells were rinsed twice with 0.1 M phosphate buffer followed by fixation with 4% paraformaldehyde (PFA; Thermo Fisher Scientific) in 0.1 M phosphate buffer for 20 minutes. After fixation, samples were rinsed (3 x 5 minutes) using phosphate buffered saline (PBS) and incubated for 90 minutes in a blocking buffer: 0.2% Tween20, 2.5% normal donkey serum (NDS; Jackson ImmunoResearch, West Grove, PA), 2.5% normal goat serum (NGS; Jackson ImmunoResearch), and 0.4% bovine serum albumin (BSA; Sigma-Aldrich) in PBS. Primary antibodies (Supplemental Table 1) were diluted in blocking buffer and incubated overnight at 4°C. Samples were rinsed (4 x 8 minutes) in PBS, followed by incubation in secondary antibody (Table 1) and 4',6-diamidino-2-phenylindole (1:50, DAPI; Invitrogen, Carlsbad, CA) nuclear stain diluted in blocking buffer and incubated for 90 minutes at room temperature. After secondary antibody incubation, wells were rinsed with PBS (4 x 8 minutes). Plates were sealed with Parafilm and stored at 4°C until ready for imaging.

Immunohistochemistry

Zebrafish larvae (2, 5, or 8-dpf) were anesthetized in 0.01% MS222 and fixed in 4% PFA in 0.1 M phosphate buffer for 4-6 hours at 4°C, then subsequently washed in PBS. For cryoprotection, fixed larvae were incubated in 5% sucrose/PBS solution for 1-3 hours at room temperature followed by 30% sucrose/PBS solution at 4°C overnight. Tissue was then placed in OCT (Fisher Healthcare, Houston, Texas) at room temperature before being flash frozen using dry ice. Sections were cut at 10 μm on a cryostat (Leica CM1850, Wetzlar, Germany), left to dry overnight on a slide warmer at 37°C, and processed directly. For antibody staining, tissue was rehydrated and permeabilized for 15 minutes in PBS with 0.1% Tween 20 (PBSTw) and blocked as described above. Sections were encircled with a histology pap pen to maintain antibody concentration over tissue. Primary antibodies (Table 1) were added in fresh blocking buffer and incubated in a humidified box at 4°C overnight. Slides were washed (3 x 10 minutes) in PBSTw, incubated in secondary antibody (Table 1) for 60 minutes at room temperature, followed by washes (4 x 10 minutes) in PBSTw. Slides were allowed to air dry, mounted using Vectashield Antifade Mounting Medium with DAPI (Vector Labs, Burlingame, CA), and left to cure overnight at 4°C. Images were taken on a LSM700 (Zeiss, Oberkochen, Germany) confocal microscope equipped with an AxioCam MRc5 using a 20x objective. For quantification of HuC/D (n = 8), 5-HT (n = 8), TH (n = 8), ChAT (n = 8), and GFAP (n = 8) immunoreactivity, the percentage of the total image area threshold (transverse section of the forebrain or midbrain) was analyzed using ImageJ [36].

Propidium iodide staining

Propidium Iodide (PI; Thermo Fisher Scientific) staining was used to detect dead cells in cultures at 3, 6 and 9 div. For these experiments, cells were cultured on ECL coated 12 mm glass coverslips. The stock solution of PI was diluted to 1.5 µM in zebrafish culture medium. For PI staining at each time-point, culture media was replaced with the PI solution and incubated for 20 minutes at room temperature. As a reagent control, one sample per time-point was incubated in 70% ethanol for 8 minutes to cause cell death before adding PI solution. After incubation, samples were rinsed with 0.1 M phosphate buffer, fixed with 4% PFA in 0.1 M phosphate buffer for 20 minutes at room temperature and rinsed with PBS. To stain cell nuclei, samples were incubated with DAPI (1:50) diluted in blocking solution for 30 minutes at room temperature. Samples were rinsed with PBS and mounted on microscope slides with DAPI Fluoromount-G mounting media for imaging.

Cell quantification and imaging

After immunocytochemistry, cells were imaged on the ImageXpress Micro high content screening system (HCS; Molecular Devices, San Jose, CA). Each 96-well plate was loaded into the ImageXpress Micro and allowed to equilibrate for 45 min at 25°C. Imaging was performed using a 20x objective. From one well, 49 microscopic fields were imaged. For imaging, four wavelengths were selected: Cy3 for primary antibodies (550 nm), GFP for endogenous transgene expression (395 nm), DAPI for nuclei (358 nm) and phase contrast. For quantification, all sites were analyzed quickly and without bias using a multiwavelength cell scoring module in the MetaXpress 4.0 software (Molecular Devices). The percentage of positively stained cells was calculated by dividing the number

of cells immunoreactive for each antibody by the total number of DAPI-stained nuclei per image. After, the average percentage of Cy3 expression was calculated and averaged across replicates.

Time-lapse imaging

For time-lapse imaging, *Tg(elavl3:GFP)* and *Tg(gfap:GFP)^{mi2001}* transgenic fish lines were dissociated and plated into an ECL coated 96-well plate as described above. After 24 hours *in vitro,* media from all wells was removed using a multi-channel pipette and rinsed with sterile HBSS. Fresh media was added to all wells and the plate was placed into the environmental chamber of the HCS system set to 25°C and the plate allowed to equilibrate for 1 hour prior to imaging. For time-lapse imaging, the 20x objective was used. Four wells per zebrafish line (*Tg(elavl3:GFP)* and *Tg(gfap:GFP)^{mi2001}*) were selected for imaging and four sites from each well were imaged. A total of 16 sites were imaged from each zebrafish line. Two wavelengths (phase contrast and GFP fluorescence) were selected for time-lapse imaging. Once the focus was established, images were captured every 5 minutes for 24 hours from all sites. Time-lapse imaging analysis for cell migration/cell tracking is described below.

Cell migration

Cells from each zebrafish transgenic line (*Tg(elavl3:GFP*) and *Tg(gfap:GFP)^{mi2001}*) were selected for analysis. Cells were tracked using MetaXpress software using the "Track objects" feature. For each cell tracked, the distance traveled, and the migration rate were collected. Cells tracked were single cells that remained within the imaging field for 24

hours. The selected cells' movements were tracked on a frame by frame basis using the cell tracker tool in the MetaXpress software. The output raw data was logged into a Microsoft Excel file. To better understand how migration may be different among cells, tracked cells were further classified based on cell morphology: spindle, flat or round). The data for average velocity of migration and total migration distance were compared between different cell morphologies using a one-way ANOVA or an ordinary t-test.

Results

Culture of zebrafish-brain derived cells

Zebrafish offer several advantages compared to mammals to study development. The zebrafish embryo is transparent and develops *ex vivo,* allowing for *in vivo* imaging and monitoring of neurodevelopment. Although *in vivo* approaches to study development have been well documented, little research has been directed to developing *in vitro* systems using zebrafish. Current protocols to dissociate cells from neural tissue have shown variable cell viability and quantitative analyses of cells [17, 24, 37, 38]. In an attempt to utilize current protocols, we made efforts to adapt those protocols with different variations but had little success (Supplemental Table 2). Therefore, the purpose of this study was to develop a new method to isolate and dissociate zebrafish neural tissue for primary culture that can be cultured for a longer period of time than current protocols. As a result of our experiments, we identified Accumax™ as the best enzymatic component for dissociation that also yielded the highest cell survival and viability. Further, our group optimized the Accumax™ incubation time in order to obtain clean cultures with viable cells (Supplemental Figure 1). Cells incubated in Accumax ™ for less than 7 minutes had many

detached cells by 2 div and those incubated for more than 7 minutes exhibited a fibroblast-like morphology. On the other hand, cells dissociated using an incubation time of 7 minutes had many cells attached at 2 div as well as a neuronal morphology with small processes emanating from the cell body.

To generate primary neural tissue, whole brains from embryonic *Tg(elavl3:GFP)*, which expresses GFP in neurons and can be easily identified in culture, and wild-type zebrafish were isolated and dissociated using the protocol described above (summarized in **Figure 1**). The cells were cultured as a monolayer on ECL-coated 96 well plates. As shown in **Figure 1**, the cells displayed a variety of morphologies such as round with short and long processes, spindle-shaped and flat fibroblast-like. During the time of plating, single cells were present for up to 6 div and cultures were observed up to 9 div. (**Figure 1** (B).

Cell viability

Propidium iodide (PI) staining was used to evaluate cell survival from the dissociated zebrafish neural tissue at 3, 6 and 9 div (**Figure 2)**. This assay uses a red-fluorescent nuclear and chromosome counterstain that is only permeable to dead cells. The dissociated neural cells were seeded onto ECL coated glass coverslips. As a positive reagent control, two different coverslips at each time-point were exposed to 70% ethanol to intentionally kill cells. At 3, 6 and 9 div, there was an average of 311± 16, 214 ± 25 and 160 ± 16 DAPI positive cells present in culture, respectively. At 3 div, approximately 27% PI-labeled cells were detected following the ethanol incubation as illustrated in **Figure 2** (A_1,B_1,C_1). The percentage of PI-labeled dead cells at 3 div (3.1%) was negligible with only a few cells labeled with PI compared to a parallel coverslip that was ethanol treated

(**Figure 2** (A_1-A_4, B_1-B_4)). At 9 div 28.2% of the cells in the primary cultures were PI-stained. (**Figure 2** (C_1-C_4)). These results indicate that our culture conditions provide survivability of dissociated zebrafish brains for up to 9 div.

Characterization of dissociated neural tissue

Embryonic wild-type and *Tg(elavl3:GFP*) zebrafish brains were isolated and dissociated in order to obtain a primary culture of neuronal cells. A total of 40 brains were dissected and dissociated for each replicate. An image-based high content screening (HCS) system using MetaXpress software coupled with immunocytochemistry using a panel of cell type specific antibodies was used to characterize the differentiation of the dissociated neural tissue. This technology enables screening a panel of cell-specific antibodies at multiple time-points. Compared to conventional imaging methods, using an HCS system is rapid and allows for non-bias characterization. For this study, adult fish from 5 different tanks represented 5 experimental replicates. From each replicate, 40 brains were dissociated and plated into 32 wells of a 96 well plate. Three replicates were plated in a single 96 well plate while the remaining 2 replicates were plated in a second plate. In each well, 49 microscopic imaging fields were taken using three fluorescent filter sets: Cy3, GFP and DAPI and transmitted light for a total of 196 images per well. For characterization, four wells were used per cell-specific antibody, leading to 784 imaging fields analyzed per replicate, for a total of 3,920 sites analyzed between all 5 replicates per antibody.

Cells were plated into an ECL coated 96 well-plate and characterized using immunostaining for various neuronal and glial cell specific antibody markers. First to

detect neurons in culture, two pan-neuronal antibodies were used: HuC/D, an early marker for neurons [39] and Acetylated Tubulin, an axonal marker which demarcates axonal tracts in the zebrafish brain [40]. These two neuronal antibodies were used together to label the nucleus and processes of the neuron (referred to as HuC/D-Acetylated Tubulin in this study). At 3 div, approximately 47% of cells were immunopositive for HuC/D-Acetylated Tubulin. In **Figure 3** (A_1), long processes are seen labeled with Acetylated Tubulin at 3 div (**Figure 3** (A_1)) and at 6 div (**Figure 3** (B_1)). Quantification revealed there was no significant difference for HuC/D-Acetylated Tubulin expression between 3 and 6 div cultures (47.6% ± 8.8 and 27.3% ± 4.3, respectively). Although there is a slight decrease in the number of cells labeled with HuC/D-Acetylated Tubulin at 6 div, this protocol allowed for longer zebrafish neuron survival *in vitro*.

To detect serotonergic neurons within cultures, we found 85% expressed 5□ hydroxytryptamine (5□HT) (**Figure 4**), a neurotransmitter important in development and neurogenesis in zebrafish [41] as well as mammals [42] however this was significantly decreased by 6 div (48% ± 5). No detectable immunolabeling was found for tyrosine hydroxylase (TH) and choline acetyltransferase (ChAT) (data not shown).

To determine if this dissociation and culturing protocol promoted the survival of other neural tissue cell types, we investigated the presence of glial cells, which are abundant in the CNS of zebrafish. Glial fibrillary acidic protein (Gfap) identifies glial cells within the zebrafish brain including radial glia and astrocytes [43]. The percentage of cells immunostained with Gfap at 3 div (26% ± 1.8) were comparable to those at 6 div (30.1% ± 2.2) indicating no loss of Gfap immunopositive cells in our cultures (**Figure 5** (A_1 and B_1)).

These results indicate our method of dissociating embryonic zebrafish neural tissue is efficient in maintaining a viable population of glial cells. Frozen-sectioned zebrafish brain tissue at comparable time-points were immunolabeled as positive controls for the antibodies (Supplemental Figure 2(A). The neuronal subtypes 5-HT, ChAT, and TH, as well as pan-neuronal marker HuC/D and the glia marker Gfap were detected in our sections, though ChAT and TH positive cells were substantially lower than HuC/D, 5-HT, and Gfap, similar to the results from the neural tissue culture (Supplemental Figure 2(B).

Thus far, using our method to dissociate zebrafish neural tissue we have created a primary culture containing neurons and glial cells. Our cultures survive up to 9 div as detected with the propidium iodide assay, with approximately 85% of cells expressing 5-HT at 3 div and neurons present as detected by HuC/D-Acetylated tubulin immunostaining for up to 6 div. Due to the low number of cells at 9 div immunocytochemistry experiments were not conducted, however using propidium iodide assays we were able to demonstrate the survival of cells up to 9 div.

Migration of cells in vitro

To investigate the behavior of neuronal and glial cells *in vitro,* embryonic brain tissue from two transgenic zebrafish lines (*Tg(elavl3:GFP*) marking the neuronal populations and *Tg(gfap:GFP)*^{mi2001} marking the glia populations were dissociated using the protocol described above. The behaviors of the dissociated cells were monitored using time-lapse digital microscopy with transmitted and fluorescence illumination of the HCS system. Multiple sites were time-lapsed imaged and used to calculate the distance travelled

for *Tg(elavl3:GFP*) (Supplemental video 1) and *Tg(gfap:GFP)^{mi2001}* (Supplemental video 2) cell types as well as their migration rates.

The average velocity of cell migration and total distance travelled by cells was obtained using MetaXpress software for both cell types. First, cells were classified based on morphology (flat, spindle or round). Distance travelled and migration rates were calculated for cells dissociated from *Tg(elavl3:GFP*) or *Tg(gfap:GFP)^{mi2001}* zebrafish larval brains. From cells dissociated from *Tg(elavl3:GFP*) neural tissue, the GFP expressing round cells (17.5 ± 1.18 μm/h) and GFP-expressing spindle shaped cells (12.04 ± 1.07 μm/h) had higher migration rates compared to flat cells (6.65 ± 0.67 μm/h) (**Figure 6A**). Additionally, the average total migration of round cells (279.28 ± 22.72 μm) during the 24-hour imaging period was higher than flat cells (117.91 ± 11.47 μm) (**Figure 6B**). These results are captured in supplementary video 1 as round cells migrate long distances towards other cells, rather than being isolated. Further, round cells are migrating towards flatter cells and often change behavior; once adhered to flatter cells, the round cells do not migrate as fast and the distance travelled is lower. Interestingly, cell behavior was distinct among different morphologies which may be associated to neuronal subtypes present in culture.

From cells dissociated using *Tg(gfap:GFP)^{mi2001}* neural tissue, we observed both GFP-expressing round and spindle shaped cells but no flat cells in culture. GFP-expressing round and spindle shaped cells migrated similar distances (336.4 ± 77.87 μm and 328.3 ± 52.89 μm, respectively) and with similar average migration rates (13.78 ± 3.17 μm/h and 13.45 ± 2.15 μm/h, respectively) over a period of 24 hours. Overall, GFP positive Gfap cells, regardless of cell morphology, migrated relatively larger distances (331.8 ± 43.39

μm) compared to GFP positive Elavl3 cells (114.2 ± 41.07 μm), demonstrating that overall, glial cells travelled longer distances than neurons *in vitro*.

Discussion

Primary cell culture is used as a tool to understand cell biology under defined conditions as an alternate to *in vivo* systems. However, zebrafish primary cultures receive little attention due to the fact that zebrafish serve as a great *in vivo* system to study genetics, development, regeneration and more. Unlike *in vivo* systems, *in vitro* systems offer several advantages, such as studying cell behavior in controlled environments and provide a better understanding of cellular mechanisms and interactions. Zebrafish primary culture can be used to investigate developmental and regenerative processes by studying cell-cell and cell-extracellular matrix (ECM) interactions, as well as for drug screening and toxicity bioassays. Currently, several protocols exist to isolate neural cells from larval and adult zebrafish tissue [12, 15-18, 24, 25, 38, 44, 45]. Only a portion of these protocols show cell survival past 7 div [19, 21, 22]. However, these protocols have not described conditions that permit survival of cells long-term and lack quantitative analysis of the dissociated cells. The current study examines a new method for isolation and dissociation of embryonic zebrafish brains with quantitative characterization of the primary culture and cultures that survive for up to 9 div. Immunohistochemistry conducted alongside immunocytochemistry experiments validate that our antibodies are properly immunostaining neuronal subtypes including ChAT and TH although they were not present *in vitro.*

Our protocol resulted in successful dissociation and culture of embryonic zebrafish neural tissue for up to 9 days *in vitro*. For optimal growth conditions, epidermal growth

factor (EGF) was necessary to promote survival of cells. Initial experiments did not include EGF and cells were not viable for longer than 3 div with very small processes. Although the process of enzymatic dissociation may affect the growth of neurons previously developed in the brain, the addition of EGF promoted cell growth and survival *in vitro* for up to 9 div. The inclusion of zebrafish embryo extract also promoted viability and growth in the culture; when omitted from culture we observed slower growth and less cell attachment. Furthermore, incubation times of Accumax™ were optimized to achieve adequate cell dissociation with extensive cell survival. We found that incubating cells for longer than 7 minutes resulting in considerably less cell attachment and survival after 1 div and incubation times less than 7 minutes resulting in substantially large clusters of undissociated tissue. Further, additional trituration performed halfway during the dissociation time increased the yield of individual cells, but at the cost of total viable cell yield. Given this, additional mechanical dissociation can be utilized in our method to segregate a greater number of individual cells if cell density is not such an important consideration for an experimental endpoint such as in this study. The amount of dissected tissue per tube was also a factor in cell viability. The cells with decreased surface area at the bottom or center of the collection tube experienced a hypoxic-like effect, ultimately effecting the likelihood of cell survival after plating. Overall cell viability and attachment probability could be estimated after plating by observing cells under phase contrast. Round, phase bright cells had higher attachment probably compared to darker cells along with debris in wells, which may indicate dead cells.

Embryonic zebrafish brain cultures contain neuronal and glial cells, with a majority of neurons co-expressing pan-neuronal marker HuC/D and serotonin (5-HT), indicating a

serotonergic phenotype. The 5-HT neurotransmitter has various roles in the CNS, stemming from the raphe nuclei and contributing to the proliferation, migration, differentiation of neuroblasts, synapse formation, and regulating neurite outgrowth [46-50]. Around 85% of cells in our culture system were 5-HT positive at 3 div, coinciding with a timeline of rapid 5-HT innervation observed in the larval zebrafish at 5-dpf [51] (brain tissue from 2 dpf + 3 div would be equivalent to 5-dpf). Interestingly, this decreases after 6 div to 48%, exhibiting a possible decrease in this developmental time point as observed *in vivo* [51]. Further, radial glial cells have been shown to proliferate and give rise to 5-HT neurons in the paraventricular organ located in the diencephalon in the adult zebrafish [41]. This is a possible explanation as to why we detected less HuC/D positive cells than 5-HT possible cells, though this remains to be investigated at the larval stage in zebrafish.

Surprisingly, immunoreactivity was not detected when using antibodies directed against other neuronal subtypes ChAT and TH, though the subtypes were observed in whole tissue sections. This could be as a result of the dissociation process, which could alter the endogenous signaling in dissociated tissue. Additionally, at the initial dissociation timepoint of ~48 hpf, secondary neurogenesis has commenced in the embryonic zebrafish brain [27]. From this timepoint on, the distribution of proliferative cells, newly determined neurons, and advanced post-mitotic neurons is dynamic, with tighter spatio-temporal restriction on the distinct populations as the brain develops [52]. The substantial differences in immunoreactivity we observed in our culture and our tissue sections of the neuronal subtypes versus the predominate labeling of serotonergic cells is possibly a result of the progressive rates of maturation in our culture post-dissociation. We also observed

Gfap-positive cells in 25% of cells after 3 div, with a slight increase to around 30% of cells after 6 div. In the developing brain, Gfap positive radial glia have been shown to be progenitors for astrocytes and neurons in mammals suggesting that radial glia were present in culture [53].

Cell culture systems allow researchers to study cell behavior in a controlled environment while being able to vary conditions, such as substrates for cell attachment and exogenous growth factors for regulating *in vitro* differentiation. In our experiments, cells were cultured on an ECL substrate, however cell migration can differ on other substrates, including Poly-L-ornithine, Poly-L-lysine or fibronectin; neural stem/progenitor cells (NSPCs) cultured on these substrates exhibited varying levels of differentiation and proliferation [54, 55]. Endogenous NSPCs grow within specialized areas of the brain, known as niches. Cells secrete an ECM within this niche and is an important contributor to essential cell functions including mitosis, cell migration, cell signaling and apoptosis [56, 57]. Because the ECM is a vital component, our current study can be expanded using other substrates to provide insight on cell functions and better understand cell behavior *in vitro*.

Using our protocol, cells were successfully dissociated from zebrafish neural tissue and used for time-lapse microscopy. Round shaped cells had a strong tendency to adhere to flatter cells, which may be indicative of radial glial cells in culture. In the CNS, radial glial cells support neuronal migration during development and guide axons to their correct targets [58, 59]. Our results support our analysis of cell migration because Gfap-positive cells migrated longer distances than Elavl3-positive neurons. Time-lapse microscopy can be used to monitor cell division, apoptosis as well as be used to study cell-cell interactions.

Therefore, our protocol is sufficient in producing a clean and viable culture that can be used for real time imaging experiments.

Overall, our method for dissociation of embryonic zebrafish brains is efficient to generate a heterogenous primary culture of neurons and glia. It requires basic microdissection skills, standard lab equipment, and minimal reagents. Further, our study examined the population in detail by conducting immunocytochemistry for neuronal subtypes as well as glial cells. Our culture method could be used to compliment studies using fluorescence-activated cell sorting (FACS) or magnetic-activated cell sorting (MACS) for more targeted cell type observations. Whether paired with *in vivo* models or utilized exclusively, zebrafish *in vitro* methods can provide further insight into the molecular mechanisms between cell-cell interactions and in a variety of applications including developmental biology and regeneration.

Acknowledgements

This work was funded by a REACH Research Grant (Awarded to Dr. Kuhlman), the Stem Cell Research Fund and the Department of Genetics, Development and Cell Biology.

References

1. Bradford, Y.M., et al., *Zebrafish Models of Human Disease: Gaining Insight into Human Disease at ZFIN.* Ilar j, 2017. **58**(1): p. 4-16.
2. Hwang, W.Y., et al., *Efficient genome editing in zebrafish using a CRISPR-Cas system.* Nature Biotechnology, 2013. **31**: p. 227.
3. Holder, N. and Q. Xu, *Microinjection of DNA, RNA, and Protein into the Fertilized Zebrafish Egg for Analysis of Gene Function*, in *Molecular Embryology: Methods and Protocols*, P.T. Sharpe and I. Mason, Editors. 1999, Humana Press: Totowa, NJ. p. 487-490.

4. Eisen, J.S., *Developmental neurobiology of the zebrafish.* J Neurosci, 1991. **11**(2): p. 311-7.
5. Kimmel, C.B., R.M. Warga, and T.F. Schilling, *Origin and organization of the zebrafish fate map.* Development, 1990. **108**(4): p. 581-94.
6. Grandel, H., et al., *Neural stem cells and neurogenesis in the adult zebrafish brain: Origin, proliferation dynamics, migration and cell fate.* Developmental Biology, 2006. **295**(1): p. 263-277.
7. Becker, T., et al., *Axonal regrowth after spinal cord transection in adult zebrafish.* J Comp Neurol, 1997. **377**(4): p. 577-95.
8. Rothenaigner, I., et al., *Clonal analysis by distinct viral vectors identifies bona fide neural stem cells in the adult zebrafish telencephalon and characterizes their division properties and fate.* Development, 2011. **138**(8): p. 1459.
9. Nedergaard, M., *Direct signaling from astrocytes to neurons in cultures of mammalian brain cells.* Science, 1994. **263**(5154): p. 1768-71.
10. Reynolds, B.A., W. Tetzlaff, and S. Weiss, *A multipotent EGF-responsive striatal embryonic progenitor cell produces neurons and astrocytes.* J Neurosci, 1992. **12**(11): p. 4565-74.
11. Reynolds, B.A. and S. Weiss, *Generation of neurons and astrocytes from isolated cells of the adult mammalian central nervous system.* Science, 1992. **255**(5052): p. 1707-10.
12. Treichel, A.J. and J.H. Hines, *Development of an Embryonic Zebrafish Oligodendrocyte-Neuron Mixed Coculture System.* Zebrafish, 2018. **15**(6): p. 586-596.
13. Acosta, J.R., et al., *Neuronal cell culture from transgenic zebrafish models of neurodegenerative disease.* Biol Open, 2018. **7**(10).
14. Sakowski, S.A., et al., *A novel approach to study motor neurons from zebrafish embryos and larvae in culture.* J Neurosci Methods, 2012. **205**(2): p. 277-82.
15. Huang, H., et al., *High-throughput screening for bioactive molecules using primary cell culture of transgenic zebrafish embryos.* Cell Rep, 2012. **2**(3): p. 695-704.
16. Andersen, S.S., *Preparation of dissociated zebrafish spinal neuron cultures.* Methods Cell Sci, 2001. **23**(4): p. 205-9.
17. Chen, Z., et al., *Primary neuron culture for nerve growth and axon guidance studies in zebrafish (Danio rerio).* PLoS One, 2013. **8**(3): p. e57539.
18. Meade, M.E., J.E. Roginsky, and J.R. Schulz, *Primary cell culture of adult zebrafish spinal neurons for electrophysiological studies.* J Neurosci Methods, 2019. **322**: p. 50-57.
19. Tapanes-Castillo, A., et al., *Characterization of a novel primary culture system of adult zebrafish brainstem cells.* J Neurosci Methods, 2014. **223**: p. 11-9.
20. Lopez-Ramirez, M.A., et al., *Isolation and Culture of Adult Zebrafish Brain-derived Neurospheres.* J Vis Exp, 2016(108): p. 53617.
21. Russo, G., et al., *Culture and Transfection of Zebrafish Primary Cells.* J Vis Exp, 2018(138).
22. Kinikoglu, B., Y. Kong, and E.C. Liao, *Characterization of cultured multipotent zebrafish neural crest cells.* Exp Biol Med (Maywood), 2014. **239**(2): p. 159-68.

23. Kroehne, V., et al., *Primary Spinal OPC Culture System from Adult Zebrafish to Study Oligodendrocyte Differentiation In Vitro.* Front Cell Neurosci, 2017. **11**: p. 284.
24. Sassen, W.A., et al., *Embryonic zebrafish primary cell culture for transfection and live cellular and subcellular imaging.* Dev Biol, 2017. **430**(1): p. 18-31.
25. Welzel, G., D. Seitz, and S. Schuster, *Magnetic-activated cell sorting (MACS) can be used as a large-scale method for establishing zebrafish neuronal cell cultures.* Sci Rep, 2015. **5**: p. 7959.
26. Ding, B. and D.L. Kilpatrick, *Lentiviral vector production, titration, and transduction of primary neurons.* Methods Mol Biol, 2013. **1018**: p. 119-31.
27. Li, M., et al., *Production of lentiviral vectors for transducing cells from the central nervous system.* J Vis Exp, 2012(63): p. e4031.
28. Maradonna, F., et al., *Assay of vtg, ERs and PPARs as endpoint for the rapid in vitro screening of the harmful effect of Di-(2-ethylhexyl)-phthalate (DEHP) and phthalic acid (PA) in zebrafish primary hepatocyte cultures.* Toxicol In Vitro, 2013. **27**(1): p. 84-91.
29. Pesonen, M.a.A., T.B., *Fish primary hepatocyte culture: an important model for xenobiotic metabolism and toxicity studies.* Aquat Toxicol, 1997. **37**: p. 253-267.
30. Ortega, F., B. Berninger, and M.R. Costa, *Primary culture and live imaging of adult neural stem cells and their progeny.* Methods Mol Biol, 2013. **1052**: p. 1-11.
31. Buehler, D.P., et al., *An optimized procedure for fluorescence-activated cell sorting (FACS) isolation of autonomic neural progenitors from visceral organs of fetal mice.* J Vis Exp, 2012(66): p. e4188.
32. Park, H.C., et al., *Analysis of upstream elements in the HuC promoter leads to the establishment of transgenic zebrafish with fluorescent neurons.* Dev Biol, 2000. **227**(2): p. 279-93.
33. Bernardos, R.L. and P.A. Raymond, *GFAP transgenic zebrafish.* Gene Expr Patterns, 2006. **6**(8): p. 1007-13.
34. Kimmel, C.B., et al., *Stages of embryonic development of the zebrafish.* Dev Dyn, 1995. **203**(3): p. 253-310.
35. Wiles, T.J., et al., *Host Gut Motility Promotes Competitive Exclusion within a Model Intestinal Microbiota.* PLoS Biol, 2016. **14**(7): p. e1002517.
36. Schneider, C.A., W.S. Rasband, and K.W. Eliceiri, *NIH Image to ImageJ: 25 years of image analysis.* Nature Methods, 2012. **9**: p. 671.
37. Ghosh, C., et al., *Cell cultures derived from early zebrafish embryos differentiate in vitro into neurons and astrocytes.* Cytotechnology, 1997. **23**(1-3): p. 221-230.
38. Acosta, J.R., et al., *Neuronal cell culture from transgenic zebrafish models of neurodegenerative disease.* Biology open, 2018. **7**(10): p. bio036475.
39. Kim, C.-H., et al., *Zebrafish elav/HuC homologue as a very early neuronal marker.* Neuroscience Letters, 1996. **216**(2): p. 109-112.
40. Chitnis, A.B. and J.Y. Kuwada, *Axonogenesis in the brain of zebrafish embryos.* J Neurosci, 1990. **10**(6): p. 1892-905.
41. Perez, M.R., et al., *Relationships between radial glial progenitors and 5-HT neurons in the paraventricular organ of adult zebrafish - potential effects of serotonin on adult neurogenesis.* Eur J Neurosci, 2013. **38**(9): p. 3292-301.

42. Lauder, J.M. and H. Krebs, *Serotonin as a differentiation signal in early neurogenesis.* Dev Neurosci, 1978. **1**(1): p. 15-30.
43. Marcus, R.C. and S.S. Easter, Jr., *Expression of glial fibrillary acidic protein and its relation to tract formation in embryonic zebrafish (Danio rerio).* J Comp Neurol, 1995. **359**(3): p. 365-81.
44. Sakowski, S.A., et al., *A novel approach to study motor neurons from zebrafish embryos and larvae in culture.* Journal of neuroscience methods, 2012. **205**(2): p. 277-282.
45. Welzel, G., D. Seitz, and S. Schuster, *Magnetic-activated cell sorting (MACS) can be used as a large-scale method for establishing zebrafish neuronal cell cultures.* Scientific Reports, 2015. **5**: p. 7959.
46. Dahlstrom, A. and K. Fuxe, *Localization of monoamines in the lower brain stem.* Experientia, 1964. **20**(7): p. 398-9.
47. Fricker, A.D., et al., *Serotonin receptor activation leads to neurite outgrowth and neuronal survival.* Brain Res Mol Brain Res, 2005. **138**(2): p. 228-35.
48. Lillesaar, C., et al., *Axonal projections originating from raphe serotonergic neurons in the developing and adult zebrafish, Danio rerio, using transgenics to visualize raphe-specific pet1 expression.* J Comp Neurol, 2009. **512**(2): p. 158-82.
49. Rubenstein, J.L., *Development of serotonergic neurons and their projections.* Biol Psychiatry, 1998. **44**(3): p. 145-50.
50. Vitalis, T. and J.G. Parnavelas, *The role of serotonin in early cortical development.* Dev Neurosci, 2003. **25**(2-4): p. 245-56.
51. McLean, D.L. and J.R. Fetcho, *Ontogeny and innervation patterns of dopaminergic, noradrenergic, and serotonergic neurons in larval zebrafish.* J Comp Neurol, 2004. **480**(1): p. 38-56.
52. Thomas Mueller, M.F.W., *Atlas of Cellular Markers in Zebrafish Neurogenesis* in *Atlas of Early Zebrafish Brain Development* M.F.W. Thomas Mueller, Editor. 2016, Elsevier. p. 27-157.
53. Noctor, S.C., et al., *Neurons derived from radial glial cells establish radial units in neocortex.* Nature, 2001. **409**(6821): p. 714-20.
54. Ge, H., et al., *Poly-L-ornithine promotes preferred differentiation of neural stem/progenitor cells via ERK signalling pathway.* Scientific Reports, 2015. **5**: p. 15535.
55. Flanagan, L.A., et al., *Regulation of human neural precursor cells by laminin and integrins.* Journal of neuroscience research, 2006. **83**(5): p. 845-856.
56. De Arcangelis, A. and E. Georges-Labouesse, *Integrin and ECM functions: roles in vertebrate development.* Trends Genet, 2000. **16**(9): p. 389-95.
57. Bokel, C. and N.H. Brown, *Integrins in development: moving on, responding to, and sticking to the extracellular matrix.* Dev Cell, 2002. **3**(3): p. 311-21.
58. Shu, T. and L.J. Richards, *Cortical axon guidance by the glial wedge during the development of the corpus callosum.* J Neurosci, 2001. **21**(8): p. 2749-58.
59. Bentivoglio, M. and P. Mazzarello, *The history of radial glia.* Brain Res Bull, 1999. **49**(5): p. 305-15.

Figures and Figure Legends

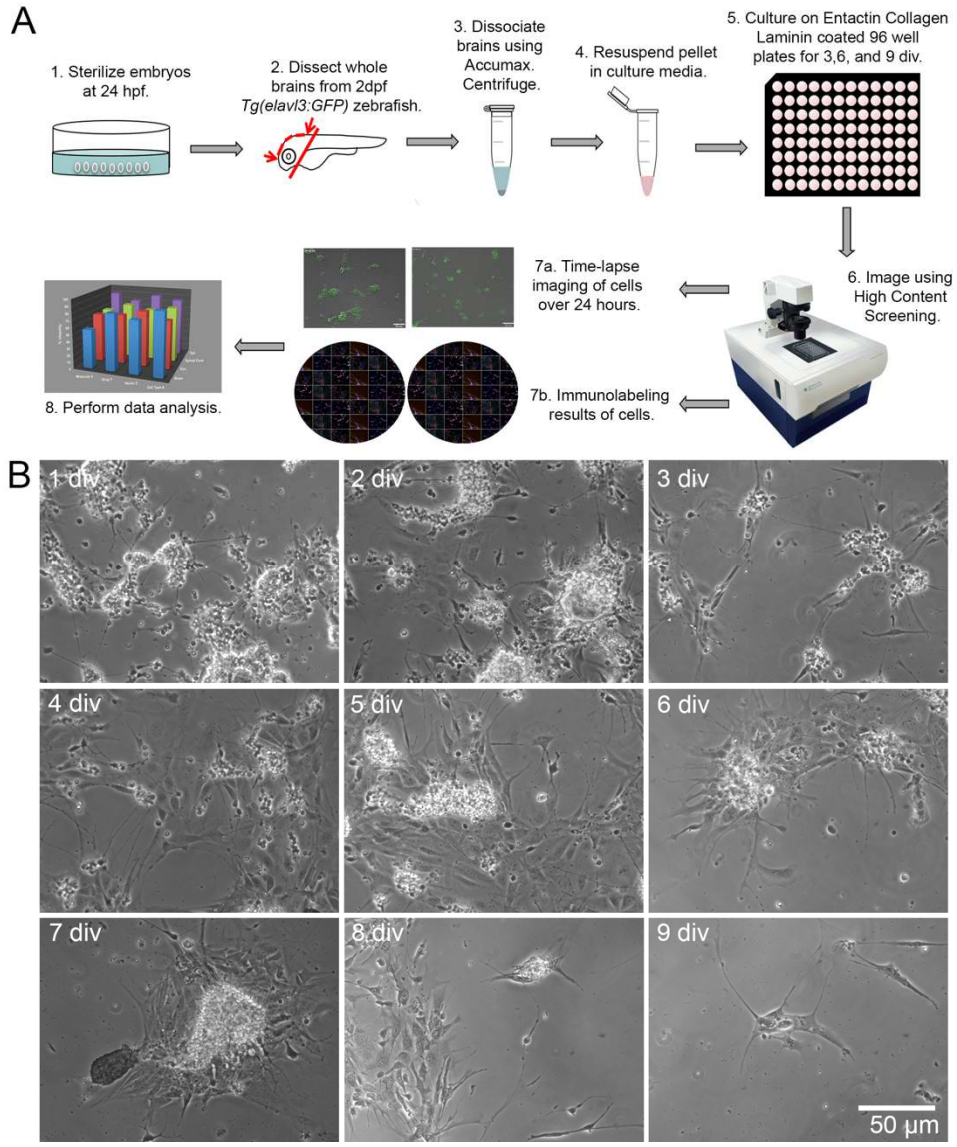

Figure 1. Primary neural cell culture from embryonic zebrafish. (A) Schematic illustration depicting (1) Embryos collection and disinfection, (2) dissection of neural tissue from 48-hpf staged embryos, (3) enzymatic dissociation at 37ºC for 7 minutes using Accumax^{TM}, (4) cell resuspension in complete media (5) and plating cells in 96 well plates maintained at ambient temperatures. Following culture period, (6) plates were used for high content imaging. Cells were (7a) time-lapsed for 24 hours or (7b) characterized using immunocytochemistry, (8) followed by data analysis performed using the MetaXpress

Figure 1. (continued) software. (B) Phase contrast images of zebrafish-brain derived cells at initial isolation (1 div) through 9 div. At 1 div, small clusters of cells along with cells with short and long processes, spindle-shape and large flatter cells are seen. In later days, a greater proportion of cells displayed a flattened morphology and cells clustered together to form sphere-like structures. Scale bar = 50 μm.

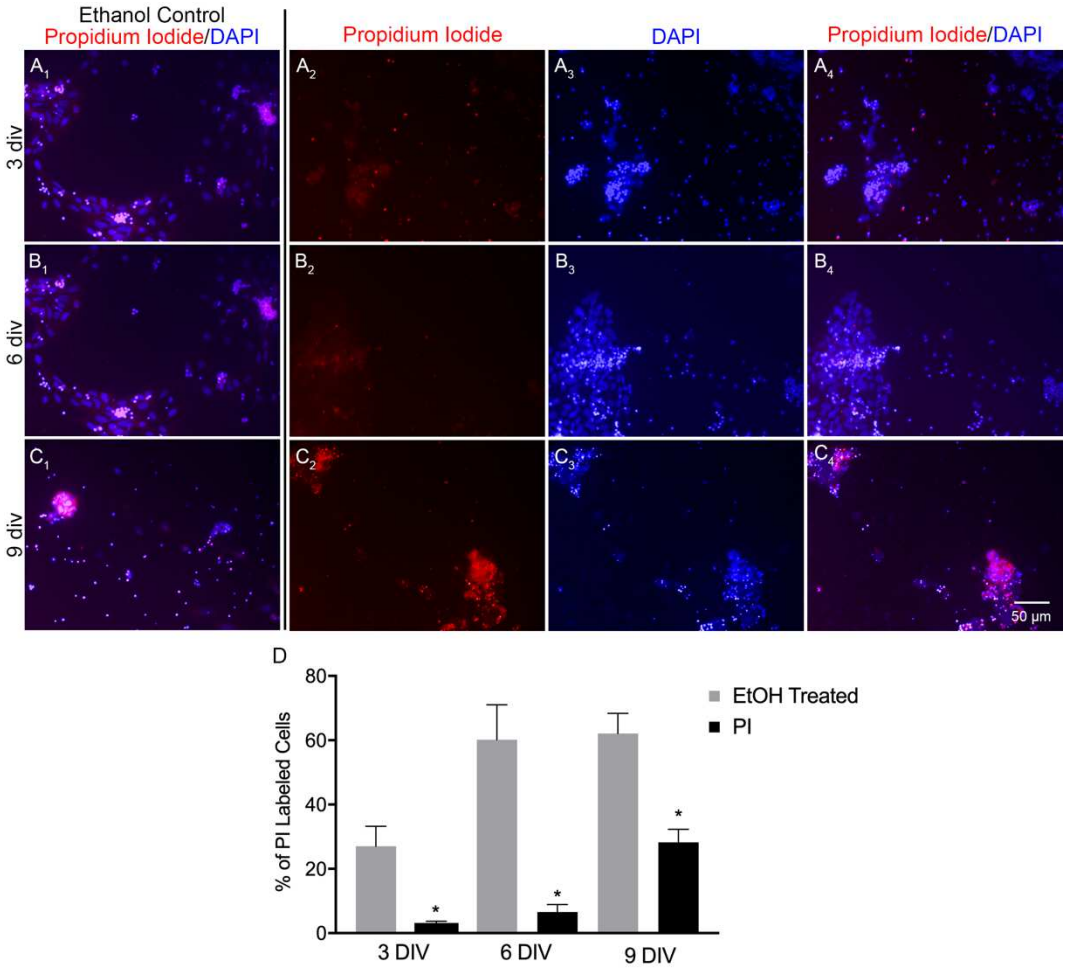

Figure 2. Propidium iodide cell viability assay at 3, 6 and 9 div of dissociated zebrafish neural tissue. (A_1,B_1,C_1) As a control for the PI reagent, samples were subjected to 70% ethanol incubation (10 minutes) to intentionally cause cell death at 3, 6 and 9 div. Dead cells were stained with PI (red) and cell nuclei stained with DAPI (blue), with pink cells indicating dead cells. (A_1-A_4) 3 div cells, (B_1-B_4) 6 div cells, and (C_1-C_4) 9 div cells. Scale bar = 50 µm. (D) Quantitative analysis for number of dead cells at various time-points. Error bar represent standard error of the mean. n= 3 independent experiments, 5 imaging fields per replicate. Abbreviations: DAPI, 4′,6□diamidino□2□phenylindole; PI; propidium iodide. *Significantly different at $p \leq 0.05$.

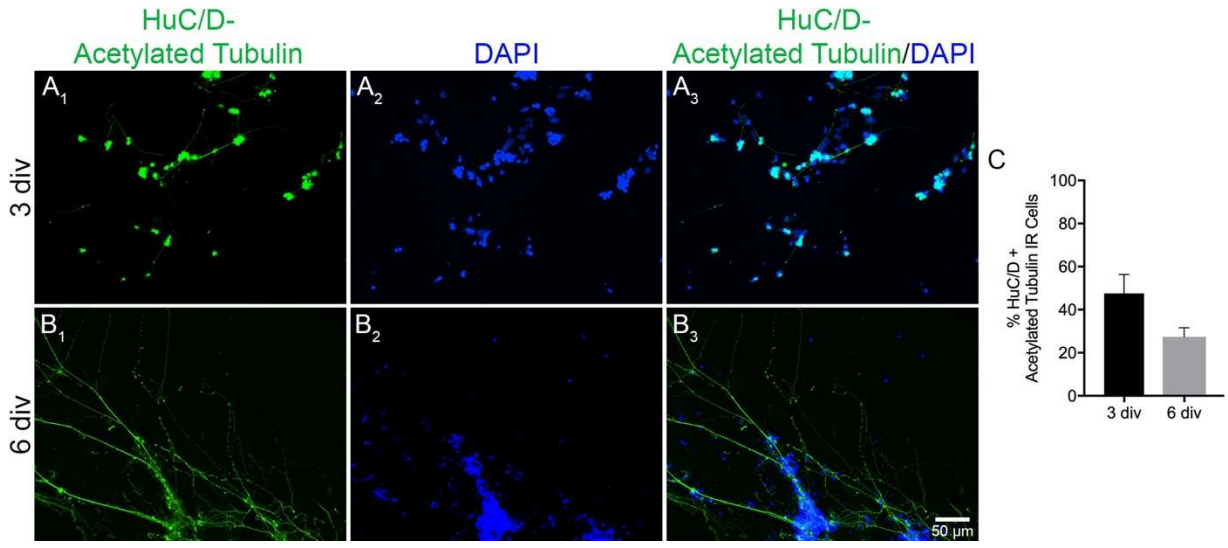

Figure 3. Dissociated zebrafish neural tissue immunolabeled with neuronal markers anti-HuC/D-Acetylated Tubulin at 3 and 6 div. Fluorescence images of zebrafish brain-derived cells illustrating immunoreactivity for HuC/D-Acetylated Tubulin at 3 div (A_1-A_3) and 6 div (B_1-B_3): HuC/D-Acetylated Tubulin:FITC (green) (to identify neuronal nuclei and processes, respectively) with DAPI staining (blue). Scale bar = 50 µm. Abbreviations: DAPI, 4',6-diamidino-2-phenylindole. (C): Quantitative analysis of zebrafish brain-derived cells immunoreactive for HuC/D-Acetylated Tubulin. Error bars represent standard error of the mean. n = 5 independent experiments, 196 imaging fields per experiment. No significant differences found between 3 div and 6 div cultures.

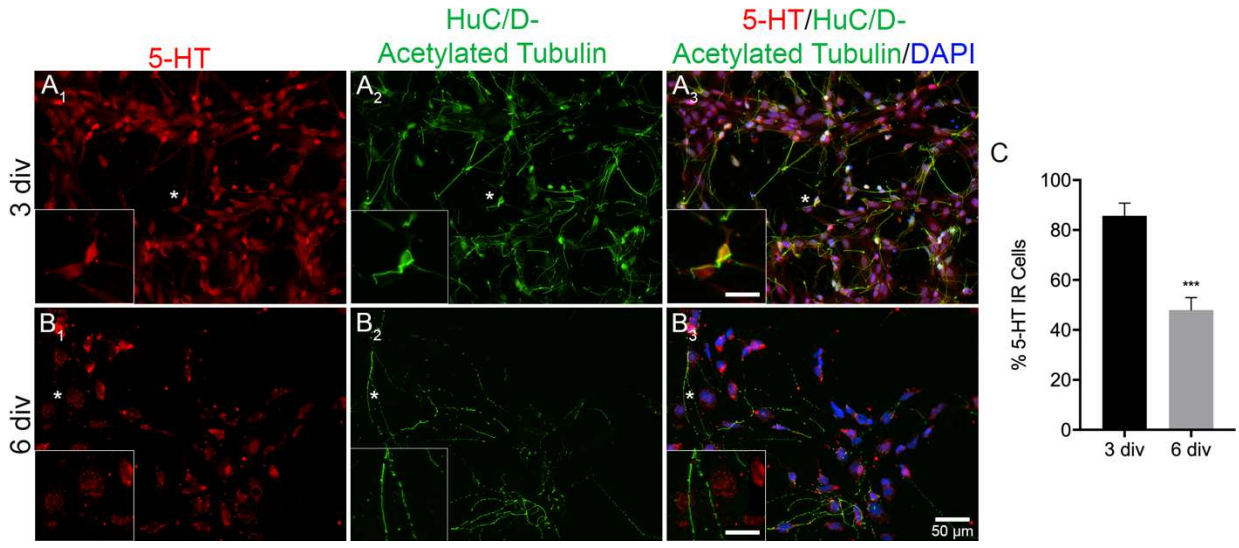

Figure 4. Co-labeling with neuronal markers, anti-5-HT, anti-HuC/D and anti-Acetylated Tubulin antibodies at 3 and 6 div of dissociated zebrafish neural tissue. Fluorescence images of zebrafish brain-derived cells illustrating immunoreactivity for 5-HT and HuC/D-Acetylated Tubulin at 3 div (A_1-A_3) and 6 div (B_1-B_3): 5-HT:Cy3 (red) and HuC/D-Acetylated Tubulin:FITC (green) with DAPI staining (blue). Scale bar = 50 µm (25 µm for insets). Abbreviations: DAPI, 4',6-diamidino-2-phenylindole. (C): Quantitative analysis of zebrafish brain-derived cells immunoreactive for 5-HT at 3 div and 6 div. Error bars represent standard error of the mean. n = 5 independent experiments, 49 imaging fields per experiment. *Significantly different at $p \leq 0.05$.

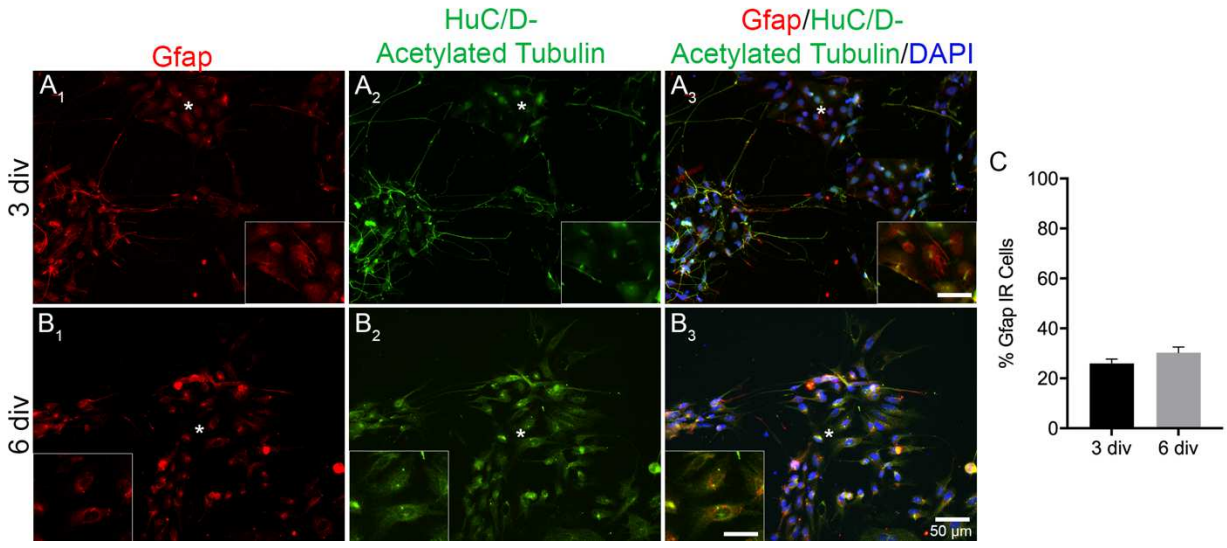

Figure 5. Co-labeling with an anti-Gfap antibody to identify glial cells and anti-HuC/D and anti-Acetylated Tubulin antibodies to identify neurons at 3 and 6 div of dissociated zebrafish neural tissue. Fluorescence images of zebrafish brain-derived cells illustrating immunoreactivity for Gfap and HuC/D-Acetylated Tubulin at 3 div (A_1-A_3) and 6 div (B_1-B_3): Gfap:Cy3 (red) and HuC/D-Acetylated Tubulin:FITC (green) with DAPI staining (blue). Scale bar = 50 µm (25 µm for insets). Abbreviations: DAPI, 4',6-diamidino-2-phenylindole. (C): Quantitative analysis of zebrafish brain-derived cells immunoreactive for Gfap at 3 div and 6 div. Error bars represent standard error of the mean. *Significantly different at $p \leq 0.05$.

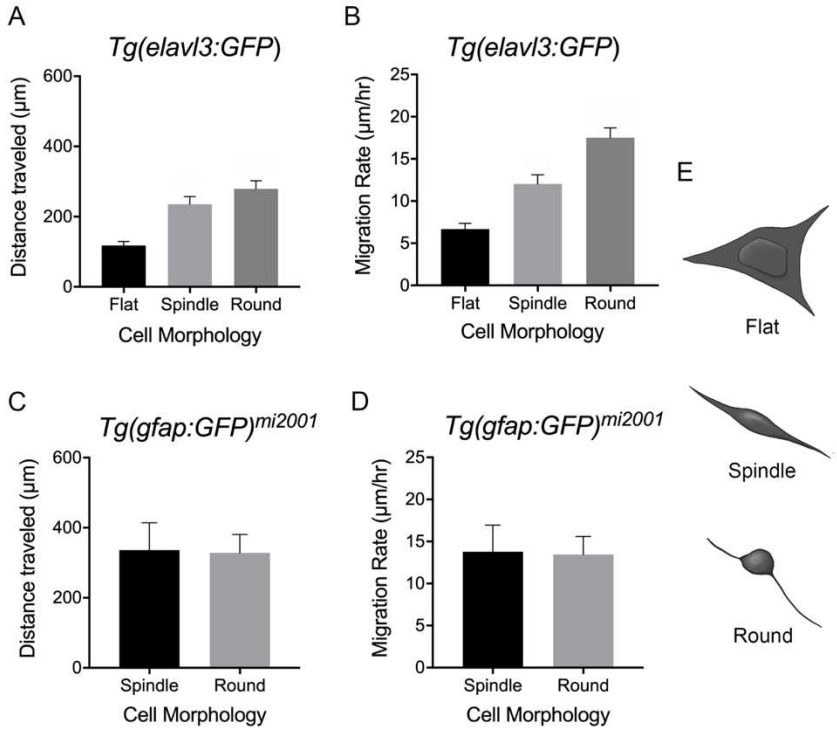

Figure 6: Zebrafish dissociated neural cells tracked with image acquisition and analysis software. (A) Average distance travelled and (B) average migration rates (expressed as µm/hr) for GFP positive *Tg(elavl3:GFP)* dissociated cells based on morphology. (C) Average distance travelled and (D) average migration rates for GFP positive *Tg(gfap:GFP)*^{mi2001} dissociated cells based on morphology. Each bar represents the average of 7-9 imaged cells from 2 time-lapse videos over 24 hours. Error bars represent standard error of the mean.

Supplemental Figures and Legends

Supplemental Table 1: Primary and Secondary Antibodies Used

Primary Antibody	**Host**	**Dilution**	**Supplier**	**Code**
HuC/D	Mouse	1:250	Thermo Fisher	A21271
Acetylated Tubulin	Mouse	1:500	Sigma Aldrich	T6793
Gfap	Rabbit	1:250	Sigma Aldrich	SAB2702475
Serotonin (5-HT)	Rabbit	1:100	Sigma Aldrich	S5545
Tyrosine Hydroxylase	Rabbit	1:100	Chemicon	AB152
ChAT	Rabbit	1:100	Sigma Aldrich	AB1582
Secondary Antibody	**Host**	**Dilution**	**Supplier**	**Code**
Mouse IgG 488	Goat	1:500	Thermo Fisher	A11029
Mouse IgG 568	Goat	1:500	Thermo Fisher	A11004
Rabbit IgG 568	Goat	1:500	Thermo Fisher	A11011

Supplemental Table 2: Enzymatic trials determining the effectiveness of specific enzymes to dissociate neural tissue from embryonic zebrafish for neuronal cultures. Temperature, volume, and incubation times varied between experiments and affected the overall cell survival and attachment rates, with Accumax™ demonstrating the optimum outcome.

Enzyme	Digestion Time	Temperature (Celsius)	Results
Trypsin 0.025%/Ringers	10, 15, 20, 25, 30 minutes	24°	No survival/attachment at 24 hours in vitro
Trypsin 0.05%/Ringers	10, 15, 20, 25, 30 minutes	24°	No survival/attachment at 24 hours in vitro
Trypsin 0.05%/Dissociation Medium (*Chen et. al, 2013*)	10, 15, 20, 25, 30 minutes	24°	No survival/attachment at 24 hours in vitro
Trypsin0.05%/Custom commercial brand solution (*Anderson et. al, 2001*)	10, 15, 20, 25, 30 minutes	24°	No survival/attachment at 24 hours in vitro
Pancreatin	3, 10 minutes	24°	No survival/attachment at 24 hours in vitro
Papain	15, 30 minutes	37°	No survival/attachment at 24 hours in vitro
Accumax™	5, 7, 10 minutes	37°	Survival and attachment up to 9 DIV

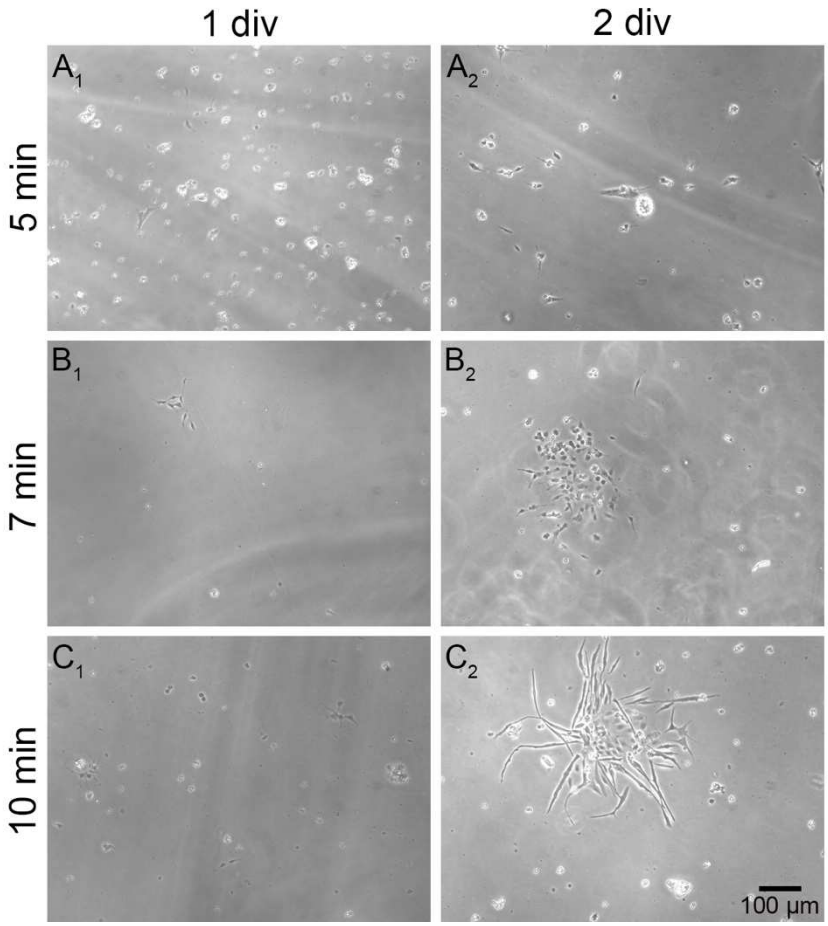

Supplemental Figure 1: Zebrafish brain derived cells after 1 and 2 div using different Accumax™ incubation times. Zebrafish neural tissue dissociated using Accumax™ for (A1-A2) 5 minutes, **(B1-B2)** 7 minutes or **(C1-C2)** 10 minutes. Cells incubated for 5 or 10 minutes after 1 div had many detached cells compared to those incubated for 7 minutes. Cells incubated for 7 minutes at 2 div displayed neuronal morphologies compared to other incubation times. Scale bar = 50 µm.

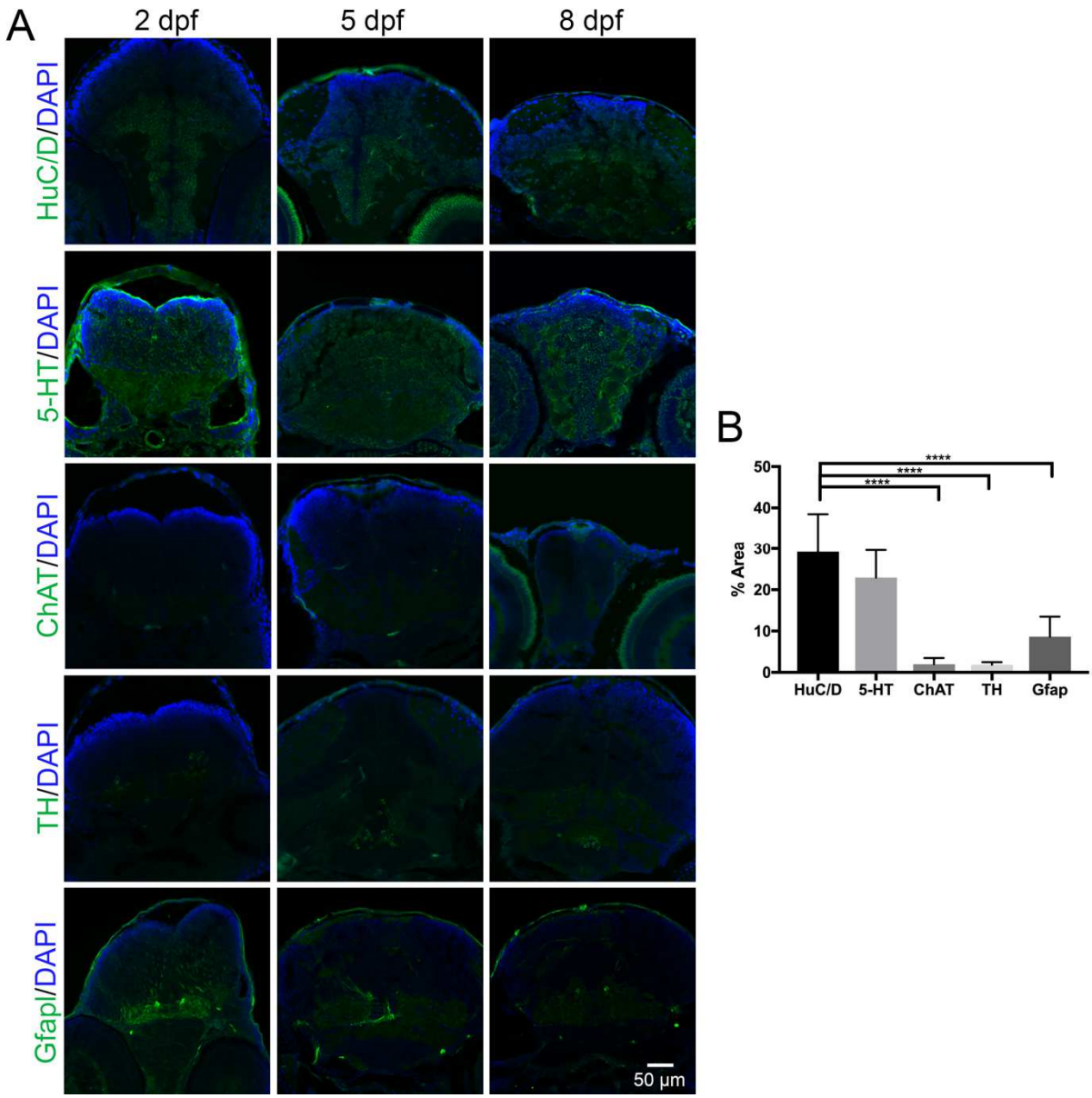

Supplemental Figure 2. Positive control for immunofluorescence staining. (**A**) Primary antibodies directed against HuC/D, 5-HT, ChAT, TH, and Gfap were used to determine localization in the larval zebrafish brain at 2 dpf, 5 dpf, and 8 dpf, respective to the time points studied *in vitro.* (**B**) Quantification of total area immunofluorescence for respective antibody. One-way ANOVA comparing the mean of each column with HuC/D; $p \leq 0.05$.

Supplemental Video 1: Time-lapse microscopy of cells dissociated from neural tissue dissected from *Tg(elavl3:GFP)* zebrafish. Images were captured every 5 minutes over 18 hours. GFP-expressing cells indicate neurons. Videos were used to analyzed cell migration and cell velocity using MetaXpress software. Scale bar = 50 μm.

Supplemental Video 2: Time-lapse microscopy of cells dissociated from neural tissue dissected from *Tg(gfap:GFP)*^{mi2001} zebrafish. GFP-expressing cells indicate glial cells. Images were captured every 5 minutes over 18 hours. Videos were used to analyzed cell migration and cell velocity using MetaXpress software. Scale bar = 50 μm.

ACKNOWLEDGEMENTS

First, I would like to acknowledge the person who conceded more than me through grad school, my husband Mark. Somehow, we managed to make it through both working on our careers and being selfish at times, but this would not have been possible without his support (mentally and financially). Also, to my mom Melanie for moving out to Des Moines to help out my family after I started grad school only for me to finish up early and leave.

I would also like to thank my major professor, Dr. Aileen Keating, for adopting me when I was an orphan and pushing me to not leave any time wasted. She was also understanding that I had a family and never made me feel that I wasn't doing enough in the lab when having to take care of things outside of it. I'm glad that my PhD experience ended up the way it did, women helping other women excel at science (or any field) is one of the most inspiring things and kept me going. I am also grateful to Dr. Don Sakaguchi, who let me hang out in his lab and do science and eat their snacks, to Dr. Jeff Essner, whose developmental biology class got me interested in research in the first place, for Dr. Jason Ross reminding me to always go HAM, and for Dr. Geetu Tuteja for being a part of my somewhat impromptu committee organization.

Special thanks to all my grad school friends over the years, Sweta Roy-Carson, Kevin Natukunda, Maggie Kline, Bhavika Patel, and those who came late in the game Hannah Spaulding, Jake Siebert, Crystal Roach, and Zoe Kiefer. Y'all the real MVPs.